

**Combustion Processes
in a Diesel Engine**

CYRIL CRUA

Combustion Processes in a Diesel Engine

Cyril Crua

A thesis submitted in partial fulfilment of the requirement of
the University of Brighton for the degree of
Doctor of Philosophy

December 2002

School of Engineering, University of Brighton
in collaboration with
Ricardo Consulting Engineers

Copyright

Attention is drawn to the fact that copyright of this thesis rests with its author. This copy of the thesis has been supplied on condition that anyone who consults it is understood to recognise that its copyright rests with its author and that no quotation from the thesis and no information derived from it may be published without the prior written consent of the author.

This thesis may be made available for consultation within the University Library and may be photocopied or lent to other libraries for the purposes of consultation.

Abstract

The effects of in-cylinder and injection pressures on the formation and autoignition of diesel sprays at realistic automotive in-cylinder conditions was investigated. A two-stroke diesel Proteus engine has been modified to allow optical access for visualisation of in-cylinder combustion processes. Various optical techniques were used to investigate the combustion processes. These include high-speed video recording of the liquid phase, high-speed schlieren video recording of the vapour phase and laser-induced incandescence for soot imaging. The spray cone angle and penetration with time data extracted from photographic and high-speed video studies are presented.

The effects of droplet evaporation, breakup and air entrainment at the initial stage of spray penetration were studied theoretically using three models. It was found that the predictions of the model combining bag breakup and air entrainment are in good agreement with the experimental measurements.

Spray autoignition was investigated using video, in-cylinder pressure, and schlieren recordings. Pseudo three-dimensional visualisation of the autoignition was achieved by simultaneous use of two high-speed video cameras at right angles to each other. The effects of elevated injection and in-cylinder pressures on the ignition delay and ignition sites have been investigated.

Laser-induced incandescence was performed to obtain maps of soot concentration for a range of engine conditions. The influence of in-cylinder and injection pressures on soot formation sites and relative soot concentration has been studied. The work has been mainly focused on the specificities of soot formation under extreme in-cylinder conditions.

Contents

COPYRIGHT	ii
ABSTRACT	iii
CONTENTS	iv
LIST OF TABLES	viii
LIST OF FIGURES	ix
ACKNOWLEDGEMENTS	xv
DECLARATION	xvi
NOMENCLATURE	xvii
1. INTRODUCTION.....	1
1.1. Background	1
1.2. Thesis structure.....	4
1.3. Objectives.....	5
2. REVIEW OF EXPERIMENTAL STUDIES OF COMBUSTION PROCESSES IN DIESEL ENGINES	6
2.1. Introduction	6
2.2. Optical techniques for in-cylinder observation	8
2.2.1. Autoignition	9
2.2.1.1. <i>Autoignition sites</i>	9
2.2.1.2. <i>Autoignition delay</i>	10
2.2.2. Soot formation sites and concentration.....	11
2.2.2.1. <i>Laser-Induced Incandescence (LII)</i>	14
2.2.2.2. <i>Laser-Induced Fluorescence (LIF)</i>	20
2.2.3. Local temperature.....	20
2.2.3.1. <i>Laser Induced Fluorescence (LIF)</i>	21
2.2.3.2. <i>Coherent Anti-stokes Raman Scattering (CARS)</i>	27
2.2.3.3. <i>Degenerate Four Wave Mixing (DFWM)</i>	29
2.2.3.4. <i>Raman Doppler Velocimetry (RDV)</i>	29
2.2.3.5. <i>Rayleigh scattering</i>	29
2.2.4. Local air-fuel ratio	31
2.2.4.1. <i>Exciplex laser-induced fluorescence</i>	31
2.2.4.2. <i>Planar Laser Rayleigh Scattering (PLRS)</i>	32
2.2.5. Velocity measurements	36
2.2.5.1. <i>Laser Doppler Anemometry (LDA)</i>	36
2.2.5.2. <i>Particle Image Velocimetry (PIV)</i>	37
2.2.6. Experimental considerations	37
2.2.6.1. <i>Refractive index gradients</i>	37
2.2.6.2. <i>Soot absorption</i>	38
2.2.6.3. <i>Molecular absorption</i>	39
2.3. Conclusions of Chapter 2	39
3. DESIGN OF THE PROTEUS HIGH-PRESSURE SPRAY RIG	42
3.1. General description.....	42
3.1.1. Control software	45
3.1.2. Health and safety features.....	46
3.2. Optical high-pressure spray chamber.....	47

3.2.1. Characteristics of the windows	50
3.2.2. Influence of window fouling	52
3.3. Fuel system	52
3.3.1. Injector nozzle library	56
3.3.2. Fuel injection calibration	59
3.4. Accuracy and calibration	60
3.4.1. Evaluation of the compression ratio	60
3.4.2. Comparability to a modern diesel engine	63
3.4.3. Errors and delays	63
3.5. Conclusions of Chapter 3	64
4. DIESEL SPRAY CHARACTERISATION	65
4.1. Background	65
4.2. Experimental apparatus and procedure	69
4.2.1. High-speed video recording of diesel sprays	69
4.2.2. Photographic imaging of sprays	72
4.2.3. Schlieren video imaging of vapour phase	74
4.3. Experimental results	75
4.3.1. Influence of injection pressure	83
4.3.2. Influence of in-cylinder temperature	86
4.3.2.1. <i>Low-temperature charge</i>	86
4.3.2.2. <i>High-temperature charge</i>	89
4.3.3. Vapour dispersion	91
4.4. A model for spray penetration	96
4.4.1. Basic equations and approximations	97
4.4.1.1. <i>Dynamics of droplets</i>	97
4.4.1.2. <i>Evaporation and droplet breakup models</i>	100
4.4.2. Effect of droplet evaporation	102
4.4.3. Effect of droplet bag breakup	103
4.4.3.1. <i>Stokes flow</i>	105
4.4.3.2. <i>Allen flow</i>	106
4.4.3.3. <i>Newton flow</i>	106
4.4.4. Effect of droplet stripping breakup	107
4.4.4.1. <i>Stokes flow</i>	108
4.4.4.2. <i>Allen flow</i>	109
4.4.4.3. <i>Newton flow</i>	109
4.4.5. Diagrammatic presentation of flow and breakup regimes	110
4.4.6. Experimental results for the initial stage of penetration	114
4.5. Conclusions of Chapter 4	118
5. AUTOIGNITION OF DIESEL SPRAYS	120
5.1. Introduction	120
5.2. Background	120
5.3. Experimental apparatus and procedure	122
5.3.1. Pseudo three-dimensional high-speed recordings	122
5.3.2. Combustion pressure peak measurements	123
5.4. Experimental results	125
5.4.1. Autoignition sites	125
5.4.2. Autoignition delay	131
5.4.2.1. <i>Spray penetration</i>	136
5.4.2.2. <i>Droplet breakup</i>	137

5.4.2.3. Droplet evaporation	138
5.4.2.4. Chemical autoignition	139
5.4.2.5. Summary of the discussion.....	139
5.5. Conclusions of Chapter 5	139
6. LASER-INDUCED INCANDESCENCE	141
6.1. Introduction	141
6.2. Background	141
6.3. Experimental configuration	142
6.3.1. Laser optics	144
6.3.2. Image acquisition	147
6.3.2.1. Camera configuration	147
6.3.2.2. Image doubling adapter.....	149
6.3.2.3. Optical filters.....	150
6.3.2.4. Image intensifier relay optics	151
6.3.3. Acquisition timing	152
6.3.4. Standard post-processing	154
6.3.5. Accuracy	157
6.3.5.1. Effect of laser fluence on LII signal.....	157
6.3.5.2. Spectral interferences.....	159
6.3.5.3. Soot particle size sensitivity	160
6.3.5.4. LII signal trapping	160
6.3.5.5. Overall accuracy.....	162
6.4. Experimental results	164
6.4.1. Influence of in-cylinder pressure.....	164
6.4.2. Influence of injection pressure	173
6.4.3. Detailed LII sequence	180
6.5. Conclusions of Chapter 6	186
7. CONCLUSIONS	188
7.1. Diesel spray characterisation.....	188
7.2. Autoignition of diesel sprays.....	189
7.3. Soot formation study	190
7.4. Recommendations for further work.....	191
REFERENCES	193
Papers published by the author	204
APPENDICES	205
APPENDIX A : DIESEL SPRAY CHARACTERISATION	A-1
Source code for high-speed video post-processing	A-1
Experimental conditions for high-speed video of spray	A-5
Experimental conditions for liquid spray photography	A-7
Experimental conditions for vapour fuel visualisation	A-11
Standard dimensionless numbers	A-14
Effect of fuel pressure on liquid spray for low-temperature charge....	A-15
Effect of fuel pressure on liquid spray for high-temperature charge ..	A-18
Effect of gas density on liquid spray for low-temperature charge	A-21
Effect of gas density on liquid spray for high-temperature charge	A-23
Effect of gas density on vapour for high-temperature charge	A-25
APPENDIX B : AUTOIGNITION OF DIESEL SPRAYS	B-1
Experimental conditions for high-speed video of spray autoignition....	B-1

APPENDIX C : LASER-INDUCED INCANDESCENCE	C-1
Characteristics of image intensifier relay optics	C-1
Example of LII data set	C-4
Experimental conditions for LII data sets.....	C-6
Experimental conditions for LII sequence	C-10
Influence of fuel pressure on soot formation.....	C-12

List of tables

Table 2-1. References on LII applied to in-cylinder soot formation.....	15
Table 2-2. Experimental configurations for references on LII. Values in italic were calculated from published data.	16
Table 2-3. Matrix of spatially accurate laser-based techniques for combustion temperatures and spectrometry (adapted from Eckbreth, 1996).	40
Table 2-4. Summary of optical techniques used for high-pressure diesel combustion diagnostic.	41
Table 3-1. Properties of the diesel fuel tested.	56
Table 3-2. Injector nozzle characteristics.....	58
Table 3-3. Delays between start of injection pulse and start of fuel delivery for a 30 mm ³ injection with a 0.2 mm VCO nozzle, with the corresponding injection pulse durations.....	60
Table 3-4. Comparison between a modern diesel engine and the Proteus.	63
Table 3-5. Summary of errors and delays for the optical Proteus spray rig.	64
Table 4-1. Table of equivalence for gas density and in-cylinder pressure, assuming a compression ratio of 9 and a polytropic coefficient of 1.3.	79
Table 4-2. Values of α_d used in Figures 4-32 to 4-34.	115
Table 6-1. Summary of the measurement errors for LII.	163
Table 6-2. Engine conditions for detailed LII sequence.....	181

List of figures

Figure 1-1. Past and projected trends in fuel injection pressure.....	2
Figure 2-1. Typical strategy for the application of LII.	17
Figure 2-2. Approximate representation of light emissions caused by a laser pulse in a sooty environment. LIF: laser-induced fluorescence.....	18
Figure 2-3. Simplified energy profile of the fluorescence signal.....	22
Figure 2-4. Energy level diagram for two-line thermometry.	23
Figure 2-5. Instrumentation setup for two-line LIF thermometry.	25
Figure 2-6. Approach for coherent anti-Stokes Raman spectroscopy.	27
Figure 2-7. Energy level diagram for resonant CARS. Real states and virtual states are indicated by solid and dashed lines respectively.	27
Figure 2-8. Experimental setup for exciplex LIF measurement. TM: partially transmitting mirror, SL: spherical lens, CL: cylindrical lens, BPF: bandpass filter.	32
Figure 2-9. Typical setup for quantitative PLRS measurements of fuel-air ratios. NDF: neutral density filter, SL: spherical lens, CL: cylindrical lens, TM: partially transmitting mirror, BPF: band pass filter.	35
Figure 2-10. Basic differential LDA system.....	36
Figure 3-1. CAD drawing and photograph of the Proteus engine.	43
Figure 3-2. Photograph of the Proteus test cell showing the gearbox and parts of the dynamometer.	44
Figure 3-3. Schematic of the test bed layout showing the Proteus, dynamometer, compressors, heaters and main valves (⊗).	45
Figure 3-4. Window blank with burst disc holder and cylinder pressure transducer.	47
Figure 3-5. Schematic of the optical chamber.	48
Figure 3-6. CFD simulation of the internal flow for loop scavenging.	49
Figure 3-7. CAD drawing of a window and its holder.	50
Figure 3-8. Measured transmittance of a typical 20 mm thick BK7 glass window used on the Proteus engine.	51
Figure 3-9. Transmittance of a 10 mm thick sapphire glass (Laser components, 2001).	52
Figure 3-10. Schematic view of the fuel injection system.....	53
Figure 3-11. Photograph of the fuel injection equipment.....	54
Figure 3-12. 160 MPa injector used for LII studies	55
Figure 3-13. Photograph of the sprays with a six-hole VCO nozzle.	57
Figure 3-14. Diagrams of VCO (a) and mini-sac (b) nozzles.	58
Figure 3-15. Injection rate diagram from standard and custom controller (100 MPa injection pressure).....	59
Figure 3-16. Pressure-volume diagram for a typical compression stroke on the Proteus engine.	61
Figure 3-17. Polytropic coefficient from a log(P) versus log(V) chart.	62
Figure 4-1. A side view of the experimental set-up for backlit spray photography.....	70
Figure 4-2. Raw digital spray image (a) and thresholded image (b) showing maximum penetration length and spray cone.	71
Figure 4-3. Experimental set-up for spray close-up study.....	72
Figure 4-4. Experimental set-up for backlit spray photography. The combustion chamber is viewed from the side.	73

Figure 4-5. Experimental set-up for schlieren video. The combustion chamber is viewed from the top. Both mirrors are 0.144 m in diameter and have a focal length of 1.2 m.	74
Figure 4-6. Comparison between 0.2 mm single-hole, 0.15 mm single-hole and 0.15 mm multi-hole VCO nozzles, for an injection pressure of 160 MPa. Times are in milliseconds after first frame showing visible liquid injection. The apparent difference in dimensions of the sprays produced by the single-hole and multi-hole nozzles are due to differences in lighting and scaling conditions.	76
Figure 4-7. Injection needle lift trace for a 0.2 mm VCO single hole nozzle, with an injection pressure of 160MPa.	77
Figure 4-8. Single and multi-hole penetrations with time for 0.2 mm VCO nozzles and an injection pressure of 160 MPa.	78
Figure 4-9. Backlit spray images taken 1 ms after the start of injection in air at 3 MPa with an injection duration of 3.41 ms at four fuel rail pressures.	80
Figure 4-10. Backlit spray images taken 1 ms after the start of injection in air at 8 MPa with an injection duration of 3.41 ms at four fuel rail pressures.	80
Figure 4-11. High-speed video sequence showing the development of areas of droplets ‘peeling’ back along the spray plume. Enlarged frames presented are from 1.1 to 1.4 ms after start of injection pulse (ASOI).	81
Figure 4-12. Backlit spray images taken 0.9 ms ASOI in air at 3 MPa with an injection duration of 0.9 ms at three fuel rail pressures.	82
Figure 4-13. Back lit spray images taken 0.9 ms ASOI in gas at 8 MPa with an injection duration of 0.9 ms at two fuel rail pressures.	82
Figure 4-14. Influence of injection pressure on penetration for low-temperature charge. 49 kg m^{-3} in-cylinder density; 0.2 mm VCO nozzle. Broken line shows time at which ignition is highly probable.	83
Figure 4-15. Slugs of fuel breaking off the spray. Broken line shows the detected spray penetration length. Low temperature charge; 160 MPa injection pressure; 7.3 MPa ICP; 32 kg m^{-3} in-cylinder density; 0.2 mm VCO nozzle.	84
Figure 4-16. Close-up images obtained by high-speed video, showing the oscillation of the liquid spray. Similar spray patterns were observed every 0.148 ms and are indicated by the white arrows. Injection pressure was 160 MPa, in-cylinder pressure was 5.2 MPa, nozzle was a 0.2 mm VCO type. Times are in milliseconds relative to the first frame showed.	85
Figure 4-17. Evolution of spray full cone angle at different injection pressures. Low temperature charge; 32 kg m^{-3} in-cylinder density; 0.2 mm single hole VCO nozzle.	86
Figure 4-18. Influence of ambient density on liquid penetration for low-temperature charge. 160 MPa injection pressure; 0.2 VCO single hole nozzle with a 30 mm^3 fuelling. Broken line shows time at which ignition is highly probable.	87
Figure 4-19. Same as Figure 4-18 with an injection pressure of 100 MPa.	87
Figure 4-20. Same as Figure 4-18 with an injection pressure of 60 MPa.	88
Figure 4-21. Comparison between mini-sac and VCO single-hole nozzles and the correlation proposed by Hiroyasu and Arai (1990) for non-	

List of figures

evaporating sprays ($P_{inj} = 160 \times 10^6$ Pa; $P_g = 6.3 \times 10^3$ Pa; $\rho_g = 42$ kg m ⁻³ ; $D_o = 0.2 \times 10^{-3}$ m).....	89
Figure 4-22. Influence of injection pressure on liquid penetration for high-temperature charge. 14 kg m ⁻³ gas density; 0.2 VCO single hole nozzle with a 30 mm ³ fuelling. Broken line shows time at which ignition is highly probable.....	90
Figure 4-23. Evolution of spray full cone angle at different injection pressures. High temperature charge; 32 kg m ⁻³ in-cylinder density; 0.2 mm single hole VCO nozzle.	91
Figure 4-24. Example of a schlieren image for an injection pressure of 100 MPa and an in-cylinder pressure of 8 MPa. Recording was performed 3.1 ms after start of injection pulse.	92
Figure 4-25. Vapour and liquid penetrations for both temperature charge conditions (160 MPa injection pressure; 28 kg m ⁻³ in-cylinder density).....	93
Figure 4-26. Vapour and liquid penetrations for both temperature charge conditions (100 MPa injection pressure; 28 kg m ⁻³ in-cylinder density).....	93
Figure 4-27. Schlieren repeatability tests. Broken line shows limits of rig optical access (140 MPa injection pressure; 21 kg m ⁻³ in-cylinder density).....	94
Figure 4-28. Influence of gas density on vapour penetration (160 MPa injection pressure; 0.2 VCO nozzle)	94
Figure 4-29. Influence of injection pressure on vapour penetration. 30 kg m ⁻³ charge density; 0.2 VCO nozzle.....	95
Figure 4-30. Threshold values of droplets velocities and droplet radii corresponding to transition from Stokes to Allen flow; Allen to Newton flow and the threshold value of applicability of the Newton flow approximation. Threshold values of droplets velocities versus droplet radii corresponding to the development of stripping breakup and bag breakup.	112
Figure 4-31. Plots of t_{ev} , t_b and t_s versus $-\log r$ for the same values of parameters as in Figure 4-30.....	114
Figure 4-32. Comparison between measured spray penetration lengths (circles) and predicted spray penetration lengths for no breakup and air entrainment (curves 1); stripping breakup process only (curves 2); bag breakup process only (curves 3); bag breakup and entrainment processes (curves 4).	116
Figure 4-33. Comparison between measured spray penetration lengths (circles) and predicted spray penetration lengths for no breakup and air entrainment (curves 1); stripping breakup process only (curves 2); bag breakup process only (curves 3); bag breakup and entrainment processes (curves 4).	117
Figure 4-34. Comparison between measured spray penetration lengths (circles) and predicted spray penetration lengths for no breakup and air entrainment (curves 1); stripping breakup process only (curves 2); bag breakup process only (curves 3); bag breakup and entrainment processes (curves 4).	117
Figure 5-1. Experimental setup for pseudo three-dimensional autoignition recording.	123

Figure 5-2. Comparison between autoignition delays detected by in-cylinder pressure rise, by flame luminosity (100 MPa injection pressure, 720 K in-cylinder temperature). Times are relative to start of injection (when droplets are first seen leaving the nozzle). The injector nozzle shuts at 3.1 ms.....	125
Figure 5-3. Schlieren imaging of vapour phase (dark) and autoignition (bright), recorded 2.4 ms ASOI (160 MPa injection pressure, 9 MPa in-cylinder pressure, 720 K in-cylinder temperature). Distances are relative to the injector nozzle (represented by a black circle). For clarity, white broken line highlights visible limits of vapour region. Liquid spray penetration for similar conditions is 35 mm (see Chapter 4).....	126
Figure 5-4. Pseudo-3D recordings of autoignitions of sprays injected at 100 MPa for a range of in-cylinder pressures. The first pair of frames for each of the 5 series corresponds to the autoignition time. Times are relative to the start of the injection.	128
Figure 5-5. Pseudo-3D recordings of autoignitions of sprays injected at 140 MPa for a range of in-cylinder pressures. The first pair of frames for each of the 5 series corresponds to the autoignition time. Times are relative to the start of the injection.	129
Figure 5-6. Pseudo-3D recordings of autoignitions of sprays injected at 160 MPa for a range of in-cylinder pressures. The first pair of frames for each of the 5 series corresponds to the autoignition time. Times are relative to the start of the injection.	130
Figure 5-7. Comparison between autoignition delays detected by in-cylinder pressure rise, by flame luminosity (100 MPa injection pressure, 720 K in-cylinder temperature), and predicted by Equation (5-1) (coefficients $A = 0.095$; $B = 8300$ K; $n = 0.980$). Times are relative to start of injection (when droplets are first seen leaving the nozzle). The injector nozzle shuts at 3.1 ms.....	131
Figure 5-8. High-speed video recordings of autoignitions of sprays injected at 100 MPa for a range of in-cylinder pressures. Times are relative to the start of the injection, in-cylinder pressures were measured at the autoignition times.....	133
Figure 5-9. Same as Figure 5-8 for a 140 MPa injection pressure.....	134
Figure 5-10. High-speed video recordings of autoignitions of sprays injected at 160 MPa for a range of in-cylinder pressures. Times are relative to the start of the injection, in-cylinder pressures were measured at the autoignition times.....	135
Figure 6-1. LII images without additive (left image) and with additive (right image). Scales indicate distances from the nozzle in millimetres. 160 MPa injection pressure, 8.0 MPa ICP at non-fired TDC, images recorded 3.7 ms after start of injection pulse.....	143
Figure 6-2. Photograph of optical arrangement with superimposition of the laser beam path.	144
Figure 6-3. (a) Properly aligned mirror. (b) Misaligned laser mirror.....	145
Figure 6-4. Photographs of a four-lens sheet forming optics.....	145
Figure 6-5. Checking the alignment of the laser beam with an iris diaphragm.	146
Figure 6-6. Experimental set-up for LII study.....	148

Figure 6-7. CCD camera lens with image-doubling adapter and interference filters.....	149
Figure 6-8. Measured transmission profiles of filters used for LII and LIS. Dotted lines show the FWHM for each filter, broken line indicates the laser wavelength (532 nm).....	151
Figure 6-9. Front panel of image intensifier control.	151
Figure 6-10. Acquisition strategy for elastic scattering and LII imaging.....	154
Figure 6-11. Method used for processing the LII data.	155
Figure 6-12. Influence of the number of images on the average image intensity. Coefficients of variation (ratio of standard deviation and mean intensity) are presented, with a power type trendline. Images were recorded 3.8 ms ASOI for a 140 MPa injection pressure and 8 MPa in-cylinder pressure.	156
Figure 6-13. Examples of standard deviation and ensemble averaged images. 140 MPa injection pressure, 8 MPa in-cylinder pressure, images recorded 3.8 ms ASOI.	157
Figure 6-14. Dependence of LII signal on laser fluence for 100 nm particle radius (adapted from Tait and Greenhalgh, 1993).....	158
Figure 6-15. Illustration of LII signal trapping by soot.	161
Figure 6-16. LII signal intensity profiles for an injection pressure of 100 MPa and a range of in-cylinder pressures (6, 7, 8 and 9 MPa at non-fired TDC). Each data point represents the average intensity of at least 27 images. Times are relative to start of injection pulse.	165
Figure 6-17. As Figure 6-16 but for an injection pressure of 140 MPa.....	166
Figure 6-18. As Figure 6-16 but for an injection pressure of 160 MPa.....	166
Figure 6-19. Comparison between flame luminosity from high-speed video (a) and ensemble averaged soot incandescence (b) for an injection pressure of 160 MPa, ICP of 8.0 MPa at non-fired TDC, 3.1 ms ASOI. ...	168
Figure 6-20. Ensemble averaged images showing the influence of ICP on initial soot formation sites. Images were recorded 2.3 ms ASOI, for an injection pressure of 100 MPa. ICPs were measured at non-fired TDC. Contrast was enhanced for clarity, white lines show ensemble averaged liquid fuel penetration obtained by simultaneous LIS, scales indicate distances from the nozzle in millimetres.	169
Figure 6-21. As Figure 6-20 but for an injection pressure of 140 MPa. Images were recorded between 2.1 and 2.3 ms ASOI.	169
Figure 6-22. As Figure 6-20 but for an injection pressure of 160 MPa. Images were recorded between 2.0 and 2.2 ms ASOI.	170
Figure 6-23. Examples of liquid and soot clusters for early and late soot formation. 160 MPa injection pressure, 6.0 MPa ICP at TDC, times are relative to start of injection pulse. Contrast of images recorded at 2.2 ms showing simultaneous LIS (upper half) and LII (lower half) was enhanced for clarity.....	171
Figure 6-24. Ensemble averaged images showing the effect of ICP on late soot concentration zones. Images were recorded between 3.5 and 3.7 ms ASOI, for an injection pressure of 100 MPa. ICPs were measured at non-fired TDC.	172
Figure 6-25. As Figure 6-24 but for an injection pressure of 140 MPa. Images were recorded between 3.4 and 3.7 ms ASOI.	172

List of figures

Figure 6-26. As Figure 6-24 but for an injection pressure of 160 MPa. Images were recorded between 3.4 and 3.6 ms ASOI.	173
Figure 6-27. LII signal intensity profiles for an in-cylinder pressure of 6 MPa at non-fired TDC and a range of injection pressures (100, 140 and 160 MPa at non-fired TDC). Each data point represents the average intensity of at least 27 images. Times are relative to the start of the injection pulse.....	174
Figure 6-28. As Figure 6-27 but for an in-cylinder pressure of 7 MPa.	174
Figure 6-29. As Figure 6-27 but for an in-cylinder pressure of 8 MPa.	175
Figure 6-30. As Figure 6-27 but for an in-cylinder pressure of 9 MPa.	175
Figure 6-31. Estimated proportion of injected fuel with time for a 30 mm ³ injection at three injection pressures (100, 140 and 160 MPa), assuming full needle lift (this takes place for at least 85% of the injection duration).....	176
Figure 6-32. As in Figure 6-27 but with the addition of the durations of the flame luminosity (obtained by still ICCD camera, with 1 μs exposure).	178
Figure 6-33. Ensemble averaged images showing the effect of injection pressure on initial soot formation sites. Images were recorded between 2.1 and 2.3 ms ASOI, for an ICP of 7.0 MPa at non-fired TDC. Contrast was enhanced for clarity, white lines show liquid fuel penetration measured by simultaneous LIS, scales indicate distances from the nozzle in millimetres.	179
Figure 6-34. Ensemble averaged images showing the influence of injection pressure on late soot concentration zones. Images were recorded between 3.5 and 3.6 ms ASOI, for an ICP of 7.0 MPa at non-fired TDC. Scales indicate distances from the nozzle in millimetres.	180
Figure 6-35. Detailed LII sequence for a 0.2 mm VCO nozzle with a 160 MPa injection pressure, 6.0 MPa ICP, and 720 K calculated temperature at TDC. Times are in milliseconds ASOI. White lines indicate liquid fuel penetration measured by simultaneous LIS.	182
Figure 6-36. Signal intensity profile for the LII sequence presented in Figure 6-35. Durations for injection pulse, nozzle opening and flame luminosity are indicated.	183
Figure 6-37. From top to bottom: in-cylinder pressure traces, spray dispersion full cone angle, fuel liquid and vapour penetrations and injection pulse width, LII of soot signal with flame luminosity duration. 160 MPa injection pressure, 6 MPa ICP, 0.2 mm VCO nozzle. Times are relative to start of injection pulse.	185

Acknowledgements

First of all, I would like to acknowledge with many thanks my supervisors, Prof. Sergei Sazhin, Prof. Morgan Heikal and Dr. Robert Morgan for their assistance and support.

I wish to express my deepest gratitude to Dr. David Kennaird, and Mr Ralph Wood, their constant support and help were much appreciated. The competence of the mechanical technicians was highly esteemed, in particular William Whitney, Ken Maris, David Stansbury and Howard Hills who contributed to this work in many ways.

I want to thank Julien Lacoste, Guillaume de Sercey, John Evans, Jérôme Sejourne and Arnaud Vasseur who helped in gathering some of the data for this project. I especially wish to thank Mike Monaghan for the corrections and improvements suggested for this thesis.

I cannot fail to acknowledge financial and technical support provided by Ricardo Consulting Engineers throughout the course of this study. Special thanks are due to Dr. Martin Gold and Dr. Robert Morgan.

Finally, I would like to take this opportunity to thank my family for their constant affection and support.

Declaration

Declaration

I hereby certify that this thesis is my own work except where otherwise indicated. I have identified my sources of information, and in particular have put in quotation marks and identified the origins of any passages that have been quoted word for word.

Signed:

Date:

Nomenclature

Roman symbols

a_e	Numerical constant, $a_e = 9\mu_g/2\rho_d r_0^2$
a_b	Numerical constant, $a_b = D\sqrt{\rho_d/(2\sigma)}$
a_{fi}	Numerical constant, $a_{fi} = \log(v_g Re_i/2)$
a_{rb}	Numerical constant, $a_{rb} = 3/(2a_b r_0^{3/2})$
$a_{th b}$	Numerical constant, $a_{th b} = \log\sqrt{6\sigma/\rho_g}$
$a_{th s}$	Numerical constant, $a_{th s} = \log[\sigma^2/2\rho_g^2 v_g^2]/3$
a_{vb}	Numerical constant, $a_{vb} = 3a_e/a_{rb}$
A	Experimental constant
b_e	Numerical constant, $b_e = 4.577\mu_g^{0.6}\rho_g^{0.4}/\rho_d r_0^{1.6}$
b_s	Numerical constant, $b_s = \sigma^2/2\rho_g\mu_g$
$b_{th b}$	Numerical constant, $b_{th b} = \log[D\sqrt{\rho_d/2\sigma}]$
$b_{th s}$	Numerical constant, $b_{th s} = \log[(C/v_d)\sqrt{\rho_d/\rho_g}]$
$b_{th (ev)}$	Numerical constant, $b_{th (ev)} = \log[L\rho_d/2k_g(T_g - T_s)]$
B	Einstein's coefficient for stimulated absorption [$m^3 J^{-1} s^{-2}$], Experimental constant
c	Speed of light in vacuum, 3×10^8 [$m s^{-1}$]
c_e	$c_e = 0.165\rho_g/\rho_d r_0$
c_p	Specific heat at constant pressure [$J kg^{-1} K^{-1}$]
c_{paraf}	Paraffin content of the diesel fuel [%]
c_s	Numerical constant, $c_s = C\sqrt{\rho_d/\rho_g}$
c_v	Specific heat at constant volume [$J kg^{-1} K^{-1}$]
C	Calibration constant, Correction time delay [s], Numerical constant, 13
C_d	Nozzle discharge coefficient
C_D	Drag coefficient
C_L	Cylindrical lens
C_n	Soot particle number density [m^{-3}]
D	Numerical constant, π
D_o	Nozzle orifice diameter [m]
D_s	Diffusion coefficient of fuel vapour near the droplet surface [$m^2 s^{-1}$]
D_S	Soot mean diameter [m]
E	Energy [J]
f_B	Boltzmann fraction
G_F	Evaporation flux from the droplet's surface [$kg m^{-2} s^{-1}$]
h	Convection heat transfer coefficient [$W m^{-2} K^{-1}$]
I_L	Laser irradiance [$W m^{-2}$]
j	Rotational quantum number

Nomenclature

k	Boltzmann's constant, 1.38×10^{-23} [J K ⁻¹], Thermal conductivity [W m ⁻¹ K ⁻¹]
K	Empirical constant
l	Path length of laser beam [m]
L	Nozzle hole length [m], Specific heat of evaporation [J kg ⁻¹]
Ma	Mach number
n	Index of refraction, Polytropic compression coefficient, Experimental constant
n _p	Soot number density [m ⁻³]
N	Normalised size distribution of soot particles
Nu	Nusselt number
Oh	Ohnesorge number
P	Pressure [Pa]
Pr	Prandtl number
r	Radius [m]
R	Ratio of fluorescence signal, Universal gas constant, 8.3144 [J mole ⁻¹ K ⁻¹]
Re	Reynolds number
R _L	Molar refractivity [m ³ mol ⁻¹]
s	Spray penetration length [m]
S	Signal intensity [W m ⁻²]
t	Time [s]
T	Temperature [K]
v	Velocity [m s ⁻¹]
V	Volume [m ³]
W	Signal windowing function
We	Weber number
x	Mole fraction, Factor of LII signal's dependence on soot particle size
Y _{Fs}	Mass fractions of fuel in the vicinity of droplets
Y _{F∞}	Mass fractions of fuel in the ambient gas
Z	Criterion for stripping breakup, $Z \equiv We/\sqrt{Re}$, Partition function

Subscripts

0	At t = 0, STP conditions
ab	Absorbing
b	Bag breakup
cal	Calibration
d	Droplet
db	Droplet bag breakup
ds	Droplet stripping breakup
evap	Evaporation
f	Fuel
fl	Fuel liquid
fv	Fuel vapour
g	Gas
i	Index of species
ini	Initial
inj	Injection
int	Liquid-vapour interface
j	Rotational quantum number
L	Laser
LIF	Laser-induced fluorescence
LII	Laser-induced incandescence
max	Maximum
mix	Mixture
R	Rayleigh
ref	Reference
s	Spray, Stripping breakup
SOC	Start of compression stroke
TDC	Top dead centre

Greek symbols

α	Numerical constant, $\alpha = 9v_g \rho_g / 2r_d^2 \rho_d$
α_d	Volume fraction of droplets in the spray
α_s	Numerical constant, $\alpha_s = (v_{d0}/c_s) + a_e r_0$
β	Numerical constant, $\beta = 4.577 v_g^{0.6} \rho_g / r_d^{1.6} \rho_d$, Numerical constant, $\beta = 3c_e v_{d0} / (a_{rb} + 3c_e v_{d0})$
β_s	Numerical constant, $\beta_s = a_e r_0^2$
ΔE	Difference in energies [J]
ΔP	Pressure difference at the nozzle ($\Delta P = P_{inj} - P_g$) [Pa]
ε	Compression ratio
ϕ	Numerical constant, $\phi = Ma \sqrt{\gamma/2}$
γ	Numerical constant, $\gamma = 0.165 \rho_g / r_d \rho_d$, Ratio of specific heats, $\gamma = c_p / c_v$

Nomenclature

κ	Isentropic compression coefficient, Numerical constant, $\kappa = 3r_s^2 \alpha_d C_D v_{d0}^2 / 8r_d r_{g0}$
λ	Wavelength [m]
λ_v	Ratio of dynamic viscosities of the droplet and surrounding air
μ	Dynamic viscosity [N s m ⁻²], Numerical constant $\mu = Nu k_g (T_g - T_s) / L \rho_d r_0^2$
ν	Kinematic viscosity [m ² s ⁻¹]
θ	Spray dispersion angle [degrees], Spray dispersion half-angle [degrees]
ρ	Density [kg m ⁻³]
ρ_s	Droplet fuel vapour density at the surface of droplets [kg m ⁻³]
σ	Rayleigh cross-section [m ² sr ⁻¹], Surface tension [J m ⁻²]
σ_e	Extinction cross-section [m ² sr ⁻¹]
τ	Autoignition delay [s]
ω	Frequency [s ⁻¹]
Ψ	Numerical constant, $\psi = 0.03Re + 0.48\sqrt{Re}$
ζ	Numerical constant, $\zeta = 2 + 0.459 Re^{0.55} \cdot Pr^{0.33}$

Acronyms

ASOI	After Start Of Injection pulse
ATDC	After Top Dead Centre
a.u.	Arbitrary Units
BPF	Bandpass Filter
BTDC	Before Top Dead Centre
CA	Crank angle
CAD	Computer Assisted Design
CARS	Coherent Anti-Stokes Raman Spectroscopy
CCD	Charge Coupled Device
CFD	Computational Fluid Dynamics
CHASE	Configurable High-speed Acquisition System for Engines
CL	Cylindrical Lens
CN	Cetane Number
cw	Continuous Wave
DFWM	Degenerate Four-Wave Mixing
DI	Direct Injection
EGR	Exhaust Gas Recirculation
FIE	Fuel Injection Equipment
FWHM	Full Width at Half Maximum
HSDI	High-Speed Direct Injection
IC	Internal Combustion
ICCD	Intensified Charge Coupled Device
ICP	In-Cylinder Pressure
ICV	In-Cylinder Volume
II	Image Intensifier
LDA	Laser Doppler Anemometry
LDV	Laser Doppler Velocimetry
LED	Light-Emitting Diode
LIF	Laser Induced Fluorescence
LII	Laser Induced Incandescence
LIS	Laser-Induced Scattering
LSV	Laser Speckle Velocimetry
M	Mirror
NBPF	Narrow Band Pass Filter
NDF	Neutral Density Filter
Nd:YAG	Neodymium Yttrium-Aluminium Garnet
NO _x	Nitric oxides
PAHs	Polycyclic Aromatic Hydrocarbons
PID	Proportional, Integral, Differential
PIV	Particle Image Velocimetry
PLRS	Planar Laser Rayleigh Scattering
ppm	Particles Per Million
RDV	Raman Doppler Velocimetry
RMS	Root Mean Square
RS	Raman Scattering
SL	Spherical Lens
SLR	Single-Lens Reflex
SOC	Start Of Compression stroke
STP	Standard Temperature and Pressure

Nomenclature

TDC.....	Top Dead Centre
TM	Partially Transmitting Mirror
TMPD.....	TetraMethyl-p-Phenylene Diamine
UV.....	Ultra-Violet
VCO	Valve-Covered Orifice

1. INTRODUCTION

1.1. Background

Within the last decade, the high-speed direct injection (HSDI) diesel engine has become a realistic alternative to the gasoline engine for modern passenger car applications. Good drivability and durability together with high economy has led to its increasing popularity in the market place. Cars powered by HSDI diesel engines enjoyed approximately 32% of the total market share in Western Europe in 2001 (Ricardo, 2002). The modern turbocharged aftercooled diesel offers an efficient, low emissions automotive power plant. European legislation is set to impose further restriction on the level of emissions that are permitted from diesel engines together with targets for fuel efficiency. The diesel engine manufacturer has therefore the task to design suitable power train systems that meet or exceed these directives. Therefore, the stringent emission legislation placed upon the modern diesel engine poses a challenge to engine designers. In order to meet these standards, the engineer has to develop new techniques and processes that can be integrated with existing engine sub-systems to reduce pollutant output. The fuel injection equipment is one such sub-system that has been found to lend itself to developments leading to improvement in engine performance and emission quality, and will continue to play a vital role in the development of improved diesel engines for the foreseeable future (Herzog, 1999).

These benefits have been achieved by more sophisticated control of the fuel injection process and the use of higher injection pressures. Ultimately the nature of the combustion process is determined by the quality of the fuel spray and its distribution and mixing within the combustion chamber. Breakup and distribution of the spray is largely determined by the in-cylinder conditions (air motion, density and temperature), the injection pressure, nozzle design and geometry. A need is therefore identified to study firstly the temporal and spatial development of diesel sprays under realistic injection and in-cylinder conditions, and secondly the effects of different injection regimes on the combustion process. Data obtained can be used to establish a link between the

injection and combustion processes, and indirectly be used in the development of models to be incorporated in CFD codes.

The data presented in Figure 1-1 shows how fuel injection pressure has risen over the last 30 years. Research has shown that there are still benefits to be realised by further increasing the injection pressure and rate (Jackson, 2000), but these developments may proceed at a slower rate due to the technical challenges of further increasing the injection pressure within the constraints of low cost and high reliability. Parallel developments in the design of the injector nozzle have led to a reduction in sac volume with the introduction of mini-sac and VCO (valve covers orifice) nozzles and a consequent improvement in engine hydrocarbon emissions (Jackson, 2000).

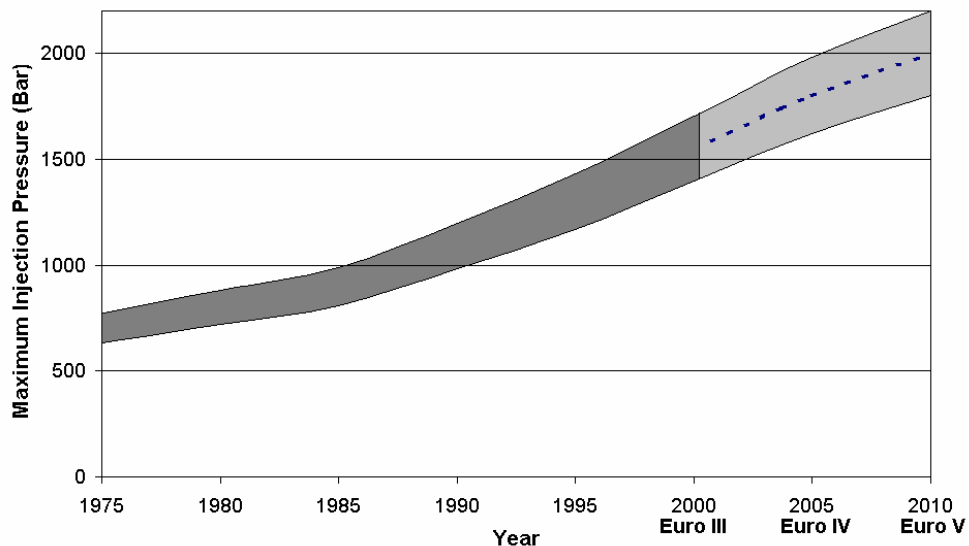


Figure 1-1. Past and projected trends in fuel injection pressure.

Although the advantages of increasing fuel pressure have been outlined, a modern HSDI engine still requires fuel injection equipment to deliver at lower rail pressures and fuelling quantities during the lower load and speed operating points. Since emission legislation drive cycles require operation within these regimes, research into these lower fuel pressure areas is of great importance.

Both injection pressure (Naber & Siebers, 1996) and nozzle design (Pots & Dittus, 2000; Bae & Kang, 2000) have been shown to influence the behaviour of the fuel spray during the formation and breakup process prior to autoignition. Two processes must be considered. Firstly, the macro effect on the spray from the introduction of fuel to the combustion chamber at higher velocities through a small orifice. This has a strong influence on the entrainment of air and subsequent breakup of the fuel spray (Naber & Siebers, 1996). Secondly, the fuel pressure and nozzle design also affect the flow behaviour of fuel inside the nozzle, possibly introducing separation and cavitation within the nozzle (Soteriou *et al.*, 1993; Arcoumanis & Whitelaw, 2000). In extreme cases this can result in hydraulic flip and a dramatic change in the structure of the spray (Soteriou *et al.*, 1993). Therefore the flow inside the nozzle must also be considered as well as the direct ‘entrainment’ process when modelling the external spray formation and breakup processes (Lefebvre, 1989; Sirignano, 2000).

The work presented here was undertaken at the University of Brighton, jointly with Ricardo Consulting Engineers, on a new compression machine based on a two-stroke diesel Proteus engine modified to allow visualisation of in-cylinder combustion processes. This new research facility has been specifically designed to enable the study of diesel sprays at realistic automotive in-cylinder conditions while simultaneously providing good optical access for both qualitative and quantitative measurements of both combusting and non-combusting sprays. The rig is constructed around a single cylinder two-stroke diesel engine with a specially designed optical chamber incorporated between the cylinder and head.

The experiments described can be broadly divided in two main groups: non-combusting spray characterisation and combustion studies. Studying non-combusting sprays allows the assessment of the location of diesel liquid and vapour. This information, which is crucial for correct analysis of combustion, was obtained by several optical techniques:

- Shadowgraphy, using a backlit high-speed CCD video camera to record complete injections.

- Shadowgraphy, using a high-speed spark light flashgun and a 35 mm SLR camera for high-quality imaging of crucial injection phases.
- Schlieren photography, using a spark light flashgun and a fast shutter CCD camera for high-resolution digital imaging.
- Schlieren cinematography with a high-speed CCD video camera.

Combustion studies were focused on the investigation of the autoignition and soot formation of diesel sprays and has been conducted using the following techniques:

- Flame high-speed cinematography, for assessing the variations of autoignition timing and location depending on various combustion parameters.
- In-cylinder pressure measurements, for comparison between combustion pressure rise and flame luminosity data.
- Laser-induced incandescence (LII), using a high power Nd:YAG laser, for planar imaging of soot formation sites and timing.

1.2. Thesis structure

The thesis comprises five main parts. The first part is a review of the literature on experimental studies of combustion processes (Chapter 2). This survey is focused on the work carried out on optical diesel test rigs. The second part provides a description of the optical Proteus spray rig used for original experimental studies (Chapter 3). The last three parts describe the work undertaken to study diesel spray, autoignition and soot formation. These topics are discussed in Chapters 4, 5 and 6 respectively. The conclusions drawn from this project and a list of recommendations for further work are presented in Chapter 7. Appendices contain additional information referring to various chapters of the thesis (Appendices A, B and C refer to Chapters 4, 5 and 6 respectively).

1.3. Objectives

The principal objective of the work described in this thesis was to provide a modern description of the diesel spray and its combustion at elevated in-cylinder pressures, in terms of:

- Liquid core penetration and dispersion with time
- Vapour phase propagation with time
- Autoignition timing and ignition sites
- Soot formation and relative concentration

All measurements were performed for a range of in-cylinder pressures (from 5 to 10 MPa) and injection pressures (from 60 to 160 MPa) representative of a modern direct injection diesel engine.

The main steps of the project were to:

- Develop a specific software package for operating the fuel injection equipment of the optical Proteus rig.
- Investigate different techniques available for diesel spray imaging.
- Study the spray liquid core penetration length with time.
- Study the vapour phase propagation with time using schlieren imaging.
- Investigate the possibility of locating spray autoignition sites both spatially and temporally.
- Study autoignition events at elevated in-cylinder pressures.
- Design and optimise a laser system capable of recording two-dimensional soot formation maps.
- Study the influence of in-cylinder and injection pressures on soot formation and concentration.

2. REVIEW OF EXPERIMENTAL STUDIES OF COMBUSTION PROCESSES IN DIESEL ENGINES

2.1. Introduction

The proportion of freight carried by rail has declined in recent years, whereas the relative amount of freight carried by road has increased steadily (Environment Canada, 1998). Due to their higher efficiency and reliability, diesel engines are usually preferred to gasoline engines. Considering the growing effects of pollution due to road transportation, engine designers are required to comply with increasingly severe regulatory limits on emissions from their engines.

The two major pollutants emitted by heavy-duty diesel vehicles are nitrogen oxides and particulate matter. Nitrogen oxide emissions contribute to environmental problems such as acid rain and ground-level ozone. Since diesel particulates are released at levels that result in direct exposure, they can be especially harmful to human health. There are two main categories of particulate matter: primary and secondary particulates. Primary particulates are formed during the fuel combustion process in the engine, and are released as exhaust from the tailpipe. Primary particulate includes soot, the soluble organic fraction which contains polycyclic aromatic hydrocarbons (PAHs), and sulphate. Secondary particulates are formed when sulphur dioxide (SO_2) emissions from diesel exhaust are converted to sulphate particulate in the atmosphere.

Considering the growing effects of emissions, diesel engine designers have to meet increasingly severe regulations whilst improving engine efficiency. Consequently, a thorough understanding of the diesel combustion processes has become critical. In order to provide engine manufacturers with phenomenological models to guide their designs, many research teams have started investigating the mechanisms of diesel combustion and especially the processes that lead to the production of soot and nitrogen oxides. The major

problem faced by these researchers lies in the need to perform various measurements inside a specific experimental engine, while at the same time run the engine under realistic, i.e. extreme, conditions. For that reason, even if physical probes such as pitot-static tubes and thermocouples could be inserted in such hostile environments, they would only disturb the characteristics of the flow that is being investigated, thus making any information they provide unreliable.

An attractive alternative to physical probing was found in optical diagnostic techniques. These are based on the measurement of the various interactions that occur between light and atoms or molecules, usually resulting in the emission of an optical signal. As these emissions can depend on factors such as the state of molecules and their quantity, information about the temperature, pressure, velocity and species content can be extracted from the region under investigation. Due to their high spatial, temporal and spectral resolutions, lasers are usually the preferred light sources. Obviously, for successful applications of optical diagnostic techniques, a knowledge of topics such as optics, quantum physics and chemical kinetics is of paramount importance. If these are carefully accounted for, optical techniques can provide a wealth of useful information, with high temporal and spatial resolution.

The main problem that arises when one intends to use optical diagnostic techniques is the necessity for at least one optical access to the region of interest. With internal combustion (IC) engines, this can be a particularly difficult task. Several attempts have been reported in the literature, including see-through flat pistons and fitting of small windows around the combustion chamber (Hentschel & Schindler, 1996; Nakagawa *et al.*, 1998), and conversion of an existing port into optical access (Espey & Dec, 1993). Of course these accesses have to withstand high pressures and temperatures typical of IC engines, and some applications require them to be transparent to ultraviolet (UV) light as well as visible light. Once these accesses have been fitted on the combustion chamber, the experimenter is confronted with the difficult task of keeping these windows optically clear. This is especially difficult when

investigating high sooting fuels such as standard diesel, and alternative fuels have to be adopted in association with lower fuelling rates and skipfiring.

Despite these limitations, optical diagnostic techniques have allowed researchers to gain much better understanding of the mechanisms of diesel combustion, and have recently provided engine designers with modern conceptual models (Dec, 1997). Nevertheless, no studies have been carried out at truly realistic engine operating conditions (i.e. high pressure and load). Therefore the validity of applying these new models at gas densities representative of modern diesel engines is as yet unknown. However, by combining experiments made at realistic conditions with computational simulations, further insight into the processes of diesel combustion is expected to be obtained.

The aim of this review is to ascertain what diagnostic techniques can be applied to internal combustion engines running at realistic conditions, with particular attention to specific features of diesel engines. Major techniques will be described in details, whereas less common methods will only be briefly mentioned. The optical techniques commonly applied to in-cylinder measurements are described in Section 2.2 for various key combustion parameters.

2.2. Optical techniques for in-cylinder observation

Laser diagnostic techniques have shown considerable advantages over physical probing when applied to the investigation of combustion phenomena. Unlike physical probes, laser-based methods are non-intrusive and most of the time non-disturbing. Lasers allow extremely high temporal and spatial resolutions. Sub-picosecond ($\leq 10^{-12}$ s) acquisition times can now be attained, with cylindrical measurement volumes down to 50 μm in diameter and 100 μm in length (Eckbreth, 1996).

The main disadvantage inherent to the use of laser diagnostic techniques is the need for an optical access to the environment, which can prove difficult when

investigating high-pressure, in-cylinder combusting sprays. Moreover, a high level of operator skill is usually required to successfully apply these techniques, especially for laser thermometry and spectroscopy as very few complete 'ready for use' types of equipment are commercially available.

This section is divided into five different subsections, each one describing the main optical techniques used for the investigation of a specific flame characteristic, i.e. autoignition sites, soot formation sites and concentration, local temperature, local air-fuel ratio, and local velocity. A sixth subsection describes the factors that can significantly affect the properties of a laser beam when propagating through a reacting environment.

2.2.1. Autoignition

2.2.1.1. Autoignition sites

By influencing the overall combustion process, the autoignition phase affects engine efficiency and noise as well as exhaust pollutant emissions. Autoignition of diesel sprays is usually described in terms of ignition delay and ignition sites location. Although the autoignition may be considered as a continuous process (Dec & Espey, 1998) it is widely accepted that autoignition is the beginning of the thermal explosion that follows a physical delay (mixing of fuel with ambient gas) and a chemical delay (chemical reactions leading to the onset of a flame) (Aggarwal, 1998).

Even before any increase in the apparent heat release rate, a weak emission can be observed soon after the start of injection (Dec & Espey, 1995). This emission, called chemiluminescence, is due to the emission of photons by molecules relaxing to their equilibrium energy state after being excited by exothermic chemical reactions. By using chemiluminescence imaging it is possible to study how the autoignition process takes place temporally. Depending on the nature of the reactions, different molecules are responsible for the chemiluminescence emission, providing an alternative way of gathering information about the combustion process. Unlike premixed flames, in hydrocarbon-fuelled diffusion flames the intensity of the chemiluminescence

signal is usually small compared to soot blackbody emissions (Eckbreth, 1996). A spectral filter can be used in order to differentiate the emission due to chemiluminescence from early luminous soot, but this might further weaken the already low autoignition signal (Dec & Espey, 1998). Another application of chemiluminescence imaging can be found in Higgins and Siebers (2001).

Most studies of autoignition sites are based on high-speed video imaging of natural flame luminosity without optical filtering. Since the only requirements for autoignition imaging are the availability of an imaging device and an optical access to the spray, the experimental study of autoignition sites is usually straightforward. The main drawback to video imaging is the fact that the images are integrated along the line of sight. Therefore there exists a spatial ambiguity, and it might not be possible to see if the reactions occur at the periphery or inside the spray. Examples of autoignition studies can be found in Edwards *et al.* (1992) and Bruneaux *et al.* (1999).

2.2.1.2. Autoignition delay

The start of ignition has been mainly related to the first appearance of a visible flame on a high-speed video recording (Lee & Iida, 2001), the pressure or temperature rise caused by the combustion (Aligrot *et al.*, 1997), or the response of a phototransistor to the change in luminosity within the combustion chamber (Edwards *et al.*, 1992). In spite of the discrepancies in the findings, due to the different methods used, similar correlations relating the ignition delay to the ambient gas condition have been found. One of these correlations is given by the relation (Aligrot *et al.*, 1997):

$$\tau = A \times P^{-n} \times e^{B/T},$$

where τ is the ignition delay, P and T are the ambient gas pressure and temperature at the time of autoignition, A , B and n are experimental constants.

Although the experimental set-up for the study of autoignition time is reasonably simple, the identification of the ignition event is not always straightforward. Imaging devices such as high-speed video cameras have a limited sensitivity to luminosity. It can therefore be argued that the autoignition

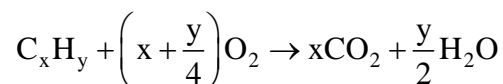
may have started before the flame luminosity is sufficiently intense to be apparent on a recording. The monitoring of ambient pressure, often used to study autoignition delay, relies on the detection of a combustion-induced ambient pressure rise. Such a technique therefore requires an accurate knowledge of the evolution of ambient pressure with time for a non-combusting cycle. This is not always possible, and alternative pressure references may have to be found. For example a common reference used for constant-volume vessels is the pressure at the time of injection. Therefore, for such devices, the ignition delay is often defined as the time at which the ambient pressure reaches the value observed at the time of injection, after the initial decrease due to droplet evaporation.

Other studies of autoignition delay for diesel fuels were reported by Miwa *et al.* (1988), Pischinger *et al.* (1988), Bruneaux *et al.* (1999), Desantes *et al.* (1999) and Kobori *et al.* (2000).

2.2.2. Soot formation sites and concentration

Diesel engine designers face increasingly severe regulatory limits on emissions of both NO_x and soot from their engines, and despite much attention focused on the mechanisms of soot formation, many details of soot formation and oxidation still have not been understood (Zhao & Ladommatos, 1998).

In a diesel engine, soot can be produced as a result of the pyrolysis¹ of liquid fuel (Kennedy, 1997), and by accumulation of oxygen depleted fuel vapour (Bellan, 1984). Soot is mostly composed of carbon, but elements such as hydrogen and oxygen are usually present in small quantities. For a stoichiometric composition, the combustion reaction is:



Under these ideal combustion conditions, hydrocarbons combine with oxygen molecules to produce carbon dioxide and water. Although the total oxygen content within the combustion chamber of a diesel engine may be sufficient to

¹ Pyrolysis is a process by which hydrogen atoms are lost, leaving a carbon-rich particulate.

produce a stoichiometric composition, localised oxygen depleted regions exist. They are usually caused by insufficient mixing and cause soot to be formed along with products such as hydrocarbons, carbon monoxide and hydrogen. The chain of events leading to the production of soot particles can be summarised as:

1. Hydrocarbons pyrolyze, producing smaller aliphatic¹ hydrocarbons and fuel fragments such as C₄, C₂H₂, C₂H₄ and C₃H₃ (Flynn *et al.*, 1999). Most of the energy release in these early reactions arises from the formation of water. The temperatures reached as a result of these reactions are of the order of 1600-1700 K.
2. The first aromatic species² (arenes) are produced from these aliphatic compounds.
3. The aromatic species grow through agglomeration with other aromatic and alkyl³ groups, to form polycyclic aromatic hydrocarbons (PAHs). The average PAH size is 20 to 50 carbon atoms (Frenklach & Wang, 1994).
4. The PAHs grow and form the smallest identifiable soot particles with diameters of the order of 1 nm.
5. These small soot particles then grow by collisional coagulation and surface growth, to spherules of diameter of about 30 to 50 nm.
6. Finally, the spherules agglomerate and form chains several hundred nanometers long, with primary diameters between 30 and 50 nm. The resulting soot particles are believed to contain between 10³ and 10⁵ carbon atoms on average (Frenklach & Wang, 1994).

Although large amounts of soot may be produced during combustion, the total soot present at the exhaust depends on the extent of the oxidation processes taking place within the engine. It is believed that oxidation results mainly from the attack by O₂ and OH molecules, and to a lower extent from oxygen atoms, O, carbon dioxide, CO₂ and water molecules, H₂O (Kennedy, 1997). Detailed discussions on formation and oxidation of soot particles can be found in Frenklach and Wang (1994) and Kennedy (1997).

¹ Hydrocarbons with no rings of carbon atoms (e.g. alkanes, alkenes and alkynes).

² Hydrocarbons with rings of carbon atoms (e.g. benzene, naphthalene, anthracene).

³ Alkane molecule less one hydrogen atom.

By advancing the injection time, the fuel-air mixing can be significantly increased before combustion takes place and therefore the burning of the fuel becomes more complete. As a result, there are less oxygen-depleted zones and soot concentration is reduced. This enhanced mixing, however, leads to higher combustion chamber temperatures and pressures, which increase the nitrogen oxide content (Brady, 1996). A number of attempts to reduce the emissions of nitrogen oxides from diesel engines exhaust were made. Albeit successful, most of them resulted in increased soot emissions (Akagawa *et al.*, 1999; Christensen, 1999; Shimazaki, 1999). The emissions of both soot particles and NO_x were shown to depend not on the composition of fuel, but on its density and viscosity (Kouremenos *et al.*, 1999). Numerous attempts to model the formation and oxidation of soot particles have been reported, ranging from purely empirical models to numerical simulation of fundamental processes that lead to soot formation. With the increase in computing power, numerical models have become ever more complex and detailed. For example, Kyriakides *et al.* (1986) combined three different models to predict in-cylinder soot formation. They used the soot model of Tesner *et al.* (1971), the soot oxidation model of Lee *et al.* (1962), with the methodology of Magnussen *et al.* (1980). The parameters usually accounted for are in-cylinder temperature at injection, engine speed, fuelling rate, kinematic viscosity of air, as well as the influence of swirl mixing rate, spray mixing rate and even chemical kinetics (Flynn *et al.*, 1999). However, some simplifications still have to be made in order to limit processing time, such as the assumption that diameters of the soot particles are constant (Khan *et al.*, 1971; Kyriakides *et al.*, 1986). Another example is found in Yoshihara *et al.* (1995) who applied the sophisticated model of Frenklach and Wang (1994) to a direct injection diesel engine to predict the exhaust soot concentration. The latter model takes into account the pyrolysis of the fuel, the nucleation of soot particles, their growth and coagulation as well as their oxidation. Many of the parameters in these models have been adjusted using the results of the measurements from a particular engine (e.g. Khan *et al.*, 1971; Kouremenos *et al.*, 1990; Mehta & Das, 1992). This usually limits these models to only predicting soot formation in a specific engine, and are not likely to be useful for other engines. An extensive survey of soot formation models for different applications has been presented by Kennedy (1997).

2.2.2.1. Laser-Induced Incandescence (LII)

Laser-induced incandescence of soot particles was first observed in 1977 by Eckbreth when it interfered with coherent anti-Stokes Raman scattering measurements (Eckbreth, 1977). LII takes place when a laser beam hits particulate matter like soot. As the particles gain energy from the beam, their temperature increases and if the energy absorption rate is high enough, the soot particles will reach incandescent temperatures (4000 K) and produce near-blackbody emission. The radiations emitted have been shown to be nearly proportional to soot volume fractions (Melton, 1984). As instantaneous planar measurements can be easily obtained, LII has emerged as an attractive and versatile technique for the measurement of soot concentrations in unsteady flows of complex geometry. For soot concentration measurements, LII has at least two significant benefits when opposed to other optical techniques, firstly it is fairly easily obtained through the use of a high-power laser, and secondly, its broadband radiation widens the range of collection strategies available to the experimenter. Subsequently, LII is widely used for investigations of in-cylinder soot formation (Dec *et al.*, 1991, 1992; Kosaka *et al.*, 1995; Choi *et al.*, 1999; Inagaki *et al.*, 1999; Schraml *et al.*, 1999), as well as for more general applications (Tait & Greenhalgh, 1993; Cignoli *et al.*, 1994; Ni *et al.*, 1995; Vander Wal *et al.*, 1997; Braun-Unkhoff *et al.*, 1998; Hilton & Black, 1998; Vander Wal, 1998; Black, 1999; Wainner and Seitzman, 1999). A summary of various LII studies is presented in Table 2-1 and Table 2-2.

Publication	Techniques	P_{inj} [MPa]	P_{TDC} [MPa]	T_{inake} [K]	T_{TDC} [K]	Engine speed [rpm]	Swirl ratio	Nozzle holes x diameter	Quantitative results	Fuel
Bruneaux <i>et al.</i> (1999)	LII	90	6		940	600 – 1800	2.92	1x0.175 mm		70% n-decane, 30% α Methylnaphthalene
Choi <i>et al.</i> (1999)	LII, LIS	24	6			1000	2.0	4x0.26 mm		
Dec <i>et al.</i> (1992)	LII, LIS, LIF	14 - 21		428		600 - 1800		4x0.125 mm		80% 2,ethoxyethyl, 20% hexadecane
Greis <i>et al.</i> (2002)	LII	80	7	313		1610	1.75	6x?		Standard Diesel CZ 54
Inagaki <i>et al.</i> (1999)	LII, two-colour LII	60, 120	5			1200	?	4x0.15 mm	✓	
Kosaka <i>et al.</i> (1995)	LII, LIS	55, 100	3		760	n/a		1x0.15 mm		22% n-C ₁₂ H ₂₆ , 54 % n-C ₁₃ H ₂₈ , 22% n-C ₁₄ H ₃₀
Schraml <i>et al.</i> (1999)	LII	100				0 - 3000		5x0.194 mm	✓	
Present study	LII, LIS	60 - 160	11	373	720	500		1x0.20 mm		99.96% Esso AF1313, 0.04% Hitec 4103

Table 2-1. References on LII applied to in-cylinder soot formation.

Publication	Laser type / Excitation wavelength [nm]	Laser pulse energy [mJ pulse ⁻¹]	Laser sheet dimensions [mm ²]	Laser fluence [MW cm ⁻²]	Laser energy density [J cm ⁻²]	Collection wavelength [nm]	Camera exposure [ns]	Camera resolution [pixels]	Comments
Braun-Unkhoff <i>et al.</i> (1998)	Nd:YAG / 532		0.20x?			450±20	100		0.5 - 2 MPa pressure flame measurement
Bruneaux <i>et al.</i> (1999)	Nd:YAG / 532	500	0.5x30	100	3.3	425±?	100		50% exhaust gas recirculation
Choi <i>et al.</i> (1999)	Nd:YAG / 532		0.20x50	190		407±35	35	640x485	
Cignoli <i>et al.</i> (1994)	Nd:YAG / 266	20				400±35		576x578	
Dec <i>et al.</i> (1992)	Nd:YAG / 532	200	0.25x50	200	1.60	< 450	70	240x388	
Geitlinger <i>et al.</i> (1999)	Nd:YAG / 532	5.3	0.20x30	11	0.09	430±16	400	576x384	Laminar, turbulent diffusion flame
Green and Witze (2002)	Nd:YAG / 532	100	3 mm beam		0.15	> 570	15	n/a	
Greis <i>et al.</i> (2002)	Nd:YAG / 532		0.30x40		1.0	415±35			
Hult <i>et al.</i> (2002)	Nd:YAG / 532	150	0.30x15		0.3	< 450	10	576x385	3D measurement (8 planes in 87.5 µs)
Inagaki <i>et al.</i> (1999)	Nd:YAG / 532		0.50x20	90-210		370	20		
Jurrg (1999)	Nd:YAG / 1064-532		1 mm beam			400/680±2	n/a		
Kosaka <i>et al.</i> (1995)	Nd:YAG / 532	100	0.20x40	138-213	1.25	400±33	40		
Ni <i>et al.</i> (1995)	Nd:YAG / 532	285	0.35x320	37	0.25	450±25	18	578x384	
Schraml <i>et al.</i> (1999)	Nd:YAG / 532			100		< 450	n/a	n/a	Measurements at exhaust
Snelling <i>et al.</i> (2000)	Nd:YAG / 1064	15	1.2 mm beam			400, 550, 780	n/a	n/a	
Tait and Greenhalgh (1997)	Nd:YAG / 1064	150	0.25x50	50		700		600x400	Turbulent propane jet flame
Vander Wal <i>et al.</i> (1997)	Nd:YAG / 1064		0.75x?	25		400±35			
Wainner (1999)	Nd:YAG / 1064-532	200 - 450	8 mm beam	37-1500	0 - 12	400±50 650±70	50-100	576x384	Study on applicability of LII technique
Wainner and Seitzman (1999)	Nd:YAG / 1064	250	8 mm beam	71	0.5 - 1.0	570-850	n/a	n/a	
Present study	Nd:YAG / 532	255	0.75x55	88	0.5 - 1.1	416±32	25	1280x1024	

Table 2-2. Experimental configurations for references on LII. Values in *italic* were calculated from published data.

An illustration of the application of LII is shown in Figure 2-1. A laser beam is formed into a sheet that intersects the region of interest. The resulting emission is filtered, amplified and then imaged using a CCD camera.

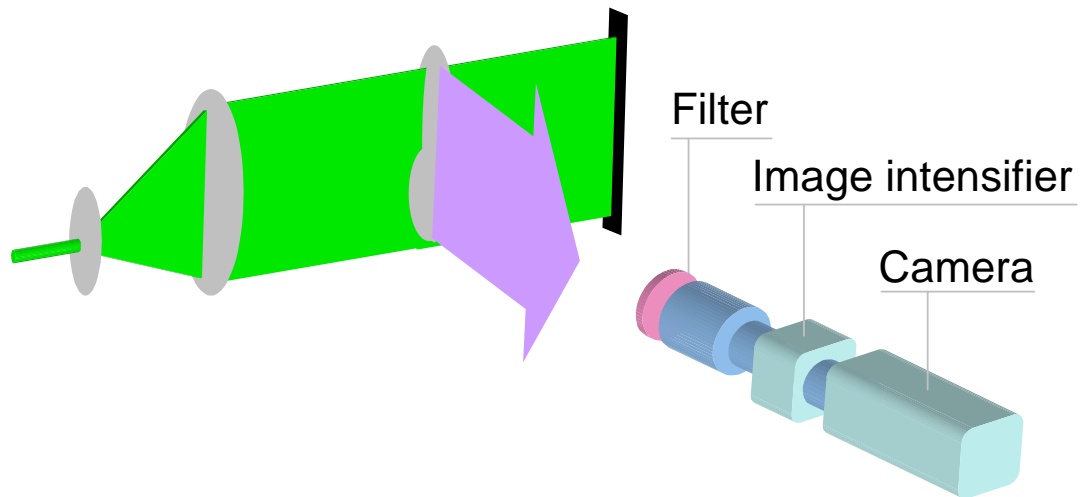


Figure 2-1. Typical strategy for the application of LII.

The light source usually preferred for LII is a frequency-doubled Nd:YAG laser running at 532 nm, with a pulse duration of about 7 ns at high power density (typically greater than 10 MW cm^{-2}). Even though a laser source at 266 nm would deliver a pulse of higher energy, and therefore ensure higher absorption efficiency, a source at 532 nm often proves to be a better choice since it offers the possibility to observe near-UV wavelengths, where little laser-induced emissions can be observed apart from LII. Hence the most widely reported use of LII was achieved with excitation at 532 nm and collection at wavelengths in the region of 400 nm. Even though an ideal exposure time for LII imaging would be about 25 ns, in order to minimise interference from flame luminosity, such a short gating was rather difficult to obtain until recently because of technical constraints. A typical spectral filtering usually consists of a short-pass filter with cut-off wavelength at 400 to 450 nm and a 532 nm laser-line mirror to completely reject the strong elastic scattering of the laser.

Figure 2-2 shows the main radiations that can possibly interfere with LII measurements.

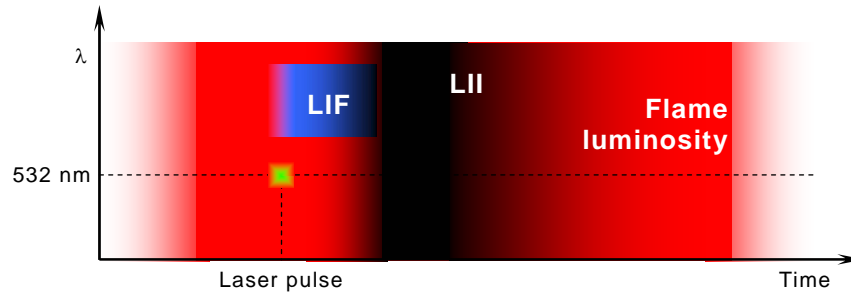


Figure 2-2. Approximate representation of light emissions caused by a laser pulse in a sooty environment. LIF: laser-induced fluorescence.

Through the energy and mass balance equations between the laser, soot and surroundings, the collected signal intensity S_{LII} can be approximated as (Zhao & Ladommatos, 1998):

$$S_{LII} = C_{cal} \int_0^{\tau} C_n(t) W(t) \int_0^{\infty} N(D_S) \int_0^{\infty} D_S^x d\lambda dD_S dt, \quad (2-1)$$

where:

- C_{cal} is the calibration constant, including characteristics of optics and detector sensitivity
- $C_n(t)$ is the soot particle number density [m^{-3}]
- $W(t)$ is the signal windowing function
- D_S is the soot mean diameter [m]
- $N(D_S)$ is the normalised size distribution of soot particles
- x is the factor of LII signal's dependence on soot particle size,
 $x = 3 + 154\lambda^{-1}$, λ being the collection wavelength in nanometres

Equation (2-1) is based on the following assumptions:

- Radiation from the wall is neglected
- Soot particles are small enough to be described by the Rayleigh theory
- Emissivity of the soot particles is equal to the absorption efficiency
- Laser intensity variations are negligible

- Fluorescence is not significant in the region of the spectrum under consideration
- Vapour is carried away from the particle by diffusion
- Laser power is high
- Soot approaches its vaporisation temperature

It is interesting to note that for widely used wavelengths (e.g. 400 nm) the collection signal is proportional to the mean soot diameter D_s raised to the power of 3.4. It is therefore widely assumed that LII signal is proportional to the soot volume fraction. This has lead some researchers to combine simultaneous LII and laser scattering (LIS) images of soot, and assume that the LIS images are proportional to D_s^6 (Rayleigh approximation). The relative soot particle diameters may be then obtained with the following equation:

$$\left(I_{\text{LIS}}/I_{\text{LII}}\right)^{1/3}$$

Examples of simultaneous LII / LIS applications can be found in Dec *et al.* (1992), Kosaka *et al.* (1995) and Choi *et al.* (1999).

It can also be observed from Equation (2-1) that absolute figures for volume fractions can only be obtained after determination of a calibration constant (C_{cal}). This is usually achieved by comparing the results obtained by LII with absolute measurements acquired through tomographic inversion on a laminar flame. Since this task can only be completed if a tomographic set-up is available, most works published on diesel soot formation only present non-calibrated data. Even though direct comparison between publications is therefore impossible, these results still allow each research group to describe trends in soot formation by altering combustion parameters and assessing the relative changes in LII intensity. Non-calibrated LII can also be applied to gather valuable data on the location of soot formation sites, and timing of the soot formation and propagation regions.

It should be noted that the high laser energies required for the LII technique alter the structure of the soot particles (Vander Wal *et al.*, 1998), and therefore consecutive measurements on the same spray should not be performed.

A detailed theoretical analysis of LII is presented by Zhao and Ladommatos (1998), and a comprehensive study on the applicability of LII for soot measurements was performed by Wainner (1999).

2.2.2.2. Laser-Induced Fluorescence (LIF)

Soot volume fraction was shown to be obtainable by vaporising soot and monitoring the presence of C₂ radicals resulting from this process. Bengtsson (1996) used a laser source at 563 nm (400 MW cm⁻²) to vaporise the soot particles and induce fluorescence of C₂ radicals at 516 nm.

The theory and applications of LIF will be discussed in more details in Sections 2.2.3.1 and 2.2.4.1.

2.2.3. Local temperature

Considering the extreme conditions that exist during the combustion process (up to 2700 K, around 100 bar), the use of thermocouples or other similar probes is unrealistic. Firstly, the insertion of such a physical probe might disturb the flow and alter the fundamental flame behaviour. Secondly, as thermocouples only measure their own temperature, not the gas temperature, corrections for radiation, convection and conduction losses must be made in order to get sensible results and these corrections depend on the environment of the measurement. Furthermore, thermocouples show very large radiation losses at such high temperatures, and their working range is limited by their melting point. Several non-intrusive optical techniques have been successfully applied for measuring temperatures in such environments. These include:

- Laser Induced Fluorescence (LIF)
- Coherent Anti-stokes Raman Scattering (CARS)
- Degenerate Four Wave Mixing (DFWM)

- Raman Doppler Velocimetry (RDV)
- Rayleigh scattering

The first two techniques are usually preferred to the others for flame temperature measurements, they will be described in more details than the other methods.

2.2.3.1. Laser Induced Fluorescence (LIF)

A significant number of molecules that play a substantial role in combustion chemistry hardly ever exceed concentrations of 100 ppm. As species at such low densities cannot produce a strong enough scattered signal, techniques based on the Raman process are generally inappropriate¹. One alternative to these inelastic scattering methods lies in the exploitation of the ability of atoms and molecules to fluoresce.

Once an atom or a molecule has been excited, it tends to return to its ground state by decreasing its own energy level. The five main energy transfer processes that can occur after excitation are (Seitzman & Hanson, 1993):

- Emission of a photon of the same wavelength as the excitation wavelength (elastic scattering).
- Absorption of an additional photon, which can excite the molecule to even higher states.
- Inelastic collisions with other molecules, as well as electronic energy transfer (often called ‘quenching’).
- Collisions between the separate atoms of the molecule.
- Spontaneous fluorescence (LIF signal).

The main problem that arises when applying LIF is the dependence of the fluorescence signal on electronic quenching. Quenching can be strongly influenced by local temperature, pressure and species concentration, which means that achieving accurate in-cylinder quantitative measurements can prove to be a rather difficult task. Since the exact influence of quenching on the

¹ Raman scattering is non-elastic and has low signal levels (1 in 10⁶ photons).

output signal is difficult to assess, no fully satisfactory model has been produced for such collisional losses, and therefore it is not possible to directly correct the results for intensity loss due to quenching processes. Some techniques have successfully reduced the existence of electronic quenching (Seitzman & Hanson, 1993), but none of them seems to be applicable to realistic in-cylinder environment for species concentration measurements.

As opposed to phosphorescence, fluorescence is the emission of light that occurs between energy states of the same electronic spin states. Fluorescence can be induced by various means, but lasers are usually preferred because of their ability to reach high temporal, spatial and spectral resolutions. A typical lifetime of fluorescence is between 10^{-10} and 10^{-5} seconds, at a wavelength usually either equal to the excitation wavelength (resonance fluorescence) or longer than the excitation wavelength (fluorescence) (see Figure 2-3).

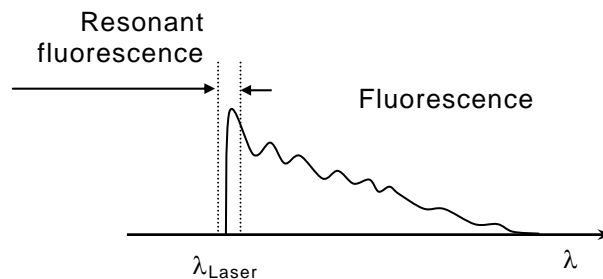


Figure 2-3. Simplified energy profile of the fluorescence signal.

Even though resonance fluorescence offers a stronger signal, its inherent susceptibility to laser-light interference limits the range of its applicability.

When LIF is used for thermometry, the exciting laser is tuned to a frequency which causes a particular combustion radical or molecule (usually NO or OH) to fluoresce. The intensity of the signal depends on the density of the species being investigated. If two different transitions are probed, the ratio of the intensities can be related to temperature via the Boltzman relationship. As well as providing a non-invasive monitoring of temperature, this method can give

instantaneous full field species concentration, velocity, pressure and density map.

The methods that have been described in the literature for temperature imaging are based on two different strategies. One is a ‘two-line’ method, which uses two laser beams at different excitation wavelengths, and the other one is a ‘monochromatic’ (i.e. single-laser) excitation method (Seitzman & Hanson, 1993).

The two-line strategy uses a pair of excitation wavelengths to produce two fluorescence signals corresponding to two distinct lower states of the same species. If the two transitions have the same upper state, any differences in quenching are avoided. Otherwise, the quenching ratio between the two signals can be reduced to a constant if quenching rates have an identical dependence on temperature and species composition. In practice, this technique requires that the species probed have two low energy states (e.g. level 0 and 1) close enough to have the same population, and a higher energy state (e.g. level 2) which is virtually unpopulated. Whilst the transition from 0 to 2 is pumped, the fluorescence from 2 to 1 is recorded. When the transition from 1 to 2 is pumped, the fluorescence from 2 to 0 is measured. This process is presented in diagram form in Figure 2-4.

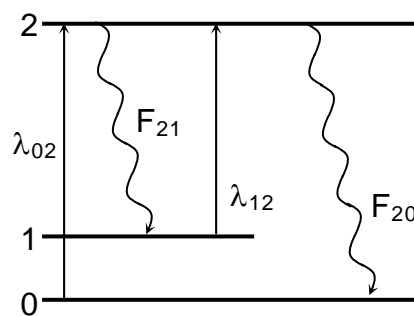


Figure 2-4. Energy level diagram for two-line thermometry.

This method can be applied to both molecules (e.g. OH, O₂, NO) and atoms (such as indium, thorium, tin or lead), either seeded or naturally occurring.

The ratio R of the two fluorescence signals is a function of the temperature as follows from the Boltzmann relation: $R \propto e^{[-\Delta E_{ab}/kT]}$, with ΔE_{ab} being the difference in energies between the two absorbing states and k Boltzmann's constant. The sensitivity of this technique can be derived from the latter relation as (Seitzman & Hanson, 1993):

$$\left| \frac{dR}{R} \right| = \frac{|\Delta E_{ab}|}{kT} \cdot \left| \frac{dT}{T} \right| \quad (2-2)$$

Uncertainties of only 5% can be reached, but the need for two tunable laser sources and two intensified CCD (ICCD) cameras makes this technique rather expensive. If the two transitions are relatively close together and if the fluorescence signals are well separated spectrally, the two tunable laser sources could be replaced by a broadband laser which could be used for simultaneous stimulation of these transitions. This approach was first applied by Andresen *et al.* (1998) who used a broadband KrF Excimer laser at 248 nm to stimulate two transitions of OH.

Dec and Keller (1986) showed that two-line LIF could provide flame temperature measurements at data acquisition rates of 5 KHz with a standard deviation of 125 K. They used a mixture of methane and indium chloride (InCl_3) seeded air with three burners (premixed laminar flame, diffusion laminar flame and dual premixed burner for turbulent flow). Two pumped dye-lasers were used, a Stilbene 1 at 410.18 nm and a Stilbene 3 at 451.13 nm, respectively delivering 30 mW and 40 mW at the probe volume (400 μm in diameter).

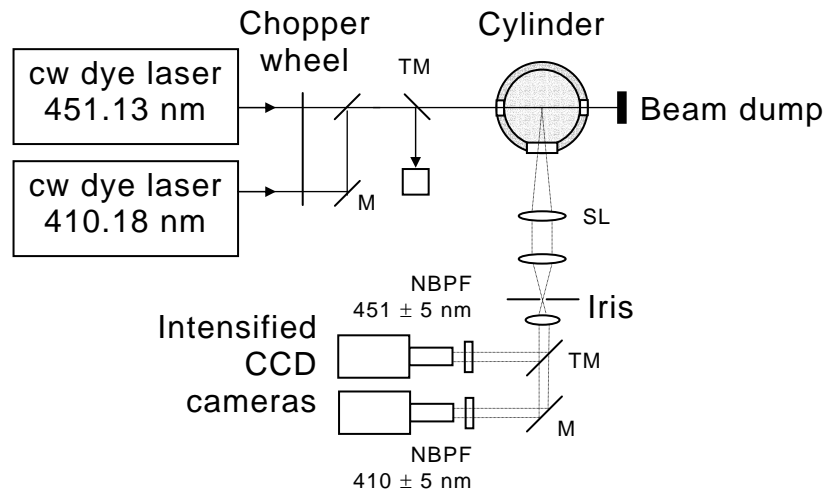


Figure 2-5. Instrumentation setup for two-line LIF thermometry.

Figure 2-5 shows a typical installation for measuring temperature with two-line thermometry. A chopper wheel allows to pulse alternatively the two laser beams. The energy of the pulse is measured before entering the cylinder in order to normalise the results given by the ICCD cameras. Each one of the cameras is mounted with a narrow band pass filter to discard flame luminescence and other background luminosity. Two-line thermometry can easily be converted to provide full field measurements, especially if a single broadband laser source is to be used.

Kido *et al.* (1998) applied LIF to measure simultaneously the temperature and the concentration of an argon jet. They used iodine as a tracer, with an Nd:YAG laser at 532 nm (350 mJ per pulse) and used the ratio of the fluorescence at 580 nm and 625 nm to yield temperature within 15% accuracy.

As for the single-laser strategy, two main variations have been reported. One of them requires to have either a fixed or known mole fraction of the probed species, and to choose a quantum state that produces strong temperature dependence. The fluorescence signal can be related to temperature through the Boltzmann fraction:

$$S_{\text{LIF}} = N \cdot f_{\text{B}} \cdot B \cdot C \cdot I_{\text{L}} \quad (2-3)$$

N being the total molecular number density, f_{B} the Boltzmann fraction, B is Einstein's absorption coefficient, C is an experimental constant, and I_{L} the irradiance of the laser (See Section 2.2.4.1 for more detailed discussion).

The Boltzmann fraction is defined as:

$$f_{\text{B}} = (2j+1) \frac{e^{\frac{-E_j}{kT}}}{Z(T)}, \quad (2-4)$$

where j is the rotational quantum number of the ground state level of the transition under study, E_j is the corresponding ground state energy, k is Boltzmann's constant, T the temperature and $Z(T)$ is the partition function.

As mentioned previously, this technique requires a constant or known mole fraction of the species to excite. This restriction can be avoided by including the excitation of a seed molecule like NO (Seitzman *et al.*, 1985; Tsujishita *et al.* 1999) in a premixed CH₄-air mixture, or the excitation of O₂ in non-reacting flows (Lee *et al.* 1987; Roller *et al.* 1995).

Tsujishita *et al.* (1999) used a premixed methane-air laminar flame at atmospheric pressure and compared the temperature measurements achieved by NO-LIF and OH-LIF with those obtained by N₂ CARS. They showed that NO-LIF results agreed with those obtained by N₂ CARS (considered as a reference) without exceeding 5% error. The temperatures given by OH-LIF were found to be 30% lower than expected.

Another monochromatic technique could be applied by exciting a species with a laser, and recording fluorescence in the energy levels directly lower and higher than the excited level. As the collisional energy transfers are supposed to be equivalent for both fluorescence signals, the ratio of these two signals should be independent from quenching processes and therefore be related to temperature.

Applications of LIF to studies of combustion process are discussed in depth by Daily (1997) and Kohse-Höinghaus (1994).

2.2.3.2. Coherent Anti-stokes Raman Scattering (CARS)

Coherent Anti-stokes Raman Scattering is a non-linear Raman technique, i.e. the scattered signal is not linearly related to the input laser intensity. Three laser beams are used to stimulate Raman scattering through the third order susceptibility of the molecules. The generated signal is produced in a coherent ‘laser-like’ beam, which can be readily separated physically and spectrally from interferences (Figure 2-6). Two of the input laser sources are at the same frequency ω_1 (termed the ‘pump’ laser), whereas the third input is at a frequency ω_2 (‘Stokes’ laser). As described in Figure 2-7, the coherent CARS signal resulting from the mixing of the pump and Stokes lasers is generated at $\omega_3 = 2\omega_1 - \omega_2$.

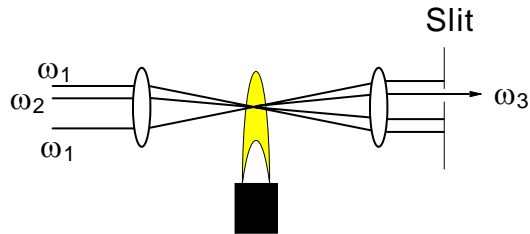


Figure 2-6. Approach for coherent anti-Stokes Raman spectroscopy.

By changing the frequency difference ($\omega_1 - \omega_2$) to a particular Raman resonance, various molecules can be probed.

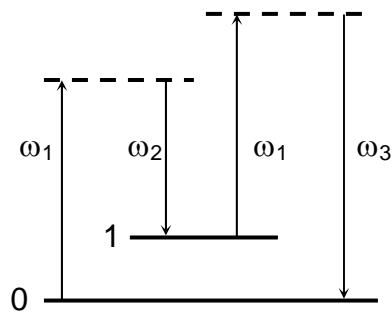


Figure 2-7. Energy level diagram for resonant CARS. Real states and virtual states are indicated by solid and dashed lines respectively.

The energy of scattered light depends quadratically on the number of molecules present (Demtröder, 1996). Therefore a measurement of the molecular number

density can be obtained. In addition, the frequency of the signal depends on the Boltzmann relationship, which means that an analysis of the frequency content allows the measurement of temperature. In the case of the spectral analysis of the signal, concentrations between 0.5% and 30% can be measured. At concentrations lower than 0.5%, the background noise becomes too significant and has to be subtracted from the signal (Eckbreth, 1996). This method can have errors less than 5% for temperatures, which is more satisfactory than most LIF results. Unlike LIF, the measurements are limited to specific points and quantitative measurements require in-depth understanding of the instrumentation and spectroscopic factors (Goss, 1993). The reason why CARS might be preferred to LIF is because of its ability to provide accurate temperature and species concentration measurements in extremely hostile environments.

Flames usually show a high concentration of N_2 , and since these molecules are stable, they are less likely to be involved in combustion reactions. For these reasons, N_2 molecules can be considered as a good indicator of temperature. As N_2 molecules do not have an absorption band in the ultraviolet to infrared region, Raman scattering has to be used.

Depending on the nature of the flow, either broadband CARS or narrow-band CARS can be used. Narrow-band CARS is based on the use of a narrow-band laser, and therefore a fine wavelength tuning has to be performed in order to match an excitation wavelength and obtain sufficiently strong output signal. In this case, the sensitivity of this technique is considerably enhanced, and the detection limit can reach several ppm (Eckbreth, 1996). Broadband CARS is achieved by using a broadband laser that does not need to be tuned to a specific excitation peak. The accuracy of broadband CARS thermometry is therefore lower than with the narrow-band method, but its main advantage lies in its ability to perform rapid measurements.

2.2.3.3. Degenerate Four Wave Mixing (DFWM)

Like CARS, DFWM is a third-order nonlinear optical process. Two high-power pump laser beams intersect with a weaker probe beam. Two of the three input beams interfere to form a grating (either spatial or temporal), whereas the third input beam is scattered by the grating to yield a fourth beam (Wolfrum, 1998). As the four-wave mixing process is an instantaneous stimulated emission, a stable excited state is not required. Therefore, unlike the LIF technique, DFWM is less sensitive to pre-dissociation and quenching processes. Furthermore, the output signal produced by DFWM is a coherent beam and so may be filtered easily from background noise.

A severe limitation of multi-line techniques such as DFWM and CARS when applied to diesel combustion lies in the occurrence of refractive index gradients after ignition of the fuel. These gradients, which are due to temperature variations through the in-cylinder mixture, can significantly steer the beams and thus preclude accurate intersecting of the laser beams. Such potential alterations of the laser beam properties will be further discussed in Section 2.2.6.

2.2.3.4. Raman Doppler Velocimetry (RDV)

Two intersecting laser beams interact via the stimulated Raman process with the molecular constituents of the flow. As with the CARS technique, this interaction depends upon the third order non-linear susceptibility and produces a small gain in the power for one of the laser beams. The forward scatter bandwidth is mainly pressure dependent, whereas the backward scattered bandwidth is principally dependent on temperature (NASA Langley, 1996). As a result, the local temperature can usually be approximated within 30% accuracy.

2.2.3.5. Rayleigh scattering

Rayleigh scattering occurs when the electrons of a molecule are excited by laser light and emit radiations at the same frequency as the laser. This type of scattering can take place for molecules and small particles ($d/\lambda < 0.05$). Its

signal intensity is proportional to the total particle number N , and the laser irradiance I_L , and can be calculated as (Eckbreth, 1996):

$$S_R = C \cdot I_L N \sum_i x_i \sigma_i, \quad (2-5)$$

where C is the calibration constant, x_i the mole fraction and σ_i the effective Rayleigh scattering cross-section of each species. The total Rayleigh scattering cross-section σ can be written as:

$$\sigma = \sum_i x_i \sigma_i \quad (2-6)$$

Using the ideal gas law, Equation (2-5) can be rewritten as:

$$S_R = C \cdot I_L \frac{PV}{RT} \sigma \quad (2-7)$$

If the Rayleigh cross-section is kept constant, the temperature of the probed volume can be calculated. The calibration constant C is found by measuring a reference temperature T_{ref} under known conditions. The measured temperature can then be related to the Rayleigh scattering signal as:

$$T = \frac{I_L}{I_{L_{ref}}} \frac{P}{P_{ref}} \frac{\sigma}{\sigma_{ref}} \frac{S_{R_{ref}}}{S_R} T_{ref}, \quad (2-8)$$

assuming that the probe volume is the same between the reference and the actual measurements.

As any particle present in the laser sheet will scatter radiation, the flame has to be free from parasite particles (e.g. soot). Hence, the use of Rayleigh scattering is restricted to very 'clean' flames.

Since Rayleigh scattering is an elastic process, the measurements are subject to surfaces and windows scattered light interferences. However, a narrowband filter centred on the excitation wavelength can be used to avoid these effects, restricting the monitoring to Doppler shifted Rayleigh scattered light (Forkey *et al.*, 1996a,b).

Rayleigh scattering is usually applied to acquire two-dimensional measurements, and flame temperatures were shown to be obtainable simultaneously with concentrations of NO by LIF (Bräumer *et al.*, 1995).

2.2.4. Local air-fuel ratio

The combustion performance of a diesel engine is strongly affected by air-fuel mixing. Therefore better understanding of the air-fuel mixing processes would help significantly to improve the combustion process. In what follows, attention will be focused on various approaches to experimental studies of the local air-fuel ratios.

2.2.4.1. Exciplex laser-induced fluorescence

Exciplex gives a simultaneous measure of liquid and vapour phases. Two additives are mixed with the diesel fuel, a fluorescing monomer and an appropriate partner molecule. When under laser excitation, the additives will fluoresce differently depending on their phase. By careful selection of optical filters, it is therefore possible to image separately the liquid and vapour phases. The most commonly used additives for exciplex fluorescence of diesel fuel are naphthalene and TMPD (tetramethyl-p-phenylene diamine). Examples of applications of exciplex LIF were reported by Bruneaux *et al.* (1999) and Beckman and Farrell (2001).

Figure 2-8 shows a typical experimental setup for in-cylinder exciplex LIF measurements. A small percentage of the laser light is directed into a device that monitors the laser output energy. The remaining laser light goes through a set of lenses that transform the beam into a thin laser sheet. The optical accesses through the cylinder are achieved by optically clear windows. In order to reduce reflections of the laser light against the cylinder, a window is made to let the laser sheet out. The fluorescence induced by the laser is filtered by band pass filters and then amplified by an image intensifier.

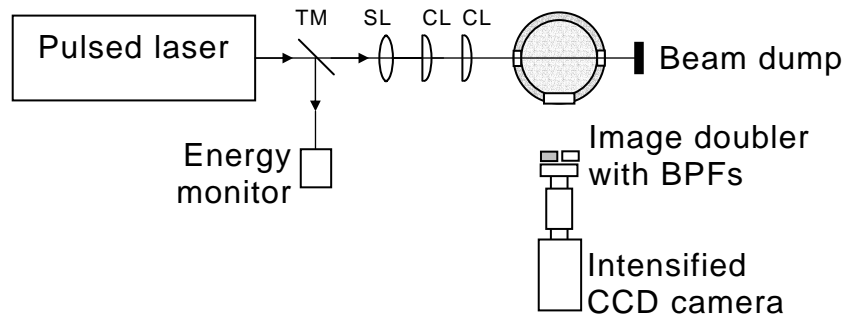


Figure 2-8. Experimental setup for exciplex LIF measurement. TM: partially transmitting mirror, SL: spherical lens, CL: cylindrical lens, BPF: bandpass filter.

2.2.4.2. Planar Laser Rayleigh Scattering (PLRS)

Rayleigh scattering is the elastic scattering process that occurs when an incident light makes a molecule or a small particle radiate ($d/\lambda < 0.05$). For larger particles, a different type of scattering occurs, called Mie scattering, which can be up to twenty orders of magnitude stronger than Rayleigh scattering (Ingle *et al.*, 1988). Therefore, in order to avoid interference with the Rayleigh signal, the probed volume has to be free from large particles (e.g. soot, dirt), and filtering of all gases is essential ($0.025 \mu\text{m}$ filter).

The intensity of Rayleigh scattered light is given by Equation (2-5), and the cross-section for Rayleigh scattering perpendicular to the plane of polarization of the incident light can be found from the following relation:

$$\sigma_i = \frac{4\pi^2}{\lambda^4} \left(\frac{n_i - 1}{N_0} \right)^2 \quad (2-9)$$

n_i is the index of refraction of species i , N_0 is the molar concentration at STP [mol m^{-3}].

If the molar refraction of each species is known for the laser wavelength, then the refractive index n_i can be calculated by means of the Lorentz-Lorentz equation (Partington, 1953):

$$R_L = \frac{n^2 - 1}{N(n^2 + 2)}, \quad (2-10)$$

where R_L is the molar refraction [$\text{m}^3 \text{mol}^{-1}$], n the index of refraction, N the molar concentration (number density) [mol m^{-3}]. A list of refractive indices of combustion gases was prepared by Gardiner *et al.* (1981) for wavelengths that are typical for laser sources.

Equation (2-10) can be applied either to individual species or to gas mixtures. In the latter case, the molar refraction is the weighted average of the molar refraction of each species (Gardiner *et al.*, 1981):

$$R_L = \sum_i x_i R_{L,i}, \quad (2-11)$$

where x_i is the molar fraction of species i .

Rayleigh cross-sections tend to increase slightly with increasing temperatures. The difference between molecules at 300 K and molecules at 1000 K is estimated to be around 2%, and therefore Rayleigh cross-sections are usually considered as constant for such ranges of temperatures. As diesel fuel molecules have relatively large Rayleigh cross-sections, the signal-to-noise ratio is also high which means that Rayleigh diagnostic can provide high measurement accuracy. Furthermore, the Rayleigh cross-section of air is far lower than for diesel fuel, and the large difference in intensity of the two signals allows fuel concentrations to be resolved even at low equivalence ratios (down to 1).

In order to simplify the calculations the vapour phase is assumed to contain only fuel and gas, and these substances are considered as pure. Hence, Equation (2-5) becomes:

$$S_R = C \cdot I_L N [x_f \sigma_f + x_g \sigma_g] \quad (2-12)$$

Since $x_f + x_g = 1$, Equation (2-12) can be simplified to:

$$S_R = C \cdot I_L N [x_f (\sigma_f - \sigma_g) + \sigma_g] \quad (2-13)$$

During the injection, the liquid fuel is heated by the hot in-cylinder gas. This means that the temperature of the fuel-air mixture is lower than the ambient gas

temperature, and therefore the total number density N will increase. Hence, both N and the fuel mole fraction x_f cannot be assumed constant and additional equations for N and x_f are needed. For the calculation of the fuel concentration, Espey *et al.* (1997) assumed that N was constant and therefore the diesel spray was assumed isothermal, whereas for the calculation of the equivalence ratio the fuel-air mixing process was considered as adiabatic. In the latter case, the mixing temperatures for all fuel-air ratios were calculated with a thermodynamic equilibrium calculation based on the conservation of energy (Espey *et al.*, 1997):

$$\int_{T_{\text{mix}}}^{T_{\text{a,ini}}} C_{p_g} dT = \frac{F}{A} \left[\int_{T_{\text{n,ini}}}^{T_{\text{int}}} C_{p_{\text{fl}}} dT + h_{v, T_{\text{int}}} + \int_{T_{\text{int}}}^{T_{\text{mix}}} C_{p_{\text{fv}}} dT \right], \quad (2-14)$$

where F/A is the fuel-air ratio by mass, the indexes g , fl and fv refer to gas, fuel liquid, and fuel vapour, respectively. The indexes ini , int and mix relate to initial, intermediate and mixture, respectively. This relation was used for regions of the spray where fuel is vaporised and transient effects are assumed to be negligible.

The reason why the spray cannot simply be considered as isothermal for the calculation of the equivalence ratio is that this ratio is strongly dependant on molar concentrations, which are inversely proportional to temperature.

Figure 2-9 shows a characteristic setup for quantitative PLRS imaging. One of the CCD cameras acquires the Rayleigh scattered laser-light, whereas the second camera records the energy profile across the laser sheet which will be used to normalize the raw images. This process is an essential part of quantitative PLRS imaging because the scattering is directly proportional to the laser irradiance, therefore any variations should be accounted for. This reduces the 20% error due to shot-to-shot energy fluctuations. The iris is used to discard the edges of the laser sheet, thus reducing the non-homogeneity of the laser sheet. The narrow band pass filter restricts the imaging to elastically scattered laser-light only. Light reflected from surfaces will strongly interfere with Rayleigh scattering and must be avoided.

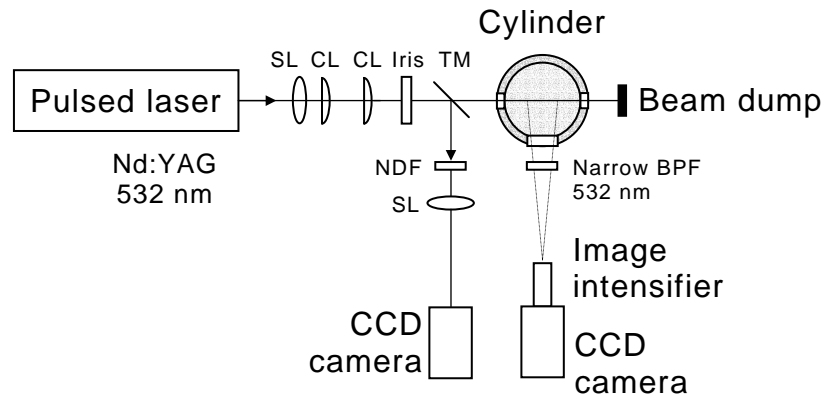


Figure 2-9. Typical setup for quantitative PLRS measurements of fuel-air ratios. NDF: neutral density filter, SL: spherical lens, CL: cylindrical lens, TM: partially transmitting mirror, BPF: band pass filter.

Espey *et al.* (1997) have successfully applied planar laser Rayleigh scattering for measurement of vapour-phase fuel concentrations. Their tests were performed for a single-cylinder, direct-injection, four-stroke heavy-duty diesel engine with optical access to the combustion chamber. The engine operated at a speed of 1200 rpm, with intake air at 433 K and 0.206 MPa, with a peak injection pressure of 68 MPa, at an average equivalence ratio of 0.25, and was fired once every 20th engine cycle. The duration of the injection was about 1.39 ms, and the two fuels used were pure heptamethylnonane for non-reacting sprays, and a mixture of 67.6% heptamethylnonane and 32.4% n-hexadecane for combusting jets. The optical setup comprised an Nd:YAG laser producing a laser sheet ($300 \mu\text{m} \times 10.5 \text{ mm}$) at a wavelength of 532 nm with an energy of about 45 mJ per pulse (7 ns).

The overall uncertainty of the results obtained by Espey *et al.* (1997) ranged between 17% and 21% for the equivalence ratio with the adiabatic mixing assumption. Quantitative fuel-vapour concentrations were obtained in the leading portion of a reacting and non-reacting jet from 4 CA to 6.5 CA after start of injection. Since the PLRS signal will be contaminated by any laser reflection, this technique is limited to particle-free flows and images can only be acquired when no fuel droplets are present.

2.2.5. Velocity measurements

2.2.5.1. Laser Doppler Anemometry (LDA)

Laser Doppler Anemometry (LDA), also known as Laser Doppler Velocimetry (LDV), measures the velocity of particles introduced into the flow field. Two laser beams intersect at a point to form a fringe pattern (Figure 2-10). Particles passing the fringe pattern reflect the laser light at each fringe. Provided the fringe spacing is known, local velocity can be determined by analysing the Doppler shifted scattered light (Watrasiwicz & Rudd, 1976).

One of the problems that occurs when applying LDA to flame measurements is the fact that the particles have to withstand high temperatures. Particles produced by combustion processes might not be uniformly spread through the flame, and they are usually too small to scatter a signal with sufficient intensity. Therefore the intake air usually has to be seeded with inert refractory solid particles such as titanium dioxide (TiO_2) (Drain, 1980).

Due to its high spatial and temporal accuracy, LDA is considered as a reference in velocity measurements. If the optical access to the combustion chamber is limited, the use of only one window can be achieved by collecting backscattered light. Unfortunately this will result in a reduction of the signal to noise ratio, and a more powerful laser will have to be used.

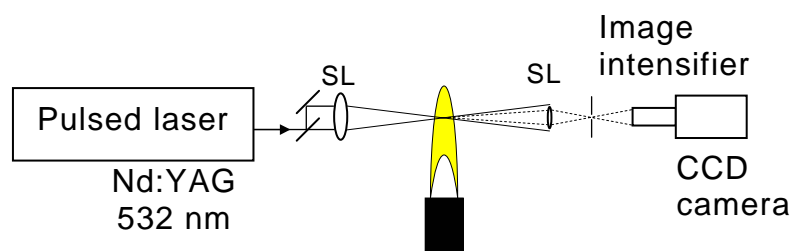


Figure 2-10. Basic differential LDA system.

Hentschel and Schindler (1996) applied LDA on a modified Volkswagen 1.9 litre diesel engine running at 1000 rpm. They monitored the backscattering from MgO molecules illuminated by a 20 W argon ion laser, to investigate the formation of the swirl during the intake and compression strokes.

2.2.5.2. Particle Image Velocimetry (PIV)

PIV is a full field non-intrusive technique, derived from Laser Speckle Velocimetry (LSV), which was first introduced in the mid-1980's and is now widely used in fluid flow metrology. PIV is achieved by shining a laser sheet through a flow and monitoring the Mie-scattering signal produced by in-flow buoyant particles. In order to resolve the speed of each particle, two consecutive shots are taken either on one single image or on two different images. Signal processing is applied to the resulting images in order to produce velocity vector fields. In the case of a multi-exposed image, an auto-correlation algorithm is usually used to isolate the two clusters of pixels corresponding to the same particle. The main drawback of this technique lies in the fact that the direction of the flow cannot be resolved automatically and therefore the velocity vector field suffers from directional ambiguity. Furthermore, low velocities correspond to merging of the particle images and cannot therefore be measured. By taking each one of the two shots on two different images, it is possible to distinguish temporally the two groups of pixels belonging to each particle. The signal-processing algorithm used in this case is referred to as a 'cross-correlation' algorithm.

One obvious limitation of PIV is the need for two optical accesses, one for the laser sheet and one for the camera. Moreover, as PIV is fundamentally two-dimensional its spatial resolution is much lower than single-point measurement techniques like LDA. It is also more sensitive to optical distortion, glares, fluid opaqueness and seeding quality (Faure, 1997).

2.2.6. Experimental considerations

Considering the extent of the alterations the in-cylinder environment can induce on the laser beam, several aspects of these interactions should be taken into account if accurate measurements are required.

2.2.6.1. Refractive index gradients

The refractive index of a medium depends on its temperature, the wavelength of the light source, and the concentration of the constituents of the mixture. If the

substance is compressible, the refractive index will also depend on pressure. As combustion takes place, significant temperature and pressure gradients can appear in the cylinder and deflect the direction of any incident light ray. The consequence of the presence of these refractive index gradients should be considered with care, especially for high-pressure applications, as a laser beam could be significantly defocused or steered (Eckbreth, 1996). This phenomenon is particularly important for the techniques that involve intersecting of several laser beams, such as CARS, DFWM, and LDA, usually restricting their application to either low-pressures or pre-ignition measurements. These effects can be easily ascertained by using a low-power visible laser to check for the degree of deflection and defocusing.

Another consequence of temperature changes is the variation in vibrational frequencies of a molecule. This effect is particularly important at UV wavelengths, and UV absorptive bands tend to shift towards longer wavelengths as the temperature increases (Braun, 1987).

2.2.6.2. Soot absorption

Particulate matter, like soot, can significantly attenuate the propagating laser beam by absorption and scattering. The attenuation will be proportional to $e^{-n_p \sigma_e l}$, where n_p is the soot number density, σ_e the extinction cross-section and l the path length of the laser beam (Eckbreth, 1996). This kind of extinction will increase with the richness of the combustion, and might even preclude measurements in diesel spray investigations.

As standard diesel fuels produce high soot concentrations, modified fuels are usually preferred in order to facilitate optical access and prevent optics fouling. Dec and Canaan (1998) have reported the use of two different fuels: a low-sooting fuel consisting of 70% tetraethoxypropane ($C_7H_{16}O_4$) and 30% heptamethylnonane ($C_{16}H_{34}$), and a Phillips research grade no. 2 diesel fuel. Apart from the difference in soot concentration, Dec and Espey (1995) showed that the low-sooting fuel had similar characteristics to the Phillips fuel (i.e. ignition delay, early soot formation processes, apparent heat release rate curve,

and boiling point of constituents). Another fuel of 67.6% heptamethylnonane ($C_{16}H_{34}$) and 32.4% n-hexadecane ($C_{16}H_{34}$) was used by Dec and Espey (1995).

Nakagawa *et al.* (1998) used a mixture of 50% in volume of iso-octane (C_8H_{18}) and 50% of n-tetradecane ($C_{14}H_{30}$) to reduce window pollution by soot.

2.2.6.3. Molecular absorption

In a similar manner to soot, molecules can progressively attenuate the laser signal during its propagation. The extinction by scattering is so weak that its effects are insignificant when compared to absorption extinction.

If the exciting laser wavelength is in the visible domain, only combustion gases containing high concentrations of NO_2 or C_2 will show a significant absorption. Molecular absorption can be far more troublesome with lasers operating at UV wavelengths, especially for non-resonant processes (Eckbreth, 1996). For non-resonant techniques (e.g. Raman based methods and non-resonant LIF), absorption wavelengths of most flame radicals are well defined and can be avoided quite easily with a tunable laser, but the broad absorption spectrum of PAHs is very difficult to avoid. Molecular absorption usually increases with increasing pressure. Therefore particular care must be taken to minimise or at least quantify these effects.

The only flame radical that seems to affect resonant processes is OH, whose concentration at high temperature can become high enough to cause substantial attenuation.

2.3. Conclusions of Chapter 2

Table 2-3 shows the main four techniques that are usually preferred for flame thermometry and spectroscopy (Eckbreth, 1996). The choice of the most

suitable method is dictated by two main parameters, the concentration of the species to be investigated and the type of radiation emitted (i.e. coherent or not). The latter parameter is often imposed on the experimenter by the optical access available. If there is access to only one optical axis, then a coherent method will have to be used. If a secondary optical access is available, either kind of approach could be used.

	Incoherent	Coherent
Minor species	LIF	DFWM
Major species	Raman Scattering	CARS

Table 2-3. Matrix of spatially accurate laser-based techniques for combustion temperatures and spectrometry (adapted from Eckbreth, 1996).

Unfortunately, techniques that provide a coherent signal require accurate intersecting of several laser beams. Although this is easily achievable in normal circumstances, high refractive index gradients can make these techniques ineffective after ignition of the injected fuel. Hence, incoherent techniques will usually be preferred for applications involving high pressure and temperature gradients.

Regarding the selection of the most suitable method for autoignition and soot investigations, very few techniques are available. For thermometry and species concentration, deciding which technique to apply is not straightforward. The exact requirements have to be carefully considered in terms of spatial and temporal accuracy, as well as in the degree of information needed (i.e. qualitative or quantitative results). For instance, if the mechanisms of formation of nitric oxides are to be investigated, only the positions and relative proportions of NO_x production need to be measured and absolute concentrations are usually not required. If combined with a map of OH production sites and full field temperature measurements, the formation of NO_x can be related to the combustion process at high-temperature regions. During typical diesel

combustions NO and OH are considered as minor species, and therefore LIF is preferred to Raman scattering techniques. In this regard, LIF of NO and OH molecules can provide qualitative concentration maps with high spatial and temporal accuracy. A summary of the most appropriate techniques for diesel engine investigations is shown in Table 2-4.

Investigation	Optical technique
Autoignition	Flame luminescence imaging
Soot formation sites	LII
Temperature	Two-line NO-LIF
NO concentration maps	LIF
OH concentration maps	LIF
Air-fuel ratio	LIF
Velocity	LDA

Table 2-4. Summary of optical techniques used for high-pressure diesel combustion diagnostic.

3. DESIGN OF THE PROTEUS HIGH-PRESSURE SPRAY RIG

3.1. General description

A high pressure and temperature spray research facility was installed in June 1999 at the University of Brighton. This facility was designed specifically to enable the gaps in the current literature (spray and combustion analysis of injections into environments above 6 MPa) to be addressed, in addition to providing a means of testing sprays at conditions anticipated for the next generation of diesel engines. This rapid compression machine is based around a single cylinder Ricardo Proteus test engine which was converted to two-stroke cycle operation by the addition of inlet and exhaust ports in the cylinder liner. This approach significantly increased the room available in the cylinder head for optical access by the removal of inlet and exhaust valves and also allowed reduced mechanical complexity, thus cutting down on engine build times. A photograph of the Proteus test cell is shown in Figure 3-1. The engine had a bore of 135 mm, a stroke of 150 mm, and a displacement of 2.2 litres.

The cylinder head was heated by a water jacket (90°C) filled with pure ethylene glycol and the sump oil by immersion heaters (85°C). This enabled the engine to be heated prior to motored testing, and therefore minimise heat losses from the compressed gas to the cylinder wall. A water-cooled Kistler pressure-transducer attached to a storage oscilloscope was used to monitor the in-cylinder pressure. An encoder with a resolution of 3600 pulses per revolution was fitted to the crankshaft and provided an additional marker pulse at TDC.

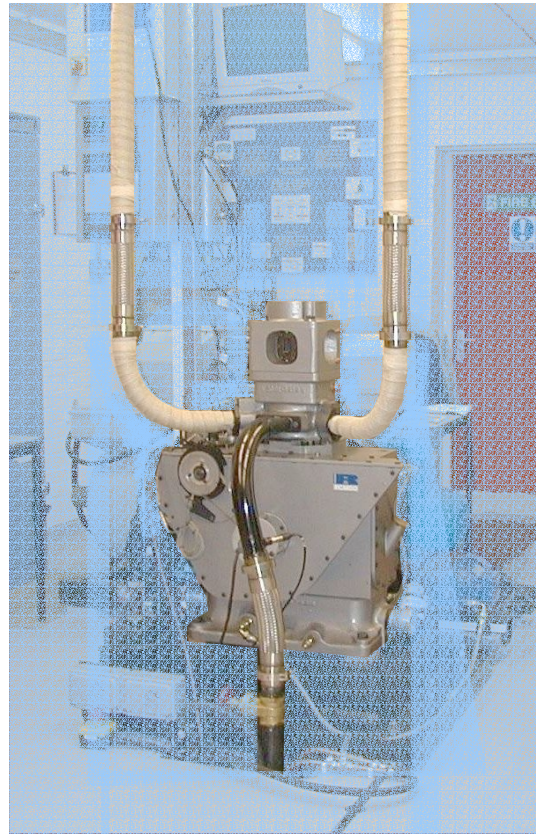
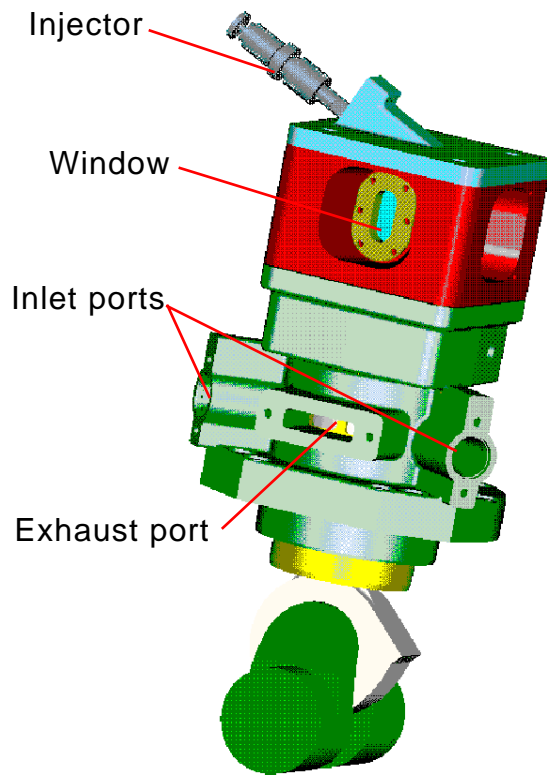


Figure 3-1. CAD drawing and photograph of the Proteus engine.



Figure 3-2. Photograph of the Proteus test cell showing the gearbox and parts of the dynamometer.

The Proteus was driven by a dynamometer through a 90° gearbox (Figure 3-2). The 90° configuration was chosen to obtain a more compact rig layout. The output shaft of the gearbox was directly connected to the Proteus flywheel and, with a reduction ratio of 6:1, reduced the dynamometer speed of 3000 rpm to 500 rpm engine speed. This was the operating engine speed for all the tests carried out in this work. A schematic of the test bed layout is presented in Figure 3-3.

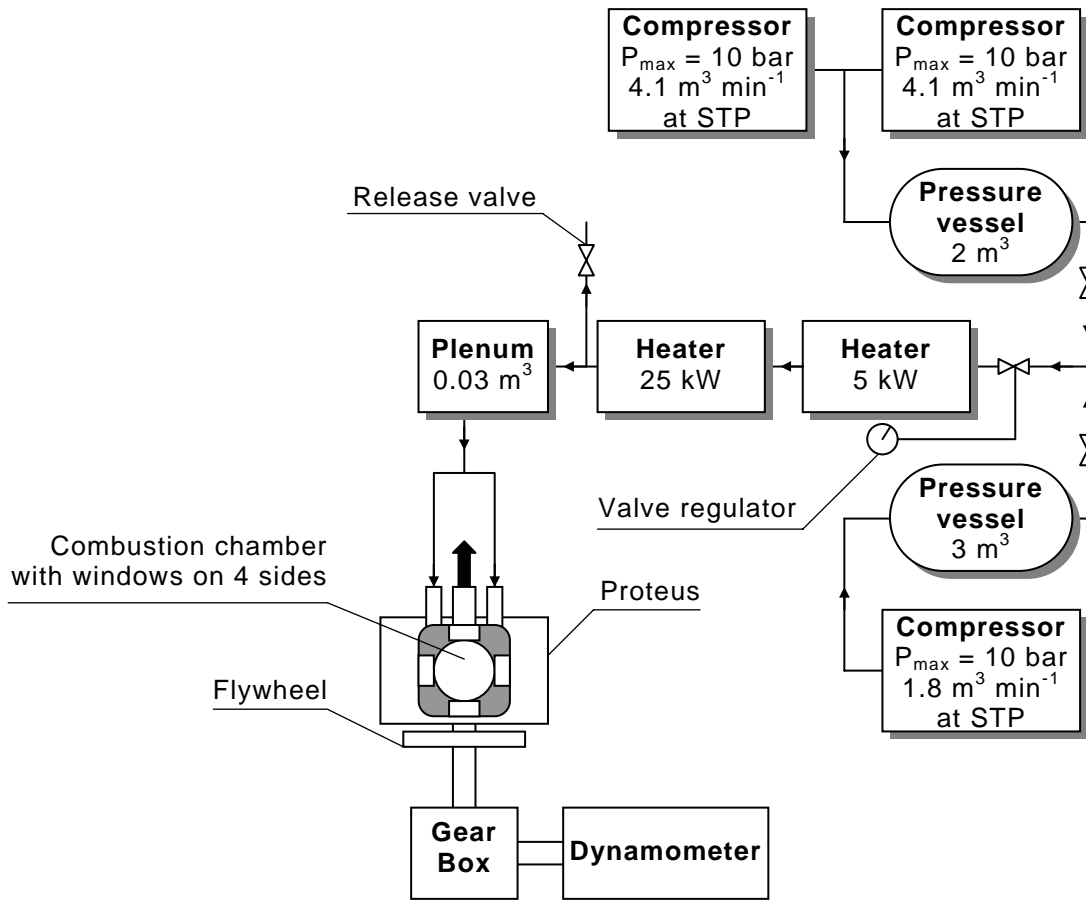


Figure 3-3. Schematic of the test bed layout showing the Proteus, dynamometer, compressors, heaters and main valves (∇).

3.1.1. Control software

The test bed equipment was controlled by a specially designed program written using HP-VEE 4.0, a commercial software package for hardware control and communication. The communication between the test bed and the software was achieved using serial interface modules. One digital module was used to control the rig equipment and ancillaries by means of mouse operated on-screen switches. Interlocks were implemented into the control software to ensure safe rig operation. For example the dynamometer could only be energised when the oil pump was running. Two multiple input analogue modules were used to display oil temperature and pressure, intake air temperature and pressure, cooling circuit temperature and exhaust pressure on screen. The acquisition of

the displayed data was fully automated. The archived data could then be viewed using a spreadsheet program such as Microsoft Excel.

3.1.2. Health and safety features

For health and safety reasons all moving parts, such as the dynamometer and engine drive shafts and the fuel pump belt drive, were guarded to minimise exposure of the operating personnel to potential hazards. All shaft guards were made of 1 mm thick stainless steel sheets. The engine flywheel guard was fitted with guiding rails to allow it to slide out of position with ease. This gave instant access to the flywheel without disturbing the optical equipment placed around the engine. This guard was fitted with an interlock switch that interrupted the power supply to the dynamometer when not properly secured. The fuel pump belt drive guard was manufactured from transparent acrylic sheets to enable visual monitoring.

The cylinder head was surrounded with a 6 mm thick transparent polycarbonate screen to minimise damage or injury in the case of a window or injector failure. Visual access to the cylinder head was maintained. Polycarbonate was selected for its high strength and transparency. However, when optical measurements were performed, the polycarbonate sheets were slid out of the optical paths in order to avoid any impact on the quality of the measurements. This resulted in a maximum clearance of 20 mm for the laser beam, and 40 mm for camera access.

One window blank was manufactured with additional fittings for a pressure transducer and a burst disc. The burst disc was a safety device designed to fail at a predetermined pressure. This limited the load on the windows and the engine should any failure have caused too high an in-cylinder pressure. Figure 3-4 shows a detailed photograph of this window blank.

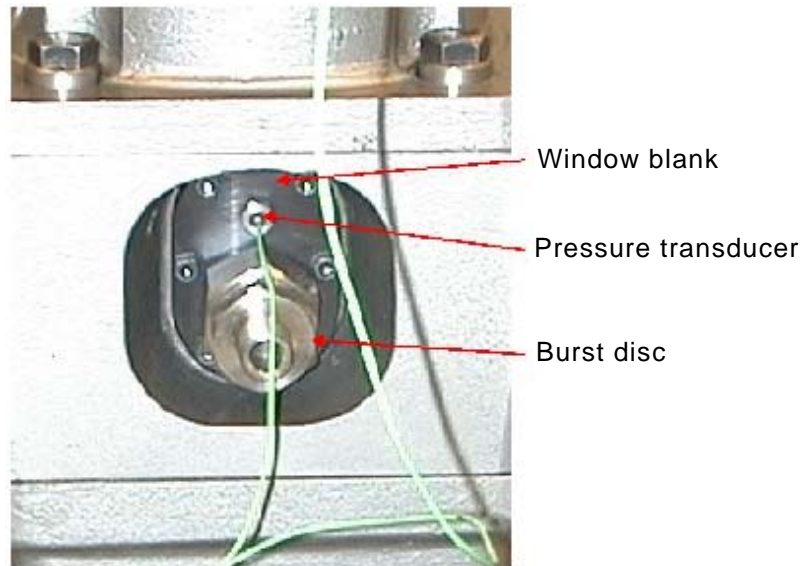


Figure 3-4. Window blank with burst disc holder and cylinder pressure transducer.

Three emergency stop buttons were fitted in different locations within the test cell. Beacons were lit at each entrance to the cell when lasers were in use. In case of an emergency a heat sensor was linked to the university fire alarm system, a fire extinguisher was present in the cell at all times, and four different exits were available including one exterior access.

Operating personnel were supplied with gas masks filtering organic vapours and particulates, laser safety goggles and radio-equipped ear defenders.

3.2. Optical high-pressure spray chamber

An optical chamber 80 mm in length and 50 mm in diameter was fitted on to the cylinder head to enable the full length of the developed fuel spray to be viewed. This chamber provided a near quiescent high-pressure environment, with realistic in-cylinder conditions being achieved by conditioning of the intake air. A schematic of the spray chamber is shown in Figure 3-5. The size and cylindrical shape of the chamber offered sufficient space for the fuel spray to develop without wall impingement. The flow field in the chamber was quiescent

to avoid disturbances by airflow motion on the spray development. The compression ratio of the engine was reduced to further increase the volume available for the optical chamber.

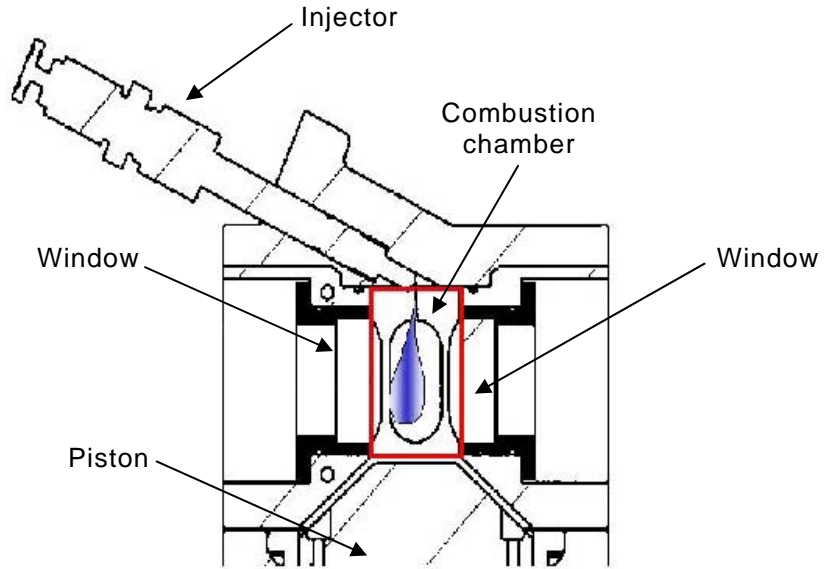


Figure 3-5. Schematic of the optical chamber.

In-cylinder temperatures and pressures representative of a modern engine were maintained by increasing the boost pressure and temperature up to 0.8 MPa and 100°C. The induced air was then compressed in the engine to achieve the desired test conditions. The air motion was designed to follow the loop scavenge two stroke cycle. The design of the inlet and exhaust ports and piston were optimised by first using the Ricardo WAVE gas exchange software to optimise the port areas. The design was refined further using the Ricardo VECTIS CFD code (Faure *et al.*, 1998) to optimise the air motion to achieve efficient scavenging and near quiescent air in the optical chamber. Good scavenging efficiency and quiescent air motion at TDC were achieved with the optimised design, as shown in Figure 3-6.

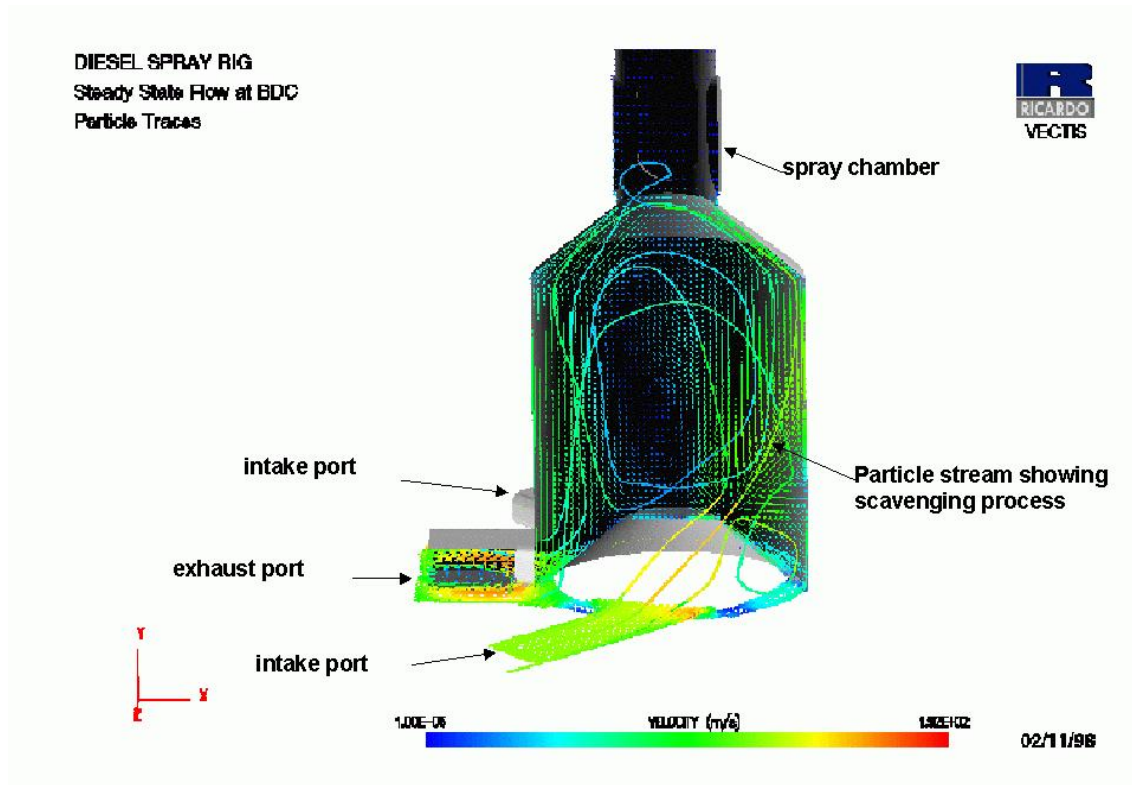


Figure 3-6. CFD simulation of the internal flow for loop scavenging.

The maximum velocity in the chamber during the injection process was predicted to be less than 1 m s^{-1} in the axial direction of the spray. Interaction with the wall was observed to be minimal for a fuel spray of the type produced by an injector used in a passenger car engine.

Optical access into the chamber was provided by four removable glass windows, shown on Figure 3-7, giving an optical access 25 mm wide and 55 mm high. The design was optimised to allow many state of the art optical techniques to be applied and enable both qualitative and quantitative measurements of fuel, air and combustion products.

The windows were easily removable for cleaning or replacement. The window holders were sealed into the optical extension casting by 'O' rings and an annealed copper gasket, the gasket also sealed the glass section against the casting. The windows were sealed in the holder by a silicon-based resin. This

arrangement performed adequately for all conditions obtained in the cylinder. The modular nature of the engine build allowed quick change over of the engine configuration, permitting a range of experimental configurations for different optical techniques and injector types.

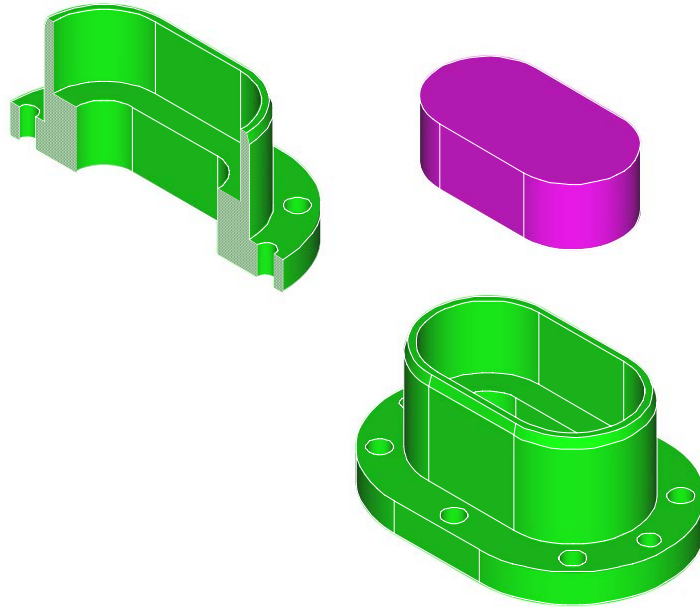


Figure 3-7. CAD drawing of a window and its holder.

The window glasses were 32 mm wide, 62 mm high and 20 mm thick.

3.2.1. Characteristics of the windows

Because the combustion chamber windows will inevitably absorb part of the emission spectrum, it had to be ensured that the material selected for the windows would not significantly affect the measurements. The material initially used for making the windows was a standard borosilicate crown optical glass BK7. BK7 is a very common material used for optical components in the visible range. This relatively hard glass showed a good scratch resistance, a very low amount of inclusions and was almost bubble-free. Another reason for choosing BK7 was the almost linear optical transmission in the visible range down to 350 nm. In order to verify the transmittance range of the glass used in this study, the absorption spectrum of a window was obtained using a spectrometer.

Figure 3-8 shows the transmission spectrum obtained from the absorption profile. This confirms that the windows comply with the requirements for the optical imaging strategies chosen in this study.

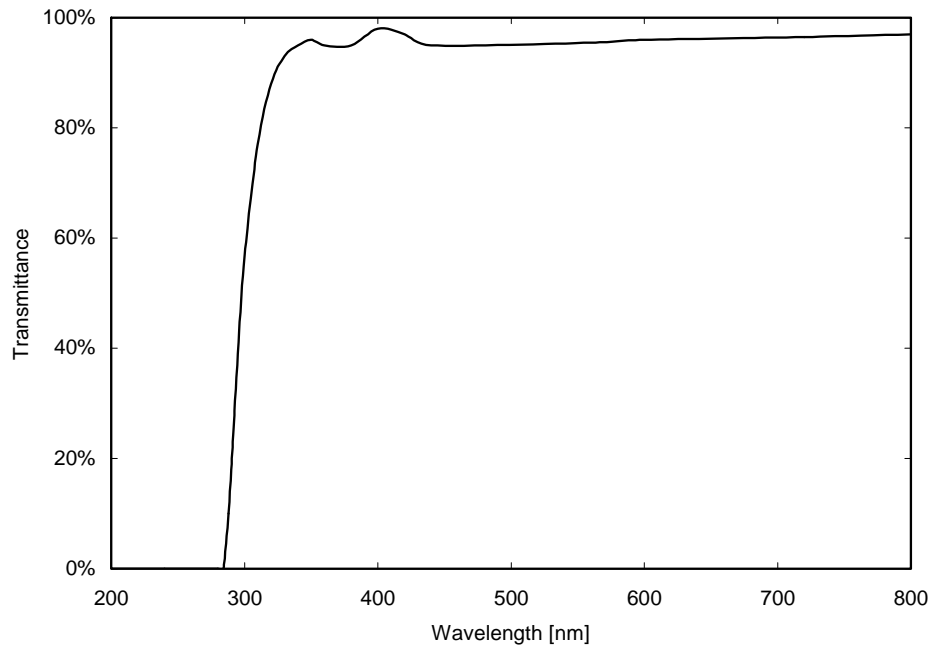


Figure 3-8. Measured transmittance of a typical 20 mm thick BK7 glass window used on the Proteus engine.

Due to a large number of failures when doing fired tests, the material for the windows was changed to sapphire glass. This material has excellent optical transmission in both the UV and infra-red, and a much higher melting point than BK7 (2030°C instead of 560°C). A typical transmission profile for sapphire glass is shown in Figure 3-9. No failure of the sapphire windows were observed.

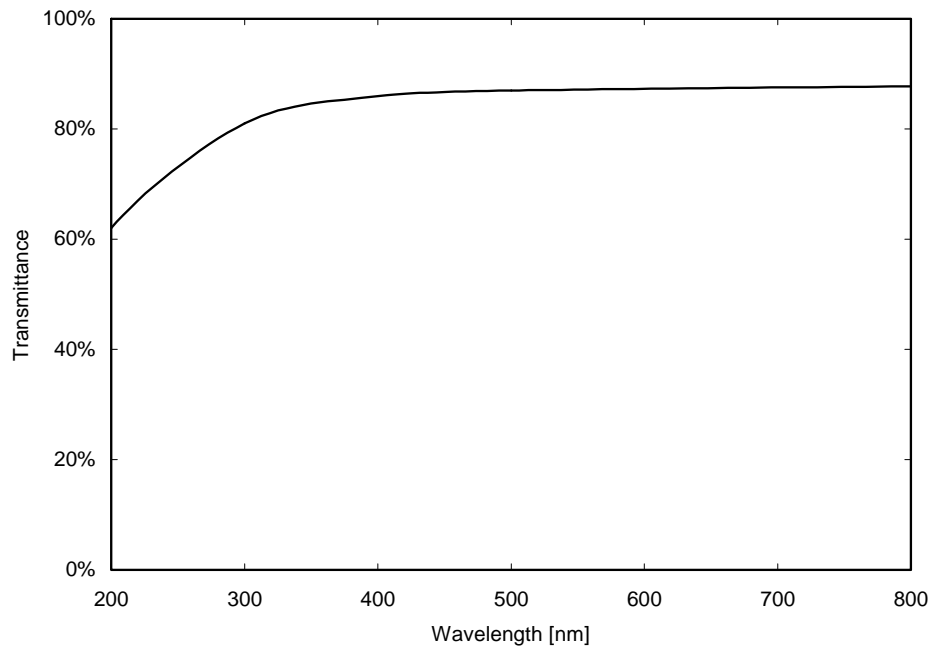


Figure 3-9. Transmittance of a 10 mm thick sapphire glass (*Laser components, 2001*).

3.2.2. Influence of window fouling

The windows were taken out and fully cleaned every day. The effect of window fouling on the images was assessed by running the engine at the same conditions before and after cleaning the windows. Comparing the results, it was subjectively concluded that the fouling of the windows did not noticeably alter the quality of the images for non-fired studies (e.g. liquid and vapour imaging). Window fouling for fired tests was not significant if the windows were cleaned daily. The fact that the camera's depth of field was kept small for all studies helped achieve good quality images by focusing only on the plane of interest.

3.3. Fuel system

A high pressure second generation Bosch common rail fuel injection equipment (FIE) was selected due to the high flexibility of common rail systems and the decreased design complications compared to the implementation of unit injector

systems. In this configuration, injection pressures up to 160 MPa were achieved. A schematic of the injection system is given in Figure 3-10.

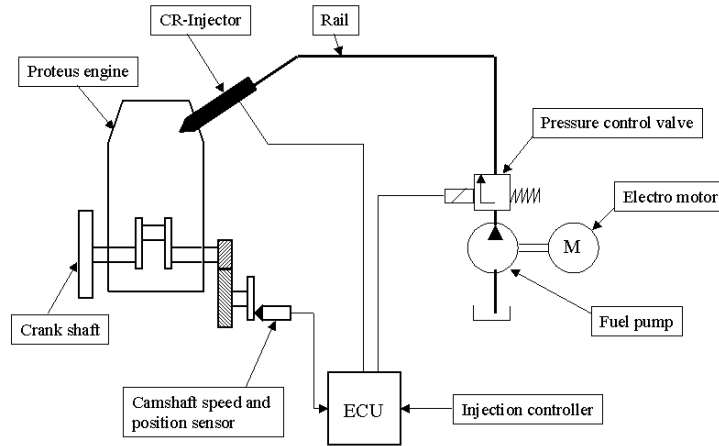


Figure 3-10. Schematic view of the fuel injection system.

The fuel pump was not driven from the crankshaft or the camshaft as is the case for production engines for two reasons. Firstly, the engine speed was too slow for the fuel pump to build up full pressure in the rail especially when a high amount of fuel was required. Secondly, when the fuel pump is driven by the crankshaft its speed is dependent on the engine speed and does not allow separate control of the pump. Therefore, the fuel pump was powered by an electric motor running at 1400 rpm which ensured a stable rail pressure with minimal fluctuation.

Figure 3-11 shows a detailed photograph of the fuel injection equipment of the Proteus. The belt drive for the fuel pump is shown on this photograph without the polycarbonate guard for better visibility.

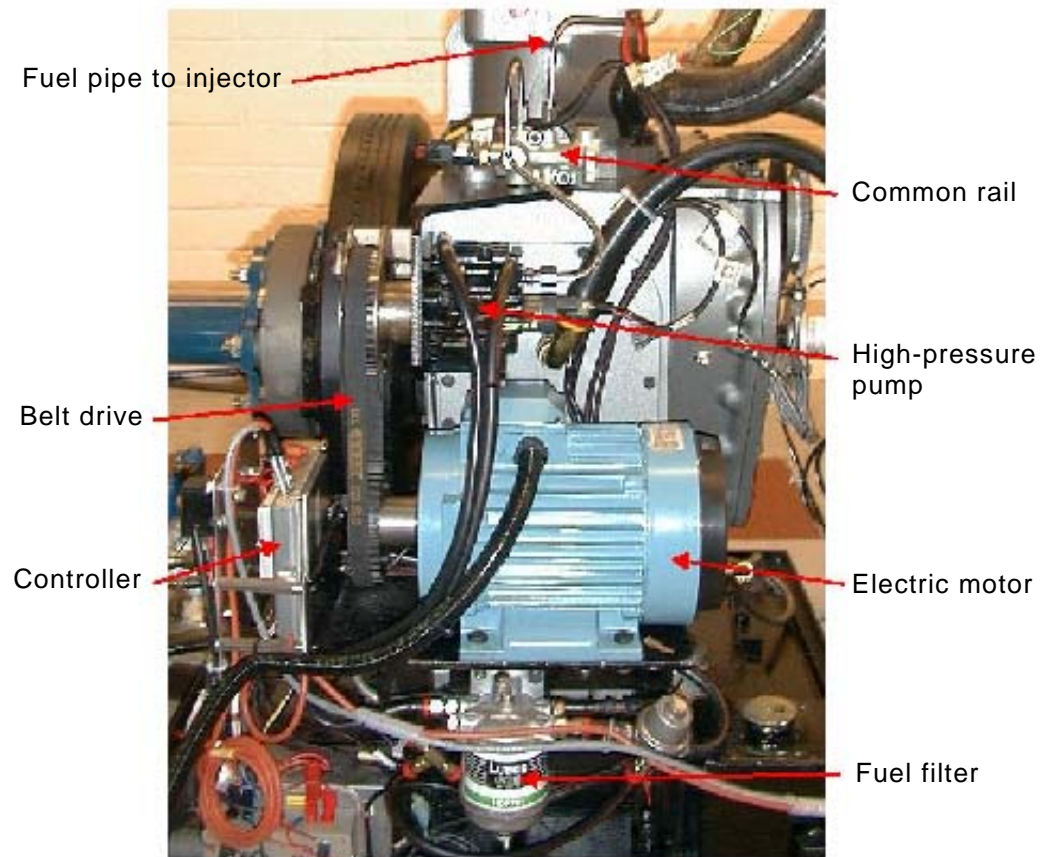


Figure 3-11. Photograph of the fuel injection equipment.

The rail and delivery pipe were both instrumented with a Kistler pressure transducer. The pipe from the rail to the injector was kept short, representative of a real vehicle system. A custom-built controller was developed (Kennaird *et al.*, 2000) to enable independent control of injection timing, number of injections per cycle, injection duration and rail pressure. This unit essentially consisted of a microprocessor dedicated to the task of triggering the injector and a secondary device (such as a laser system, flashgun or CCD camera). Before each series of experiments, a personal computer was used to upload the injection parameters to the FIE unit (e.g. injection angle, injection duration, rail pressure, delay of secondary trigger, etc.). This gave high timing accuracy and good parameter control. The custom controller also allowed control of initial needle drive current and PID control of the fuel rail pressure.

The fuel injector used was a modern electro-magnetic actuated common rail injector as shown in Figure 3-12. This injector was specially equipped with a needle lift sensor to obtain the exact needle position during the injection. The injector nozzles were interchangeable and therefore allowed testing of different nozzle types and nozzle hole diameters.

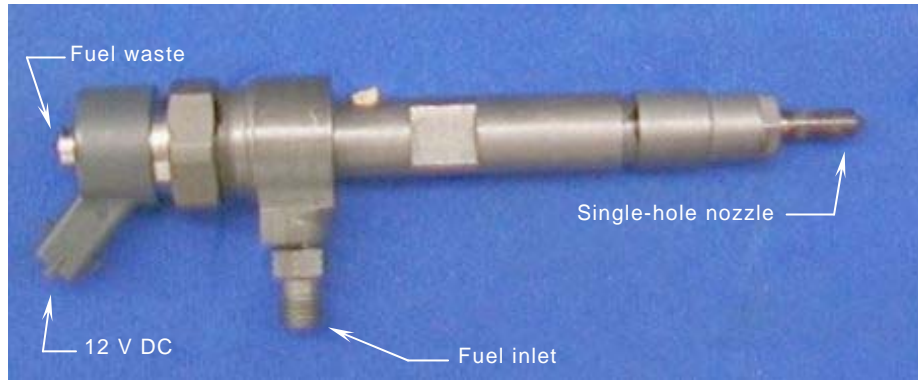


Figure 3-12. 160 MPa injector used for LII studies

For all the experimental work low-sulphur Esso AF1313 diesel fuel was used. Its main properties are listed in Table 3-1.

Fuel property	Specification
Ash content	0.005% (mass)
Carbon content	86.4% (mass)
Cetane number	55
Density at 15°C	830 kg m ⁻³
Flash point	70.5°C
Gross calorific value	45.8 MJ kg ⁻¹
Hydrogen content	13.4% (mass)
Kinematic viscosity at 40°C	2.87×10 ⁻⁶ m ² s ⁻¹
Oxygen content	<0.05% (mass)
Particulate matter	<10 mg kg ⁻¹
Sulphur content	0.02% (mass)
Water content	42 ppm

Table 3-1. Properties of the diesel fuel tested.

3.3.1. Injector nozzle library

For common rail injection systems VCO (Valve-Covered Orifice) nozzles, mini-sac nozzles and more recently micro-sac nozzles are used for fuel direct injection. In VCO nozzles the holes lead directly to the needle seat area and are therefore shut by the needle itself. Because of this feature, the fuel injection timing and quantities are very accurate but fuel distribution to the different holes is very sensitive to needle/nozzle concentricity during needle lift. This could lead to large discrepancies in spray formation between the different holes at small needle lifts, as shown in Figure 3-13 where only three sprays out of the five are well developed.



Figure 3-13. Photograph of the sprays with a six-hole VCO nozzle.

In mini-sac nozzles the holes lead to a sac volume below the needle tip and are not directly closed by the needle (Figure 3-14). The fuel sprays obtained with a mini-sac nozzle are not sensitive to needle dislocation since the fuel distribution to each hole is balanced by the sac volume (Kennaird *et al.*, 2002). A disadvantage of mini-sac nozzles when compared to VCO nozzles is that the fuel in the sac can result in fuel droplets leaving the injector after the needle has shut.

Micro-sac nozzles are the latest nozzle type of the three. More accurate production methods offer the possibility to reduce the volume of the sac and minimise the disadvantages it causes. A smaller sac volume results in a more accurate timing response and needle lift, but fewer spurious droplets on closing the needle.

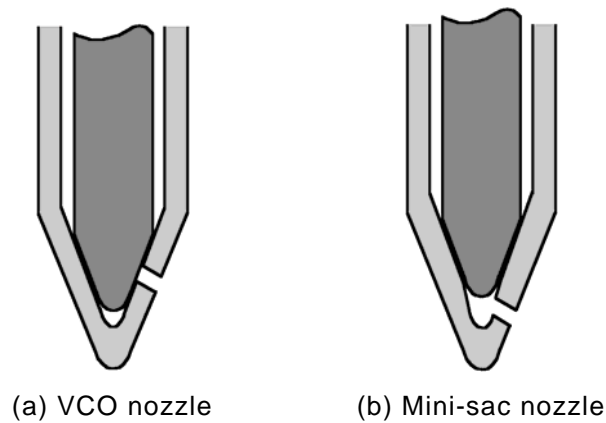


Figure 3-14. Diagrams of VCO (a) and mini-sac (b) nozzles.

A number of nozzles were used in this study, as summarised in Table 3-2.

Type	Orifice Diameter [mm]	L/D _o
VCO	0.15	6.8
VCO	0.20	5.0
Mini-sac	0.15	5.6
Mini-sac	0.20	4.5

Table 3-2. Injector nozzle characteristics.

The nozzles were of a single-hole design with an equivalent cone angle of 130° . The injector was inclined at an angle of 65° so the fuel spray from the single orifice was orientated vertically into the chamber. The holes were manufactured by a conventional spark erosion technique and then micro-honed by hydro-grinding to produce an entry radius and surface finish representative of a production nozzle. The needle was instrumented with a Hall effect type needle lift sensor. Fuel rail pressure and needle lift were monitored on a digital storage oscilloscope. The nozzles and controller were calibrated on a Moewald test bed to establish the injection pulse lengths required for different fuellings. Nozzle delivery rates were measured using a Lucas rate gauge.

3.3.2. Fuel injection calibration

The complete fuel system, including pump, rail, pipe-work and controller was calibrated on a Lucas rate gauge. This was initially done to verify that the new controller matched the injection rate diagram produced from a Bosch production Engine Control Unit. The injection rate diagram presented in Figure 3-15 shows that an equivalent injection rate to that of a typical common rail fuel system was achieved using the custom controller. Each nozzle was calibrated to establish a correlation between injection duration and injected fuel mass. Fuel flow was not measured during the imaging experiments but was derived from the injection duration and nozzle calibration. The same injector was used for the duration of these experiments. The injection rate was checked on the Lucas rate gauge after each nozzle change to confirm that the injector was performing correctly prior to testing on the spray rig.

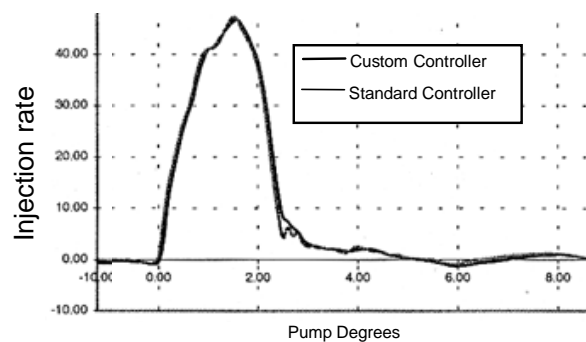


Figure 3-15. Injection rate diagram from standard and custom controller (100 MPa injection pressure).

The time for the first fuel droplets to exit the injector was measured with a high-speed camera pointed at the nozzle. The injection pulse duration was adjusted in order to keep the injected fuel mass constant. The delay between the start of injection pulse and the first droplets entering the combustion chamber varied with the injection pressure (Table 3-3). Unless otherwise mentioned, the data presented here have been adjusted to compensate for this delay.

Injection pressure	Injector delay	Pulse duration
60 MPa	0.60 ms	4.2 ms
100 MPa	0.45 ms	3.1 ms
140 MPa	0.39 ms	2.7 ms
160 MPa	0.37 ms	2.4 ms

Table 3-3. Delays between start of injection pulse and start of fuel delivery for a 30 mm³ injection with a 0.2 mm VCO nozzle, with the corresponding injection pulse durations.

3.4. Accuracy and calibration

3.4.1. Evaluation of the compression ratio

A series of tests were carried out on the on the optical Proteus rig in order to establish the compression ratio ε of the current build and the polytropic coefficient of compression n . These parameters need to be known to establish the performance of the build in terms of in-cylinder temperature and therefore the air density during injection. The compression stroke was assumed to be a polytropic process, therefore the isentropic laws were used in conjunction with an empirical polytropic coefficient n instead of the usual isentropic coefficient κ . The in-cylinder pressure during a typical compression stroke of the Proteus was recorded and plotted against the in-cylinder volume in Figure 3-16. The starting point, labelled SOC, corresponds to the instant when the inlet ports are shut whereas point TDC corresponds to top dead centre. The volume of the combustion chamber was determined by filling it with water a number of times and averaging the volumes measured. The swept volume of the Proteus was calculated and the volume into which the intake gasses were compressed was determined from the specified engine data and the measured clearance volumes.

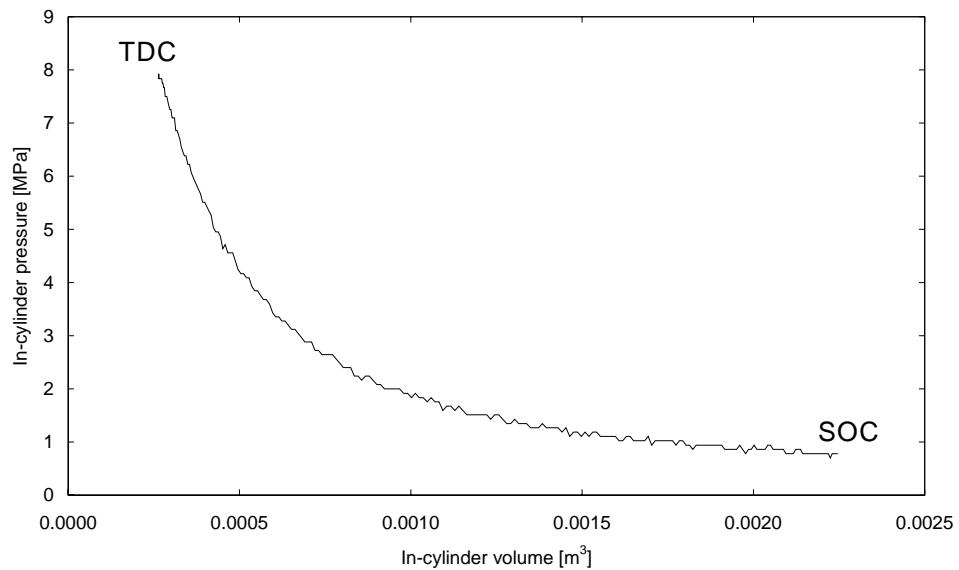


Figure 3-16. Pressure-volume diagram for a typical compression stroke on the Proteus engine.

Figure 3-17 shows a logarithmic plot of the in-cylinder pressure against the in-cylinder volume during a typical non-firing compression stroke¹. The slope of the trendline corresponds to the experimental polytropic coefficient of the engine at these particular conditions. In this case, the ICP was 8 MPa and the cylinder block was heated to 100°C. To warm the engine further, and therefore better match the conditions found under normal operation, the engine was fired several times prior to recording the ICP.

¹ The compression stroke was assumed to start when the piston ring shuts the inlet ports, i.e. 219 CA ATDC.

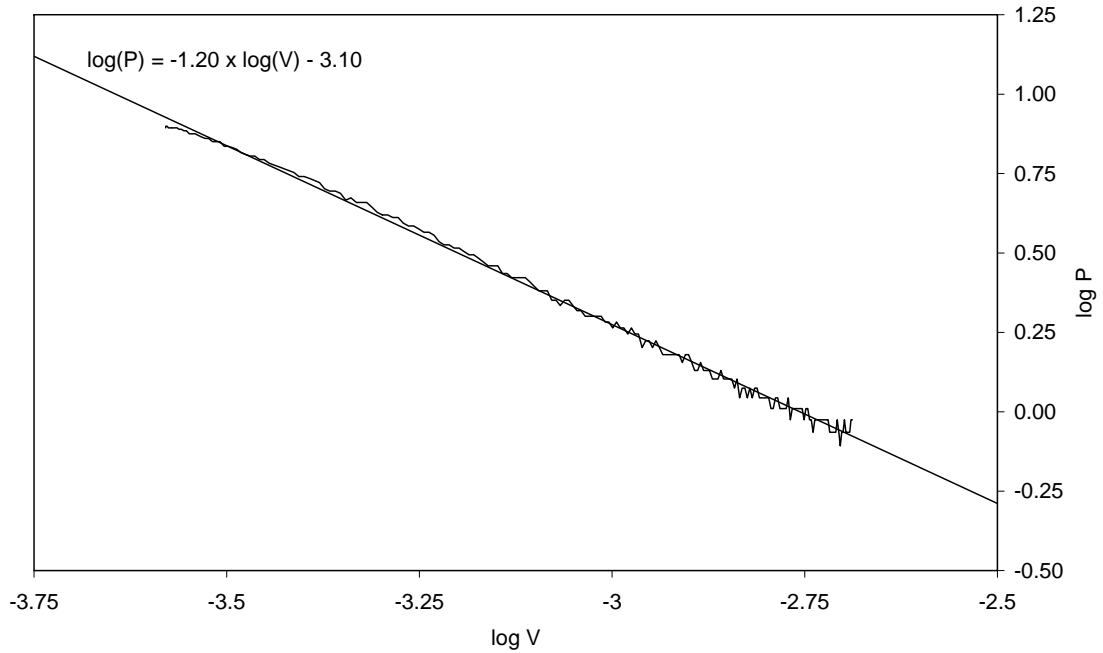


Figure 3-17. Polytropic coefficient from a $\log(P)$ versus $\log(V)$ chart.

It can be concluded from Figure 3-17 that the polytropic coefficient for that particular test was 1.2. An average value of 1.3 was established for the Proteus spray rig after repeating this process at various engine conditions.

The actual compression ratio can then be calculated by using the standard polytropic law:

$$P_{\text{SOC}} V_{\text{SOC}}^n = P_{\text{TDC}} V_{\text{TDC}}^n \quad (3-1)$$

The subscript SOC indicates that the values are taken at the start of compression, and the subscript TDC denotes the values at top dead centre. n is the polytropic compression coefficient. By rearranging Equation (3-1):

$$\frac{P_{\text{SOC}}}{P_{\text{TDC}}} = \left(\frac{V_{\text{TDC}}}{V_{\text{SOC}}} \right)^n \quad (3-2)$$

Remembering the definition of the volumetric compression ratio of an engine:

$$\varepsilon = \frac{V_{\text{SOC}}}{V_{\text{TDC}}} \quad (3-3)$$

Compression ratio can be related to the pressure ratio as:

$$\varepsilon = \left(\frac{P_{\text{TDC}}}{P_{\text{SOC}}} \right)^{\frac{1}{n-1}} \quad (3-4)$$

In the case described here, P_{SOC} and P_{TDC} were measured to be 0.78 MPa and 7.9 MPa, respectively. Thus, the resulting compression ratio was about 9:1.

3.4.2. Comparability to a modern diesel engine

The maximum TDC conditions that can be achieved in the Proteus spray rig compared to equivalent conditions in a real engine are shown in Table 3-4. For a modern DI diesel engine a compression ratio of 19:1 was assumed. The specific heat ratio (polytropic coefficient) was measured on the Proteus as described in Section 3.4.1.

DI DIESEL ENGINE		PROTEUS SPRAY RIG	
Compression ratio	19 : 1	Compression ratio	9 : 1
Specific heat ratio	1.3	Specific heat ratio	1.3
Intake air temperature	313 K	Intake air temperature	373 K
Intake air pressure	0.2 MPa	Intake air pressure	0.8 MPa
Temperature at TDC	757 K	Temperature at TDC	721 K
Pressure at TDC	9.2 MPa	Pressure at TDC	13.9 MPa

Table 3-4. Comparison between a modern diesel engine and the Proteus.

3.4.3. Errors and delays

A summary of the errors and delays for the Proteus spray rig is shown in Table 3-5.

Possible cause of error	Error magnitude	Assessment method
Engine speed fluctuations (non-fired)	Not quantified	
Engine speed fluctuations (fired)	0.25%	Measured ¹
Engine speed drop due to increased ICP	< 0.5%	Measured ²
Injection pressure fluctuations	< 5%	Measured

Possible delays	Error magnitude	Assessment method
Secondary trigger pulse ³ delay (relative to injection pulse)	+1.6 μ s	Measured
Needle lift delay (relative to camera pulse, $P_{inj} = 60$ MPa)	+0.60 ms	Measured ⁴
Needle lift delay (relative to camera pulse, $P_{inj} = 100$ MPa)	+0.45 ms	Measured ⁴
Needle lift delay (relative to camera pulse, $P_{inj} = 140$ MPa)	+0.39 ms	Measured ⁴
Needle lift delay (relative to camera pulse, $P_{inj} = 160$ MPa)	+0.37 ms	Measured ⁴

Table 3-5. Summary of errors and delays for the optical Proteus spray rig.

3.5. Conclusions of Chapter 3

A new high pressure diesel test facility has been designed and commissioned at the University of Brighton with industrial partnership from Ricardo Consulting Engineers. Initial tests on the rig have shown that it is able to simulate both current and anticipated in-cylinder conditions, while at the same time allowing good optical access of the diesel spray. The optical access windows that were fitted during these test conditions were inspected after the trial and showed no signs of degradation or wear.

¹ Measured using a scope set to persistence mode, thus showing the variations in TDC pulse timing.

² For an increase in in-cylinder pressure from 6 to 10 MPa.

³ The FIE controller secondary trigger pulse was used to trigger devices such as high-speed video cameras.

⁴ Measured with high-speed video recording at 45,000 frames per second.

4. DIESEL SPRAY CHARACTERISATION

4.1. Background

As the air-fuel mixing process is a key event in diesel combustion, a good knowledge of the formation of the spray is essential to improve mixing efficiency. The spray penetration length and spray penetration rate from a fuel injector are the parameters used to judge fuel spray performance. The merits of high or low penetration largely depend on engine design and geometry. Shorter spray penetration may be of an advantage where it reduces fuel impingement, but in larger engines may inhibit maximum air utilisation (Bergstrand & Denbratt, 2001). Many correlations for fuel spray penetration have been proposed in the literature, a review of early correlations by Hay and Jones (1972) has shown that there was disagreement in the results from the proposed correlations, although most investigators agreed that penetration was dependent on ambient density and injection pressure. Many of the initial investigations of spray performance were focused on low-pressure sprays injected into ambient or low density conditions (Kuniyoshi *et al.*, 1980). More recent investigations by Hiroyasu and Arai (1990), Naber and Siebers (1996) have shown a strong dependency of spray penetration upon both in-cylinder pressure and fuel injection pressure. Hiroyasu and Arai (1990) undertook comprehensive testing of the penetration and dispersion of both evaporating and non-evaporating sprays, and showed that the spray behaviour is strongly dependant on in-cylinder density. It was also concluded that in a higher density environment, wider dispersion of the spray occurred with increased amounts of air entrainment. This entrainment had a direct effect upon the momentum of the spray and hence reduced the penetration rate of the spray.

The study of Hiroyasu and Arai (1990) also concluded that the in-cylinder temperature has a significant effect on spray penetration, reducing the penetration by as much as 20% compared to sprays injected at non-evaporating conditions. Dent (1971) suggested the inclusion of a term to compensate for these temperature effects:

$$S \propto \left(\frac{294}{T_g} \right)^{0.25} \quad (4-1)$$

However, the observations of Naber and Siebers (1996) and Morgan *et al.* (2001) showed that this term does not fully compensate for the temperature effect on the liquid phase penetration.

A similar dependence of the liquid spray penetration on gas density and in-cylinder pressure was observed by both Hiroyasu and Arai (1990) and Dent (1971), who found the following correlation:

$$s = 2.95 \left(\frac{P_{inj} - P_g}{\rho_g} \right)^{0.25} \sqrt{D_o \cdot t}, \quad (4-2)$$

where P_{inj} is the fuel pressure, P_g the gas pressure, ρ_g the ambient gas density, D_o the nozzle orifice diameter. It is important to state that the above correlation was based on investigations using mechanical pump injection systems. Modern common rail fuel injection equipment were used in the investigations of Naber and Siebers (1996) and Morgan *et al.* (2001), while injecting into high-density environments. Their results showed that this correlation over-predicts the liquid penetration length. It is clear from the above that although the influence of injection parameters has been widely investigated, information on the effects of in-cylinder density and fuel rail pressure on spray and fuel vapour distribution are still not conclusive.

It is generally accepted that injection rate profile and injection nozzle geometry have a major influence on both the penetration and distribution of the fuel spray within the cylinder (Bae & Kang, 2000). A reduction in the nozzle orifice diameter has also been shown to have an effect on the emissions (Bergstrand & Denbratt, 2001). This was concluded to be caused by the decreased size of droplets produced by smaller diameter nozzles. These smaller droplets mix and evaporate faster leading to shorter ignition delays. The internal flow structures within the nozzle are also thought to affect the spray performance. Hence different spray structures may not be attributed to differences in nozzle diameter only, but also to the nozzle type. Investigations into these flow

process have been undertaken in both large scale and full size nozzles (Soteriou *et al.*, 1995; Badock *et al.*, 1999). The effects of cavitation within the nozzle have been identified as a major influence on the subsequent liquid/droplet behaviour. The variation in the behaviour of various nozzle types and the influence of injection rate may go some way to explaining the apparent differences in the correlations for penetration with time and dispersion found in the literature. This, again, highlighted the strong dependence of the fuel spray behaviour on the nozzle geometry and hence the dangers of applying generic correlations derived from experiments based on a limited specific nozzle type.

The multi-hole injection investigations of Bae and Kang (2000) found that there was little hole-to-hole variation when injecting diesel through a VCO nozzle; however, an orifice-to-orifice variation was observed in spray angle when a sac nozzle was investigated. The experimental approach of Bae and Kang (2000) allowed all orifices to discharge in the measurement vessel. However, in the investigations of Campanella *et al.* (1994) where the discharges from all but one orifice were captured, variations in the performance of each orifice of a five hole VCO nozzle was found. It was also noted that the alteration of the needle seat construction had a strong influence on nozzle performance. Bae and Kang (2000) used a double-guided needle in this work and commented that previous results using a single-guided needle showed variations in penetration and dispersion. It is unclear whether the needle in the experiments of Campanella *et al.* (1994) was single or double-guided.

From the above, many of the experiments investigating spray characteristics have been undertaken with specially manufactured nozzles to facilitate data gathering. This normally means that a special single orifice nozzle is used or that all but one orifice discharge is captured. Measurements are then concentrated on one particular hole. The validity of such approach is often questioned, as the adoption of this practice may influence the behaviour of the injection process. The data available in the literature pertaining to the investigation of multiple orifices versus single orifice nozzles is sparse. In addition, the information available on the hole-to-hole variation of sprays from particular injectors is contradictory and often appears to be dependent on the

particular experimental approach adopted (Campanella *et al.*, 1994; Bae & Kang, 2000).

The fuel evaporation, penetration with time and dispersion is important to the combustion process as it provides the transport of the fuel vapour into the chamber. Using Rayleigh scattering Dec (1997) measured the simultaneous development of the liquid and vapour phases of the fuel spray. In this work it was found that the vapour did not penetrate further than the liquid core until the maximum liquid penetration length was reached. After this period the vapour continued to penetrate into the chamber. The width of the vapour phase was observed to develop to twice that of the liquid at the location of maximum liquid core penetration. As yet the influence of the injector characteristics on the vapour distribution process has not been fully investigated.

In summary, although investigation of liquid penetration from diesel sprays has been quite extensive, a reliable correlation for the prediction of penetration with time has still to be developed. It is believed that the discrepancies in the models presented are caused by the difference in injection nozzle geometries. The ambiguity over the effect of nozzle types on liquid phase penetration also extends to the vapour phase propagation. It is therefore clear that the effect of nozzle type and in-cylinder conditions on the injection and mixing processes are not fully understood.

The current work gives details of experiments undertaken to quantify both the liquid and vapour distribution of a diesel fuel injected through a modern common rail fuel injection system into realistic engine environments (high-temperature charge experiments) and into in-cylinder conditions at lower temperatures than expected in a working engine (low-temperature charge). The rationale for investigating the low temperature charge conditions was initially to look at the effects of temperature on the evaporative processes of the spray and for later use as validation for CFD models.

By simply visualising the diesel jet, a number of characteristics of the spray, such as its penetration length with time, cone angle, liquid core length and fuel breakup can be obtained.

Two different acquisition strategies can be adopted:

- High-speed visualisation
- Single-frame acquisition

In the high-speed case several photographs of a single spray are acquired consecutively, with an exposure time low enough to minimise blurring due to spray movement. This technique can be applied either with a high-speed video camera using light-sensitive film, or with a charge-coupled device (CCD) camera. The former has the major inconvenience of requiring the processing of thousands of photographs for every injection. Therefore, the analysis of such large quantity of stills is not easily achieved, and the use of post-processing software is made tedious by the need to digitise every single photograph. CCD cameras offer the opportunity to observe a complete injection at high recording speed, but the resolution of the images is significantly lower than with standard film. Because the output is readily available in digital format and can be observed instantly, this technique was preferred to standard film recording.

After analysis of the high-speed recordings, the most critical phases of the diesel injection were then photographed using a 35 mm still camera and a high-speed flashgun. This allowed a set of high resolution photographs to be obtained, thus giving more-detailed images at important timings. The results are compared with other experimental data and empirical models.

4.2. Experimental apparatus and procedure

4.2.1. High-speed video recording of diesel sprays

The CCD video camera used in this series of experiments was a Kodak Ektapro HS Motion Analyzer (model 4540), with a recording rate adjustable from 30 to 4500 frames per second at full resolution (256×256 pixels × 256 grey levels), and from 9000 to 40500 frames per second at progressively reduced resolution. The best compromise between acquisition rate and image resolution was obtained with a frame rate of 18000 to 27000 pictures per second, with a corresponding resolution of 256×64 pixels × 256 levels of grey, and 128×64 pixels × 256 levels of grey, respectively. The camera was used in

intensified gain mode, with a gamma correction factor of 1.0 in order to maximise the intensity of the recorded images. The sprays were backlit by a halogen flood light fitted with a diffuser (Figure 4-1).

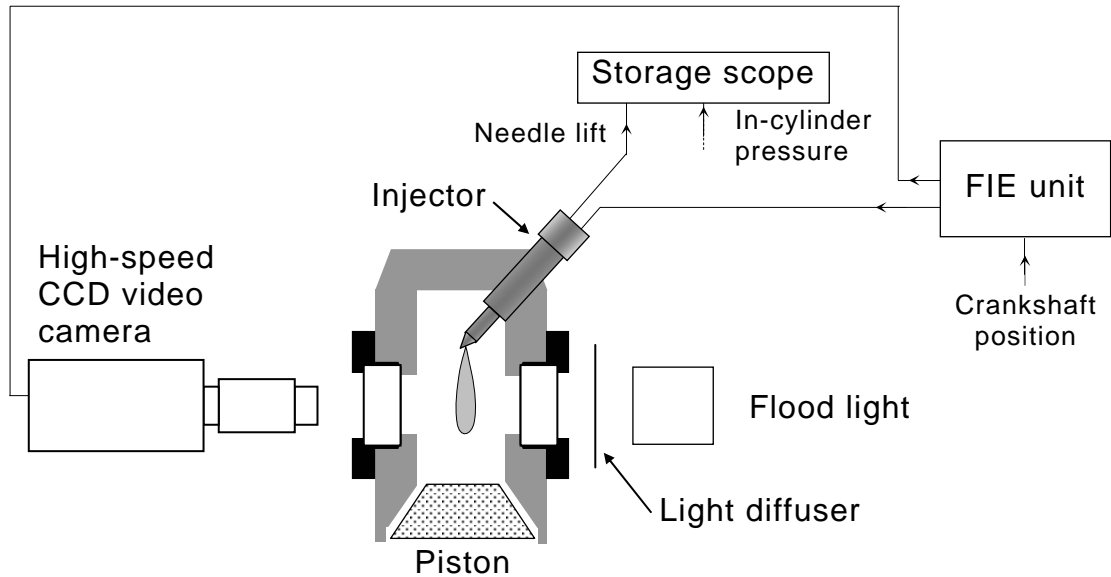


Figure 4-1. A side view of the experimental set-up for backlit spray photography.

The injection timing was controlled by means of the custom-built FIE. All the injections observed were then downloaded to a computer directly from the CCD camera. The injector needle lift and in-cylinder pressure were acquired by a digital storage oscilloscope for each recorded injection, and then downloaded to the computer.

The processing of the videos was performed by purpose-developed software that measures the spray penetration length and spray cone angle at each video frame after suitable pixel thresholding (Morgan *et al.*, 2001). A typical unprocessed image is shown in Figure 4-2a, the spray nozzle tip is located 20 mm above the top of the window edge and is therefore not visible. The images were thresholded to pick out the spray outline from the background. The threshold level was subjectively chosen by selecting one image from the batch of images generated by a test run and varying the threshold to obtain optimum results. Since the quality of images remained the same during a test run, this threshold value was suitable for all the images in that batch. The maximum

spray penetration was calculated by finding the spray pixel furthest from the nozzle. The software calculated the spray penetration for each image, the results of which were saved as a spreadsheet, and in graphical format as seen in Figure 4-2b.

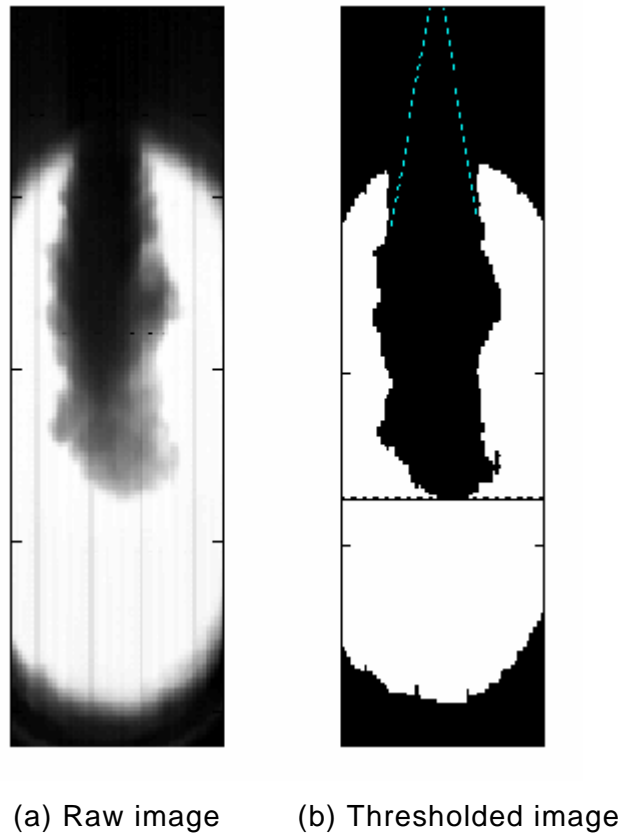


Figure 4-2. Raw digital spray image (a) and thresholded image (b) showing maximum penetration length and spray cone.

The source code for this post-processing software can be found in Appendix A.

In order to be able to observe the first 20 mm of the spray, a window blank was modified to allow the injector to be fit as shown in Figure 4-3. Since the post-processing software could not be adapted to analyse the data obtained with this set-up, the liquid spray penetration and spray dispersion angles were measured manually for each frame of each recording.

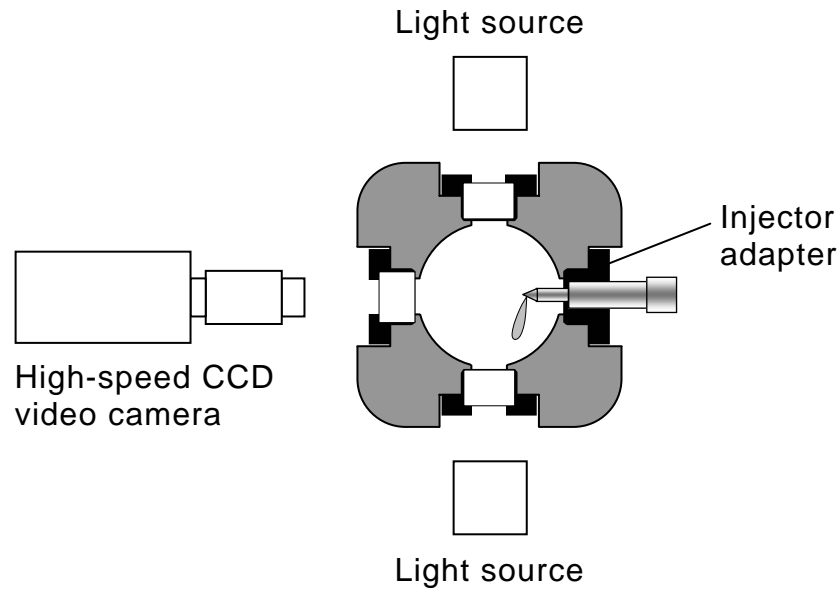


Figure 4-3. Experimental set-up for spray close-up study.

Repeatability tests were performed to assess the variability in penetration for a range of test conditions. The variation in penetration length was found to be $\pm 4\%$ from the average curve. The camera resolution was measured to be 0.3 mm per pixel, hence the overall uncertainty was estimated to be $\pm 6\%$. The calculated results were found to be insensitive to the threshold level chosen with a 12.5% variation in threshold level giving a 1% change in measured penetration.

4.2.2. Photographic imaging of sprays

A fully manual Pentax still camera was used with a telephoto lens (125 mm, f/4-f/22) and two extension tubes (1+3 cm). This combination was found to give the best compromise between magnification and focal distance. During the tests, a high-speed argon flash lamp was synchronised with the engine and delayed relative to TDC by means of the FIE controller. For each photograph, the shutter of the camera was kept open until an injection occurred. The duration of the flash was less than 5 μs . A diffused backlighting was preferred to side-lighting for a more homogeneous illumination of the spray background. Kodak 400 ISO films were used and the camera aperture was set to f/8. These

settings were found to give a good compromise between sensitivity of the film, quality of the prints and depth of field (measured to be about 4 mm at f/8). Even though a smaller lens aperture would have provided a much larger depth of field (i.e. better focusing of the whole spray), the amount of light available with the argon flashgun was not sufficient to give correct exposure.

For each one of the three different fuelling rates tested, two photographs were taken at different timings: one around the maximum liquid length and one showing the breakup of the spray. Because the tip of the nozzle was not visually accessible through the windows, the beginning of the injection could not be observed.

A flash lamp was used to backlight the sprays and therefore these photographs show the overall shape of the spray, integrated along the line of sight. The scaling factor for the plane of the spray was measured to be 1:0.28 (i.e. 1 cm on a photograph is equivalent to 0.28 cm in reality), which corresponds to a magnification factor of 3.6.

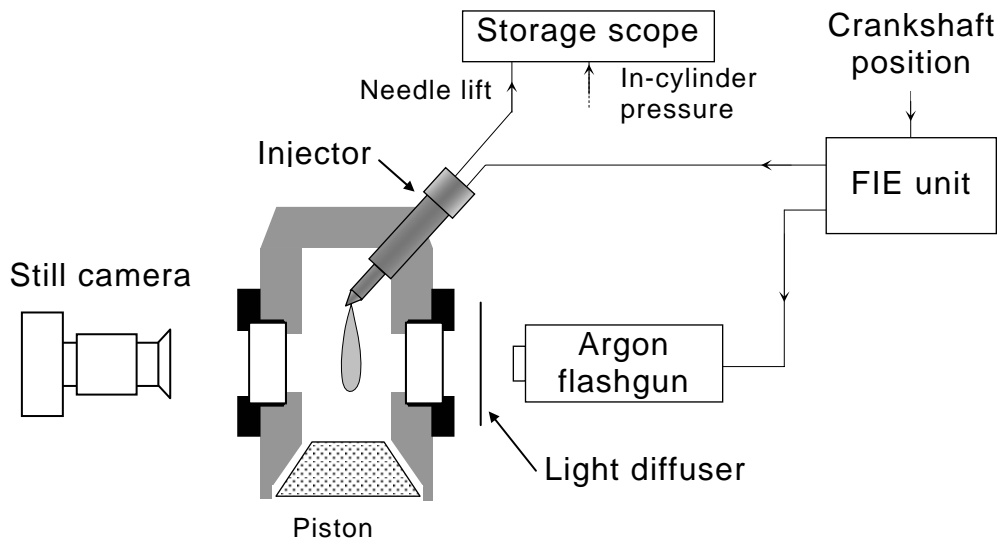


Figure 4-4. Experimental set-up for backlit spray photography. The combustion chamber is viewed from the side.

4.2.3. Schlieren video imaging of vapour phase

A schlieren set-up consisting of a light source, a diaphragm, two parabolic mirrors, a knife-edge and a fast CCD still camera was mounted on the Proteus engine (Figure 4-5). Different light sources were tested, and the best one available was found to be a sodium lamp. A diaphragm was placed in front of the lamp in order to eliminate any astray rays of light and therefore produce a point source. The use of focusing lenses was not necessary as sufficient light was emitted through the iris to give proper exposure. The first parabolic mirror was used to collimate the cone of light produced by the sodium lamp/diaphragm arrangement. The collimated light source thus created was oriented towards the optical chamber where changes in density cause slight changes the direction of the light rays. A second parabolic mirror focused the disturbed light. Because the density gradients altered the course of photons, the focal point is slightly different for each ray of light. When a knife-edge was set to crop some of the light at the focal plane, the whole image darkened uniformly and the density gradients became observable as scales of grey. This was because of the fact that the light let past the knife-edge was affected by density changes, and interference with the rest of the disturbed light was prevented by inserting the knife-edge.

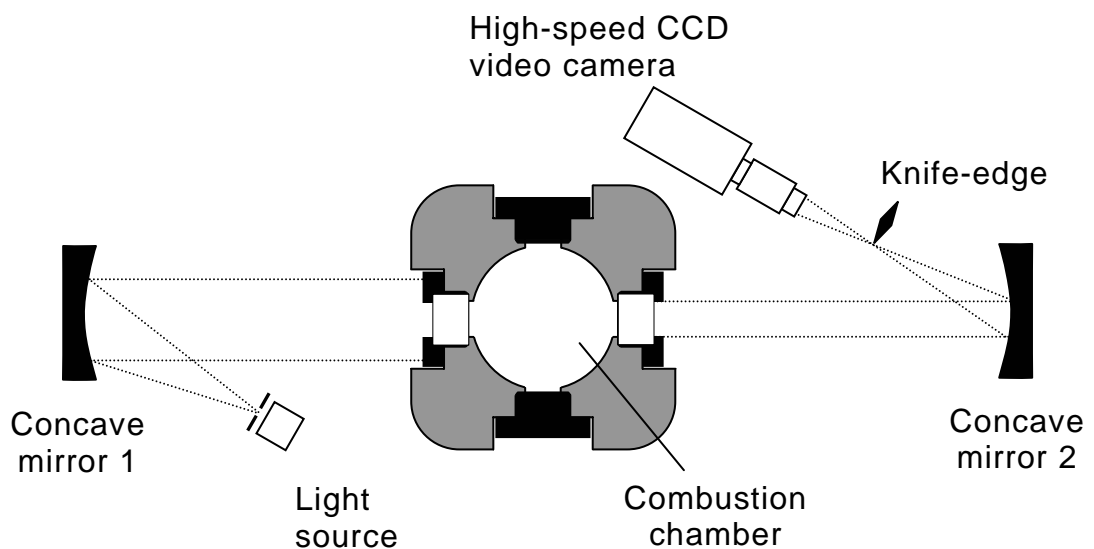


Figure 4-5. Experimental set-up for schlieren video. The combustion chamber is viewed from the top. Both mirrors are 0.144 m in diameter and have a focal length of 1.2 m.

The schlieren images were directly recorded with a high-speed CCD video camera, without using an intermediate screen in order to optimise the quality of the video recordings. This technique therefore allowed the vapour phase of diesel sprays to be visualised, providing valuable information on evaporation that could be related to autoignition sites and soot formation zones. Additional measurements were performed using a still CCD camera instead of the high-speed video camera for improved spatial resolution.

4.3. Experimental results

The exact conditions for the data presented in this chapter can be found in Appendix A.

In order to substantiate the use of single-hole nozzles, high-speed video tests were performed with the set-up described in Figure 4-3 using single and multi-hole nozzles at similar conditions. Figure 4-6 illustrates a comparison between a 0.2 mm single-hole nozzle and a 0.15 mm single-hole nozzle, along with a five-hole 0.15 mm nozzle.

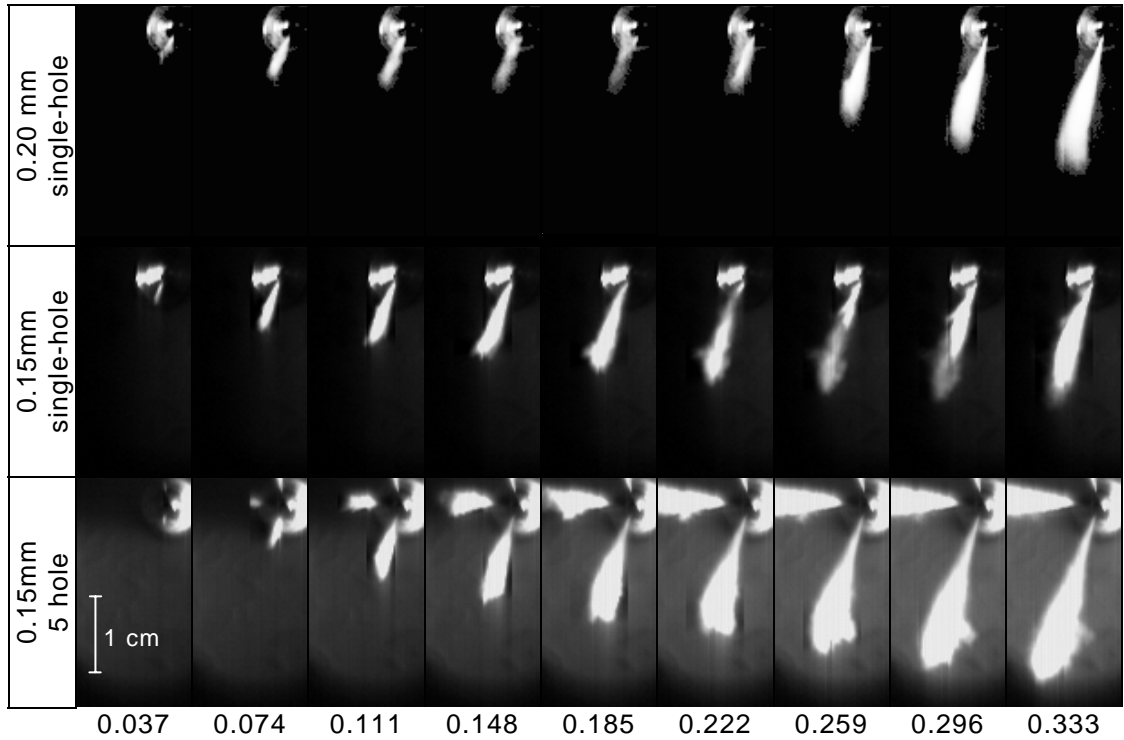


Figure 4-6. Comparison between 0.2 mm single-hole, 0.15 mm single-hole and 0.15 mm multi-hole VCO nozzles, for an injection pressure of 160 MPa. Times are in milliseconds after first frame showing visible liquid injection. The apparent difference in dimensions of the sprays produced by the single-hole and multi-hole nozzles are due to differences in lighting and scaling conditions.

At about 0.148 ms after the spray became first visible, the 0.2 mm single-hole injector orifice seemed to shut very shortly before the needle reached full lift. The same effect was visible to a lesser extent with the 0.15 mm single-hole nozzle at 0.185 ms. No such behaviour was observed with the multi-hole VCO and the mini-sac type nozzles tested. Needle lift traces showed that the needle continued to lift during this hesitation period (Figure 4-7), leading to the conclusion that the needle shut the orifice by moving transversally rather than vertically.

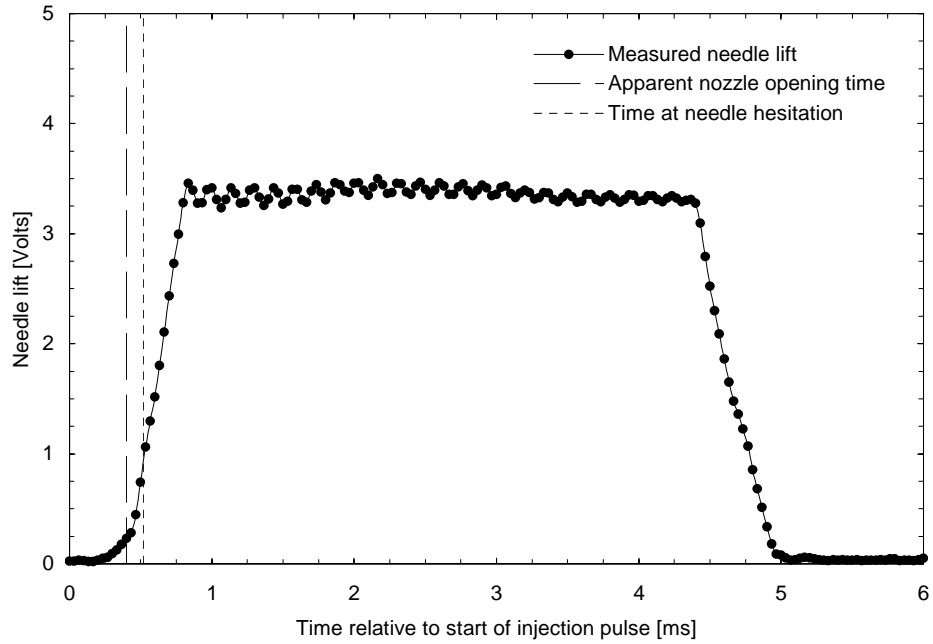


Figure 4-7. Injection needle lift trace for a 0.2 mm VCO single hole nozzle, with an injection pressure of 160MPa.

Figure 4-8 graphically represents the liquid spray tip penetration and demonstrates the early hesitation in the opening phase of the single hole nozzle. Similar data were observed for the penetration profiles of each individual hole of a three-hole nozzle as shown in Figure 4-8. As can be clearly seen the effect of the hesitation in opening was to delay the spray penetration with time. However, the curve for the three-hole nozzle was offset to allow direct comparison of the penetration rates. The penetration rate from each hole was the same for the single and multi-hole nozzles once the nozzle was fully open. The same was true when comparing five-hole and single-hole VCO nozzles. It is therefore considered valid to use single-hole nozzles to characterise spray penetration, as long as the limitations mentioned above are taken into account.

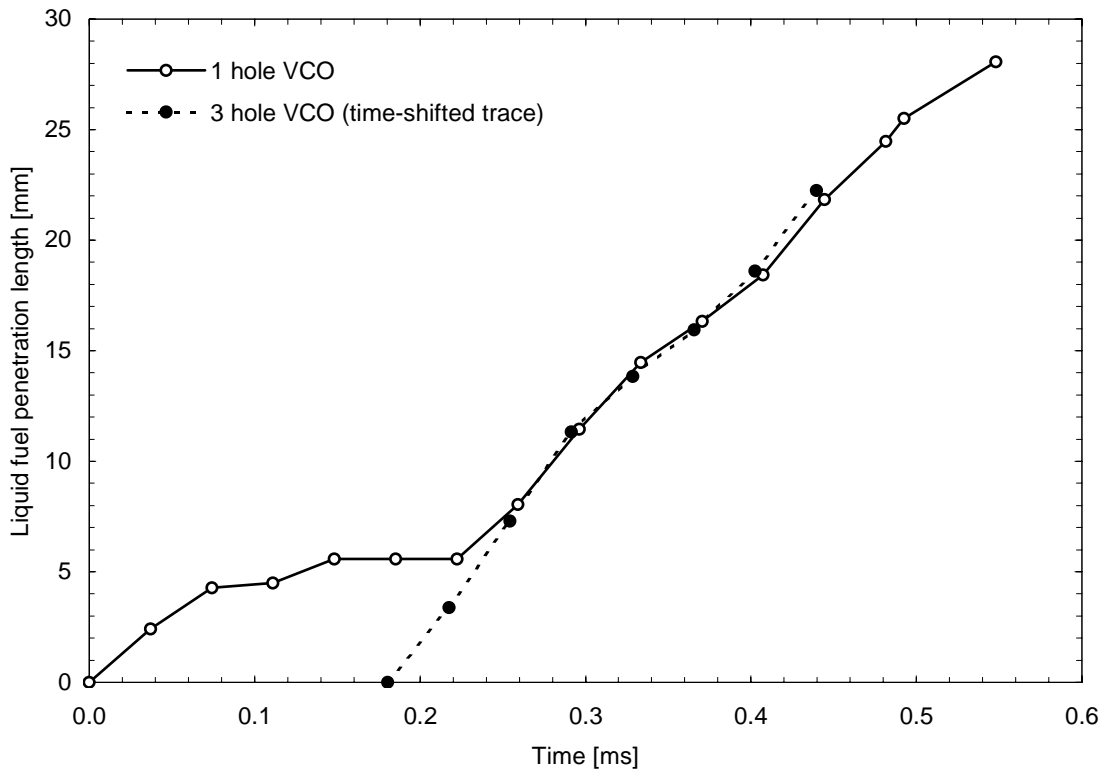


Figure 4-8. Single and multi-hole penetrations with time for 0.2 mm VCO nozzles and an injection pressure of 160 MPa.

High-speed video recordings of full length sprays were performed at three different injection pressures (60, 100 and 160 MPa), two intake air temperatures (20°C and 100°C), and several in-cylinder densities (14, 28, 34, 42, and 49 kg m⁻³ at TDC for 20°C air intake; 14, 28, 35 and 40 kg m⁻³ at TDC for 100°C air intake). The majority of the tests were performed with a single-hole 0.2 mm VCO nozzle, with additional experiments performed on 0.2 mm mini-sac for comparison purposes. Good repeatability was obtained, in terms of both liquid penetration length, spray cone angle and vapour penetration length.

A table of equivalence between gas density and in-cylinder pressure for the conditions tested is presented in Table 4-1.

20°C air intake (570 K at TDC)		100°C air intake (720 K at TDC)	
Density [kg m ⁻³]	ICP [MPa]	Density [kg m ⁻³]	ICP [MPa]
14	2.2	14	2.8
28	4.5	28	5.7
34	5.5	35	7.1
42	6.8	40	8.2
49	7.9		

Table 4-1. Table of equivalence for gas density and in-cylinder pressure, assuming a compression ratio of 9 and a polytropic coefficient of 1.3.

Preliminary high-speed video imaging identified a number of areas of interest for high-resolution photography. Photographic tests were performed at:

- Fuel pressures between 60 and 160 MPa
- Ambient air pressures between 3 and 8 MPa at TDC
- Ambient air temperature of 570 K at TDC
- Injection duration from 0.9 to 3.41 ms
- Single-hole VCO nozzle with 0.2 mm diameter

A sequence of images taken 1 ms after the start of injection for a 3.41 ms injection is shown in Figure 4-9. Images were taken at two values of ambient pressure and four values of rail pressure at an ambient temperature of 570 K. The evaporation of the spray at this temperature can be considered minimal (Luard, 1994). The expected increase in penetration resulting from an increase in injection pressure or decrease in gas pressure is observed. The structure of the spray is consistent with previous observations (Yule & Salters, 1995; Mouqualid *et al.*, 1998), with areas of atomised droplets being entrained at the edge of the spray where fuel air mixing takes place. The influence of gas pressure can be clearly seen from Figure 4-9 and Figure 4-10, with the higher gas pressure resulting in a noticeable reduction in spray tip penetration, particularly for the lower injection pressures.

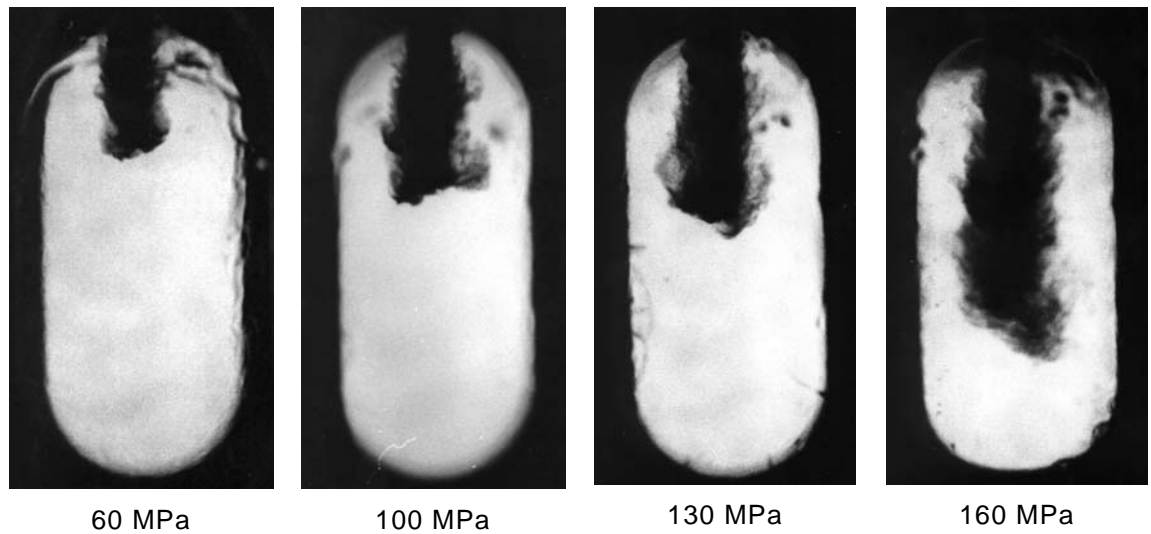


Figure 4-9. Backlit spray images taken 1 ms after the start of injection in air at 3 MPa with an injection duration of 3.41 ms at four fuel rail pressures.

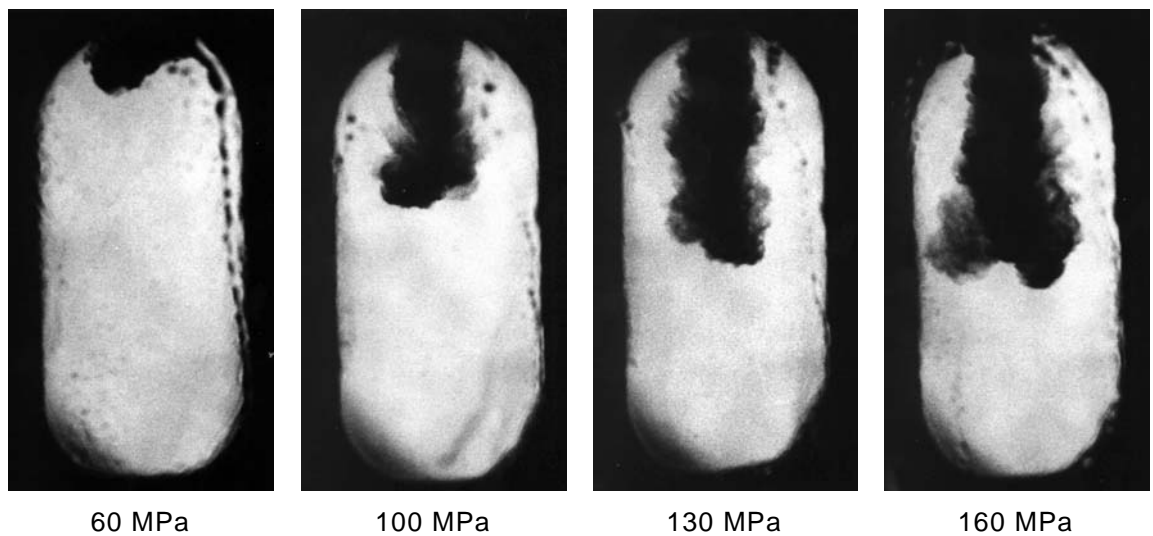


Figure 4-10. Backlit spray images taken 1 ms after the start of injection in air at 8 MPa with an injection duration of 3.41 ms at four fuel rail pressures.

During the initial stages of injection a concentrated ‘bunching’ of spray at the leading edge of the jet is formed as droplets penetrate the stagnant gas field, re-circulating areas of droplets are observed to ‘peel’ back along the edge of the spray cone from this area. This droplet stripping process was observed for all injection conditions and is shown in Figure 4-11 (negative images are shown to

improve clarity). The formation of a head vortex due to the entrainment of dense air can be seen more clearly at the higher air density cases.

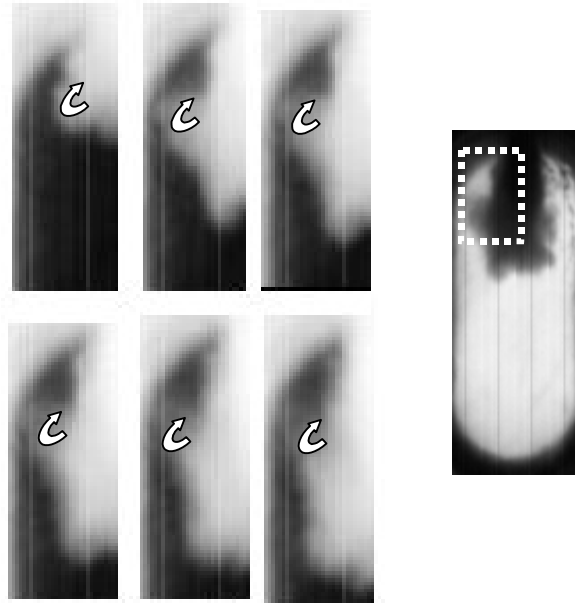


Figure 4-11. High-speed video sequence showing the development of areas of droplets 'peeling' back along the spray plume. Enlarged frames presented are from 1.1 to 1.4 ms after start of injection pulse (ASOI).

A similar sequence of photographs is shown in Figure 4-12 and Figure 4-13 for a 0.9 ms injection duration. The spray structure is observed to be slightly different when compared with the 3.41 ms injection case. In the 0.9 ms period case, the injector needle only briefly reaches full lift, resulting in a throttling of the fuel flow under these conditions. Fuel is therefore predominantly injected during throttling, hence the orifice internal flow structure would be expected to be different to that of the 3.41 ms case. This effect has been observed in steady state large scale nozzle tests (Soteriou *et al.*, 1993) particularly with VCO nozzles. It demonstrates the importance of understanding the effect of internal orifice flow structure on the behaviour of the spray.

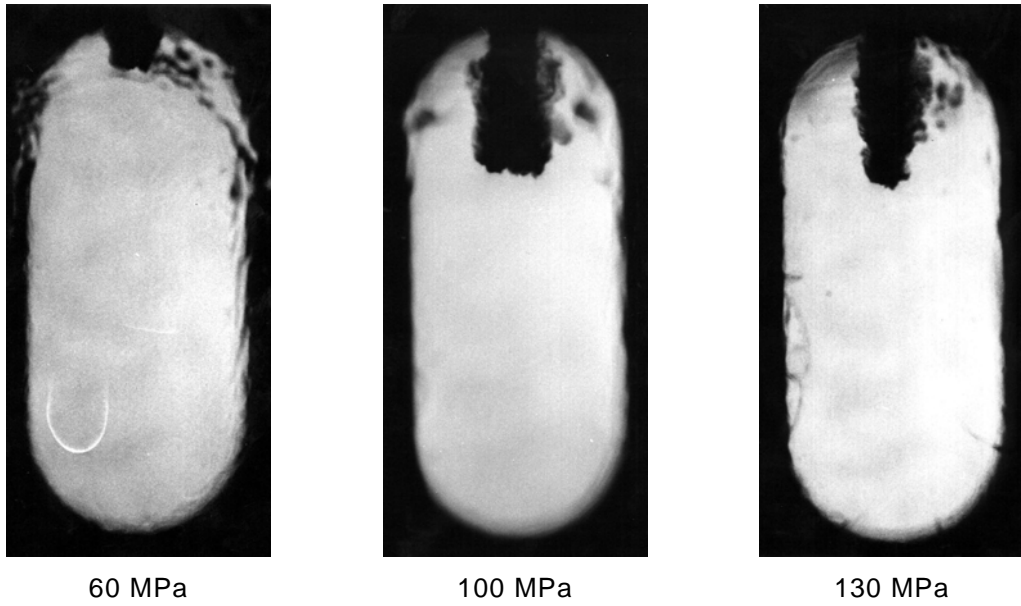


Figure 4-12. Backlit spray images taken 0.9 ms ASOI in air at 3 MPa with an injection duration of 0.9 ms at three fuel rail pressures.

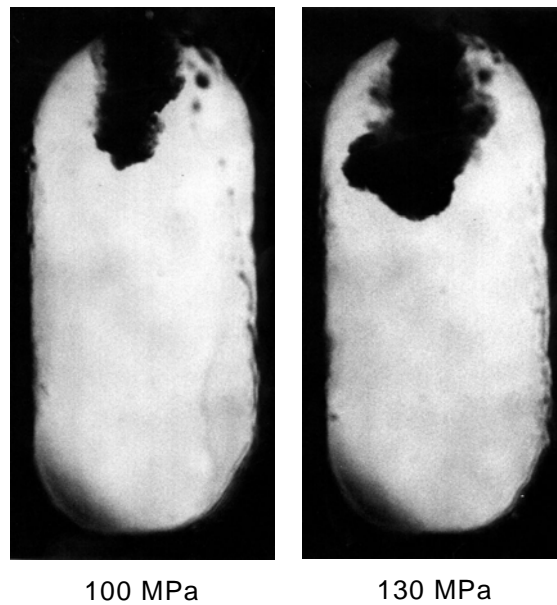


Figure 4-13. Back lit spray images taken 0.9 ms ASOI in gas at 8 MPa with an injection duration of 0.9 ms at two fuel rail pressures.

4.3.1. Influence of injection pressure

Figure 4-14 shows the effects of increasing fuel rail pressure on a VCO nozzle spray obtained by high-speed video (additional profiles are shown in Appendix A). The injection pressure was found to have a significant effect on the rate of penetration of the liquid core, for a constant injected fuel quantity (injection time was varied as detailed in Table 3-3). As expected, higher injection pressures produce fully developed sprays in a shorter time, thus improving the vaporisation process as the surface area of the liquid core increases.

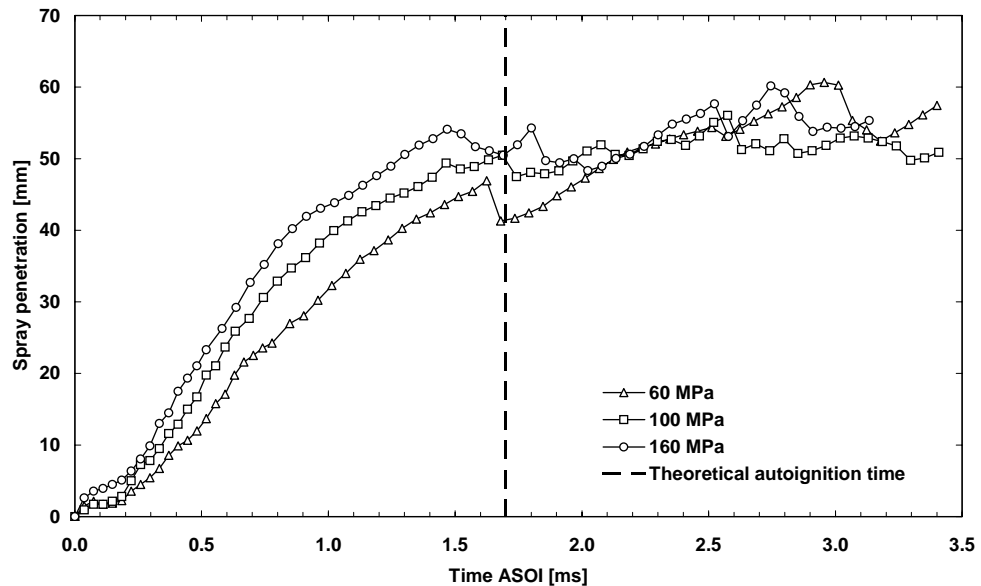


Figure 4-14. Influence of injection pressure on penetration for low-temperature charge. 49 kg m^{-3} in-cylinder density; 0.2 mm VCO nozzle. Broken line shows time at which ignition is highly probable.

During the latter phase of the injection (from 1.5 ms ASOI), the liquid penetration profiles fluctuate around a slowly increasing average. These fluctuations were found to be the result of slugs of concentrated liquid fuel breaking away from the main liquid core. The sequence showed in Figure 4-15 illustrates this phenomenon.

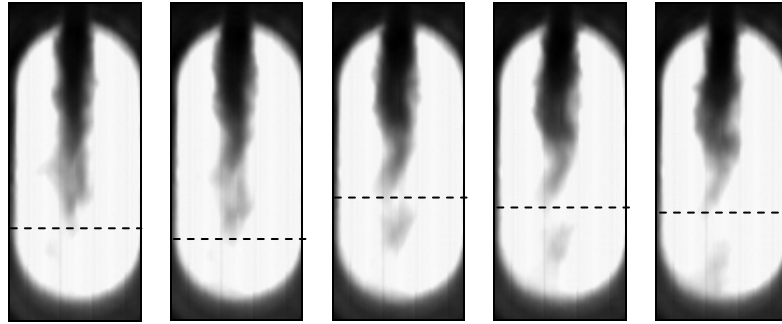


Figure 4-15. Slugs of fuel breaking off the spray. Broken line shows the detected spray penetration length. Low temperature charge; 160 MPa injection pressure; 7.3 MPa ICP; 32 kg m⁻³ in-cylinder density; 0.2 mm VCO nozzle.

The slugs of fuel in Figure 4-15 are believed to be produced as a result of oscillations of the spray's body. These oscillations were observed for all conditions and could be the result of the air entrainment caused by the spray itself. Oscillations were also observed on sprays from a five-hole nozzle, suggesting that they are not specific to single-hole nozzles. Images of simultaneous liquid and vapour phases published by Baritaud *et al.* (1994) exhibit similar detachments of clusters of liquid droplets.

Figure 4-16 shows an example of spray oscillation. The spray was found to exhibit cyclic movements in the transversal direction to the spray jet. An estimate of the frequency of these oscillations was obtained by calculating the time difference between two frames showing similar spray shape (0.148 ms on Figure 4-16). The frequency was found to be approximately 6800 Hz. It is interesting to note that needle lift traces showed cyclic variations in the vertical direction when full lift was achieved (Figure 4-7). Considering that the needle oscillations appear to be damped with time, it is believed that they are not caused by electrical interferences. The frequency of the needle oscillations was estimated to be 6700 Hz (20 cycles in 3 ms). Since this frequency is very close to the estimated spray oscillation frequency, it is suggested that those two effects could be related. If this is the case, the formation of fuel slugs may be associated to needle oscillations.

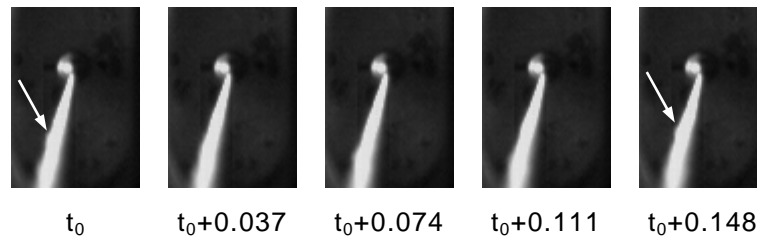


Figure 4-16. Close-up images obtained by high-speed video, showing the oscillation of the liquid spray. Similar spray patterns were observed every 0.148 ms and are indicated by the white arrows. Injection pressure was 160 MPa, in-cylinder pressure was 5.2 MPa, nozzle was a 0.2 mm VCO type. Times are in milliseconds relative to the first frame showed.

It must be considered that these tests were performed under non-firing conditions, and therefore any data gathered after the theoretical firing time may not be directly relevant to real engine conditions. However it offers an improved understanding of spray formation.

Sprays injected into the 32 kg m^{-3} in cylinder density at different injection pressures showed similar dispersion trends to those reported by Naber and Siebers (1996). After an initial wide spray cone, the cone angle steadily reduced reaching a stable dispersion full cone angle of 11° (Figure 4-17). No noticeable relationship between the injection pressure and the spray dispersion angle were found.

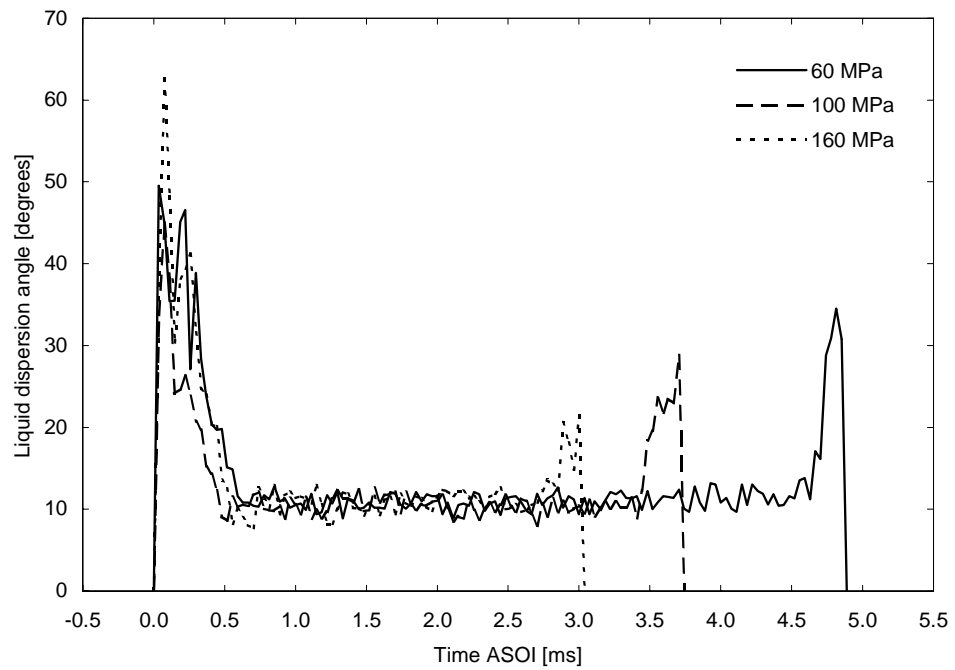


Figure 4-17. Evolution of spray full cone angle at different injection pressures. Low temperature charge; 32 kg m^{-3} in-cylinder density; 0.2 mm single hole VCO nozzle.

4.3.2. Influence of in-cylinder temperature

4.3.2.1. Low-temperature charge

After the initial hesitation the liquid penetration profiles for low-temperature charge clearly show two distinct phases: an almost linear increase in penetration lasting between 0.6 ms (160 MPa injection) and 1.2 ms (60 MPa) with a rapid transition to a steadier penetration length (Figures 4-18 to 4-20).

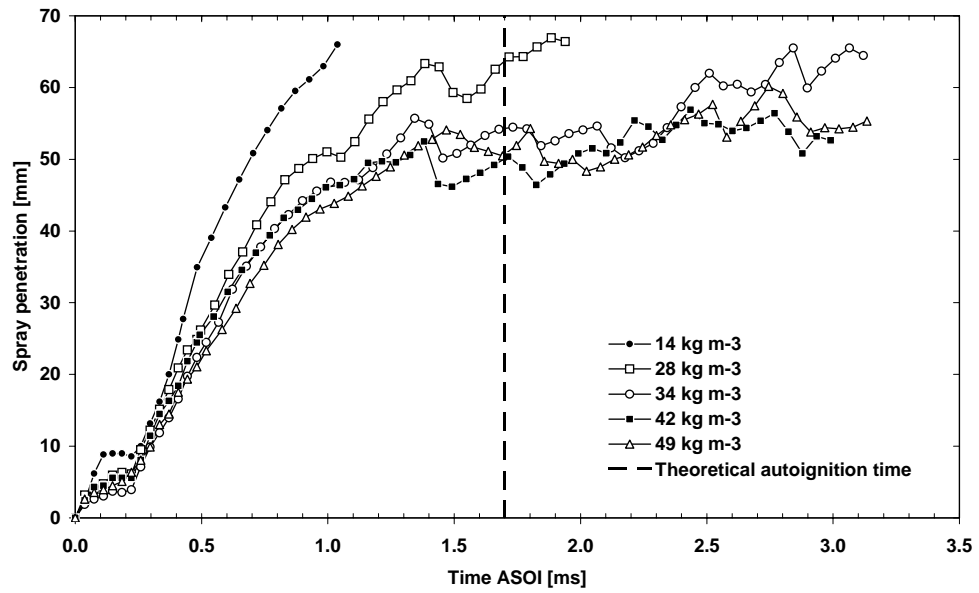


Figure 4-18. Influence of ambient density on liquid penetration for low-temperature charge. 160 MPa injection pressure; 0.2 VCO single hole nozzle with a 30 mm³ fuelling. Broken line shows time at which ignition is highly probable.

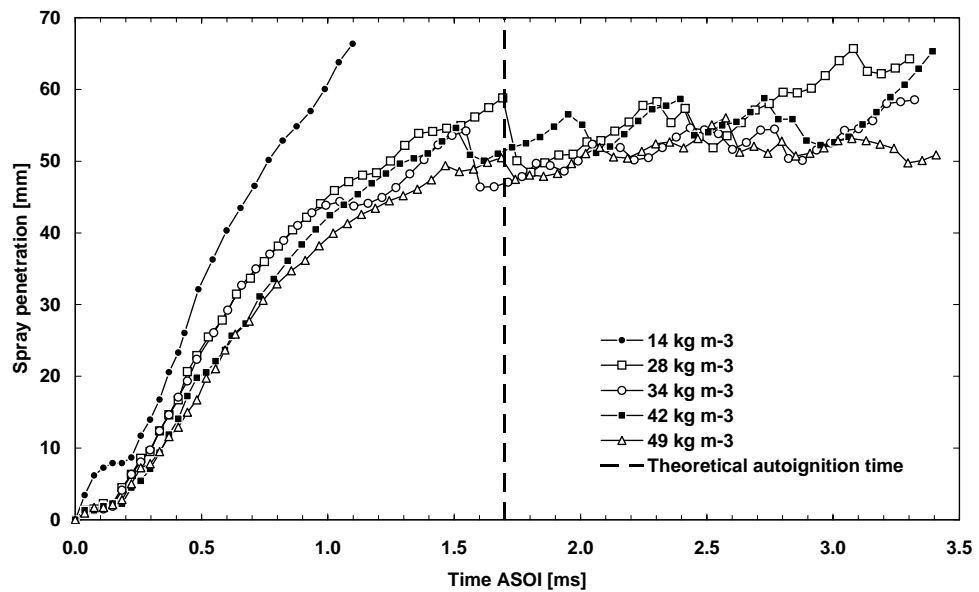


Figure 4-19. Same as Figure 4-18 with an injection pressure of 100 MPa.

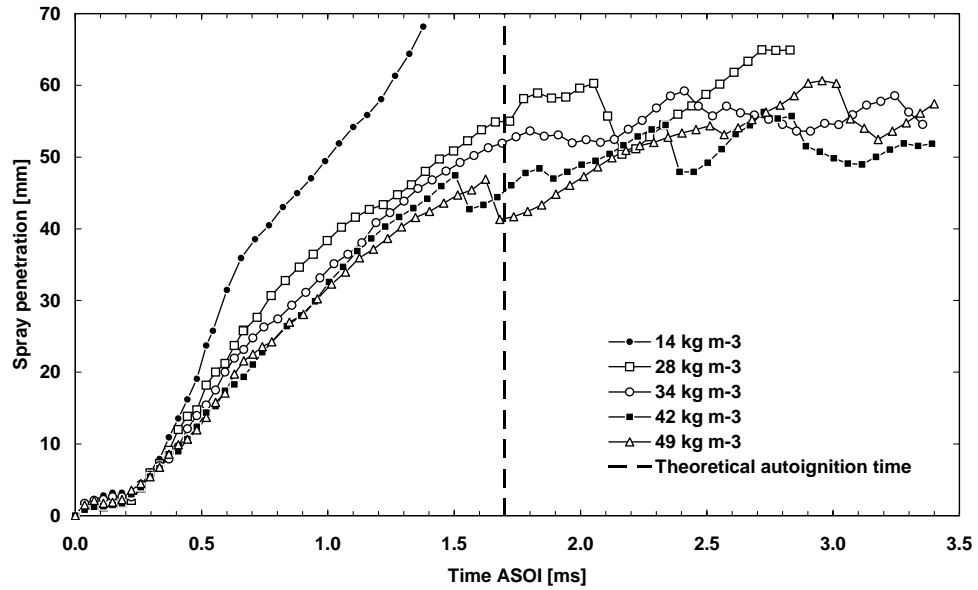


Figure 4-20. Same as Figure 4-18 with an injection pressure of 60 MPa.

The effect of gas density on spray penetration profiles was found to follow the trends observed by Naber and Siebers (1996), although a comprehensive comparison cannot be made at this stage because of the more focused density range used here (14 to 49 kg m⁻³, as opposed to 3.6 to 124 kg m⁻³ in Naber and Siebers (1996)).

At in-cylinder densities between 28 and 49 kg m⁻³, the ultimate spray penetration length varied between 50 and 60 mm, and was directly dependant on ambient density and injection pressure.

The spray penetration profile data were compared with the correlations proposed by Hiroyasu and Arai (1990). Unlike the sprays of Hiroyasu and Arai (1990), in the current tests, the spray breakup was observed to be almost instantaneous. The linear correlation of Hiroyasu and Arai (1990) for the breakup period was therefore not applicable in this case. Figure 4-21 illustrates the application of their logarithmic correlation used for the post breakup period described in the following relation:

$$s = K \left(\frac{P_{inj} - P_g}{\rho_g} \right)^{0.25} \sqrt{D_o \cdot (t - C)}, \quad (4-3)$$

where s is the spray penetration, K is an empirical constant, P_{inj} the injection pressure, P_g the ambient gas pressure, ρ_g the ambient density, D_o the injector orifice diameter, t is the time after start of injection and C is a correction time delay.

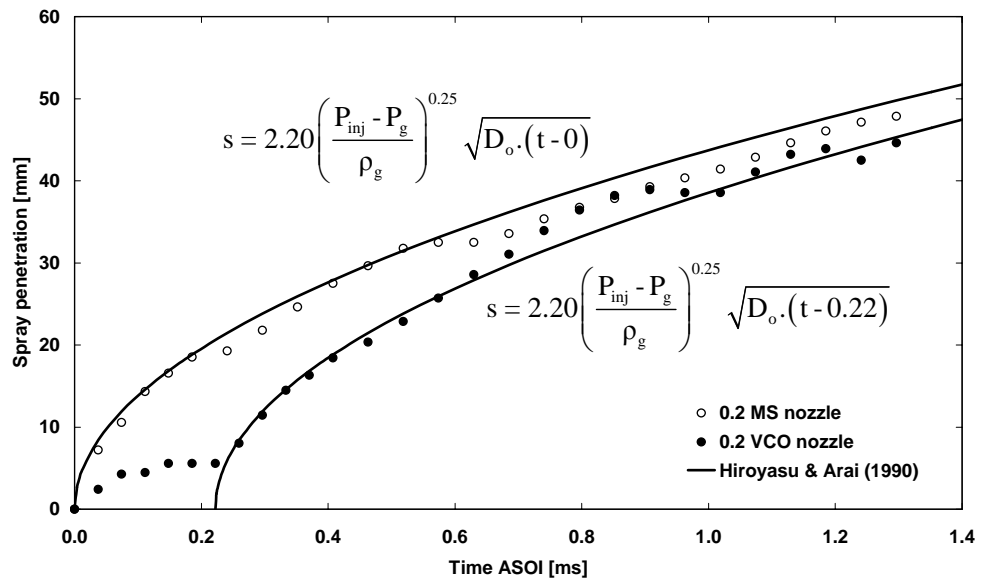


Figure 4-21. Comparison between mini-sac and VCO single-hole nozzles and the correlation proposed by Hiroyasu and Arai (1990) for non-evaporating sprays ($P_{inj} = 160 \times 10^6$ Pa; $P_g = 6.3 \times 10^3$ Pa; $\rho_g = 42$ kg m⁻³; $D_o = 0.2 \times 10^{-3}$ m).

A coefficient (K) of 2.20 instead of 2.95 suggested by Hiroyasu and Arai (1990) was found to give best agreement with the experimental data, both for mini-sac and VCO type nozzles. For the single-hole VCO nozzles, the initial injection hesitation period was taken into account by the addition of a time delay C (Kennaird *et al.*, 2002).

4.3.2.2. High-temperature charge

The liquid penetration profiles are similar in shape as for the low-temperature charge tests, except that the liquid sprays were still viewable through the window at the lowest ambient density (Figure 4-22 and Appendix A). The

profiles also show a similar rapid penetration followed by fluctuations around a slowly increasing average penetration length. Unlike the low-temperature charge tests, the ambient density has a noticeable effect on the ultimate penetration length: the higher the density, the shorter the liquid penetration (from about 50 mm at 14 kg m^{-3} to 30 mm at 40 kg m^{-3}). In addition the injection pressure and ambient density were also found to have a greater influence on the initial increase in penetration with time.

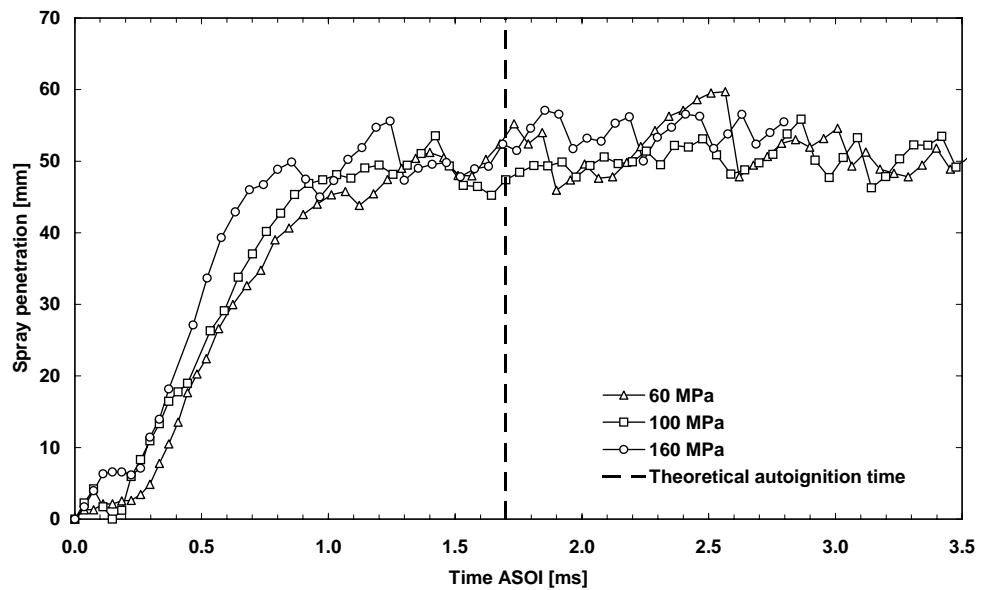


Figure 4-22. Influence of injection pressure on liquid penetration for high-temperature charge. 14 kg m^{-3} gas density; 0.2 VCO single hole nozzle with a 30 mm^3 fuelling. Broken line shows time at which ignition is highly probable.

A wide spray cone angle was also found at the very beginning of the injections, progressively reducing to a narrower mean spray full cone angle of 10° (Figure 4-23). The occurrence of wide spray cone angles was linked to an oscillation of the sprays when the injector's needle was at a short distance from the nozzle orifice.

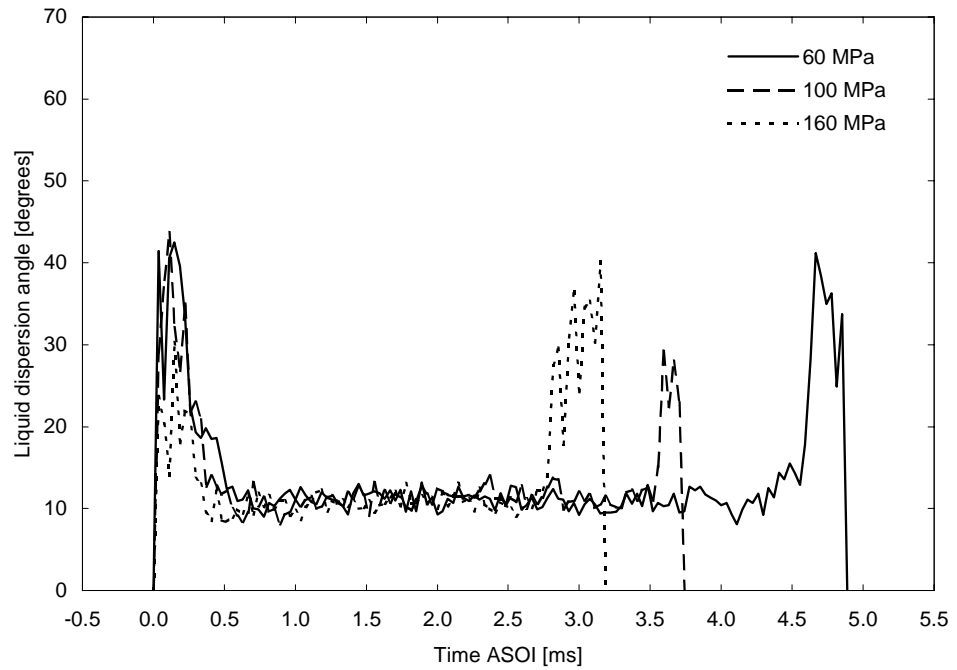


Figure 4-23. Evolution of spray full cone angle at different injection pressures. High temperature charge; 32 kg m^{-3} in-cylinder density; 0.2 mm single hole VCO nozzle.

4.3.3. Vapour dispersion

The vapour penetration was observed using schlieren video imaging. An example of a schlieren image is shown in Figure 4-24. In this example the vapour phase of the fuel extends beyond the viewing limits.

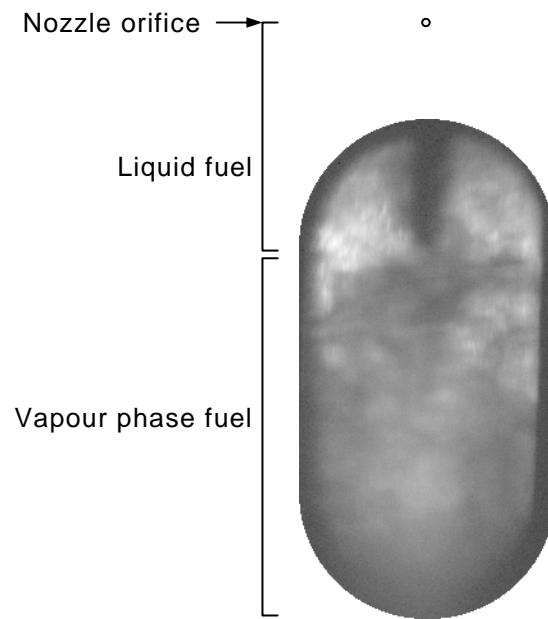


Figure 4-24. Example of a schlieren image for an injection pressure of 100 MPa and an in-cylinder pressure of 8 MPa. Recording was performed 3.1 ms after start of injection pulse.

The following trends were observed in the videos at all test conditions. The vapour developed alongside the liquid core during the early stages of injection with the width of the vapour cloud becoming larger as the liquid penetrated into the chamber. This was believed to be a consequence of the combination of local turbulent mixing and the gradual increase in vapour concentration. When the liquid core reached its ultimate stable length, the vapour continued to penetrate into the chamber at a similar rate to the liquid spray injected into an equivalent ambient density of lower charge temperature (Figure 4-25 and Figure 4-26). The vapour cloud increased in width as it penetrated, ultimately occupying the width of the visible chamber, becoming obscured by the window holders.

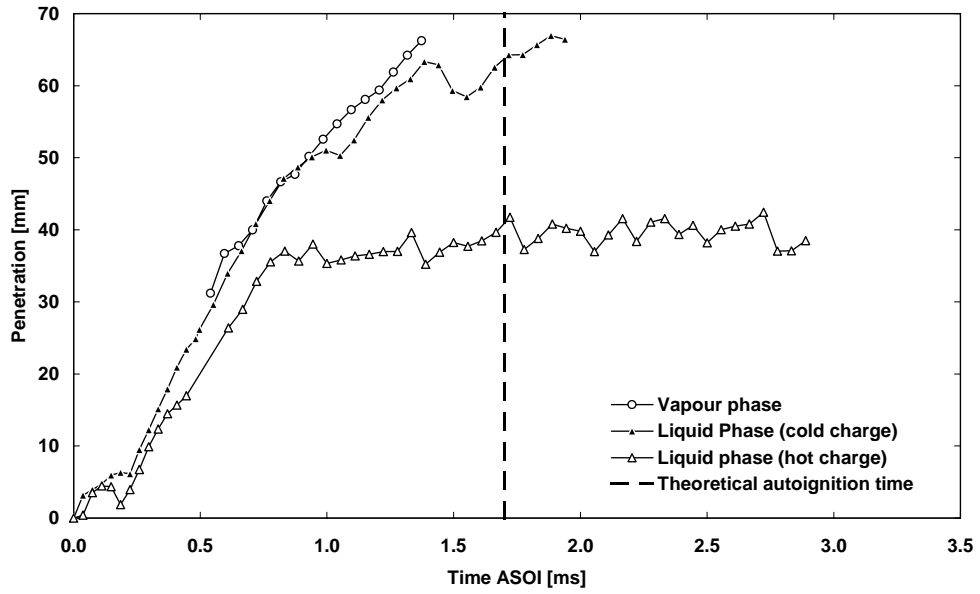


Figure 4-25. Vapour and liquid penetrations for both temperature charge conditions (160 MPa injection pressure; 28 kg m^{-3} in-cylinder density).

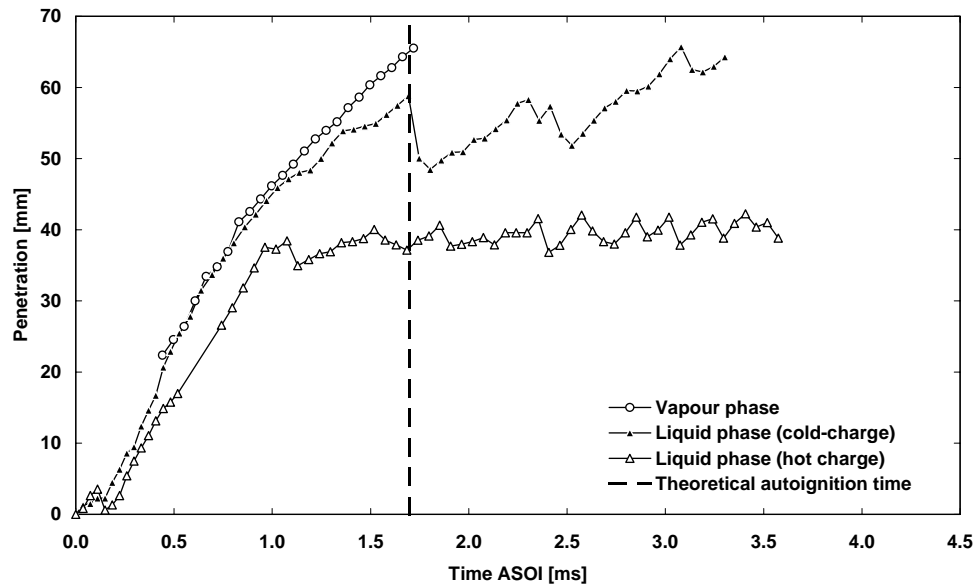


Figure 4-26. Vapour and liquid penetrations for both temperature charge conditions (100 MPa injection pressure; 28 kg m^{-3} in-cylinder density).

Tests were performed to determine the repeatability of the results obtained from the schlieren experiments (Figure 4-27). The same test was conducted four

times in a row. The average error of each measurement was 8.7% with a standard deviation below 7.5% for the entire data set.

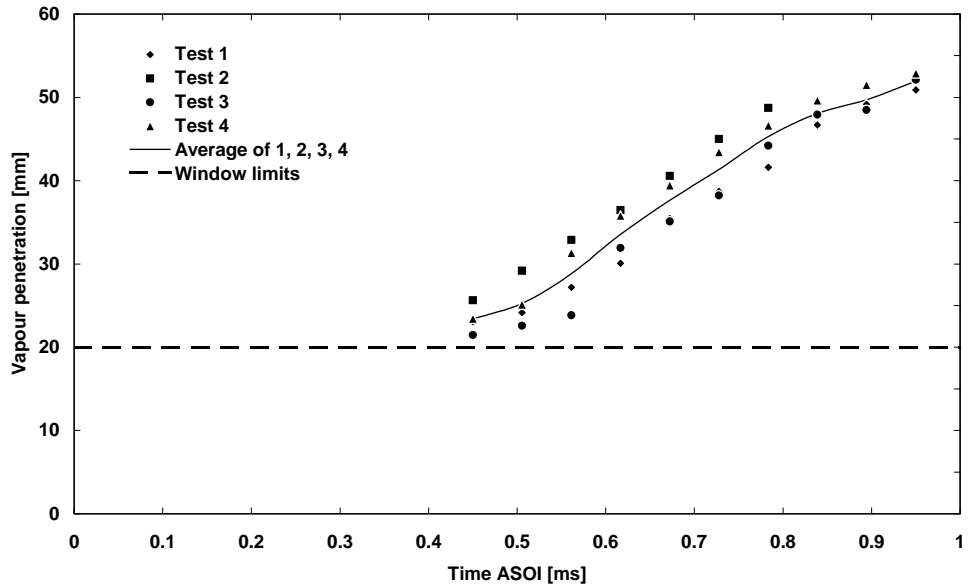


Figure 4-27. Schlieren repeatability tests. Broken line shows limits of rig optical access (140 MPa injection pressure; 21 kg m^{-3} in-cylinder density).

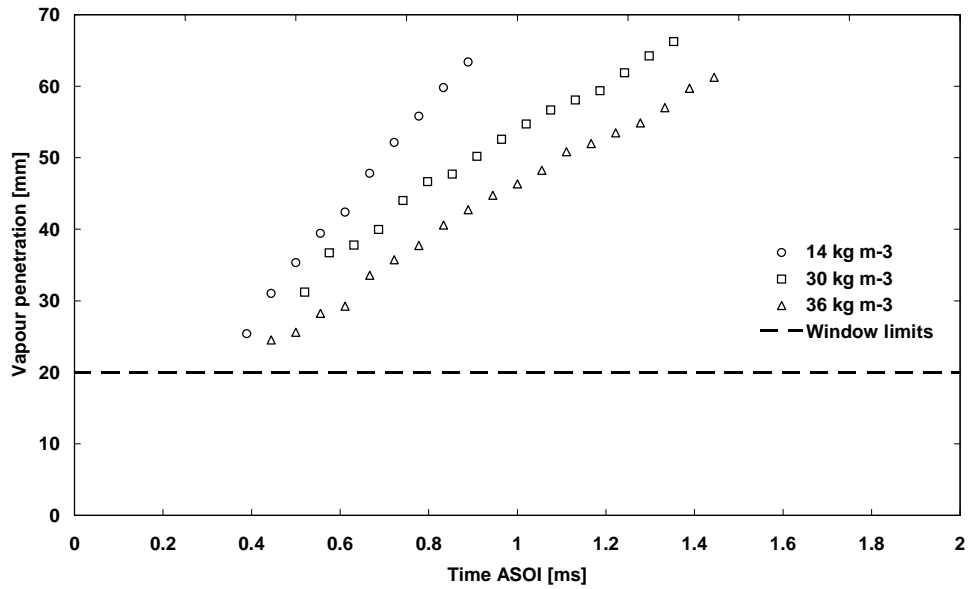


Figure 4-28. Influence of gas density on vapour penetration (160 MPa injection pressure; 0.2 VCO nozzle)

The vapour penetration linearly increased with time for all conditions tested (Figure 4-28, Appendix A). The profiles slowly diverge after 0.5 ms from the start of injection. The rate of diversion depended on the ambient density and injection pressure. Not surprisingly, the highest rate of vapour propagation was found to occur with the highest injection pressures into gas with the lowest densities. It was observed that higher injection pressures seemed to promote faster vapour propagation at the early stage of the injection (Figure 4-29).

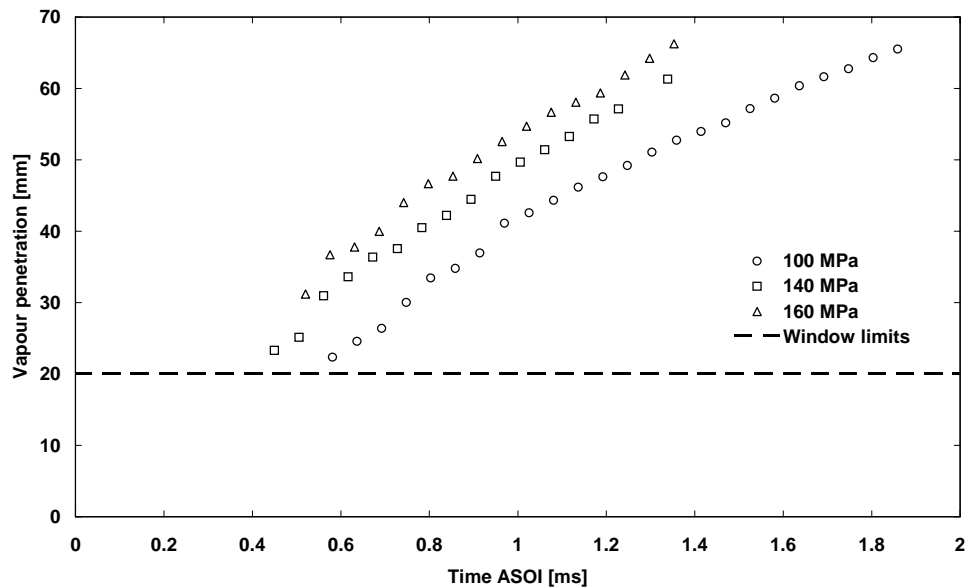


Figure 4-29. Influence of injection pressure on vapour penetration. 30 kg m^{-3} charge density; 0.2 VCO nozzle.

The findings of this work agree with both those by Dec (1997) and Naber and Siebers (1996), where vapour was observed to linearly penetrate across the chamber with time. It is suggested that the mechanism for the vapour transport is the gas motion induced by the liquid phase exchanging momentum from the droplets to the gas phase. Increased penetration of the vapour was observed at higher injection pressures and lower gas densities, i.e. when the liquid phase had a higher momentum. If the air motion generated by the spray is the carrier of the vapour phase, then care must be taken in applying vapour penetration results from single-hole to multi-hole scenarios (Rhim & Farrell, 2001).

4.4. A model for spray penetration

The importance of the problem of spray penetration for various applications is well recognised and has been extensively studied experimentally and theoretically (Reitz, 1987; Hou *et al.*, 1995; Bo *et al.*, 1997; Habchi *et al.*, 1997; Borman & Ragland, 1998; Huh *et al.*, 1998; Favennec & Lebrun, 1999; Kong *et al.*, 1999; Hentschel, 2000; Loth, 2000; Savic, 2000; Sazhin *et al.*, 2001a; Iyer *et al.*, 2002; Pozorski *et al.*, 2002). A rigorous theory of spray penetration would be very complex as it would have to include the modelling of the formation of ligaments and their breakup, droplet breakup and evaporation, the entrainment of air and the effects of turbulence (Faeth *et al.*, 1996). A self-consistent modelling of all these processes is still a major challenge. However, this modelling is not always essential for understanding the process and engineering applications. On many occasions it is far more important to establish a ‘hierarchy’ of the importance of the various processes and develop simplified models suitable for practical applications.

The spray penetration process can be divided into two main stages: initial stage and two phase flow (Sazhin *et al.*, 2001a) The analysis of the initial stage of spray penetration effectively reduces to the analysis of trajectories of individual droplets. This approach is applicable in the region close to the nozzle. During the process of spray development, however, the velocity of entrained air becomes close to droplet velocity and the dynamics of the whole spray can be described in terms of the two-phase flow. Analysis of spray dynamics in terms of the two-phase flow has been performed by Savic (2000), who effectively ignored the contributions of the initial stage and the transition from the initial stage to two-phase flow. This approach was certainly acceptable as the initial stage of the analysis. More refined analysis, taking into account the contribution of the initial stage and transition period, would be expected as the next stage of model development.

Some work in this direction has been reported (Sazhin *et al.*, 2001a) where simple analytical models describing spray penetration and droplet breakup have

been derived. The reduction of droplet size due to breakup has been considered, but an unrealistic assumption that droplet velocity remains constant was used. The effects of reduction of droplet size during the penetration process due to effects of evaporation and breakup were ignored. These assumptions will be taken into account in the present analysis.

The effects of droplet evaporation, breakup and air entrainment on diesel fuel spray penetration have been studied theoretically at the initial stage of spray penetration when the influence of air entrainment is small (up to 0.1 - 0.2 ms ASOI). Theoretical plots of spray penetration versus time are compared with spray penetration measured experimentally using high-speed video recordings. Three models of spray penetration have been compared. In the first model, neither breakup nor air entrainment are taken into account. The breakup processes (bag and stripping) are taken into account in the second model, while in the third model both bag breakup and air entrainment processes are considered. It has been found that the agreement between the predictions of the third model with experimental measurements is better than for the first two models.

Basic equations and approximations are discussed in Section 4.4.1. In Section 4.4.2 the effect of droplet evaporation on spray penetration is briefly considered. In Sections 4.4.3 and 4.4.4 the effects of bag and stripping breakup on spray penetration will be discussed. A schematic presentation of flow and breakup regimes is discussed in Section 4.4.5. Some relevant experimental results referring to the initial stage of spray penetration will be presented and discussed in Section 4.4.6.

4.4.1. Basic equations and approximations

4.4.1.1. Dynamics of droplets

The initial formation of droplets from a liquid fuel jet has been discussed by a number of authors (see review by Lefebvre, 1989). The analysis of this problem is beyond the scope of this work. It is important to note, however, that for the values of parameters used in the experiments (discussed later in Section 4.4.6)

Reynolds number was of the order of 10^3 and Ohnesorge¹ number was of the order of 10^{-1} . In this case the expected breakup regime lies between the first wind induced breakup and second wind induced breakup (Lefebvre, 1989). The contribution of jet in spray penetration process can be ignored as a first approximation in both cases. The initial sizes of droplets will be assumed equal to the nozzle diameter (Sazhin *et al.*, 2001a).

At the initial stage of spray penetration the analysis can be focused on the equation describing the dynamics of an individual droplet (Feng, 2001):

$$\frac{d^2s}{dt^2} = -\frac{3}{8r_d} C_D \frac{\rho_g}{\rho_d} \left(\frac{ds}{dt} - v_g \right) \left| \frac{ds}{dt} - v_g \right|, \quad (4-4)$$

where s is the distance measured from the nozzle, C_D is the drag coefficient, which depends on the Reynolds number $Re = 2\rho_g |v_d - v_g| r / \mu_g$, ρ_g and ρ_d are the gas and droplet density respectively, r is the droplet's radius, $v_d = \frac{ds}{dt}$, v_g is the gas velocity and t is time.

When deriving Equation (4-4) it was assumed that the droplet is a perfect sphere. The solution of this equation requires the knowledge of C_D and v_g . A number of approximations for C_D has been suggested (Wallis, 1969; Morsi & Alexander, 1972; Yanenko *et al.*, 1980; Panton, 1996; Borman & Ragland, 1998). Expressions for C_D suggested by these authors can be used for numerical analysis of Equation (4-4), but they are not suitable for analytical estimates, which are sometimes convenient in engineering applications. A much simpler approximation was suggested by Douglas *et al.* (1995), where three ranges of Reynolds numbers were considered: $Re \leq 2$ (Stokes flow), $2 < Re \leq 500$ (Allen flow) and $500 < Re \leq 10^5$ (Newton flow). The functions $C_D(Re)$ for these flows are given by the following expressions: $C_D = 24/Re$ (Stokes flow), $C_D = 18.5/Re^{0.6}$ (Allen flow) and $C_D = 0.44$ (Newton flow). These expressions do not take into account the effects of droplet acceleration, internal circulation, burning, non-spherical shape and vibrations and heating processes. They cannot be applied when the Mach number is close to or greater than 1 (Levich, 1962;

¹ Definitions of dimensionless numbers are included in Appendix A.

Yanenko *et al.*, 1980; Borman & Ragland, 1998). The condition $Re < 10^5$ is always satisfied for droplet motion in diesel engines.

The drag force acting on the droplets leads not only to deceleration of droplets but also to momentum transfer from droplets to the gas entrained into the spray. The latter process has been discussed by Ghosh and Hunt (1994), who derived the following equation for gas velocity in the spray zone:

$$\frac{d}{ds}(\pi r_g^2 v_g^2) = \frac{3\pi r_s^2 \alpha_d}{8r_d} C_D (v_d - v_g)^2, \quad (4-5)$$

where r_g and r_s are radii of the gas/air jet and the spray itself respectively at a certain position s , α_d is the volume fraction of droplets in the spray. r_g is usually slightly larger than r_s , but as a first approximation it will be assumed that they both are equal to $s \tan \theta$, θ being the half angle of the spray cone.

It is assumed that v_g is so small compared with v_d that its contribution in the right hand side of Equation (4-4) can be ignored altogether. Remembering the definitions of C_D for the three types of flow, Equation (4-4) can be simplified to:

$$\frac{d^2s}{dt^2} = -\frac{9}{2} \frac{\mu_g}{\rho_d r^2} \frac{ds}{dt} \quad (\text{Stokes flow}) \quad (4-6)$$

$$\frac{d^2s}{dt^2} = -\frac{4.577 \mu_g^{0.6} \rho_g^{0.4}}{\rho_d r^{1.6}} \left(\frac{ds}{dt}\right)^{1.4} \quad (\text{Allen flow}) \quad (4-7)$$

$$\frac{d^2s}{dt^2} = -\frac{0.165 \rho_g}{\rho_d r} \left(\frac{ds}{dt}\right)^2 \quad (\text{Newton flow}) \quad (4-8)$$

Assuming that r is constant (no evaporation and breakup) the solutions of Equations (4-6) - (4-8) can be easily found (Sazhin *et al.*, 2001a). The effect of air entrainment can be considered as the perturbation to the solutions of Equations (4-6) - (4-8) (Sazhin *et al.*, 2001a):

$$\Delta s = \frac{4}{15} \alpha \kappa \sqrt{v_{d0}} t^{5/2} \quad (\text{Stokes flow}) \quad (4-9)$$

$$\Delta s = 0.373 \kappa v_{d0}^{0.9} \beta t^{5/2} \quad (\text{Allen flow}) \quad (4-10)$$

$$\Delta s = 0.533\gamma\kappa v_{d0}^{3/2} t^{5/2} \quad (\text{Newton flow}) \quad (4-11)$$

where v_{d0} is the initial droplet velocity,

$$\kappa = \frac{3r_s^2 \alpha_d}{8r_d r_{g0}} C_D v_{d0}^2, \quad \alpha = \frac{9v_g \rho_g}{2r_d^2 \rho_d}, \quad \beta = \frac{4.577v_g^{0.6} \rho_g}{r_d^{1.6} \rho_d}, \quad \gamma = \frac{0.165\rho_g}{r_d \rho_d}.$$

In what follows the solutions of Equations (4-6) - (4-8) will be generalised taking into account the effects of evaporation and droplet breakup.

4.4.1.2. Evaporation and droplet breakup models

Ignoring the initial stage of droplet evaporation (heat-up period):

$$L \frac{dm}{dt} = h 4\pi r^2 (T_g - T_s), \quad (4-12)$$

where L is the specific heat of evaporation, h is the convective heat transfer coefficient, T_g is the gas temperature, and T_s is the temperature of the droplet's surface. Considering that, for a sphere, $dm = \rho_d 4\pi r^2 dr = \rho_d 2\pi r dr^2$, the time evolution of the droplet's radius in the isothermal approximation can be described by the following equation:

$$\frac{dr^2}{dt} = -\frac{\text{Nu } k_g (T_g - T_s)}{L \rho_d} = -\mu r_0^2, \quad \text{with } r_0 = r(0) \quad (4-13)$$

where Nu is the Nusselt number, k_g is the gas thermal conductivity, ρ_d is the density of the droplet.

A number of other expressions for Nu have been discussed by Yanenko (1980) and Feng and Michaelides (2001). The simplest and the most widely used approximation for this parameter is the following:

$$\text{Nu} = 2 + 0.6 \text{Re}^{1/2} \cdot \text{Pr}^{1/3}$$

In the case when Re is small $\text{Nu} = 2$ and Equation (4-13) can be integrated to give (Sazhin *et al.*, 2001b):

$$r = r_0 \sqrt{1 - \mu t} = r_0 \sqrt{1 - \frac{2k_g (T_g - T_s)}{L \rho_d r_0^2} t}, \quad (4-14)$$

where r_0 is the initial droplet radius.

Several droplet breakup models have been suggested (Lefebvre, 1989; Shraiber *et al.*, 1996; Chigier & Reitz, 1998; Lin, 1998; Borman & Ragland, 1998). One of the most popular models is based on the comparison between the proper frequency of droplet oscillations and the frequency of turbulent pulsation in the surrounding gas. This allows the determination of the maximal stable droplet diameter. The predictions of this model are in good agreement with some experimental observations (Sevik & Park, 1973). In the present case, however, the driving force of droplet breakup is not the external turbulence, but the kinetic energy of the droplets themselves. In this case a different approach would seem to be more appropriate. As in Sazhin *et al.* (2001a), this study will be based on the model developed by Reitz and Diwakar (1986, 1987) which is particularly attractive for analytical and numerical analysis and is widely used in CFD codes. In this model two droplet breakup regimes are identified. These are bag breakup when:

$$We \equiv \frac{\rho_g v_d^2 r}{\sigma} > 6, \quad (4-15)$$

and stripping breakup when:

$$Z \equiv \frac{We}{\sqrt{Re}} > 0.5, \quad (4-16)$$

where σ is the surface tension and We is the Weber number.

The first regime is an analogue of the Rayleigh – Taylor instability accompanied by the development of normal stresses. The second regime is an analogue of the Kelvin – Helmholtz instability accompanied by the development of tangential stresses. The breakup processes described by Equations (4-15) and (4-16) can take place simultaneously. In this case the dominant process will be determined by the shortest lifetime as described below. Sometimes a more stringent criterion for the stripping instability ($Z > 0.7$) has been used (Borman & Ragland, 1998). The modification of this analysis to meet this criterion would be straightforward. It is important not to confuse the parameter Z with the Ohnesorge number Oh (Borman & Ragland, 1998).

The lifetimes of unstable droplets were estimated using the following formulae (Reitz & Diwakar, 1987):

$$t_b = D \left[\frac{\rho_d r^3}{2\sigma} \right]^{1/2} \quad (\text{bag breakup}) \quad (4-17)$$

$$t_s = C \frac{r}{v_d} \sqrt{\frac{\rho_d}{\rho_g}} \quad (\text{stripping breakup}) \quad (4-18)$$

where D was taken equal to π and C to 13.

As a first approximation the creation of droplets of different radii during the breakup process was not taken into account. The radii of unstable droplets are allowed to change continuously following the equation:

$$\frac{dr}{dt} = -\frac{r - r_{db(s)}}{t_{b(s)}}, \quad (4-19)$$

where t_b and t_s are defined by Equations (4-17) and (4-18) respectively, $r_{db(s)}$ are marginally stable radii determined by the conditions $We = 6$ and $Z = 0.5$ respectively. This approximation is justified by the fact that the contribution of smaller droplets generated during the breakup is relatively small and can be ignored. Combined solutions of Equation (4-19) and Equations (4-6), (4-7) or (4-8) for spray penetration for Stokes, Allen and Newton regimes respectively will be investigated for the bag and stripping breakup regimes.

4.4.2. Effect of droplet evaporation

In the case of the Stokes flow Equation (4-6) can be simplified to:

$$\frac{d^2s}{dt^2} = -\frac{a_e}{1 - \mu t} \frac{ds}{dt}, \quad (4-20)$$

where $a_e = \frac{9}{2} \frac{\mu_g}{\rho_d r_0^2}$.

Integration of Equation (4-20) gives (Demirtzi, 2001):

$$\frac{ds}{dt} = v_{d0} (1 - \mu t)^{a_e/\mu} \quad (4-21)$$

$$s = v_{d0} \frac{1 - (1 - \mu t)^{(a_e + \mu)/\mu}}{a_e + \mu} \quad (4-22)$$

where v_{d0} is the initial velocity of the droplet. The life time of evaporating droplets is $t_{ev} = \mu^{-1}$. During this time the value of s reaches its maximum:

$$s_{max} = v_{d0} / (a_e + \mu).$$

In the limit of slow evaporation ($\mu \rightarrow 0$), Equation (4-22) can be simplified to (see Equation (3) in Sazhin *et al.*, 2001a):

$$s \approx \frac{v_{d0}}{a_e} \left[1 - (1 - \mu t)^{a_e/\mu} \right] = \frac{v_{d0}}{a_e} \left[1 - 1 + \frac{\mu a_e}{\mu} t - \frac{1}{2} \mu^2 t^2 \left(\frac{a_e^2}{\mu^2} \right) + \dots \right] = \frac{v_{d0}}{a_e} (1 - e^{-a_e t}) \quad (4-23)$$

The range of validity of Equations (4-22) and (4-23) is defined by the condition:

$$Re = \frac{2\rho_g v_{d0} r_0 (1 - \mu t)^{(2a_e + \mu)/2\mu}}{\mu_g} \leq 2 \quad (4-24)$$

If condition (4-24) is valid at $t = 0$ it will remain valid at all $t > 0$. No simple expressions for spray velocity and spray penetration have been obtained in the case of Allen and Newton flows due to dependence of μ on Re .

4.4.3. Effect of droplet bag breakup

From Equation (4-15) it is obtained:

$$r_{db} \equiv \frac{6\sigma}{\rho_g v_d^2} \quad (4-25)$$

Having substituted Equation (4-17) into Equation (4-19) the following equation is obtained:

$$\frac{dr}{dt} = -\frac{r - r_{db}}{a_b r^{3/2}}, \quad (4-26)$$

where $a_b = D\sqrt{\rho_d/(2\sigma)}$. Equation (4-26) is valid for $r > r_{db}$. Otherwise $r = \text{const}$.

Assuming that $r \gg r_{db}$ the right hand side of Equation (4-26) can be simplified to:

$$\frac{dr}{dt} = -\frac{1}{a_b \sqrt{r}} \quad (4-27)$$

The solution to this equation can be written as:

$$r = r_0 (1 - a_{rb} t)^{2/3}, \quad (4-28)$$

where $a_{rb} = 3 / (2a_b r_0^{3/2})$.

When r approaches r_{db} , the term proportional to r_{db} in Equation (4-26) can be considered as a perturbation. In this case the solution of Equation (4-26) will be in the form:

$$r = r_\ell + \Delta r, \quad (4-29)$$

where r_ℓ is defined by Equation (4-28).

The combination of Equations (4-26), (4-28) and (4-29) gives:

$$\frac{d\Delta r}{dt} = -\frac{1}{2a_b r_0^{3/2} (1 - a_{rb} t)} \Delta r + \frac{r_{db}}{a_b r_0^{3/2} (1 - a_{rb} t)}, \quad (4-30)$$

where $r_{db}(t)$ is defined by Equation (4-25). The solution to Equation (4-30) is:

$$\Delta r = -2r_{db} \left[1 - (1 - a_{rb} t)^{-1/2 a_b a_{rb} r_0^{3/2}} \right] \quad (4-31)$$

The fact that $\Delta r(t=0) = 0$ was taken into account. The time limit is determined by the conditions $r \gg r_{db}$ and $t < a_{rb}^{-1}$. Equation (4-31) contains the unknown function $r_{db}(t)$ which depends on droplet velocity and cannot be explicitly calculated. In the limiting case, when $r \rightarrow r_{db}$, $dr/dv_d \rightarrow 0$. $r = \text{const}$ at $r < r_{db}$. In this case the solution of Equations (4-6) - (4-8) reduces to the ones considered by Sazhin *et al.* (2001a).

The solution of Equation (4-26) was investigated by Sazhin *et al.* (2001a) under the assumption that the velocity of droplets is constant. In this section this assumption will be relaxed but the restriction $r \gg r_{db}$ will be imposed. The

values of the velocity of droplets will be found using Equation (4-28). The solution to the corresponding equations for Stokes, Allen and Newton flows will be presented in the following subsections.

4.4.3.1. Stokes flow

Having substituted Equation (4-28) into Equation (4-6):

$$\frac{d^2s}{dt^2} = -\frac{a_e}{(1-a_{rb}t)^{4/3}} \frac{ds}{dt}, \quad (4-32)$$

where a_e is the same as in Equation (4-20).

Integration of Equation (4-32) gives:

$$\frac{ds}{dt} = v_{d0} e^{\left[-a_{vb} \left(\frac{1}{(1-a_{rb}t)^{1/3}} - 1 \right) \right]}, \quad (4-33)$$

$$s = v_{d0} \frac{a_{vb}^3}{a_{rb}} e^{a_{vb}} \left[\frac{1}{2} \left(E_1(a_{vb}) - E_1 \left(\frac{a_{vb}}{(1-a_{rb}t)^{1/3}} \right) \right) + e^{-\frac{a_{vb}}{(1-a_{rb}t)^{1/3}}} \left[-\frac{1-a_{rb}t}{a_{vb}^3} + \frac{(1-a_{rb}t)^{2/3}}{2a_{vb}^2} - \frac{(1-a_{rb}t)^{1/3}}{2a_{vb}} - e^{-a_{vb}} \left[-\frac{1}{a_{vb}^3} + \frac{1}{2a_{vb}^2} - \frac{1}{2a_{vb}} \right] \right] \right] \quad (4-34)$$

where:

$$E_1(z) = \int_z^\infty \frac{e^{-t}}{t} dt; \quad a_{vb} = \frac{3a_e}{a_{rb}}$$

The conditions for the validity of these equations can be presented as:

$$r_0 (1-a_{rb}t)^{2/3} \gg \frac{6\sigma}{\rho_g v_{d0}^2} e^{\left[2a_{vb} \left(\frac{1}{(1-a_{rb}t)^{1/3}} - 1 \right) \right]} \quad (\text{Condition } r \gg r_{db}) \quad (4-35)$$

$$r_0 (1-a_{rb}t)^{2/3} < \frac{v_g}{v_{d0}} e^{\left[a_{vb} \left(\frac{1}{(1-a_{rb}t)^{1/3}} - 1 \right) \right]} \quad (\text{Stokes flow: } Re < 2) \quad (4-36)$$

4.4.3.2. Allen flow

Dividing Equation (4-7) by Equation (4-27), taken in the limit $r \gg r_{db}$:

$$\frac{dv_d}{dr} = \frac{b_e r_0^{1.6} a_b v_d^{1.4}}{r^{1.1}} \quad (4-37)$$

$$\text{where } b_e = \frac{4.577 \mu_g^{0.6} \rho_g^{0.4}}{\rho_d r_0^{1.6}}.$$

Integration of Equation (4-37) gives:

$$v_d = \frac{ds}{dt} = \frac{v_{d0}}{\left[1 + 4b_e r_0^{1.6} v_{d0}^{0.4} a_b \left(\frac{1}{r^{0.1}} - \frac{1}{r_0^{0.1}}\right)\right]^{2.5}} = \frac{v_{d0}}{\left[1 + 4b_e r_0^{1.5} v_{d0}^{0.4} a_b \left(\frac{1}{(1-a_{rb}t)^{1/15}} - 1\right)\right]^{2.5}} \quad (4-38)$$

The conditions for the validity of these equations can be presented as:

$$r_0 (1-a_{rb}t)^{2/3} \gg \frac{6\sigma}{\rho_g v_{d0}^2} \left[1 + 4b_e r_0^{1.5} v_{d0}^{0.4} a_b \left(\frac{1}{(1-a_{rb}t)^{1/15}} - 1\right)\right]^5 \quad (4-39)$$

(Condition $r \gg r_{db}$)

$$\frac{v_g}{v_{d0}} \left[1 + 4b_e r_0^{1.5} v_{d0}^{0.4} a_b \left(\frac{1}{(1-a_{rb}t)^{1/15}} - 1\right)\right]^{2.5} \leq r_0 (1-a_{rb}t)^{2/3} < \frac{250v_g}{v_{d0}} \left[1 + 4b_e r_0^{1.5} v_{d0}^{0.4} a_b \left(\frac{1}{(1-a_{rb}t)^{1/15}} - 1\right)\right]^{2.5} \quad (4-40)$$

(Allen flow: $2 \leq Re < 500$)

4.4.3.3. Newton flow

Having substituted Equation (4-28) into Equation (4-8):

$$\frac{d^2s}{dt^2} = -\frac{c_e}{(1-a_{rb}t)^{2/3}} \left(\frac{ds}{dt}\right)^2, \quad (4-41)$$

$$\text{where } c_e = \frac{0.165\rho_g}{\rho_d r_0}.$$

Integration of (4-41) gives:

$$\frac{ds}{dt} = v_{d0} \left[1 - \frac{3c_e v_{d0} \left[(1 - a_{rb} t)^{1/3} - 1 \right]}{a_{rb}} \right]^{-1} \quad (4-42)$$

$$s = \frac{1}{c_e} \left\{ \frac{(1 - a_{rb} t)^{2/3} - 1}{2} + \frac{(1 - a_{rb} t)^{1/3} - 1}{\beta} + \frac{1}{\beta^2} \ln \left| \frac{\beta(1 - a_{rb} t)^{1/3} - 1}{\beta - 1} \right| \right\} \quad (4-43)$$

where $\beta = \frac{3c_e v_{d0}}{a_{rb} + 3c_e v_{d0}}$.

In the limit of small a_{rb} (no breakup), Equation (4-43) reduces to Equation (5) of Sazhin *et al.* (2001a). The conditions for the validity of these equations can be presented as:

$$r_0 (1 - a_{rb} t)^{2/3} \gg \frac{6\sigma}{\rho_g v_{d0}^2} \left[1 - \frac{3c_e v_{d0}}{a_{rb}} \left[(1 - a_{rb} t)^{1/3} - 1 \right] \right]^2 \quad (4-44)$$

(Condition $r \gg r_{db}$)

$$r_0 (1 - a_{rb} t)^{2/3} < \frac{250v_g}{v_{d0}} \left[1 - \frac{3c_e v_{d0}}{a_{rb}} \left[(1 - a_{rb} t)^{1/3} - 1 \right] \right] \quad (4-45)$$

(Newton flow: $Re \geq 500$)

4.4.4. Effect of droplet stripping breakup

From Equation (4-16) it is obtained:

$$r_{ds} = \frac{b_s}{v_d^3}, \quad (4-46)$$

where $b_s = \frac{\sigma^2}{2\rho_g \mu_g}$.

Having substituted Equations (4-18) and (4-46) into Equation (4-19) the following equation is obtained:

$$\frac{dr}{dt} = -\frac{rv_d - \frac{b_s}{v_d}}{c_s r}, \quad (4-47)$$

where $c_s = C\sqrt{\rho_d/\rho_g}$. Equation (4-47) is valid for $r > r_{ds}$. Otherwise $r = \text{const}$.

Assuming that $r \gg r_{ds}$ Equation (4-47) can be simplified to:

$$\frac{dr}{dt} = -\frac{v_d}{c_s} \quad (4-48)$$

The contribution of the term proportional to b_s can be studied similarly to Section 4.4.3. In contrast to the case of bag breakup this equation cannot be solved unless the time dependence of v_d is known. The values of the velocity of droplets will be found from Equation (4-48) and the solution of the corresponding equations for Stokes, Allen and Newton flows in the following subsections.

4.4.4.1. Stokes flow

Division of Equation (4-6) by Equation (4-48) taken for $r \gg r_{ds}$ gives:

$$\frac{dv_d}{dr} = a_e c_s \frac{r_0^2}{r^2} \quad (4-49)$$

This equation can be integrated to give:

$$v_d = v_{d0} + a_e c_s r_0^2 \left(\frac{1}{r_0} - \frac{1}{r} \right) \quad (4-50)$$

Having substituted Equation (4-50) into Equation (4-48) and integrating the latter equation:

$$t = \frac{r_0 - r}{\alpha_s} + \frac{\beta_s}{\alpha_s^2} \ln \left| \frac{\beta_s - \alpha_s r_0}{\beta_s - \alpha_s r} \right|, \quad (4-51)$$

where $\alpha_s = \frac{v_{d0}}{c_s} + a_e r_0$; $\beta_s = a_e r_0^2$

The combination of Equations (4-50) and (4-51) gives an implicit expression for droplet velocity. On the other hand the integration of Equation (4-48) gives:

$$r = r_0 - \frac{S}{c_s} \quad (4-52)$$

The combination of Equations (4-51) and (4-52) gives an implicit expression for droplet penetration. The range of applicability of these equations can be determined in a similar manner to the case of bag breakup, although explicit expressions for droplet velocity have not been obtained.

4.4.4.2. Allen flow

The combination of Equations (4-7) and (4-48) taken for $r \gg r_{ds}$ gives:

$$v_d = v_{d0} \left[1 - \frac{b_e r_0^{1.6} c_s}{v_{d0}^{0.6}} \left(\frac{1}{r^{0.6}} - \frac{1}{r_0^{0.6}} \right) \right]^{5/3} \quad (4-53)$$

The combination of Equations (4-48) and (4-53) taken for $r \gg r_{ds}$ gives:

$$t = -\frac{c_s}{v_0} \int_{r_{i0}}^r \frac{dr}{\left[1 - \frac{b_e r_0^{1.6} c_s}{v_{d0}^{0.6}} \left(\frac{1}{r^{0.6}} - \frac{1}{r_0^{0.6}} \right) \right]^{5/3}} \quad (4-54)$$

Equations (4-52), (4-53) and (4-54) give an implicit expression for droplet velocities and penetration. The range of applicability of these equations can be determined similarly to the case of the bag breakup.

4.4.4.3. Newton flow

The combination of Equations (4-8) and (4-48) taken for $r \gg r_{ds}$ gives:

$$v_d = v_{d0} \left(\frac{r}{r_0} \right)^{c_e c_s r_0}, \quad (4-55)$$

or

$$r = r_0 \left(\frac{v_d}{v_{d0}} \right)^{1/c_e c_s r_0}, \quad (4-56)$$

where c_e is the same as in Equation (4-41).

Having substituted Equation (4-56) into Equation (4-8) the following expression is obtained:

$$\frac{dv_d}{dt} = -c_e v_{d0}^{1/c_e c_s r_{d0}} v_d^{(2c_e c_s r_{d0}-1)/c_e c_s r_{d0}} \quad (4-57)$$

If $(2c_e c_s r_{d0} - 1)/c_e c_s r_{d0} \neq 1$ then Equation (4-57) can be integrated to give:

$$v_d = \frac{v_{d0}}{\left[1 + c_e v_{d0} \left(1 - \frac{1}{c_e c_s r_{d0}} \right) t \right]^{c_e c_s r_{d0} / (c_e c_s r_{d0} - 1)}} \quad (4-58)$$

If $(2c_e c_s r_{d0} - 1)/c_e c_s r_{d0} = 1$ then Equation (4-57) can be integrated to give:

$$v_d = v_{d0} e^{-c_e v_{d0} t} \quad (4-59)$$

When deriving Equation (4-59) the fact that the condition $(2c_e c_s r_{d0} - 1)/c_e c_s r_{d0} = 1$ is satisfied when $r_{d0} = 1/c_e c_s$ was taken into account. Integration of Equations (4-58) and (4-59) gives:

$$s = r_{d0} c_s \left\{ 1 - \left[\frac{1}{1 + c_e v_{d0} \left(1 - \frac{1}{c_e c_s r_{d0}} \right) t} \right]^{1/(c_e c_s r_{d0} - 1)} \right\} \quad (4-60)$$

$$s = \frac{1}{c_e} \left[1 - e^{-c_e v_{d0} t} \right] \quad (4-61)$$

Equation (4-60) is valid when $r_{d0} \neq 1/c_e c_s$. Otherwise, Equation (4-61) needs to be used.

4.4.5. Diagrammatic presentation of flow and breakup regimes

In the previous sections a number of approximate solutions referring to different types of flow and different breakup mechanisms have been presented. At the same time the analysis presented so far does not allow one to recognise, in an easy way, the situation in which each equation may be applied. This will be clarified in this section. The values of velocities and droplet radii for which the Stokes, Allen and Newton flow approximations are valid will be identified. Also, the regions of bag and stripping breakups will be identified. Then the

characteristic times for droplet evaporation, and bag and stripping instabilities will be compared for typical values of fuel droplets and gas parameters in diesel engines.

The applicability of approximations of Stokes, Allen and Newton flows is determined by the values of Re . Let Re_i be the threshold values between flow types. Between Stokes and Allen flows $Re_1 = 2$, Allen and Newton flows $Re_2 = 500$ and for the upper limit of the Newton flow $Re_3 = 10^5$. The boundaries between these flows are determined by the equation:

$$v_d = \frac{v_g}{2r} Re_i \quad (4-62)$$

Taking the decimal logarithm of both sides of Equation (4-62), it can be rewritten as:

$$\log v_d = a_{fi} - \log r, \quad (4-63)$$

where $a_{fi} = \log(v_g Re_i/2)$, both v_d and r are dimensional (in SI units).

In a similar way, from Equations (4-25) and (4-46) the thresholds for bag and stripping breakups can be presented as:

$$\log v_d = a_{th b} - \frac{1}{2} \log r \quad (4-64)$$

$$\log v_d = a_{th s} - \frac{1}{3} \log r \quad (4-65)$$

where

$$a_{th b} = \log \sqrt{\frac{6\sigma}{\rho_g}}, \quad a_{th s} = \frac{1}{3} \log \left[\frac{\sigma^2}{2\rho_g^2 v_g} \right].$$

Using the same values of parameters for sprays as in Sazhin *et al.* (2001a) it is assumed that $\rho_g = 19.7 \text{ kg m}^{-3}$, $v_g = 3.3 \times 10^{-6} \text{ m}^2 \text{ s}^{-1}$, $\sigma = 21.8 \times 10^{-3} \text{ N m}^{-1}$ and obtained: $a_{f1} = -5.48$; $a_{f2} = -3.08$; $a_{f3} = -0.78$; $a_{th b} = -1.09$; $a_{th s} = -0.24$. Since the dependence of these parameters on ρ_g , v_g and σ is rather weak, these values can be considered as typical for practical applications.

The plots of $\log v_d$ versus $-\log r$ for these values of parameters are presented in Figure 4-30. Since all plots on this diagram are straight lines, they can be easily adjusted to any other combination of input parameters. Typical droplet radii in sprays are greater than 10^{-6} m and their velocities are greater than 1 m s^{-1} . In this case, as follows from this diagram, the Stokes flow approximation is generally not applicable to the analysis of sprays in engines. At $r > 10^{-5}$ m the threshold velocities for the stripping breakup are higher than for the bag breakup. The opposite takes place for $r < 10^{-5}$ m. The range of applicability of the conditions $r \gg r_{db}$ and $r \gg r_{ds}$ can be checked by showing that the point on the diagram corresponding to v_d and r under consideration is not close to the threshold lines for bag and stripping instabilities.

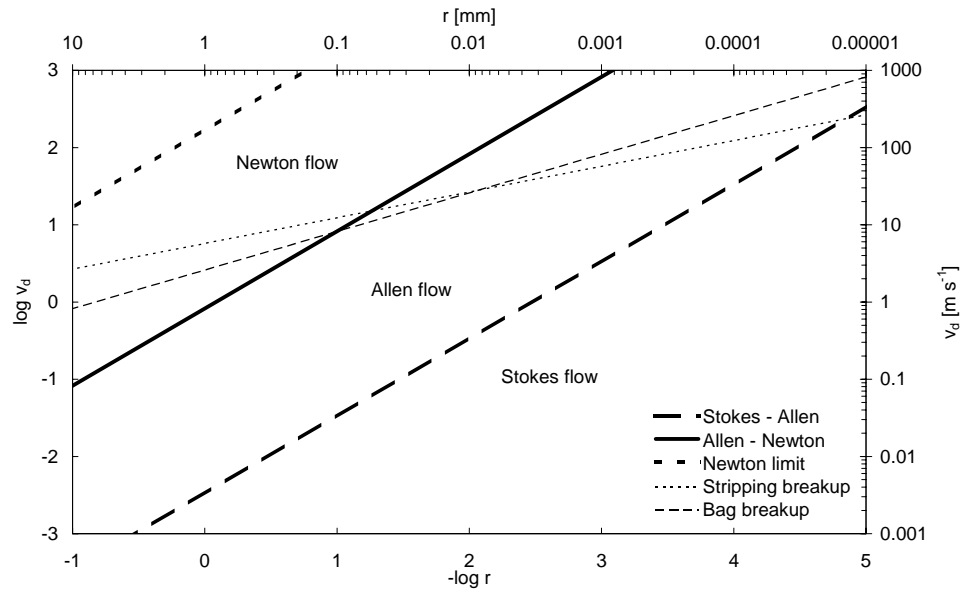


Figure 4-30. Threshold values of droplets velocities and droplet radii corresponding to transition from Stokes to Allen flow; Allen to Newton flow and the threshold value of applicability of the Newton flow approximation. Threshold values of droplets velocities versus droplet radii corresponding to the development of stripping breakup and bag breakup.

Other parameters which need to be taken into account when deciding the applicability of the approximations discussed in the previous sections are the lifetimes of unstable droplets (t_b and t_s), defined by Equations (4-17) and

(4-18), and the evaporation time $t_{ev} = \mu^{-1}$. From Equations (4-17), (4-18) and (4-14) the following expressions are obtained:

$$\log t_b = b_{th\ b} + \frac{3}{2} \log r \quad (4-66)$$

$$\log t_s = b_{th\ s} + \log r \quad (4-67)$$

$$\log t_{ev} = b_{th\ (ev)} + 2 \log r \quad (4-68)$$

where

$$b_{th\ b} = \log \left[D \sqrt{\frac{\rho_d}{2\sigma}} \right], \quad b_{th\ s} = \log \left[\frac{C}{v_d} \sqrt{\frac{\rho_d}{\rho_g}} \right], \quad b_{th\ (ev)} = \log \left[\frac{L\rho_d}{2k_g (T_g - T_s)} \right],$$

all parameters are in SI units (t and r are dimensional).

Taking the same numerical values of parameters as before, and $\rho_d = 830 \text{ kg m}^{-3}$, $v_d = 190 \text{ m s}^{-1}$, $L = 2.5 \times 10^5 \text{ J kg}^{-1}$, $k_g = 0.061 \text{ W m}^{-1} \text{ K}^{-1}$, $T_s = 315 \text{ K}$ and $T_g = 720 \text{ K}$, the following numerical values are obtained: $b_{th\ b} = 2.637$, $b_{th\ s} = -0.353$, $b_{th\ (ev)} = 6.662$.

Plots of $\log t_i$ versus $-\log r$ are shown in Figure 4-31, where $t_i = t_b$, t_s or t_{ev} . As follows from this figure, for $r < 0.01 \text{ } \mu\text{m}$ t_{ev} is smaller than t_b and t_s . This means that the evaporation is the dominant process for these radii and the contribution of droplet breakup can be ignored. For $r > 1 \text{ } \mu\text{m}$ t_s is smaller than t_b and t_{ev} . This means that for droplets with these radii the dominant process which needs to be accounted for is stripping breakup. Plots similar to those shown in Figure 4-31 can be presented for other values of parameters (e.g. temperatures of gas and droplets and droplet velocities).

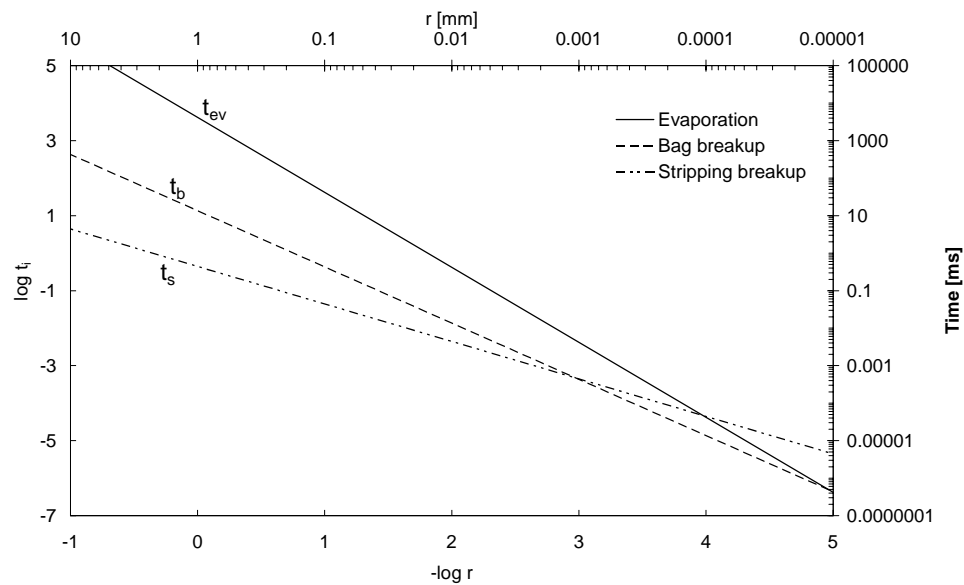


Figure 4-31. Plots of t_{ev} , t_b and t_s versus $-\log r$ for the same values of parameters as in Figure 4-30.

4.4.6. Experimental results for the initial stage of penetration

Spray penetration lengths were measured for injection pressures in the range from 60 to 160 MPa and ambient densities in the range from 25 kg m^{-3} to 56 kg m^{-3} . The results of measurements were compared with the predictions of the models taking into account bag and stripping breakup processes. The range of injection parameters correspond to the Newton flow regime, therefore the results presented in Sections 4.4.3.3 and 4.4.4.3 were used. Since measurements were performed for a low-temperature charge (570 K), the evaporation effects were assumed to be negligibly small in the experiments. The results of the comparison are shown in Figures 4-32 to 4-34 for various gas and injection pressures. The plots are presented using the following approximations: no breakup and air entrainment are taken into account (curves 1); breakup processes (stripping and bag) are taken into account, but not air entrainment (curves 2 and 3, respectively); bag breakup and entrainment processes, based on Equations (4-9) - (4-11), are taken into account (curves 4). In the case of air entrainment, the value of α_d was adjusted for each set of conditions, as shown

in Table 4-2. This choice of α_d provided the best agreement between experimental results and theoretical plots.

Injection pressure [MPa]	Gas density [kg m ⁻³]	α_d
160	56	0.000080
160	49	0.000070
160	37	0.000045
160	25	0.000025
100	37	0.000600
60	37	0.002500

Table 4-2. Values of α_d used in Figures 4-32 to 4-34.

All the plots are presented in the range of validity of the models: $r \gg r_{db(s)}$ (approximated as $0.3r \geq r_{db(s)}$) and $t < a_{rb(s)}^{-1}$. As follows from estimates, the range of validity of the stripping breakup model (about 0.05 - 0.1 ms) is noticeably narrower than that of the bag breakup model (about 0.25 ms). Hence the plots are presented in two time ranges: 0 - 0.1 ms and 0 - 0.3 ms. Since the bag breakup model has a wider range of validity, the effect of air entrainment will be investigated for this model.

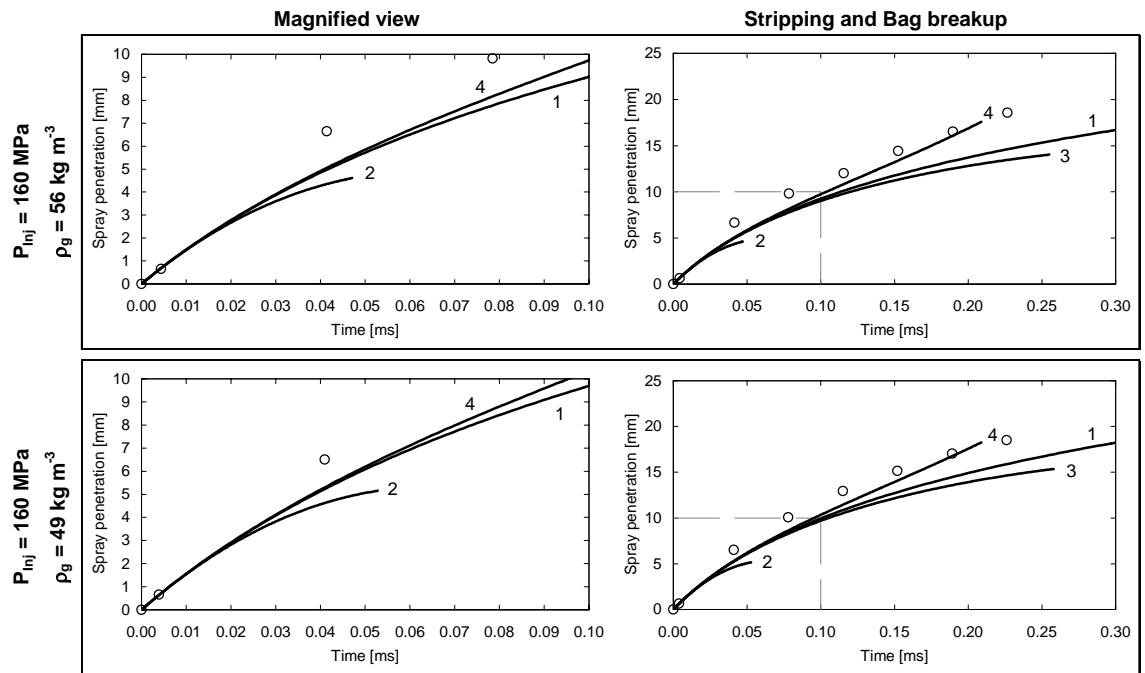


Figure 4-32. Comparison between measured spray penetration lengths (circles) and predicted spray penetration lengths for no breakup and air entrainment (curves 1); stripping breakup process only (curves 2); bag breakup process only (curves 3); bag breakup and entrainment processes (curves 4).

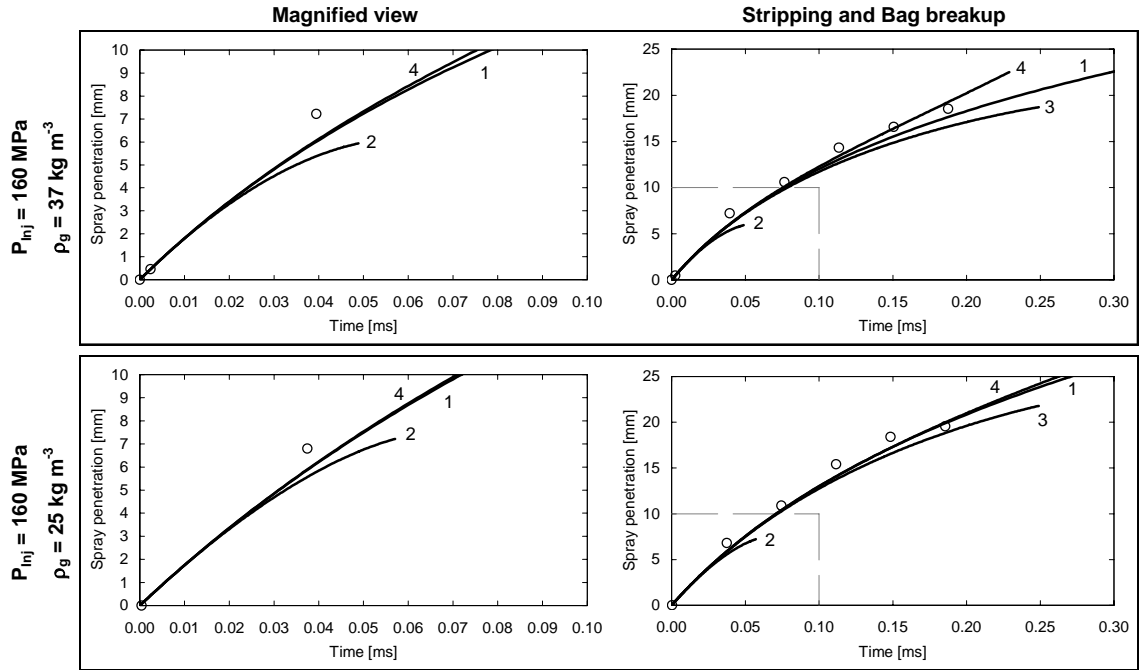


Figure 4-33. Comparison between measured spray penetration lengths (circles) and predicted spray penetration lengths for no breakup and air entrainment (curves 1); stripping breakup process only (curves 2); bag breakup process only (curves 3); bag breakup and entrainment processes (curves 4).

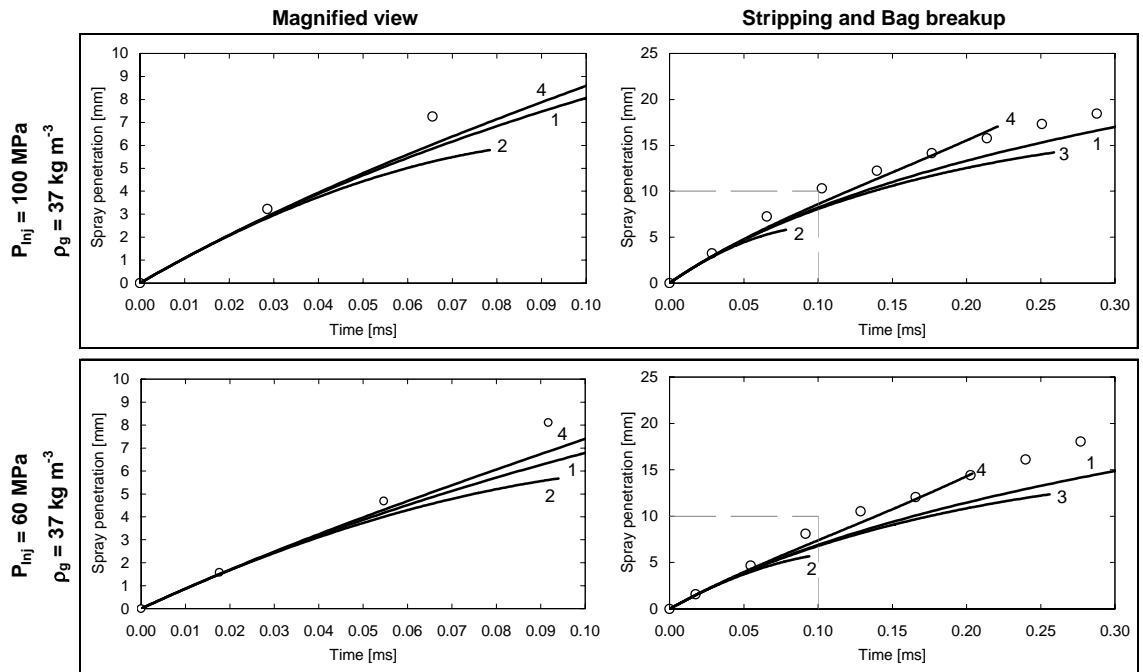


Figure 4-34. Comparison between measured spray penetration lengths (circles) and predicted spray penetration lengths for no breakup and air entrainment (curves 1); stripping breakup process only (curves 2); bag breakup process only (curves 3); bag breakup and entrainment processes (curves 4).

As can be seen from Figures 4-32 to 4-34, in all cases presented the simplest model (no breakup and air entrainment, curves 1) clearly underestimates the observed spray penetration lengths. Taking into account the effects of breakup alone increases the deviation between the theoretical curves and experimental points even further (curves 2 and 3). Good agreement between theoretical and experimental plots is achieved only when both effects of breakup and air entrainment are accounted for (curves 4). Even in this case, however, the model is not valid at times greater than about 0.1 - 0.2 ms. At greater times the two phase flow approximation needs to be used (Sazhin *et al.*, 2001a).

4.5. Conclusions of Chapter 4

Through the acquisition of high temporal resolution images, the influence of the injector nozzle type on the formation, breakup and evaporation of a diesel spray have been studied. These are the main conclusions of this investigation:

- Needle deflection resulted in a different early stage injection behaviour for the single-hole VCO nozzle when compared to its multi-hole counterpart. Although this resulted in the addition of a predictable delay at the beginning of the liquid penetration process the subsequent liquid penetration rate was unaffected. It is therefore valid to use a single-hole VCO nozzle and derive effects for the multi-hole if this initial delay is taken into account.
- The liquid core penetration profile for different nozzles was dependent on the injection pressure and in-cylinder conditions, in agreement with results reported previously (Hiroyasu & Arai, 1990; Naber & Siebers, 1996). The effects of fuel pressure and gas temperature on liquid spray penetration and dispersion have been explained.
- Oscillations of the injector needle in the vertical direction were observed, and are believed to lead to oscillations of the liquid fuel spray at approximately 6800 Hz. As a result of these oscillations, slugs of fuel were seen detaching from the spray.
- A new coefficient for the empirical model of Hiroyasu and Arai (1990) was derived from the experimental data. This coefficient was shown to be

applicable for both the mini-sac and VCO nozzles. The VCO required an additional time offset constant to counteract the initial hesitation period.

- It was observed that the leading edge of the vapour phase penetrated at a similar rate to the liquid core until the liquid core had reached its ultimate length. After this time the vapour phase penetrated deeper into the chamber due to earlier liquid/air momentum transfer.
- The vapour penetration profiles were shown to depend on both injection pressure and in-cylinder density. It was suggested that the mechanism for the vapour transport is the gas motion induced by the liquid phase transferring momentum from the droplets to the gas phase. Increased penetration of the vapour was observed at higher injection pressures and lower gas densities, i.e. when the liquid phase had a higher momentum.
- The effects of droplet evaporation, breakup and air entrainment on spray penetration have been studied theoretically in three regimes: Stokes, Allen and Newton flows. Theoretical plots have been compared with spray penetration measured experimentally. It has been shown that the agreement between the predictions of the model that included bag breakup and air entrainment processes was reasonably good. All models are expected to be valid for 0.1 - 0.2 ms after start of injection.

5. AUTOIGNITION OF DIESEL SPRAYS

5.1. Introduction

In this chapter the results of studies on diesel autoignition in the range of injection pressures 100 to 160 MPa, and the range of in-cylinder pressures 5 to 9 MPa are reported. The autoignition of diesel sprays at in-cylinder pressures from 5 to 9 MPa and injection pressures from 100 to 160 MPa was investigated. A pseudo three-dimensional view was obtained by using two high-speed video cameras recording the autoignition process simultaneously from two different viewpoints. This enabled the positional ambiguity of the ignition sites to be removed. The autoignition recordings were related to spray liquid core and vapour phase video recordings reported previously, in order to obtain a detailed understanding of the structure of the sprays. The autoignition delay was found to decrease with the increase of the in-cylinder pressure up to 7 MPa. However, contrary to common belief, a reverse in this trend was observed at higher pressures with a rapid increase in the delay at in-cylinder pressures above 7 MPa. This effect was related to decrease in spray penetration, decrease of diffusion coefficient and increase in chemical delay.

Experimental apparatus and procedure are discussed in Section 5.3. The main results of the measurements are presented in Section 5.4. The conclusions drawn from the work presented in this chapter are summarised in Section 5.5.

5.2. Background

The most widely reported correlation relating the ignition delay to the ambient gas condition is given by the relation (Aligrot *et al.*, 1997):

$$\tau = A P_g^{-n} e^{B/T_g}, \quad (5-1)$$

where τ is the ignition delay, P_g and T_g are the ambient gas mean pressure and temperature before autoignition takes place, A , B and n are experimental constants. This relationship reflects the widely accepted view that the

autoignition delay τ decreases as the in-cylinder pressure P_g or the in-cylinder temperature T_g increase.

Although many experimentalists successfully correlated their data with Equation (5-1), the values reported for the coefficients A, B and n have varied by several orders of magnitude. Aligrot *et al.* (1997) suggested that this was caused by the differences in experimental apparatus and fuels tested, and offered more general expressions for the coefficients in Equation (5-1) by taking into account the cetane number (CN), the gas kinematic viscosity (ν_g) and the paraffin content (c_{paraf}) of fuels:

$$A = e^{a \times \text{CN} + b \times c_{\text{paraf}} + c}, \quad B = f \times \text{CN} + g \times c_{\text{paraf}} + h, \quad n = d \times \nu_g + e,$$

where a, b, c, d, e, f, g and h are empirical coefficients. In experiments with a divided chamber diesel system (Astarita *et al.*, 1999), the boiling point of the fuel was found to have no effect on the ignition delay.

There seems to be some disagreement regarding the effects of fuel injection pressure on the ignition delay. This might be related to the difficulty of altering the injection pressure without affecting the delivered fuel quantity and fuel flow rate. Some researchers simply altered the nozzle hole diameters to induce a change in injection pressure (Pischinger *et al.*, 1988), others simultaneously altered the nozzle hole diameters and the number of holes to preserve fuel flow rate (Kobori *et al.*, 2000), or adjusted the injection pump duty cycle (Desantes *et al.*, 1999), while others simultaneously varied the nozzle hole diameter and injection pressure to maintain fuel flow rate (Bruneaux *et al.* 1999). For example, Desantes *et al.* (1999) have suggested Equation (5-1) to be generalised as:

$$\tau = A P_g^{-n} e^{B/T_g} P_{\text{inj}}^{-m}, \quad (5-2)$$

where P_{inj} is the injection pressure, m is an experimental constant. At the same time Bruneaux *et al.* (1999) did not observe any noticeable influence of the injection pressure on τ , even though they and Desantes *et al.* (1999) used a common rail injection system over a similar injection pressure range. In contrast to Desantes *et al.* (1999), Bruneaux *et al.* (1999) kept the injected fuel

mass flow rate constant by altering the injector nozzle hole diameter and the injection pressure simultaneously. Hence, it can be expected that for a given nozzle hole diameter, an increase in injection pressure induces a rise in fuel mass flow rate, which in turn may affect the ignition delay. Indeed, if the engine is under conditions typical of a cold start, the heat lost by the charge through spray evaporation usually exceeds the heat gained from the engine's cool walls, resulting in a flame extinction effect and extended ignition delay (Pischinger *et al.*, 1988). Once the engine's walls reach temperatures in excess of 800 K, ignition delays seem to be unaffected by increases in injected fuel quantities (Miwa *et al.*, 1988), suggesting that the wall temperature compensates for heat losses caused by fuel evaporation.

Edwards *et al.* (1992) used high-speed video recording to study the autoignition location of diesel sprays. They observed that ignition occurred simultaneously at multiple sites near the injector's nozzle. Their study was realised using a constant-volume vessel with an ambient pressure of 3 MPa and a temperature of 980 K. The injection pressure was of 17 MPa. Bruneaux *et al.* (1999) found that as the injection pressure was increased from 46 to 150 MPa, the autoignition sites were located further away from the nozzle. The ambient pressure was 6 MPa and the temperatures 940 K.

5.3. Experimental apparatus and procedure

5.3.1. Pseudo three-dimensional high-speed recordings

In order to record the autoignition process, two high-speed CCD video cameras recording 27000 frames per second were placed at 90° from each other as shown in Figure 5-1. Both cameras were triggered by the same dedicated signal emitted by the custom-built FIE controller. The resolution of the video recordings was of 128×64 pixels × 256 grey levels, with a sensitivity equivalent to 3000 ISO. In order to further maximise the sensitivity of the recordings, the lens was set to its widest aperture (f/1.9). Recordings were performed at three injection pressures (100 MPa, 140 MPa and 160 MPa), and a range of in-cylinder pressures (from 5 to 9 MPa).

In order to assess the time delay between the actual start of the injection and the start of the video recording, a light-emitting diode (LED) was linked to the injector pulse signal and positioned within the field of view of one of the cameras. It was found that the start of the video recordings and the start of the injection pulse (as represented by the LED) matched. It is therefore concluded that these two events have been separated by less than 0.04 ms (exposure time for 1 frame), and can be assumed coincident. The times at which the first fuel droplets were seen leaving the nozzle were measured to be 0.45 ms, 0.39 ms and 0.37 ms after the start of the recording for injection pressures of 100 MPa, 140 MPa and 160 MPa, respectively. The data presented here have been adjusted to compensate for this delay.

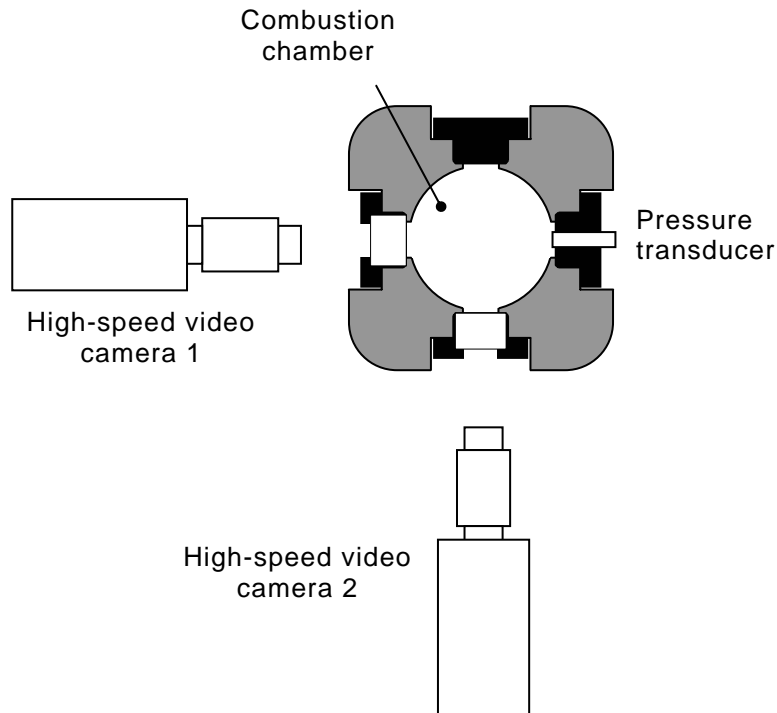


Figure 5-1. Experimental setup for pseudo three-dimensional autoignition recording.

5.3.2. Combustion pressure peak measurements

In order to supplement the ignition delay data obtained by video recordings, in-cylinder pressure traces were acquired with a Ricardo Configurable High-

speed Acquisition System for Engines (CHASE) while the boost pressure was varied. The acquisition sampling rate was between 0.1 CA and 1 CA, depending on the number of recorded channels. The timing uncertainty was therefore between 0.033 ms and 0.33 ms, resulting in errors from $\pm 0.83\%$ to $\pm 8.3\%$ for timing of pressure data. Since the in-cylinder pressure transducer was located at the periphery of the combustion chamber, the time taken by the combustion pressure wave to propagate from the flame location to the pressure sensor had to be taken into account. Assuming that the flame initiates at the centre of the combustion chamber (i.e. 25 mm away from the pressure sensor) and an average in-cylinder temperature equal to 720 K, the recorded pressures are expected to have an average time lag of 0.05 ms (i.e. 0.15 CA). The pressure history data have been corrected accordingly. Since the initiation of the flame does not always occur at the exact centre of the combustion chamber, the temporal error in calculating the overall time delay caused by the preceding assumption was estimated to be not greater than $\pm 1.5\%$.

The start of combustion pressure rise was defined as the last data point of a pressure trace coinciding within 1% with the corresponding curve for non-fired cycle. A software package was built using Visual Basic in order to automate this task. The validity of all the results was inspected visually.

In order to assess the agreement between both techniques, pressure measurements and video recordings were performed simultaneously. The combustion pressure rise was observed after the first traces of luminosity were measured (Figure 5-2). The difference between these two events reduced as the in-cylinder pressure was increased. This agrees with the observations made for conditions representative of a DI diesel at low to high loads (Higgins *et al.*, 2000). Although the ignition delays as measured by the two techniques do not give the same absolute ignition delays, they follow comparable trends.

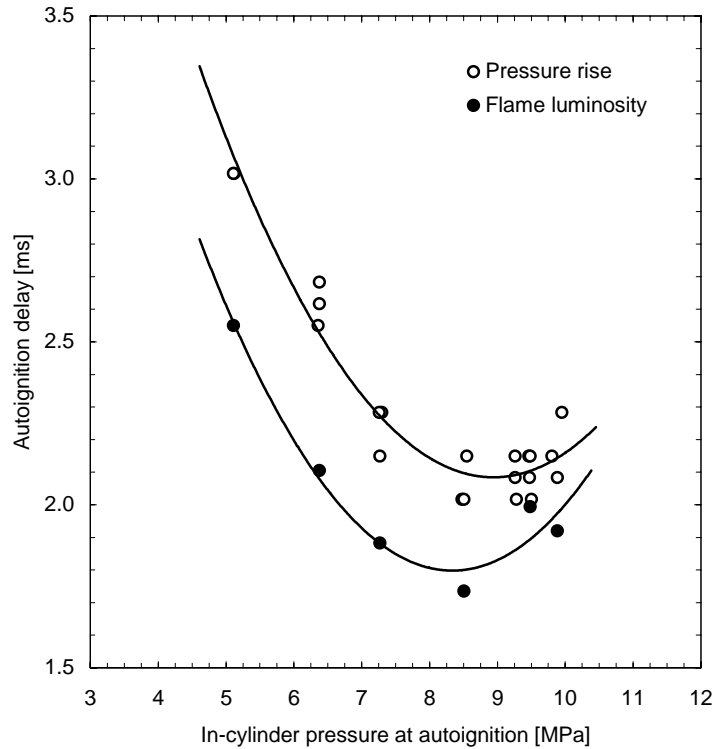


Figure 5-2. Comparison between autoignition delays detected by in-cylinder pressure rise, by flame luminosity (100 MPa injection pressure, 720 K in-cylinder temperature). Times are relative to start of injection (when droplets are first seen leaving the nozzle). The injector nozzle shuts at 3.1 ms.

5.4. Experimental results

5.4.1. Autoignition sites

From high-speed video recordings of the liquid spray and schlieren imaging, it is observed that ignition takes place within the vapour phase (see Figure 5-3), usually a short distance downstream of the tip of the liquid core. On some occasions the ignition sites are located around the liquid core, especially at high in-cylinder pressures. This observed location of autoignition sites agrees with the current understanding of the combustion processes in diesel engines (Flynn *et al.*, 1999) and computer simulation of the phenomenon (Sazhina *et al.*, 2000).

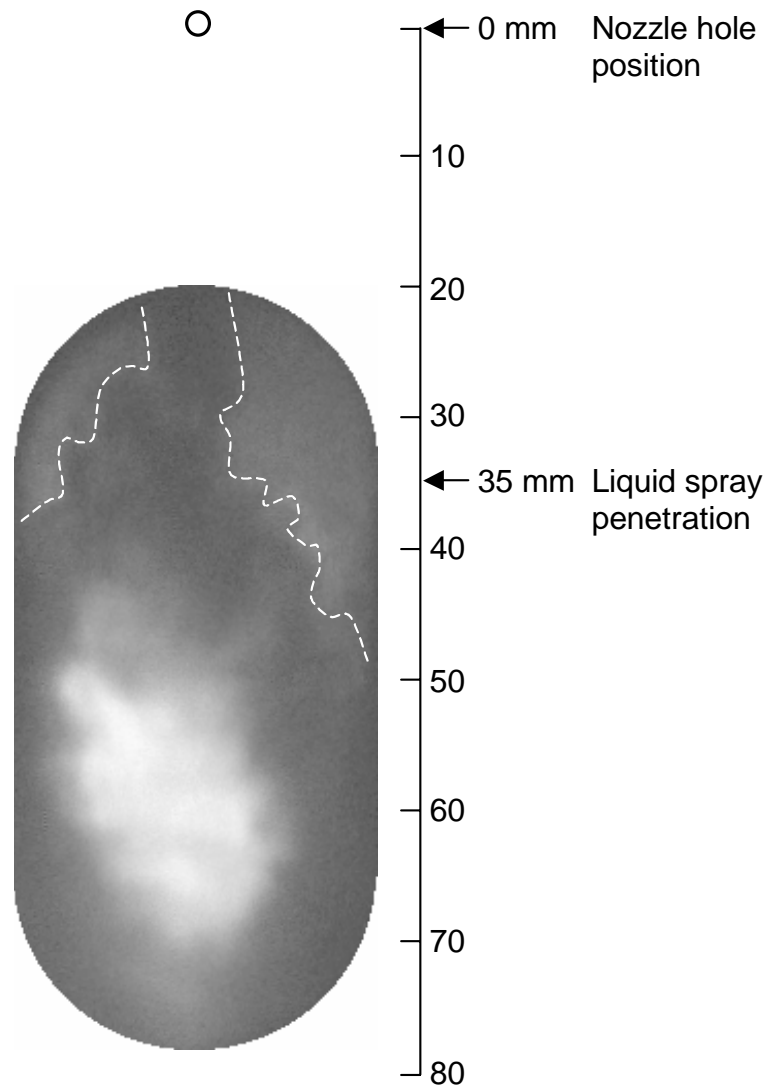


Figure 5-3. Schlieren imaging of vapour phase (dark) and autoignition (bright), recorded 2.4 ms ASOI (160 MPa injection pressure, 9 MPa in-cylinder pressure, 720 K in-cylinder temperature). Distances are relative to the injector nozzle (represented by a black circle). For clarity, white broken line highlights visible limits of vapour region. Liquid spray penetration for similar conditions is 35 mm (see Chapter 4).

Three series of images from high-speed video recordings showing the development of the ignition process are shown in Figure 5-4, Figure 5-5, and Figure 5-6 for injection pressures of 100 MPa, 140 MPa and 160 MPa, respectively. It can be seen that in many instances ignition occurred simultaneously at multiple sites. Ignition sites merged in less than 0.15 ms and formed a flame at the tip of the liquid phase for the duration of the injection.

For an injection pressure of 140 MPa (Figure 5-5), it can be observed that at the lowest in-cylinder pressures the flame has a spatially uniform appearance, indicating a high level of mixing. At higher in-cylinder pressures, the ignition sites and the boundaries of the subsequent flame are markedly more delimited. This suggests that under elevated in-cylinder pressures the mixing process gets increasingly difficult. This leads to a slower flame development and propagation. It is interesting to note that for a similar in-cylinder pressure range, all flames obtained with an injection pressure of 100 MPa appear noticeably delimited (Figure 5-4), whereas for 160 MPa all flames exhibit a uniform appearance (Figure 5-6). It is therefore believed that the difference in pressure ΔP between the fuel and the ambient gas, rather than the in-cylinder pressure P_g alone, affects the mixing quality.

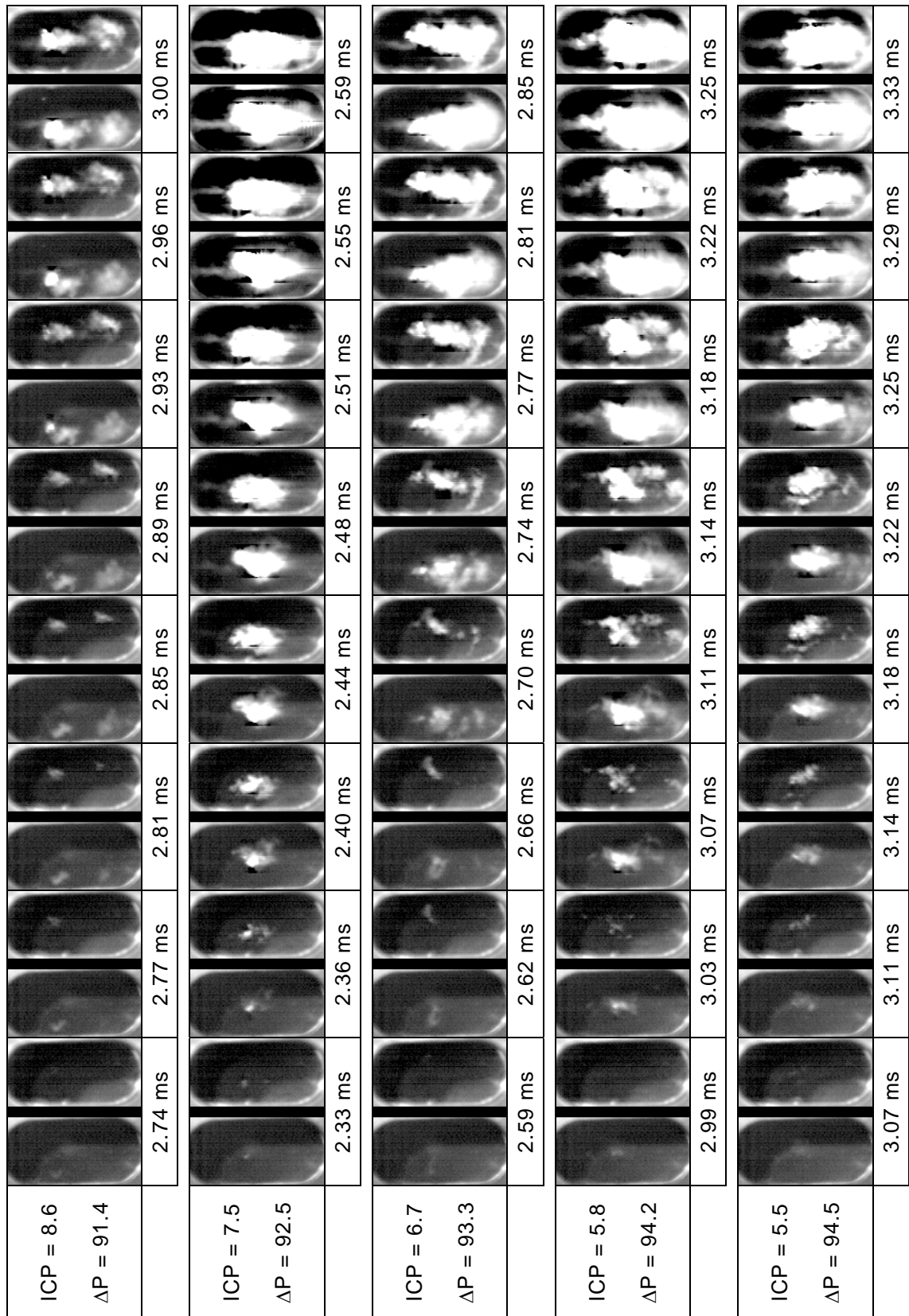


Figure 5-4. Pseudo-3D recordings of autoignitions of sprays injected at 100 MPa for a range of in-cylinder pressures. The first pair of frames for each of the 5 series corresponds to the autoignition time. Times are relative to the start of the injection.

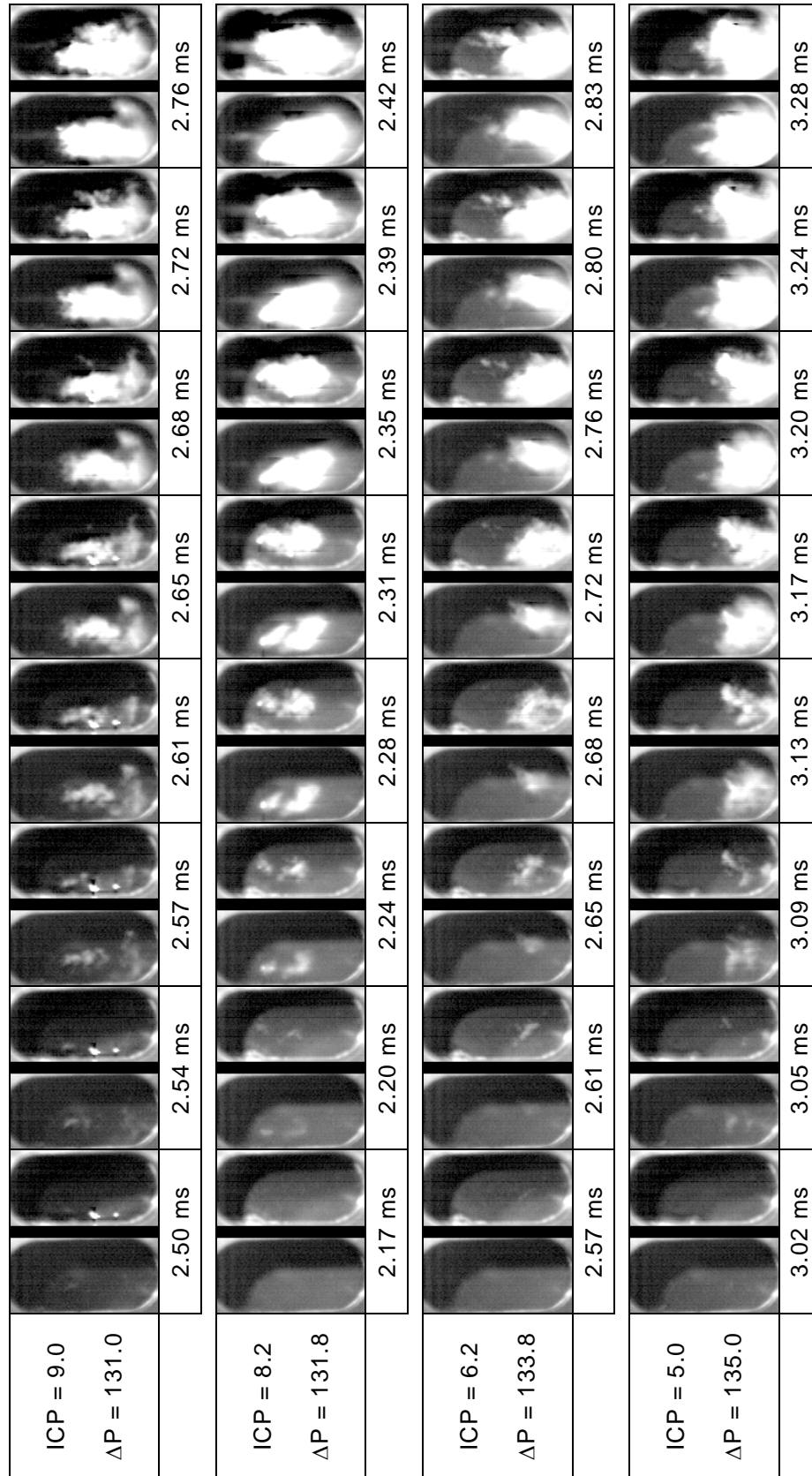


Figure 5-5. Pseudo-3D recordings of autoignitions of sprays injected at 140 MPa for a range of in-cylinder pressures. The first pair of frames for each of the 5 series corresponds to the autoignition time. Times are relative to the start of the injection.

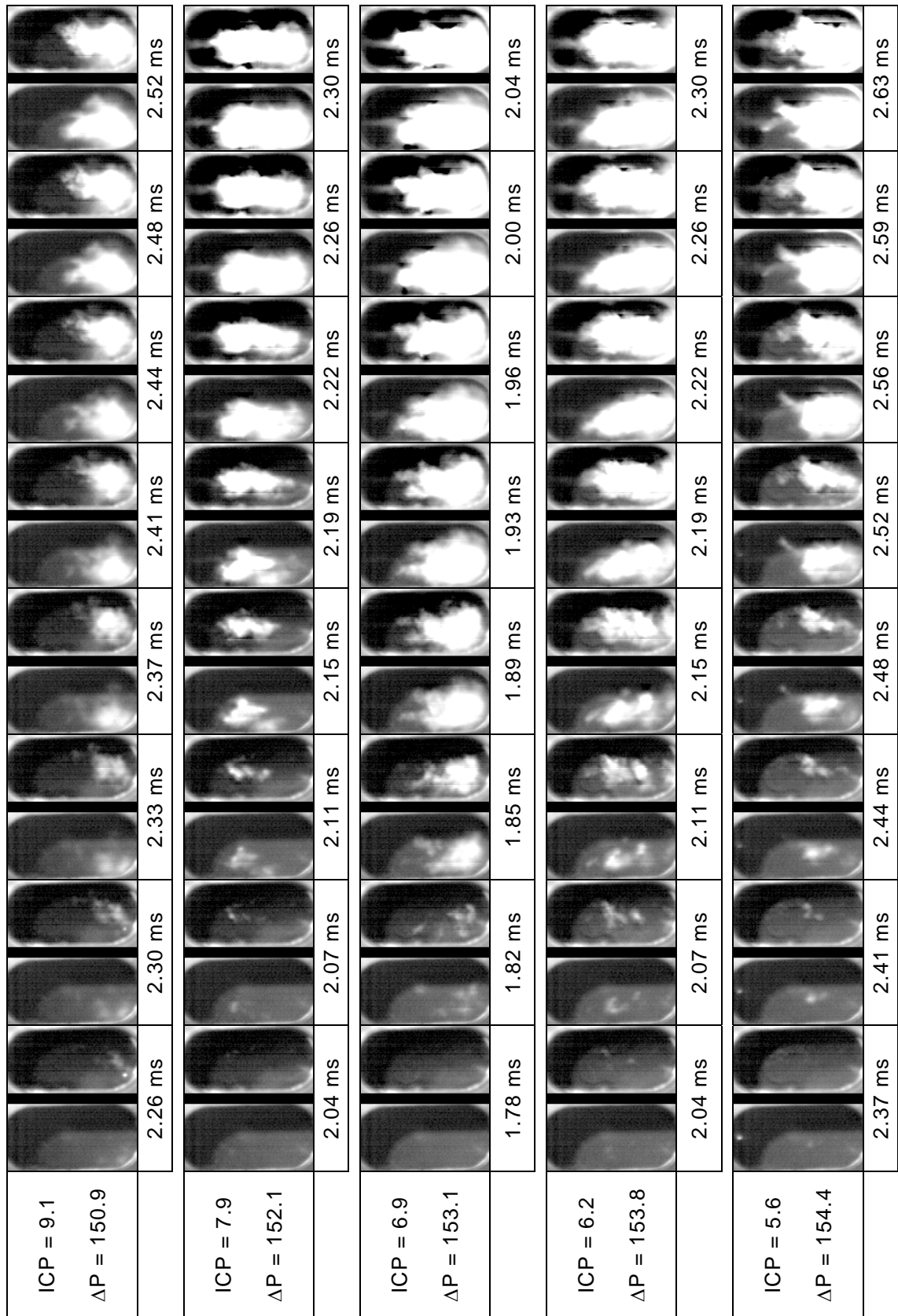


Figure 5-6. Pseudo-3D recordings of autoignitions of sprays injected at 160 MPa for a range of in-cylinder pressures. The first pair of frames for each of the 5 series corresponds to the autoignition time. Times are relative to the start of the injection.

For all the conditions tested, the flames were observed to propagate strictly downstream for the duration of the injection. Only after the injection had stopped, were flames observed to propagate towards the nozzle.

5.4.2. Autoignition delay

The plots of ignition delay versus in-cylinder pressure at the time of autoignition are shown in Figure 5-7. In the same figure the ignition delay as predicted by Equation (5-1) is shown.

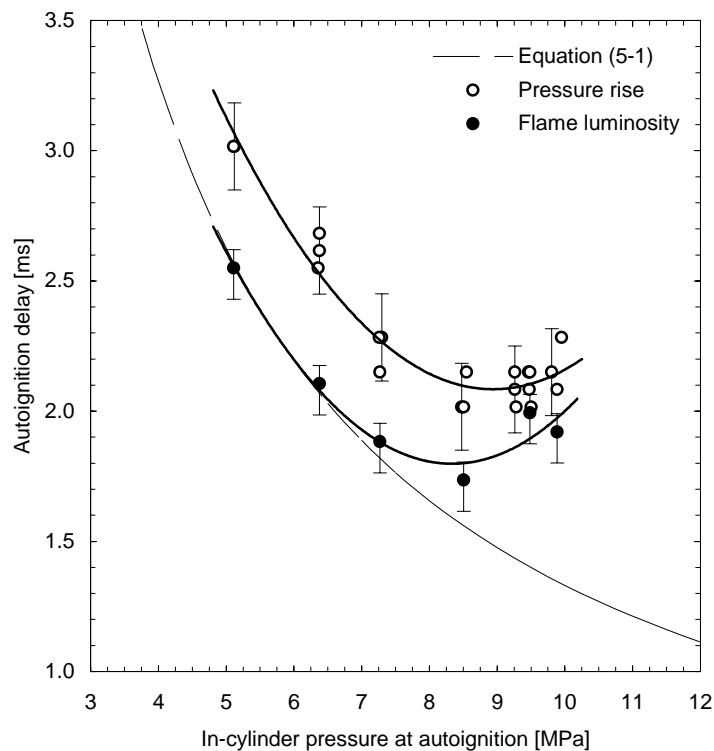


Figure 5-7. Comparison between autoignition delays detected by in-cylinder pressure rise, by flame luminosity (100 MPa injection pressure, 720 K in-cylinder temperature), and predicted by Equation (5-1) (coefficients $A = 0.095$; $B = 8300$ K; $n = 0.980$). Times are relative to start of injection (when droplets are first seen leaving the nozzle). The injector nozzle shuts at 3.1 ms.

Although the latter relation could successfully be used to model the autoignition data at pressures up to 7 MPa, it no longer correlates reliably with the ignition delay when the ambient pressure exceeds this value. Indeed, as the

in-cylinder pressure was increased beyond 7 MPa the autoignition delays were found to increase rapidly. This effect can be clearly observed in Figures 5-8, 5-9 and 5-10 for injection pressures of 100 MPa, 140 MPa and 160 MPa, respectively. This autoignition delay reversal was observed both for pressure measurements and video recordings, and for all injection pressures tested.

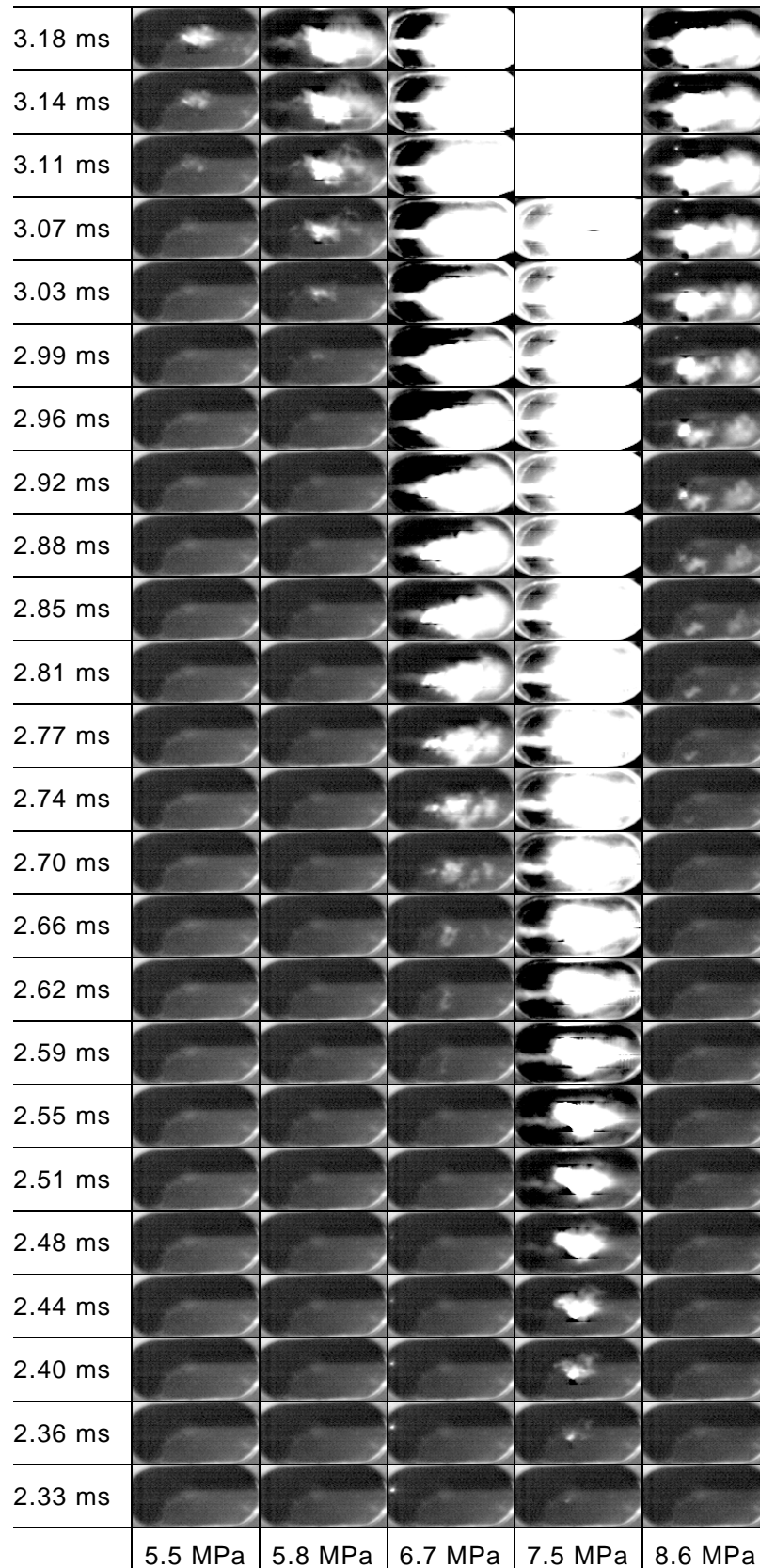


Figure 5-8. High-speed video recordings of autoignitions of sprays injected at 100 MPa for a range of in-cylinder pressures. Times are relative to the start of the injection, in-cylinder pressures were measured at the autoignition times.

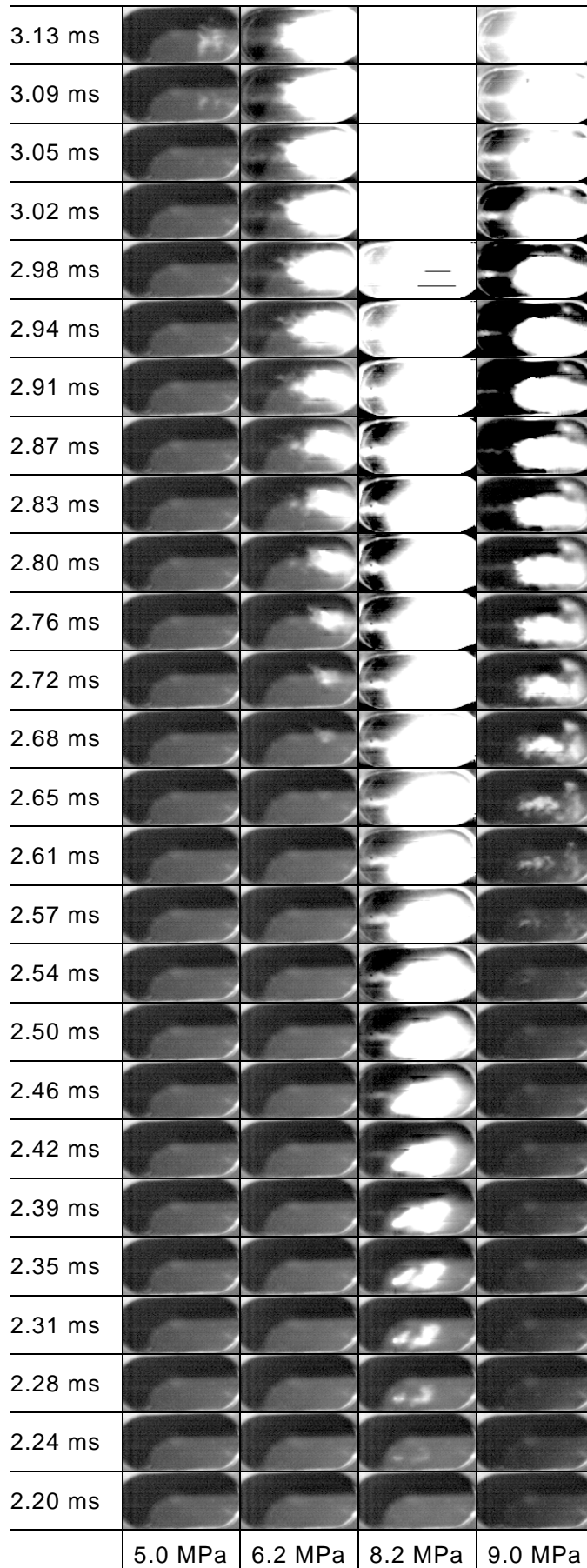


Figure 5-9. Same as Figure 5-8 for a 140 MPa injection pressure.

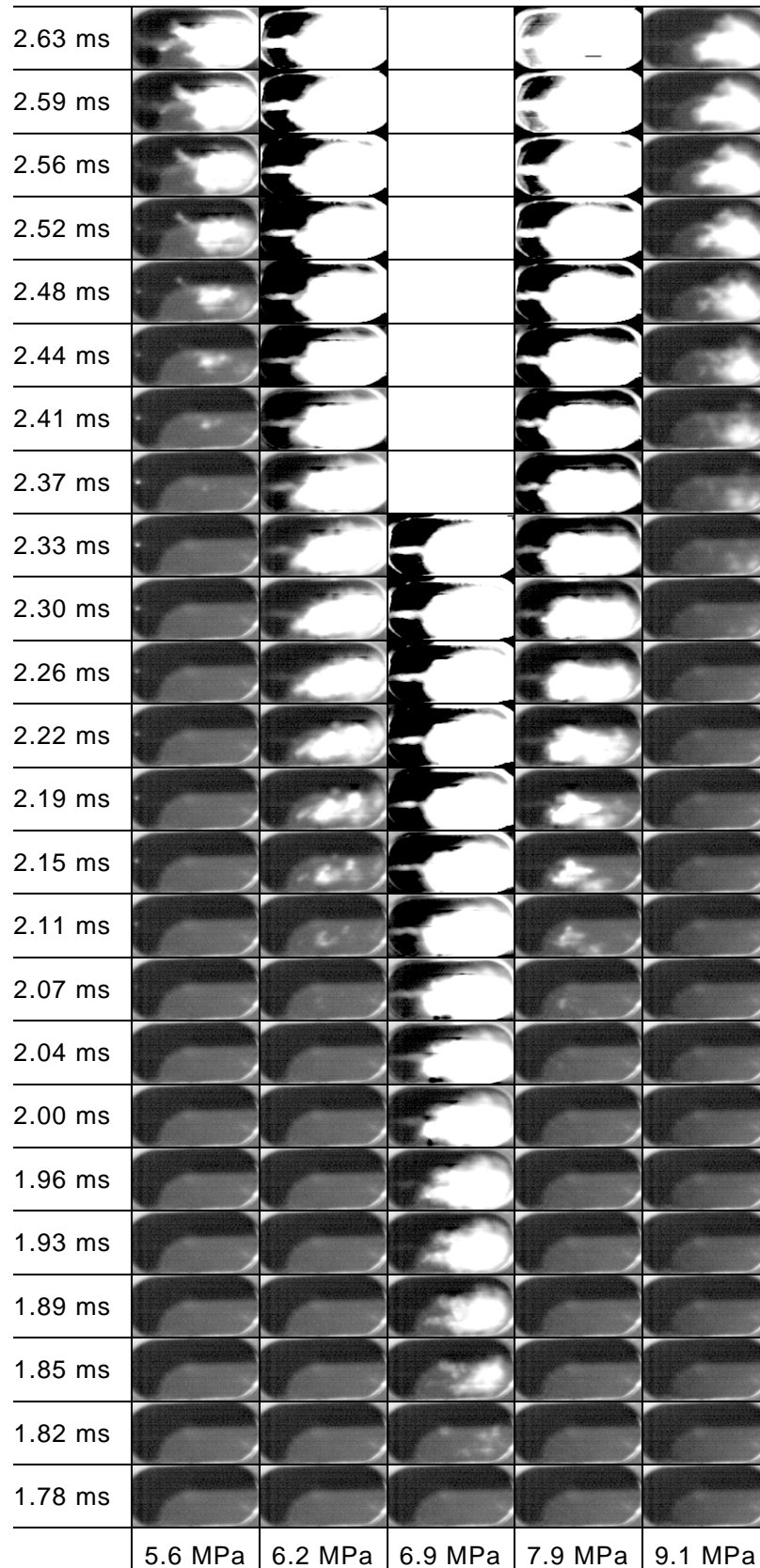


Figure 5-10. High-speed video recordings of autoignitions of sprays injected at 160 MPa for a range of in-cylinder pressures. Times are relative to the start of the injection, in-cylinder pressures were measured at the autoignition times.

The ignition delay measured is effectively a sum of physical and chemical delays. The physical delay is the time required for droplets to penetrate into the surrounding gas, breakup and evaporate. The chemical delay is controlled by the time required for the chemical reactions to develop. Rigorous mathematical description of all these processes is based on a highly non-linear system of coupled differential equations and is not feasible at the moment. In what follows an attempt will be made to provide a qualitative analysis of these processes and relate their current understanding to the experimental results.

5.4.2.1. Spray penetration

Apart from the immediate vicinity of the nozzle, spray dynamics can be described as a two-phase flow (Sazhin *et al.*, 2001a; Pozorski *et al.*, 2002). Equations for mass and momentum conservation for sprays lead to the following equation for spray penetration (Sazhin *et al.*, 2001a):

$$s = \frac{\sqrt{v_{ini} D_o t}}{(\rho_g / \rho_f)^{1/4} \sqrt{\tan \theta}}, \quad (5-3)$$

where v_{ini} is the initial velocity of spray, D_o is the diameter of the nozzle orifice, ρ_g and ρ_f are gas and liquid fuel droplet densities respectively, θ is the half spray cone angle.

When deriving Equation (5-3), it was assumed that θ is constant and the effects of turbulent dispersion of sprays were ignored (these effects were considered in (Pozorski *et al.*, 2002). θ is controlled mainly by the injector geometry (Lefebvre, 1989) and can be assumed constant in the analysis. As follows from Equation (5-3):

$$s \propto \sqrt{v_{ini}} = \left(2 C_d^2 \frac{\Delta P}{\rho_f} \right)^{1/4}$$

C_d is the discharge coefficient, ΔP is the pressure difference at the nozzle (injection pressure – air pressure). This is consistent with the observation that autoignition delay decreases with increasing ΔP . The same Equation (5-3) predicts that $s \propto \rho_g^{-1/4}$. Since $\rho_g \propto P_g$ for a fixed gas temperature T_g , it can be

expected that the delay due to penetration should increase with increasing P_g . This is observed at $P_g > 7$ MPa, but not at $P_g < 7$ MPa.

5.4.2.2. Droplet breakup

There are no self-consistent models capable of describing all the complexities of the droplet breakup process (see discussion in Shraiber *et al.*, 1996). For practical purposes, however, simplified models can be used. Following Reitz and Diwakar (Reitz & Diwakar, 1986, 1987) it is assumed that two mechanisms control droplet breakup. These are bag breakup which takes place when:

$$We \equiv \frac{\rho_g v_d r_d}{\sigma} > 6 \quad (5-4)$$

and stripping breakup when

$$Z \equiv \frac{We}{\sqrt{Re}} > 0.5, \quad (5-5)$$

where We and Re are the droplet Weber and Reynolds numbers respectively, σ is the surface tension, v_d and r_d are droplet velocity and radius respectively.

The minimal stable radii predicted by Equations (5-4) and (5-5) are defined as:

$$r_{\min(\text{bag})} = \frac{6\sigma}{\rho_g v_d} \quad (5-6)$$

$$r_{\min(\text{strip})} = \frac{0.5\sigma^2}{\rho_g v_d \mu_g}, \quad (5-7)$$

where μ_g is the gas dynamic viscosity. Assuming that μ_g does not depend on pressure (see Fig 1.3.1 (Bird *et al.*, 2002)) it can be seen that both Equations (5-6) and (5-7) predict that $r_{\min} \propto \rho_g^{-1}$. This means that the increased in-cylinder pressure, leading to increased ρ_g will result in smaller r_{\min} and smaller delay times (due to the increase of the surface area of the droplets). This is consistent with the observations at in-cylinder pressures below 7 MPa but not for pressures higher than 7 MPa.

5.4.2.3. Droplet evaporation

The evaporation flux from a droplet's surface is given by the following expression (Kuo, 1986):

$$G_F = \rho_s D_s \frac{\ln(1+B)}{r_d}, \quad (5-8)$$

where ρ_s is the droplet fuel vapour density at the surface of droplets, D_s is the diffusion coefficient of fuel vapour near the droplet surface, B is the Spalding number, $B = (Y_{Fs} - Y_{F\infty}) / (1 - Y_{Fs})$, Y_{Fs} and $Y_{F\infty}$ are the mass fractions of fuel in the vicinity of droplets and in the ambient gas (it can be assumed that $Y_{F\infty} = 0$). Remembering that D_s is inversely proportional to pressure (see Bird *et al.*, 2002, page 523) it can be expected that $G_F \propto P_g^{-1}$ and the ignition delay due to this effect should increase with increasing P_g . This is consistent with observations at $P_g > 7$ MPa but not at $P_g < 7$ MPa. Note that when Y_{Fs} is close to unity, a droplet can approach the critical state, and the analysis of this condition would require a different approach (Arias-Zugasti *et al.*, 1999).

From schlieren high-speed videos of the spray vapour phase, it was observed that in-cylinder density has a noticeable effect on vapour dispersion (Kennaird *et al.*, 2002). The vapour phase expands slower as in-cylinder density is increased (Figure 4-28). At very low ambient densities the vapour will visibly propagate at high velocities, resulting in a large dispersion but of low vaporised-fuel concentration and therefore low probability of autoignition. As density is increased, the vapour phase expands slower and consequently agglomerates into a region where conditions for autoignition are more likely to be found. From this reasoning, it is supposed that if in-cylinder density is increased even further, the diesel vapour will propagate so slowly that the effect of cold fuel being injected remains significant for a longer time, resulting in an overall colder vapour that will require more time to reach autoignition conditions.

5.4.2.4. Chemical autoignition

Once the concentration of vapour in the vicinity of droplets approaches the stoichiometric value, chemical reactions start to develop. Complete mathematical analysis would include hundreds of equations for hundreds of species. However, a reasonably accurate prediction of chemical time delay can be achieved with the help of reduced mechanisms such as the so-called Shell model (Halstead *et al.*, 1977; Sazhin *et al.*, 1999; Sazhina *et al.*, 1999). This model predicts an increase in ignition delay with a decrease in the equivalence ratio (Sazhina *et al.*, 2000). A decrease of equivalence ratio is expected to accompany an increase of gas pressure. Hence the chemical delay is expected to increase with increase of gas pressure. This is consistent with observations at in-cylinder pressures higher than 7 MPa. Note that in most cases in diesel engines, the chemical ignition delay is much smaller than the physical delay (Sazhin *et al.*, 2001b).

5.4.2.5. Summary of the discussion

To summarise the analysis of this section, the decrease of delay time with pressures below 7 MPa can be attributed to the enhanced droplet breakup. The increase of the delay time with pressures higher than 7 MPa may be related to the decrease of the liquid spray and vapour penetrations, the decrease of diffusion coefficient and the increase in chemical delay. More rigorous self-consistent analyses of all these processes are beyond the scope of this study.

5.5. Conclusions of Chapter 5

The effects of elevated in-cylinder and injection pressures on the autoignition of diesel sprays were studied by combining pseudo three-dimensional video of the flame propagation with previous high-speed video observations of the liquid core and vapour phase. The conclusions drawn from this investigation are summarised below:

- It was observed that the difference in pressure between the fuel and the ambient gas, rather than the in-cylinder pressure alone, affected the mixing quality.

- Autoignition was found to occur simultaneously at multiple sites within the vapour phase, downstream of the liquid core, that merged and spread quickly through the vapour region.
- For all the conditions tested, the ignition sites were observed to propagate strictly downstream for the duration of the injection. Only after the injection had stopped, were flames observed to propagate towards the nozzle.
- A reversal in the reported autoignition delay trends was observed for all injection pressures tested. The decrease in autoignition delay time with in-cylinder pressures lower than 7 MPa has been related to enhanced droplet breakup and is consistent with current correlations and understanding. The increase of this time with ambient pressures higher than 7 MPa is not consistent with current correlations but has been explained by a decreased spray penetration, decreased diffusion coefficient and increased chemical delay.

6. LASER-INDUCED INCANDESCENCE

6.1. Introduction

In this chapter, the results of the LII experiments conducted on the optical Proteus are presented. This chapter is divided into three main sections followed by the conclusions. The first section presents a summary of the previous publications on LII applied to diesel engines. The configuration of the laser system commissioned for this work is described in Section 6.3. Then details of the results obtained and their analysis are presented.

6.2. Background

Several attempts have been made to obtain in-cylinder measurements of soot concentration within DI diesel engines. Most studies focused on the observation of soot location sites, evolution of soot concentration with time, and soot size distribution across the spray. Schraml *et al.* (2000) observed that the initial rise in LII signal coincided with the establishment of a diffusion flame. This may seem suspicious since soot formation is believed to start before the combustion has initiated, during the pyrolysis of the liquid fuel. Soot formation was observed to initiate in the central region of the flame (Dec *et al.*, 1992; Kosaka *et al.*, 1995; Dec, 1997; Flynn *et al.*, 1999; Inagaki *et al.*, 1999). In this region, soot particle diameters are small and their number density is high (Kosaka *et al.*, 1995; Choi *et al.*, 1999; Greis *et al.*, 2002). Soot particulates agglomerate as they travel down the plume and form larger particulates (Kosaka *et al.*, 1995; Dec, 1997; Choi *et al.*, 1999; Flynn *et al.*, 1999; Inagaki *et al.*, 1999). Soot is found throughout the combusting region, but at higher concentrations near the leading edge of the plume (Dec *et al.*, 1992; Bruneaux *et al.*, 1999). Studies by Choi *et al.* (1999) and Greis *et al.* (2002), performed with swirl flows, have shown that the highest soot densities are found not near the leading edge of the plume but upstream, closer to the injector nozzle. They have also reported that higher soot temperatures are observed at the leading edge of the flames. Flynn *et al.* (1999) observed that particulates were completely consumed by the hot diffusion flame sheath while high heat release rates persisted. The LII signal

decay rate was found to be dependent on soot particles primary diameter (Schraml *et al.*, 1999). Schraml *et al.* (1999) also reported that cold start conditions did not alter soot size but increased soot concentration. It is believed that soot growth and oxidation were unaffected, but the initial number of soot particles significantly increased.

Only a few attempts have been made to investigate the influence of engine parameters, such as injection pressure and timing, on soot parameters. It was found that for higher injection pressures (100 MPa compared to 50 MPa), soot was usually located further downstream of the spray (Dec *et al.*, 1992; Kosaka *et al.*, 1995; Inagaki *et al.*, 1999), and the average soot volume fraction was reduced (Kosaka *et al.*, 1995; Inagaki *et al.*, 1999). Bruneaux *et al.* (1999) observed that for a 50% exhaust gas recirculation (EGR), significantly less soot was produced during combustion than without EGR. Exhaust particulates measurement made for the same conditions showed that, although EGR reduced soot formation during combustion, higher soot concentrations were emitted from the tailpipe. Bruneaux *et al.* (1999) suggested that EGR significantly lowered the effectiveness of post-combustion soot oxidation.

No studies of the influence of in-cylinder pressure on soot formation were found in the literature. This is certainly explained by the fact that LII is a relatively new technique, and although it has been the subject of thorough investigations for ambient pressure flames, its application to in-cylinder measurements is difficult due to the requirement for extensive engine modifications.

6.3. Experimental configuration

The laser used was a Spectra-Physics Quanta-Ray GCR 150 pulsed Nd:YAG laser, capable of delivering pulses of 300 mJ at a frequency of 10 Hz. The laser pulses were spatially and temporally Gaussian with beam diameter of 8.7 mm and pulse width of 6-7 ns at FWHM.

In order to minimise the effects of window fouling by soot deposit, a fuel additive was used. This additive, Ethyl Hitec 4103, was diluted at the rate of 0.375 cm^3 per litre and raised the fuel cetane number from 55 to 57. The chemical formula for Ethyl Hitec 4103 is $\text{C}_8\text{H}_{17}\text{NO}_3$ (2-ethylhexyl nitrate). Its effect on soot concentration is illustrated in Figure 6-1. It is apparent from the left image in Figure 6-1 that the high soot concentrations attenuated the laser pulse within a few millimetres. This was not observed when the fuel additive was incorporated (right image in Figure 6-1), and soot formation zones scattered across the window were recorded, as expected.

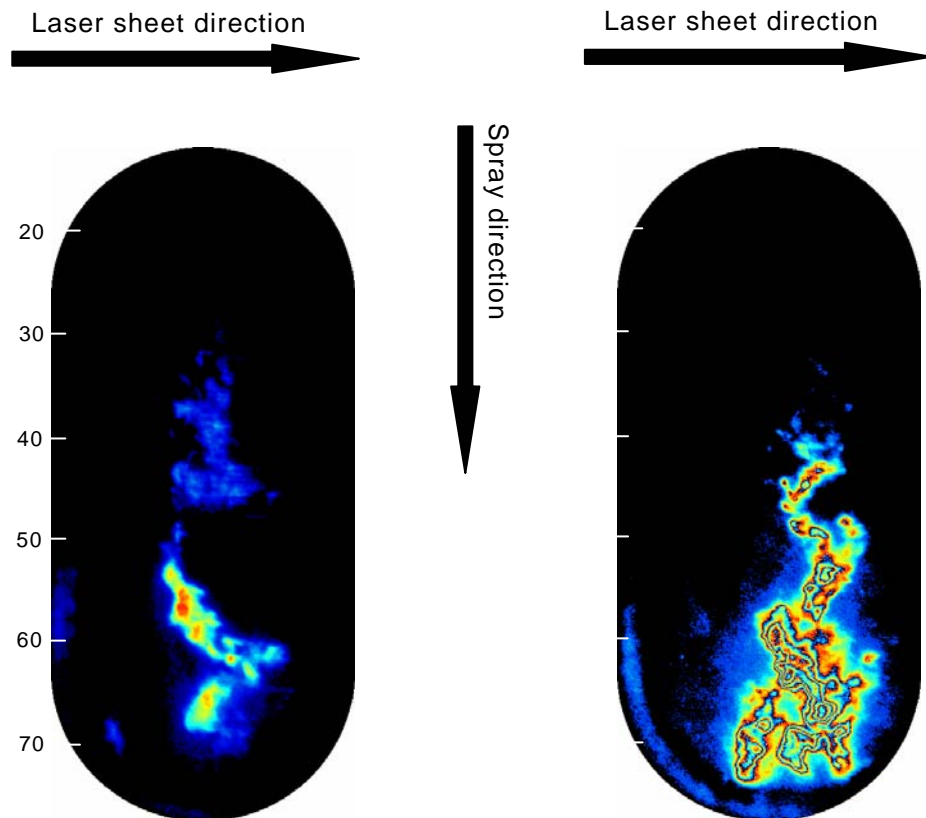


Figure 6-1. LII images without additive (left image) and with additive (right image). Scales indicate distances from the nozzle in millimetres. 160 MPa injection pressure, 8.0 MPa ICP at non-fired TDC, images recorded 3.7 ms after start of injection pulse.

6.3.1. Laser optics

The optical set-up consists of an arrangement of three mirrors reflecting green light and some sheet-forming optics. Even though only two mirrors are required to bring the laser beam down to the right height, the use of a third mirror allowed an easier transversal positioning of the laser sheet and the potential to simplify the alignment of the sheet in different planes (Figure 6-2).

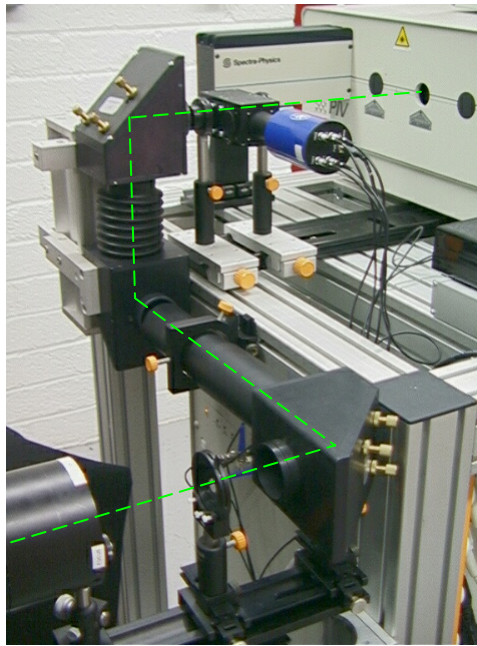


Figure 6-2. Photograph of optical arrangement with superimposition of the laser beam path.

When mirrors are to be used one has to bare in mind that their optical properties cannot be guaranteed at the edges. Hence, to ensure good reflection of the beam, the laser should hit only the centre of a mirror (usually not more than 80% of their diameter). This can be easily checked by running the laser at low power and placing a white card after the mirror. As shown in Figure 6-3, the laser beam will appear surrounded by a halo. This weak disc of light, which is emitted by the mirror when hit by a laser, should be centred with the laser beam.

The laser mirrors and sheet-forming optics used in this study were optimised for high-reflectance of 532 nm wavelength. The measured laser energy output,

290 mJ per pulse, was slightly below the manufacturer's specifications of 300 mJ per pulse. The energy lost through the optical path, i.e. from the laser output to the measurement location, was less than 10 mJ. Hence the laser pulses for LII acquisition had an average energy of 280 mJ each.

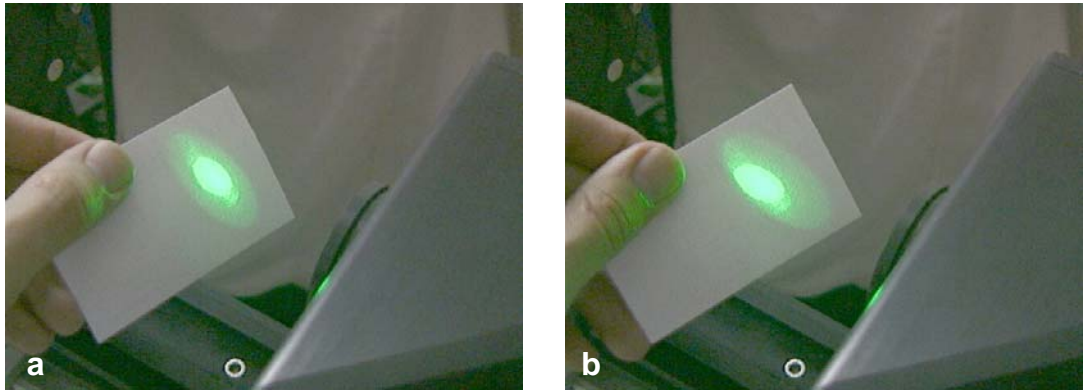


Figure 6-3. (a) Properly aligned mirror. (b) Misaligned laser mirror.

The sheet-forming optics used on this particular system consist of four lenses, which can be seen in Figure 6-4b. The first lens expands the laser beam vertically, and the second lens collimates the resulting cone. As the beam diameter is rather large (8.7 mm), a second set of two lenses is necessary to produce a thin laser sheet. Therefore the third lens narrows the thick sheet, and the fourth lens collimates the laser into a thin sheet. The resulting laser sheet has a thickness of 0.75 mm and a height of 55 mm at the focal point (measurement plane).

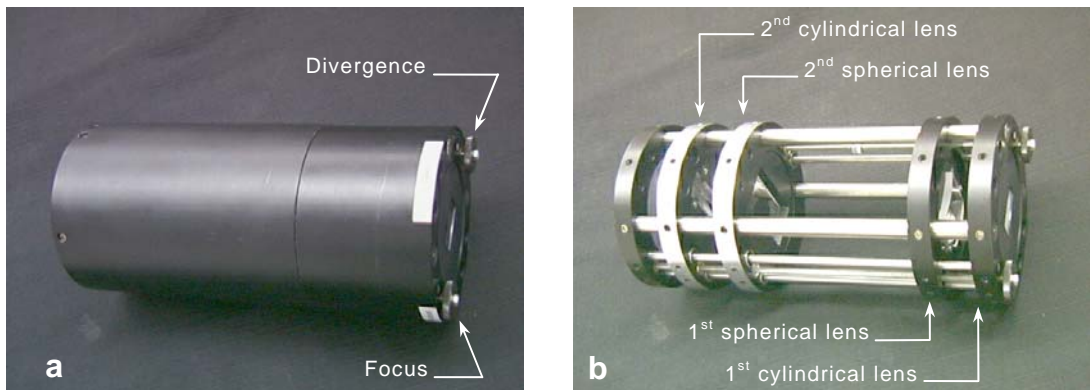


Figure 6-4. Photographs of a four-lens sheet forming optics.

In order to produce a well-formed and homogeneous laser sheet, a sound alignment of the laser optics is of the utmost importance. If the mirrors and the sheet-forming optics are not positioned correctly, the resulting laser sheet may not have a typical Gaussian profile but a three-dimensional form with a ‘banana’ shaped cross-section. Such laser sheet cannot be focused properly and therefore the laser cannot be used at its maximum potential. To avoid this unwanted effect the laser beam must follow the central axis of the sheet forming optics. The alignment of the laser beam can be simply checked by placing an iris diaphragm on the same rail as the sheet-forming optics and centred on the laser beam. By closing the iris down until only the outer region of the laser beam remains blocked, it is possible to visualise the outline of the laser beam. When the iris is slid along the rail, the contour of the laser beam should still be centred with the iris (cf. Figure 6-5). If this is not the case then the laser beam is not parallel to the main rail and sheet-forming optics.

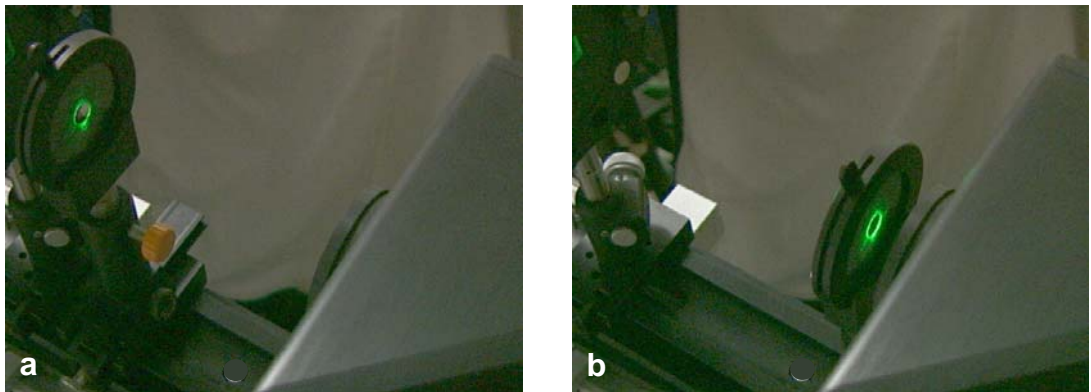


Figure 6-5. Checking the alignment of the laser beam with an iris diaphragm.

Once a proper Gaussian laser sheet has been obtained, it is necessary to position the sheet in the desired plane and at the right distance from the targeted area. As the sheet-forming optics do not have an infinite focal length, it is necessary to make sure that the measured area is within the depth of field of the optics. Minor adjustments of the focal length and divergence of the laser sheet can be made by means of two thumb wheels located on the sheet-forming optics assembly (Figure 6-4a).

When the laser has been properly focused, the laser sheet can be shifted to the desired plane by operating two knurled wheels on the transversal rail. This allows for minor corrections of the laser sheet angle. The angle of the laser sheet relative to the measurement area can be evaluated with a white card inserted between the sheet-forming optics and the combustion chamber window. Two lines should appear on the card, a strong one which is the actual laser sheet, and a weaker one which is a reflection from the window. Those lines should be close to each other but superimposition should be prevented to avoid back reflection of focused laser light towards the laser optics.

6.3.2. Image acquisition

6.3.2.1. Camera configuration

The ICCD cameras used here were two high-resolution DoubleShutter SensiCam[®] manufactured by Pulse Photonics Ltd. These cameras can acquire monochromatic images of up to 1280×1024 pixels with a frame rate of about 9 fps, and a resolution of 12 bits (4096 levels of grey). Their spectral sensitivity ranges from 340 to 700 nm FWHM, but the use of an image intensifier will affect the overall spectral range of the final images. The resolution of the images presented in this chapter was measured to be $73 \times 73 \mu\text{m}$ per pixel, by recording a scaled image.

Along with these two CCD cameras, two different lenses (50 mm and 100 mm focal length) and an image intensifier were available. The intensifier allowed very high temporal resolution (5 ns minimum exposure), which is crucial for LII experimentation. Only one camera being required for LII imaging, the spare CCD camera could be used simultaneously to provide complementary information such as elastic scattering (LIS). This double-camera configuration was discarded for two reasons, firstly, as the two lenses available have a different focal length, optical distortions between the pairs of images would not allow satisfactory post-processing. Secondly, only one image intensifier was available, therefore the minimum exposure for LIS would have had to be the minimum gate width of the CCD camera, that is 100 ns. Such a long exposure would have necessitated an extremely efficient set of filters to reject the

interference from LII and flame luminosity and only allow the elastic scattering through. For these reasons, a simple image-doubling extension was fitted onto the camera to duplicate the view of the combusting spray. Therefore two views of the spray were recorded on one single image, and a different optical filtering could be applied to each half image (cf. Section 6.3.2.2). The main drawbacks inherent to this method lie in the necessity to set the image intensifier so that proper exposure is obtained for both LII and LIS, and the slight optical distortions caused by the optical arrangement. A schematic of the equipment layout used for simultaneous LII / LIS is shown in Figure 6-6.

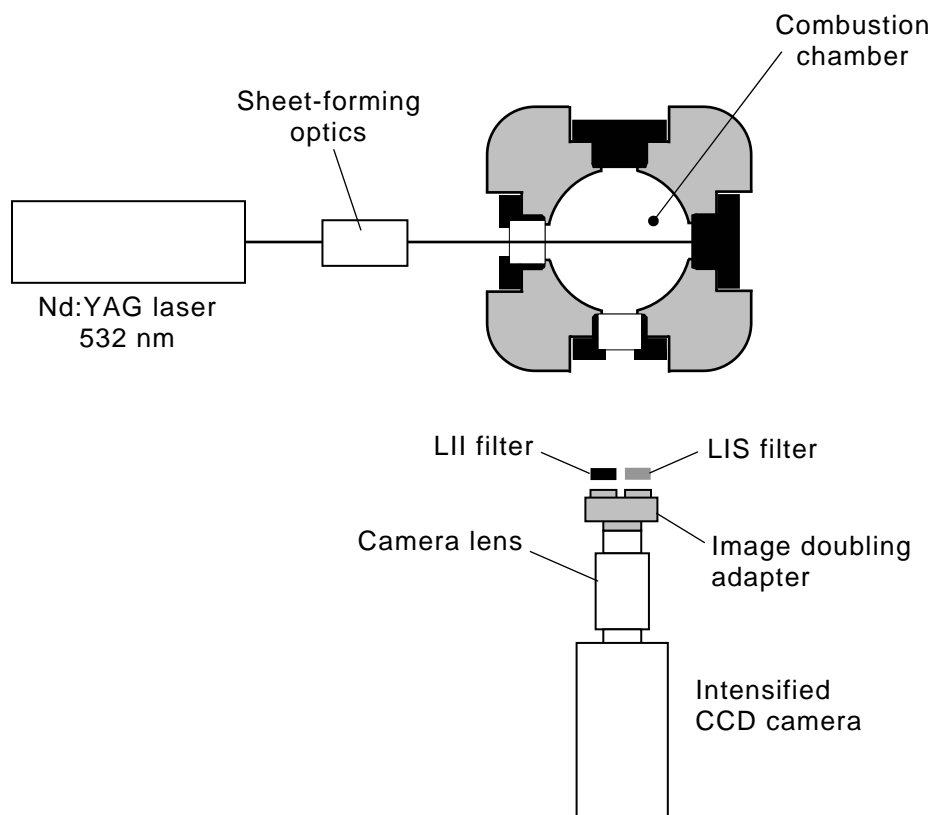


Figure 6-6. Experimental set-up for LII study.

The safest way of focusing the camera for LII imaging is to set the intensifier gain to zero, switch the laser to low-energy mode and remove all optical filters. After making sure that the laser sheet is properly aligned at the desired position, the acquisition process can begin. Depending on whether the engine is fully operational or not, the focusing can either be done on a non-combusting spray, nebulised water or a piece of white paper. A beam dump must be used

when the laser light is not fully contained within the combustion chamber. It is also essential to check that the camera's lens diaphragm aperture is set to the value that is going to be used for the actual experiment. Otherwise the depth of field will not be the same and the focusing procedure may have to be repeated.

6.3.2.2. Image doubling adapter

An image-doubling unit, which can be screwed onto the camera lens as shown in Figure 6-7, facilitated the acquisition of two similar views of the same object in one single image. Each one of these views can be individually fitted with optical filters, thus providing two spectrally different representations of the same event. Although this image doubler included a filter holder, this had to be removed because of its inadequate design. This holder could only receive square filters of 50×50 mm, and was designed in such a way that the filters were significantly off-centre relative to the two optical axes. This can be considered as a severe design flaw since the optical qualities of filters cannot be guaranteed at their edges. Therefore the defective holder was removed and individual holders were used for each filter, as shown in Figure 6-7.

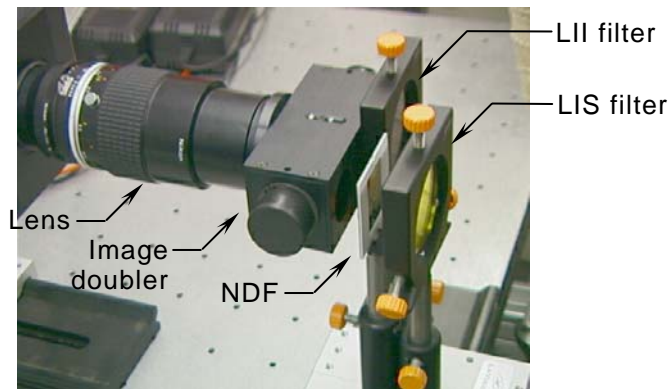


Figure 6-7. CCD camera lens with image-doubling adapter and interference filters.

The original intention was to collect simultaneous LII and LIS of soot particles to produce maps of relative soot particle diameter, as explained in Section 2.2.2.1. Although LII was successfully obtained with this configuration, LIS of soot could not be observed. Because the diesel droplets present during

the injection scatter much more light than the soot particles, sufficient exposure of the soot scattering could not be obtained without the risk of overloading the photomultiplier tube with droplet scattering. An alternative would have been to gather simultaneous LII / LIS only after the injection had stopped, when no fuel droplets would be expected to be present. Unfortunately, it was observed that this constraint resulted in at least 50% of the soot formation period being discarded. It was also found that interference from LII was not negligible with the LIS filter, resulting in a potentially significant error. Furthermore, for reasons that will be detailed in Section 6.3.5, it is expected that the accuracy of any results obtained by simultaneous LII / LIS would be particularly poor.

Therefore, it was decided that simultaneous LIS of fuel droplets would be recorded to complement the LII of soot. This strategy provides valuable information on the location of the liquid fuel spray relative to the soot formation regions.

6.3.2.3. Optical filters

Interference filters were selected to suit the requirements for the study of soot formation. For LII imaging, a wide-bandpass filter was selected, with a measured peak transmission at 416 nm and a full width at half maximum (FWHM) of 64.4 nm. This filter maximised the LII signal and offered excellent rejection of interference from elastic scattering, fluorescence and flame luminosity.

For LIS imaging, a narrow bandpass filter centred on the laser wavelength (i.e. 532 nm) was chosen with a 9.4 nm FWHM. Because the elastic scattering was particularly intense, a set of neutral density filters was used to avoid overloading the image intensifier and CCD camera.

The transmission characteristics for these filters are presented in Figure 6-8.

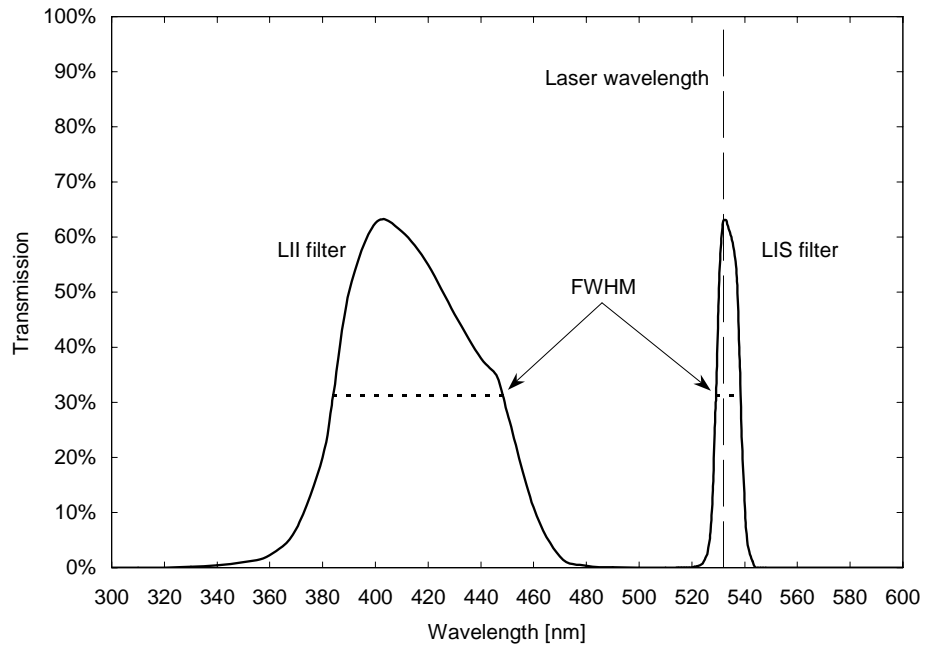


Figure 6-8. Measured transmission profiles of filters used for LII and LIS. Dotted lines show the FWHM for each filter, broken line indicates the laser wavelength (532 nm).

6.3.2.4. Image intensifier relay optics

The image intensifier consists of a photo-multiplier tube, mounted between the CCD camera and the lens, and a control box shown on Figure 6-9. The exact characteristics of the image intensifier are detailed in Appendix C.



Figure 6-9. Front panel of image intensifier control.

The 'Delay' value corresponds to the delay in microseconds between the acquisition trigger and the actual opening of the intensifier shutter. This delay can be adjusted up to 999.999 μs , in increments of 1 ns. The 'Width' input allows the level of opening of the intensifier shutter to be changed from 5 to 999.999 μs . The minimum width to obtain an image was measured to be about 5 ns. It must be noted that the camera shutter also has to be triggered in order to take an image, and that the usual exposure of the camera CCD should be about 1 ms in order to allow for the photo-multiplier decay time, whatever the actual exposure is. The 'Gain' input controls the amplification factor of the image intensifier. Great care must be taken while manipulating this control since overloading the photo-multiplier tube could permanently damage the intensifier. The gain can be adjusted from 0 to 100, but it was found that gains above 85 would affect the quality of the images. The gain was therefore set to 70 for all acquisitions.

6.3.3. Acquisition timing

A good understanding of the acquisition timing is of the utmost importance in order to obtain sensible LII images. All the signal delays intrinsic to the system must be carefully assessed and as some of these delays show cycle-to-cycle variations, it is highly recommended that they be monitored continuously throughout the test session. This is best achieved with a fast digital storage oscilloscope that offers good triggering functions. The model used was a LeCroy Waverunner, offering an actual sampling frequency of 200 MHz. The most sensible signal to trigger the oscilloscope was found to be the injection pulse. The rising edge of the injection pulse was therefore taken as a reference for the acquisition timing scheme and used to evaluate the cycle-to-cycle time variation of the image acquisition. This was done by switching the oscilloscope to 'persistence trace' mode when the acquisition process started, hence showing all the image intensifier gate pulses superimposed. The maximum deviation was found to be within ± 0.05 ms (i.e. ± 0.15 CA).

The complete acquisition timing was based on the signals coming from the encoder fitted onto the Proteus' crankshaft. This encoder provided 3600 pulses

per revolution as well as a marker pulse at TDC. Both the FIE and the laser system used these signals as a reference clock.

The laser system included an engine-synchronisation module (YEX) that allowed the laser to run close to its optimum frequency (i.e. 10 Hz) and still match the intrinsic frequency of the engine cycle. This was achieved by only making an acquisition when the operations of both the engine and the laser were synchronised, i.e. the engine was firing and the laser was ready to release a pulse. The Proteus operating speed was 500 rpm (i.e. 8.33 Hz) and was fired at a rate of 1:4 cycles (1 fired cycle followed by 3 non-fired cycles). Skipfiring was necessary to ensure proper purging of the combustion chamber and minimise window fouling by soot deposit. Hence the firing frequency was approximately 2.08 Hz. Fortunately, this frequency is close to an integer fraction of the laser frequency ($2.08 \times 5 = 10.4$ Hz). Considering that the allowed laser frequency range was from 9.30 to 10.90 Hz, a measurement could be performed for every fired cycle. The shift in laser frequency from 10.0 Hz to 10.4 Hz resulted in a 10% drop in pulse energy. Consequently the average pulse energy for the acquisition of the LII images presented in this chapter was 255 mJ, corresponding to a power density of 88 MW cm^{-2} . The laser manufacturer quoted a pulse-to-pulse energy fluctuation less than 3% and long term power drift less than 5% over 8 hours.

The acquisition strategy selected for simultaneous LIS and LII is shown in Figure 6-10. The image intensifier gate was open 5 ns before the laser pulse, and the total exposure was set to 40 ns. As the LII signal rise occurs approximately 10 ns after the start of the laser pulse (Zhao & Ladommatos, 1998), the LII signal was integrated for approximately 25 ns.

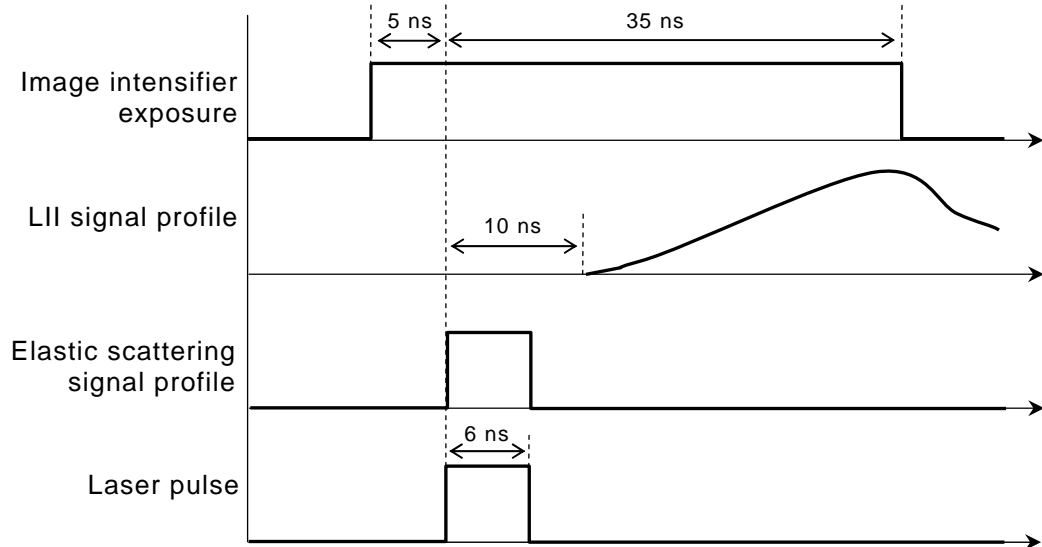


Figure 6-10. Acquisition strategy for elastic scattering and LII imaging.

6.3.4. Standard post-processing

LII images were recorded throughout the soot formation period for three different injection pressures (100, 140 and 160 MPa) and a range of in-cylinder pressures (6, 7, 8 and 9 MPa at non-fired TDC). Because of the turbulent nature of in-cylinder combustion, cycle-to-cycle variations in the position of dense soot regions were expected. This is accentuated by the fact that LII provides a map of soot concentration for a very narrow section of the flame. Therefore, although there may not be significant variations in the flame structure when observed with high-speed video, the positions of dense soot regions may fluctuate greatly within the flame. Hence, consistent information on the characteristics of soot formation cannot be obtained without acquiring a range of images for every combination of engine parameters. Data sets were recorded from the start of soot formation until no soot could be detected, with a time interval between two sets of 0.33 ms (1 CA). Each data set included between 27 and 30 images acquired consecutively during the same run. All images were inspected visually to ensure they were recorded properly and that the repeatability was adequate. Data sets were then post-processed to produce ensemble averaged and standard deviation images for each condition.

intensity of the average image converged rapidly. For data sets of at least 27 images, the coefficient of variation (ratio of standard deviation and mean intensity) was less than 1.7%. Apart from justifying the selected data set size (between 27 and 30 images), Figure 6-12 proves the non-random nature of the LII images (convergence is observed). For reasons explained in Section 6.4.3, the example presented below is expected to correspond to a phase in soot production where fluctuations are particularly high.

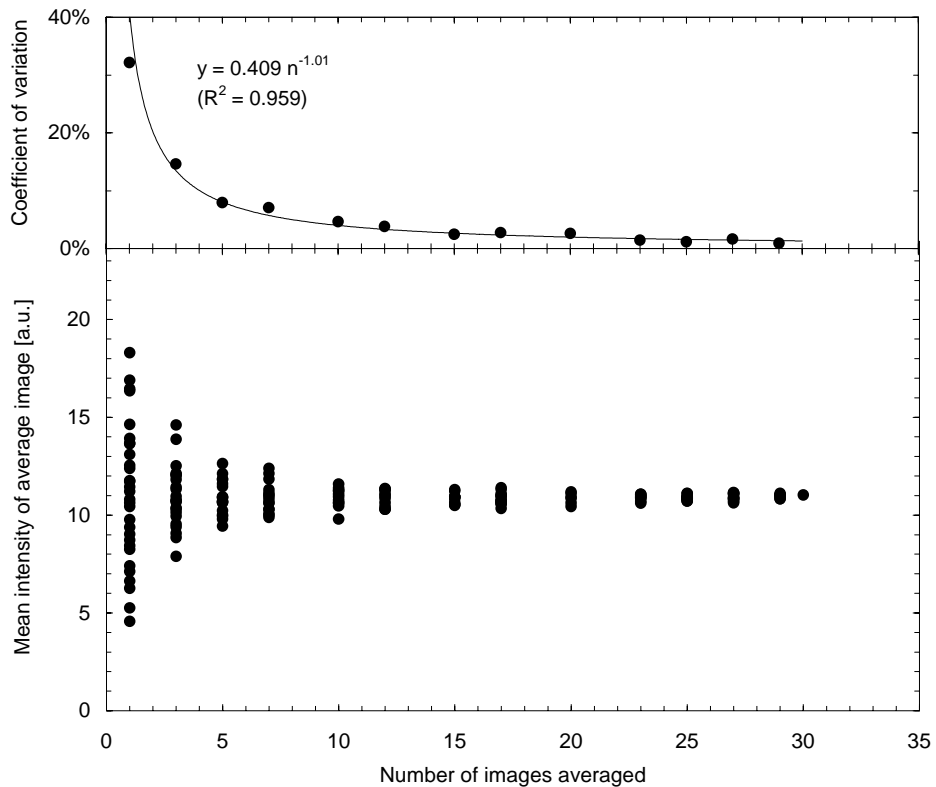


Figure 6-12. Influence of the number of images on the average image intensity. Coefficients of variation (ratio of standard deviation and mean intensity) are presented, with a power type trendline. Images were recorded 3.8 ms ASOI for a 140 MPa injection pressure and 8 MPa in-cylinder pressure.

Examples of average and standard deviation images are presented in Figure 6-13. It can be seen from these two examples that the standard deviation is large where the average intensity is high. This confirms the expected fact that the locations of dense soot regions fluctuate from one cycle to another, but

within a restricted area. The complete data set used to produce these images is presented in Appendix C.

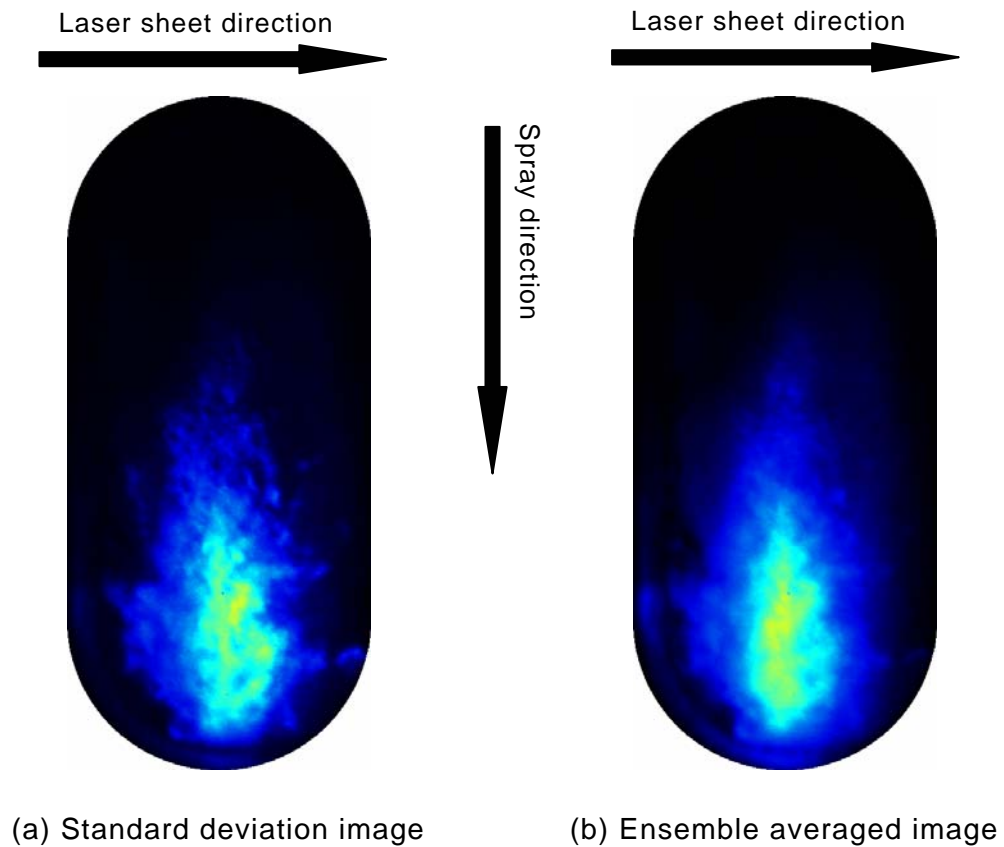


Figure 6-13. Examples of standard deviation and ensemble averaged images. 140 MPa injection pressure, 8 MPa in-cylinder pressure, images recorded 3.8 ms ASOI.

‘Phase 2’ of the post-processing provided a number representative of the intensity of the ensemble averaged image. This number is assumed to be representative of the amount of soot present in the combustion chamber.

6.3.5. Accuracy

6.3.5.1. Effect of laser fluence on LII signal

Since the intensity of the LII signal is greatly dependent on the laser pulse power density, the laser fluence should be selected with care prior to

conducting measurements. Tait and Greenhalgh (1993) reported that the LII dependence on laser fluence differs significantly for Gaussian and rectangular beam profiles.

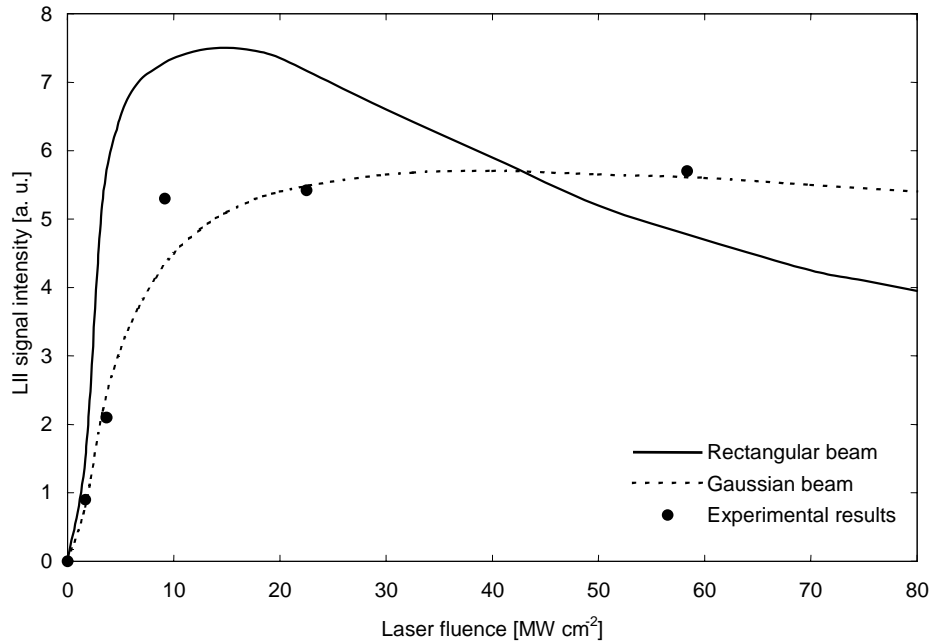


Figure 6-14. Dependence of LII signal on laser fluence for 100 nm particle radius (adapted from Tait and Greenhalgh, 1993).

As observed from Figure 6-14, the LII signal intensity is strongly dependent on laser power density for both beam profiles. Below 20 MW cm⁻², the LII signal increases rapidly with increased laser fluence. This is explained by the strong influence of laser fluence on soot particle temperature, and therefore on the incandescence signal. Beyond 20 MW cm⁻², the LII signal intensity obtained for a rectangular beam profile decreases rapidly as the laser fluence is increased further. This is due to the soot particles losing significant mass through vaporisation (Tait & Greenhalgh, 1993). For a Gaussian beam profile, the LII signal intensity is almost unaffected by variations in laser fluence between 20 and 80 MW cm⁻². For this power density range, the error caused by laser fluence fluctuations has an average of 1.9% and a maximum of 3%. This low sensitivity to variations in laser power is believed to be due to the fact that, for

a Gaussian beam, an increase in laser energy results in an increase in the effective beam diameter (Zhao & Ladommatos, 1998).

Since the laser system used for gathering the LII data had a Gaussian beam with a fluence between 60 and 80 MW cm⁻², it can be assumed that the results presented here were not significantly affected by shot-to-shot energy fluctuations and longer term fluence drifts. Another advantage of this type of beam lies in the fact that the progressive attenuation of the laser sheet across the dense soot regions of the spray will not result in a reduction of the LII signal. This significantly simplifies the post-processing and the interpretation of the LII data, since normalization of the images is not required.

6.3.5.2. Spectral interferences

The vaporisation of soot particles induced by the laser results in the production of molecular carbon species (e.g. C₂, C₃). C₃, although believed to be the major vapour constituent, was not observed to produce emissions in LII studies (Wainner, 1999). C₂ is known to produce potentially intense emissions over a broad spectrum, especially at high laser intensities. Since some emission bands of C₂ (438.3, 473.7, 516.5 and 563.6 nm) are well within the preferred LII observation bandwidth (see Table 2-2), fluorescence from this molecule must be taken into account in order to ensure minimal (or at least quantified) contamination of the LII signal.

Wainner (1999) observed that for a laser fluence below 2 J cm⁻² at 532 nm, the interference from C₂ fluorescence was not significant for collection wavelengths below 440 nm. The characteristics of the laser system commissioned for this study satisfy this condition (laser wavelength = 532 nm; laser fluence < 1.2 J cm⁻²; collection at 416±32 nm). Wainner (1999) also reported that fluorescence from PAHs, although possibly significant at excitation wavelengths in the UV, was not detected for a laser wavelength of 532 nm. It is therefore concluded that the LII results presented here were not significantly contaminated by fluorescence from PAHs or C₂ molecules.

6.3.5.3. Soot particle size sensitivity

Ni *et al.* (1995) showed that the LII signal intensity decay was highly dependent on soot particle diameter. They observed that the LII signal could first be detected between 10 and 12 ns after the start of the laser pulse. The rise in signal intensity was reported to last approximately 12 ns and was found to be unaffected by particle size. Following the peak in LII signal intensity, a decay was observed to last up to several hundred nanoseconds. The decay time was shown to be longer for larger soot particles. Ni *et al.* (1995) thus recommended that LII signal should be imaged shortly after the laser pulse, and with reduced exposure times so that size-dependence be minimized. For an exposure of 50 ns, they reported an error of up to 10% due to the size effect. This inherent sensitivity of LII decay time to soot size was used to obtain a measurement of soot primary diameter (Schraml *et al.*, 1999).

The settings used for gathering the LII data presented here follow the recommendations of Ni *et al.* (1995), with an effective LII exposure time of 25 ns. It is estimated from Ni *et al.* (1995) that the resulting error caused by size-dependence should be less than 4%.

6.3.5.4. LII signal trapping

Signal trapping is caused by regions of dense soot, located between the laser plane and the measuring device (e.g. CCD camera, spectrometer), and can potentially cause considerable attenuation of the LII signal intensity. Although LII signal trapping is believed to result in significant reductions in signal intensity, very few researchers have tried to quantify or correct its effects. Figure 6-15 illustrates this effect for a spherical soot cloud. Estimation of the extent of signal trapping performed by Wainner (1999) on laminar flames suggest that measured LII signals could be underestimated by as much as 45%.

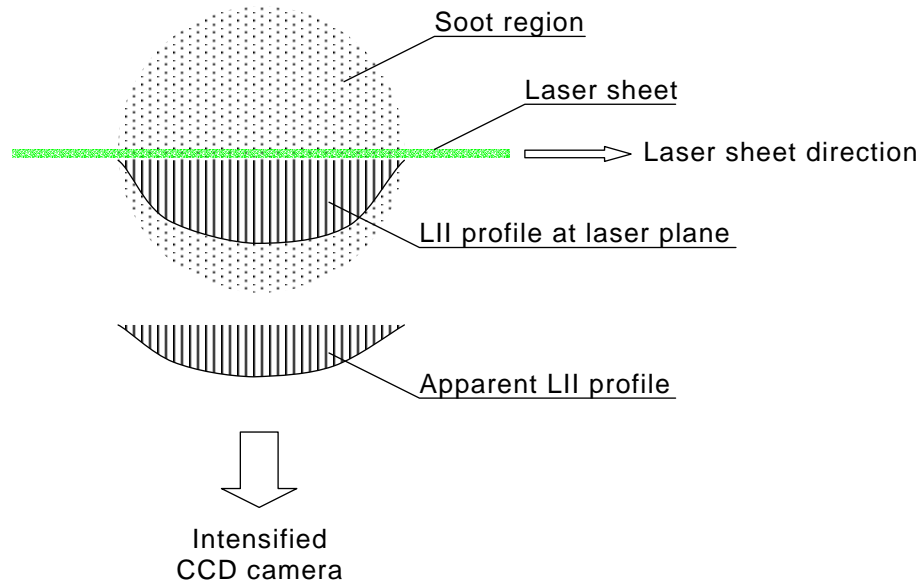


Figure 6-15. Illustration of LII signal trapping by soot.

Inagaki *et al.* (1999) proposed a set of equations that could be used for post-processing LII signals. They calibrated their method on a laminar flame and applied the results to LII images taken from a DI diesel engine. It should be noted that since the soot distributions for a laminar flame and a swirled diesel spray are unlikely to be similar, the validity of such calibration is questionable. Furthermore, signal correction requires accurate knowledge of the three-dimensional soot distribution within the cylinder, both in terms of soot volume fraction and soot diameter. It is not clear how Inagaki *et al.* (1999) fulfilled these requirements. This limitation certainly cast doubt on the validity of any quantitative measurements obtained with the LII technique (including simultaneous LII / LIS) for turbulent flames. However, when used qualitatively, LII images still supply highly valuable information on timing and location of soot formation sites. Potentially, this technique can provide high-resolution data, both temporally and spatially, and has proven invaluable for improving the understanding of combustion processes in diesel engines.

6.3.5.5. Overall accuracy

The overall accuracy with which LII images are recorded is a complex function of the error introduced by every single element in the acquisition chain. Most laser-based measurement techniques are sensitive to contamination by molecular emission and scattering. Generally, such contaminations are not readily apparent from recorded images and can only be ascertained by using a spectrometer. Fortunately, several comprehensive theoretical and applicability studies on LII were reported, and the potential contaminations have been evaluated. These include fluorescence from C_2 , C_3 and PAHs, that can be easily avoided by spectral filtering. Inaccuracies caused by laser energy fluctuations, laser extinction and LII signal trapping by soot are predominantly related to the experimental set-up and need to be assessed independently.

It was observed that the time at which the LII images were recorded was accurate within 3%. The error caused by contaminations and particle size dependence for the LII data presented here was estimated to be less than 6% (Table 6-1). Since this value represents the proportion of spurious emissions within the LII images it can be concluded that it represents the overall measurement error, and consequently, 94% of the recorded intensities originated from incandescence of soot particles. Signal trapping by soot, window fouling and laser energy fluctuations can be seen as attenuations, rather than contaminations, of the LII intensity. Although their effects must be accounted for if quantitative data is required, they need not be accurately assessed for qualitative observations as long as they are not ignored altogether. In the present study laser energy fluctuations were found to affect the LII signal intensity by less than 3%, window fouling resulted in less than 20% attenuation, and LII signal trapping by soot was not quantified but was expected to be moderated by the use of the low-sooting fuel. A summary of the most important sources of error for LII measurement is presented in Table 6-1.

Possible cause of error	Error magnitude	Assessment method
Attenuation of laser intensity across soot region	Not detected	Measured ¹
Attenuation of laser intensity by window fouling	< 20%	Measured ²
Attenuation of LII signal by window fouling	< 10%	Measured ²
Contamination from C ₂ fluorescence	< 1.2%	Literature ³
Contamination from C ₃ fluorescence	Not detected	Literature ⁴
Contamination from CCD background noise	< 1%	Measured ⁵
Contamination from elastic scattering (532 nm)	Not detected	Measured ⁶
Contamination from flame luminosity	Not detected	Measured ⁷
Contamination from PAH fluorescence	Not detected	Literature ⁸
Contamination from photomultiplier background noise	Not detected	Measured ⁹
Data set size limitation	< 1.7%	Estimated ¹⁰
Laser pulse energy fluctuations	≈1.9% (< 3%)	Calculated ¹¹
Soot particle size beyond Rayleigh limit	0%	Literature ¹²
Soot particle size dependence of LII signal	< 4%	Literature ¹³
Time of image acquisition jitter	< 3%	Measured
Trapping of LII signal by dense soot region	Not quantified ¹⁴	

Table 6-1. Summary of the measurement errors for LII.

- ¹ Attenuation of laser is unmistakably apparent when it occurs, since it results in an abruptly interrupted image. Such images were not observed with the low-sooting fuel.
- ² Assuming windows are cleaned daily.
- ³ For a laser fluence less than 2 J cm^{-2} at 532 nm in $416 \pm 32 \text{ nm}$ bandwidth (Wainner, 1999).
- ⁴ See Wainner (1999).
- ⁵ Assuming CCD background noise subtraction, noise = 1 count and minimum LII signal is 100 counts.
- ⁶ Scattering off a non-combusting liquid spray was not detected.
- ⁷ No signals other than background noise were observed while the laser was temporarily switched off, suggesting that all signals recorded were laser-induced.
- ⁸ PAH fluorescence is only significant for UV excitation wavelengths, not 532 nm (Wainner, 1999).
- ⁹ No background noise from the image intensifier was observed for gains below 850. All acquisitions were performed with a gain of 70.
- ¹⁰ For data set sizes between 27 and 30 images (see discussion in Section 6.3.4).
- ¹¹ Calculated for Gaussian laser beam profile with fluence between 20 and 80 MW cm^{-2} (see Figure 6-14).
- ¹² Rayleigh limit = $\lambda_{\text{Laser}} / \pi = 169 \text{ nm}$. Soot particle diameters are from 30 to 50 nm (Kennedy, 1997; Kittelson, 1998)
- ¹³ Estimated from Ni *et al.* (1995) for an effective LII exposure time of 25 ns.
- ¹⁴ Cannot be reliably quantified for a turbulent flame.

6.4. Experimental results

The effects of in-cylinder and fuel pressures are reported in Sections 6.4.1 and 6.4.2, respectively. In Section 6.4.3 a LII sequence obtained with a high temporal resolution is presented.

The exact conditions for each data set presented in this chapter can be found in Appendix C. In order to provide a factual examination of the performance of the injection equipment used, correction based upon the nozzle opening delays mentioned in Section 3.3.2 (see Table 3-3) were not applied. Consequently, unless otherwise stated, all timings quoted in this section are relative to the start of the injection pulse. All data presented were obtained with a single-hole single guided VCO type nozzle, with an orifice diameter of 0.2 mm. All LII images correspond to a field of view approximately 30 mm in width and 65 mm in height.

6.4.1. Influence of in-cylinder pressure

Figures 6-16, 6-17 and 6-18 show LII intensity profiles for injection pressures of 100, 140 and 160 MPa, respectively, and a range of in-cylinder pressures. The effective nozzle opening durations are represented as solid black lines on the upper parts of each chart. They were obtained beforehand with a high-speed video camera pointed at the nozzle orifice, with a frame rate of 27000 images per second. The uncertainty on the times of opening and closing of the orifice is 1 frame, corresponding to less than 0.04 ms (i.e. 0.12 CA).

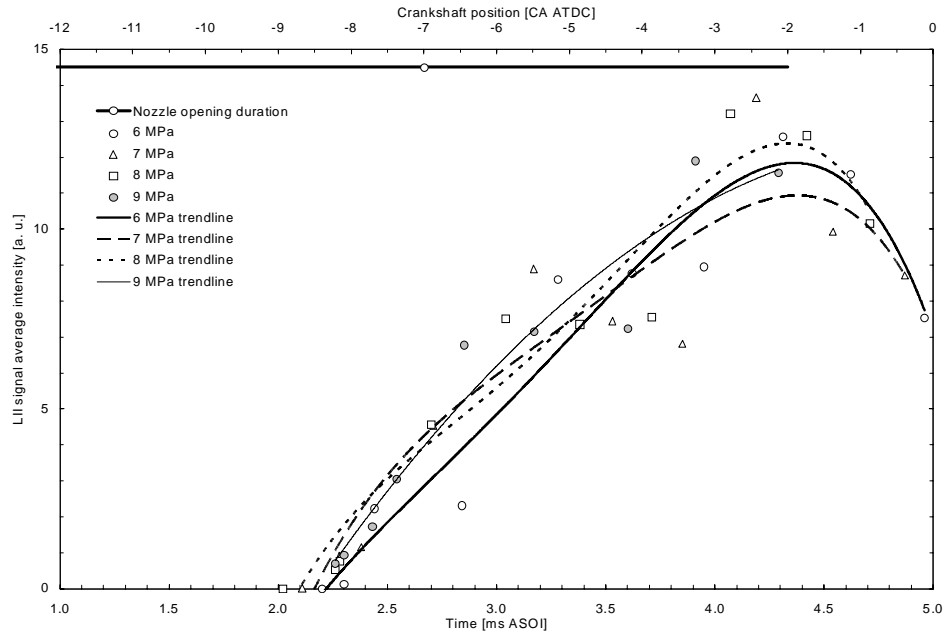


Figure 6-16. LII signal intensity profiles for an injection pressure of 100 MPa and a range of in-cylinder pressures (6, 7, 8 and 9 MPa at non-fired TDC). Each data point represents the average intensity of at least 27 images. Times are relative to start of injection pulse.

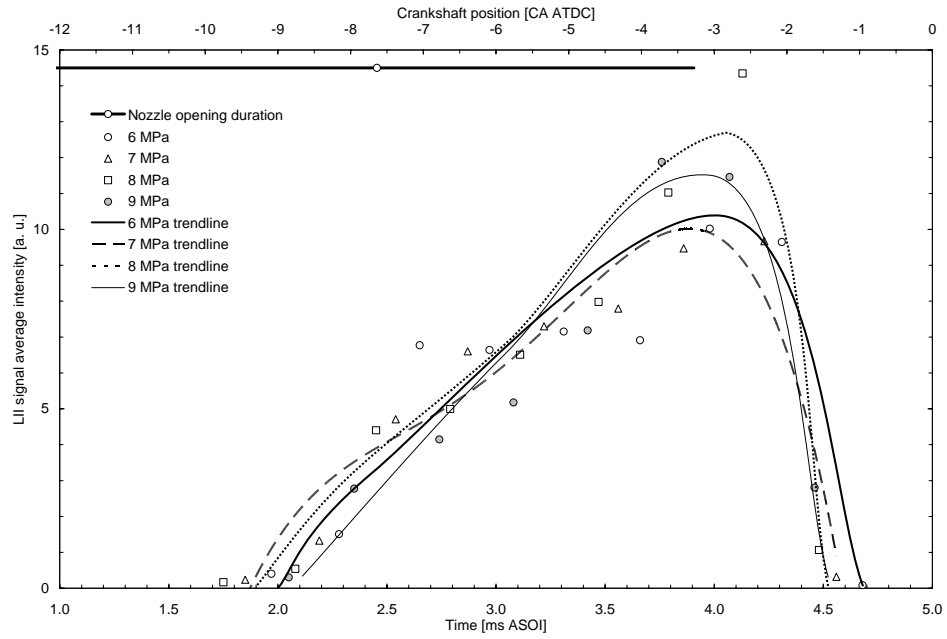


Figure 6-17. As Figure 6-16 but for an injection pressure of 140 MPa.

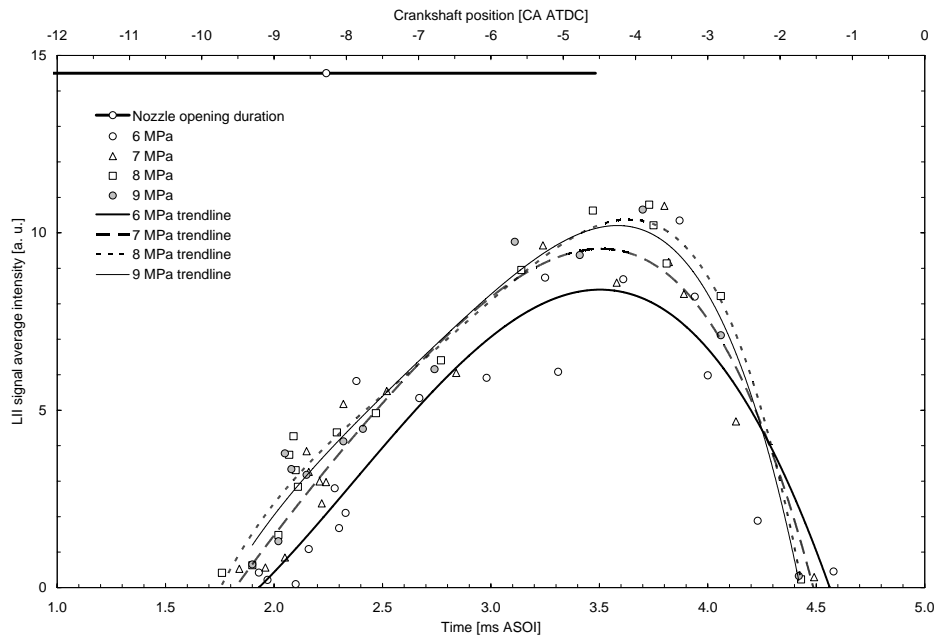


Figure 6-18. As Figure 6-16 but for an injection pressure of 160 MPa.

It can be observed for all profiles that the time at which the LII signal was first detected appears to be independent of in-cylinder pressure. Since the ignition delay is strongly dependent on in-cylinder pressure (see Chapter 5), it is concluded that the formation of the first soot particles is not related to the

appearance of a flame. This supports the fact that soot production starts during the initial high-temperature pyrolysis of fuel droplets (Kennedy, 1997).

For all conditions, LII profiles exhibit an almost linear increase in intensity before reaching a peak value. The actual amplitude of the peak, and the time at which the maximum intensity was reached, both appear to be unaffected by in-cylinder pressure. It can be observed from Figures 6-16 to 6-18 that the LII signal intensity peaks are strongly related to the instant at which the last fuel droplets were seen leaving the nozzle orifice. These observations appear to substantiate the speculations of Flynn *et al.* (1999) that the end of production of soot precursors coincides with the end of injection. The swift LII signal intensity decay that follows is believed to correspond to the oxidation of the soot particles at the diffusion flame sheath. The decline in soot concentration across the diffusion flame sheath is clearly apparent when comparing the extent of signals from high-speed video recordings of flame and LII images of soot (Figure 6-19). In the images presented in Figure 6-19, the location of the soot agrees with the model of Dec (1997), although some discrepancies regarding the apparent shape of the diffusion flame were observed in the region near the tip of the liquid fuel spray.

It can be concluded from the observation of Figures 6-16 to 6-18, that changes in in-cylinder pressure did not markedly affected the amount of soot produced during combustion.

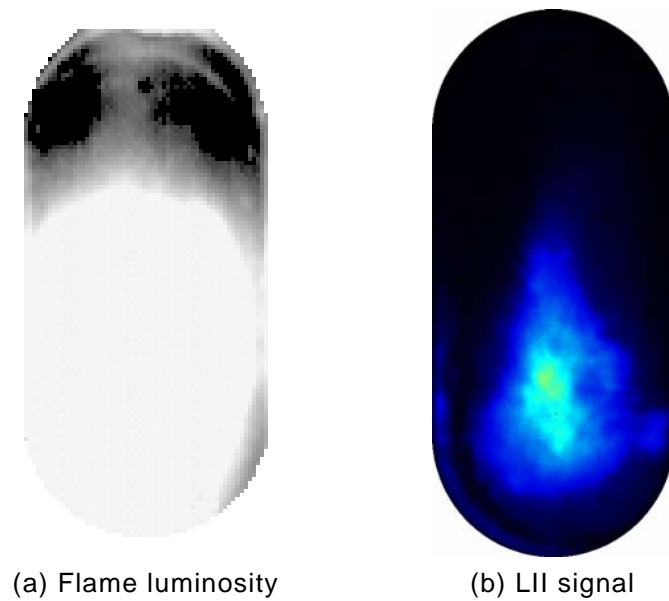


Figure 6-19. Comparison between flame luminosity from high-speed video (a) and ensemble averaged soot incandescence (b) for an injection pressure of 160 MPa, ICP of 8.0 MPa at non-fired TDC, 3.1 ms ASOI.

Examples of ensemble averaged images showing the influence of in-cylinder pressure on early soot formation are shown in Figures 6-20 to 6-22. From the images presented in Figure 6-20 it can be seen that for a 6 MPa in-cylinder pressure the average liquid fuel penetration length was 28 mm, and soot was found approximately 15 mm below the tip of the spray. The initial soot formation regions spread over a height of 15 to 25 mm. It appears that the distance between the spray tip and the initial soot formation zone remained relatively constant at 15 mm for most conditions, although a slightly shorter distance (≈ 12 mm) was observed for the highest injection pressure.

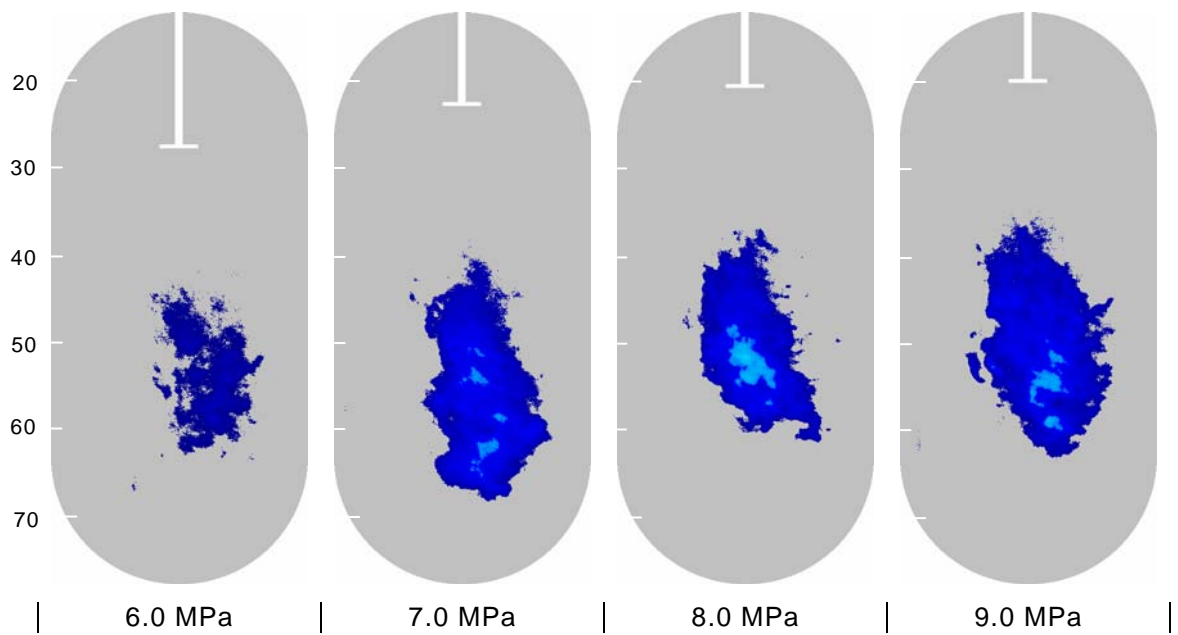


Figure 6-20. Ensemble averaged images showing the influence of ICP on initial soot formation sites. Images were recorded 2.3 ms ASOI, for an injection pressure of 100 MPa. ICPs were measured at non-fired TDC. Contrast was enhanced for clarity, white lines show ensemble averaged liquid fuel penetration obtained by simultaneous LIS, scales indicate distances from the nozzle in millimetres.

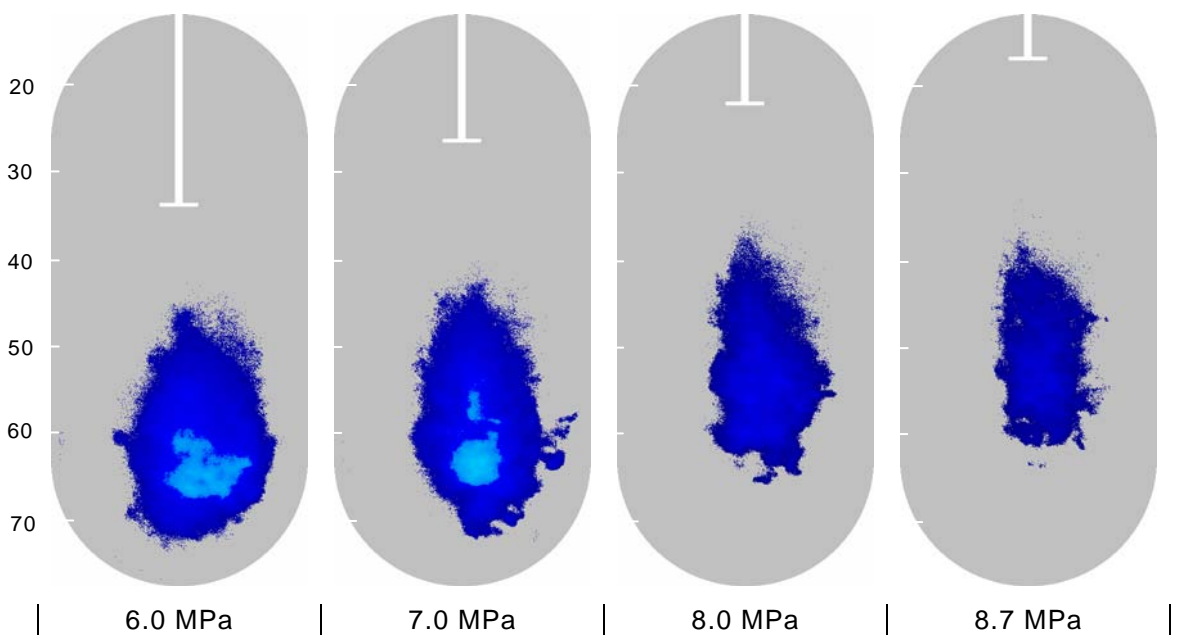


Figure 6-21. As Figure 6-20 but for an injection pressure of 140 MPa. Images were recorded between 2.1 and 2.3 ms ASOI.

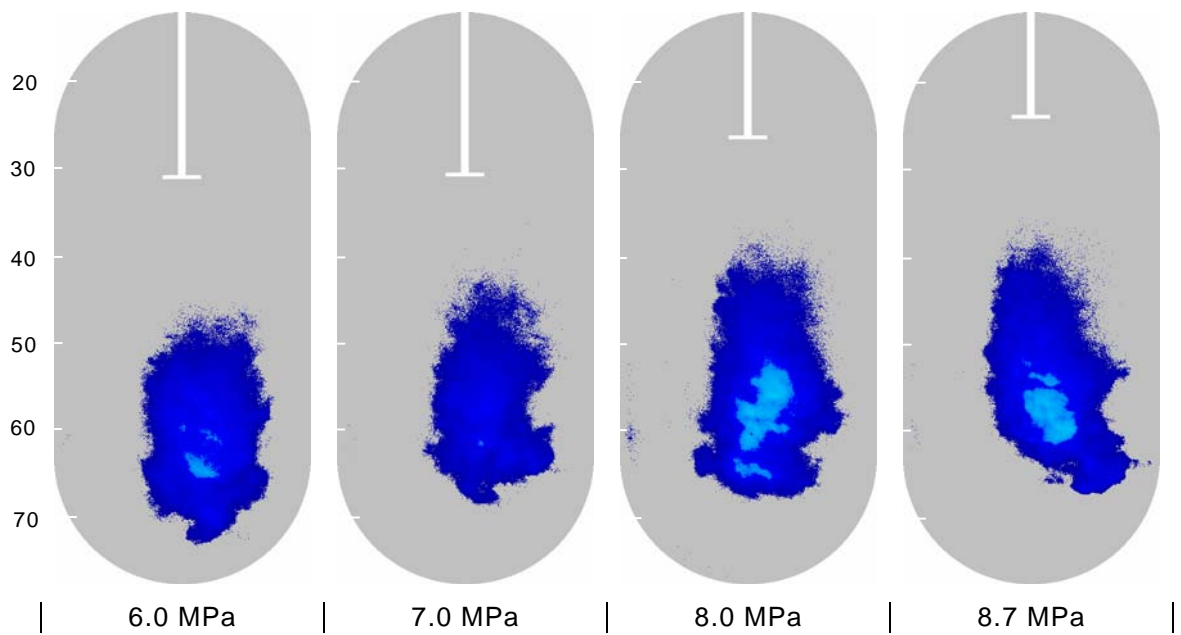


Figure 6-22. As Figure 6-20 but for an injection pressure of 160 MPa. Images were recorded between 2.0 and 2.2 ms ASOI.

While Figures 6-20 to 6-22 provide information on the average location of soot and liquid fuel for a large number of cycles, individual LII images can give additional evidence on the structure of soot regions within the flame. In Figure 6-23, instantaneous images obtained for early (2.2 ms ASOI) and late (3.9 ms ASOI) soot formation are presented. Simultaneous LIS measurement of liquid fuel is shown for the image recorded at 2.2 ms ASOI. As the injection ended at 3.6 ms, no liquid fuel was observed at 3.9 ms. The occurrence of fuel slugs, previously mentioned in Section 4.3, and the clustered distribution of dense soot regions are apparent in Figure 6-23. Although spray vaporisation and soot formation have been described as progressive and continuous processes (Dec, 1997; Flynn *et al.*, 1999), LII images of diesel sprays in the literature (Dec *et al.*, 1992; Kosaka *et al.*, 1995; Dec, 1997; Bruneaux *et al.*, 1999; Inagaki *et al.*, 1999; Greis *et al.*, 2002) clearly show clustered distributions similar to those presented here. It is expected that such detachments of groups of droplets should favour soot agglomeration and be strongly detrimental to soot oxidation because of the associated local depletion of oxygen.

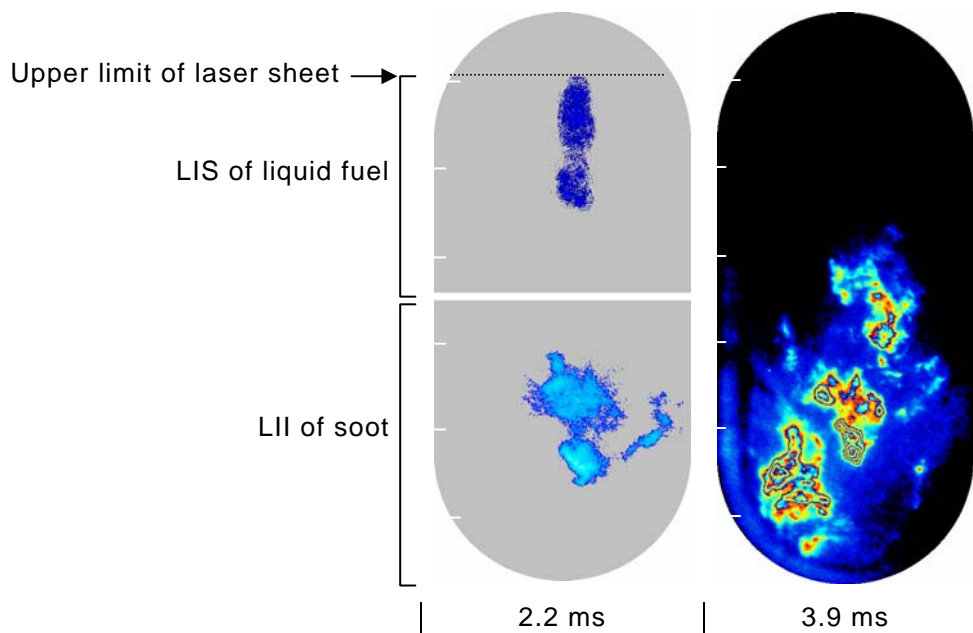


Figure 6-23. Examples of liquid and soot clusters for early and late soot formation. 160 MPa injection pressure, 6.0 MPa ICP at TDC, times are relative to start of injection pulse. Contrast of images recorded at 2.2 ms showing simultaneous LIS (upper half) and LII (lower half) was enhanced for clarity.

Examples of ensemble averaged images showing the influence of in-cylinder pressure on late soot formation are shown in Figures 6-24 to 6-26. Unlike the initial soot formation zones, soot regions at later times are unaffected by in-cylinder pressure. The location, dimension and intensity of the dense soot regions were not appreciably altered by changes in pressure from 6 to 9 MPa.

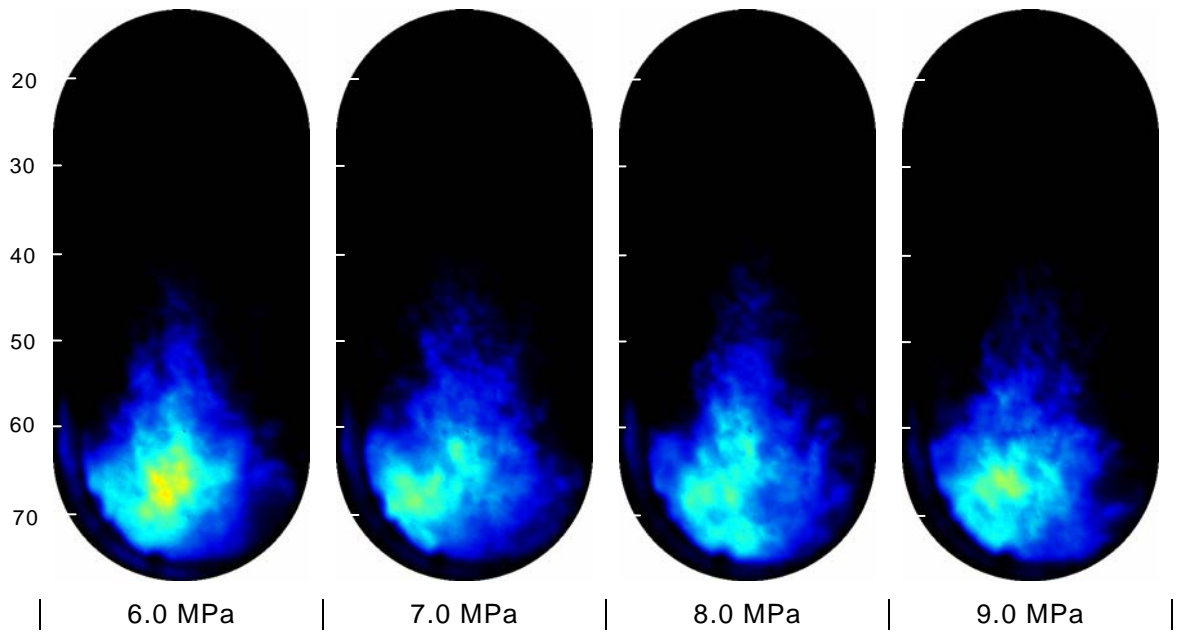


Figure 6-24. Ensemble averaged images showing the effect of ICP on late soot concentration zones. Images were recorded between 3.5 and 3.7 ms ASOI, for an injection pressure of 100 MPa. ICPs were measured at non-fired TDC.

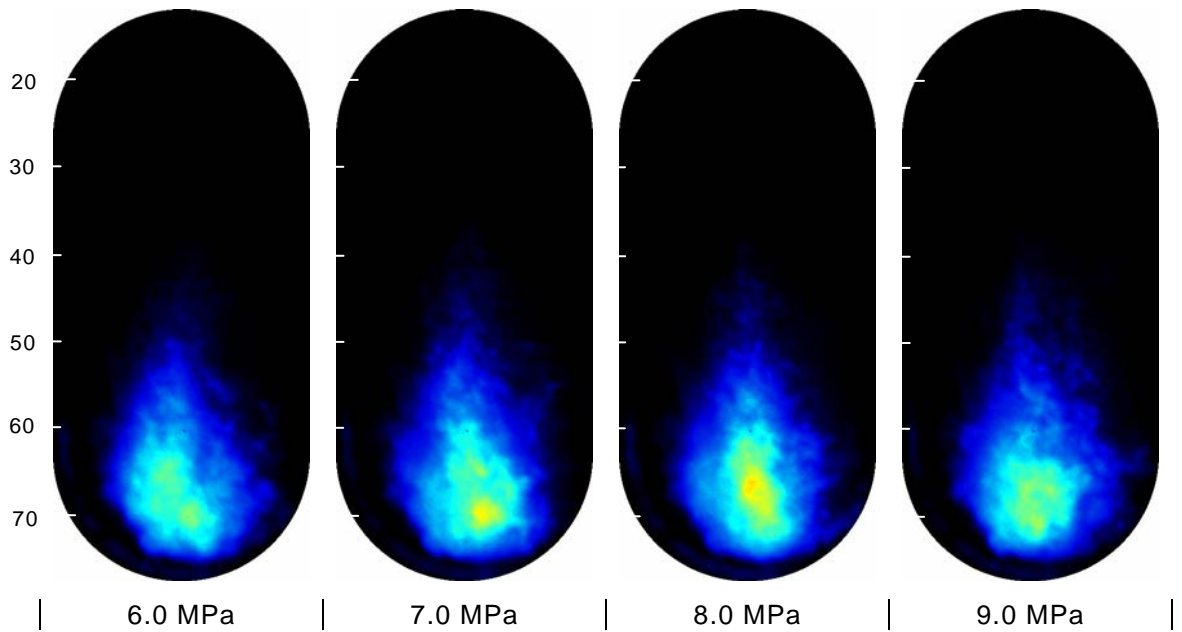


Figure 6-25. As Figure 6-24 but for an injection pressure of 140 MPa. Images were recorded between 3.4 and 3.7 ms ASOI.

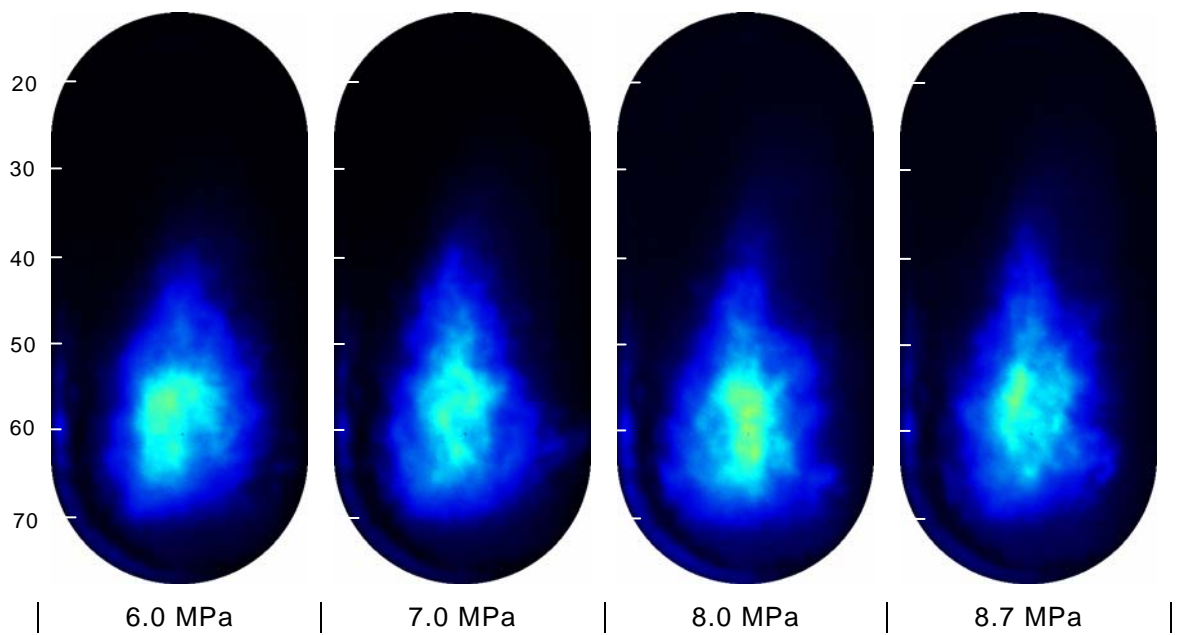


Figure 6-26. As Figure 6-24 but for an injection pressure of 160 MPa. Images were recorded between 3.4 and 3.6 ms ASOI.

6.4.2. Influence of injection pressure

Figures 6-27 to 6-30 show LII intensity profiles for in-cylinder pressures of 6, 7, 8 and 9 MPa, respectively, and a range of injection pressures.

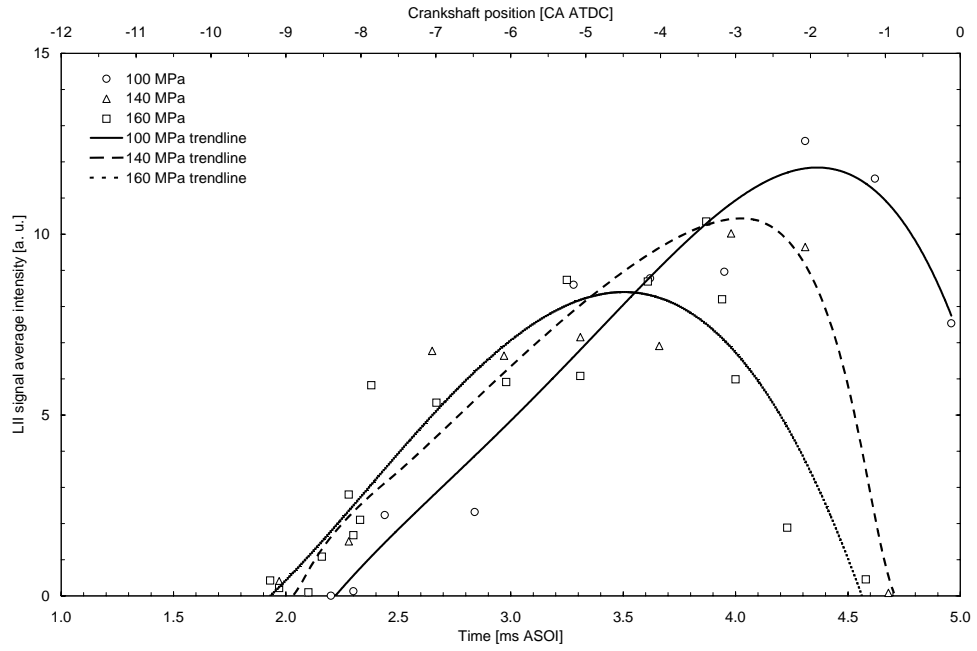


Figure 6-27. LII signal intensity profiles for an in-cylinder pressure of 6 MPa at non-fired TDC and a range of injection pressures (100, 140 and 160 MPa at non-fired TDC). Each data point represents the average intensity of at least 27 images. Times are relative to the start of the injection pulse.

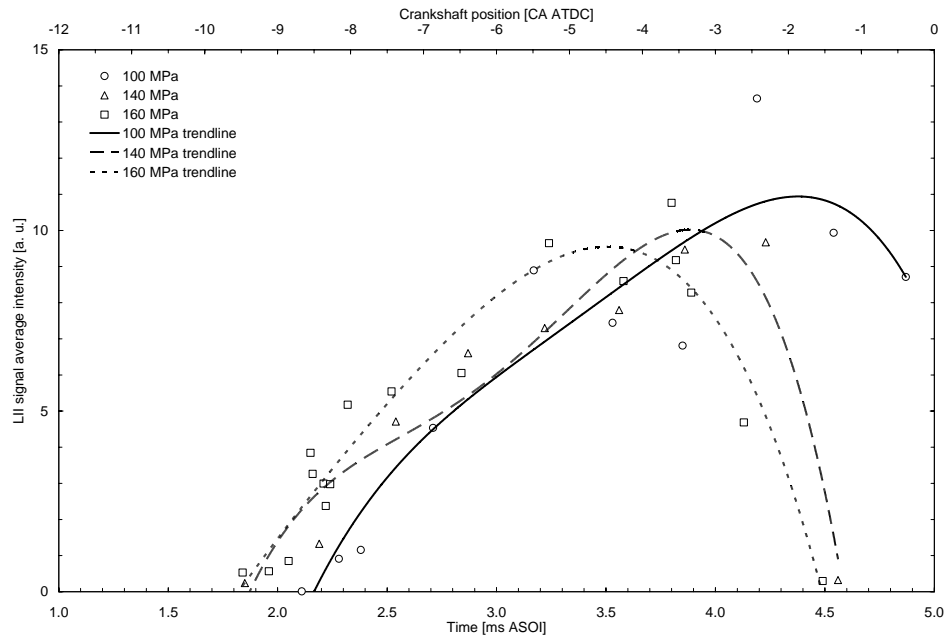


Figure 6-28. As Figure 6-27 but for an in-cylinder pressure of 7 MPa.

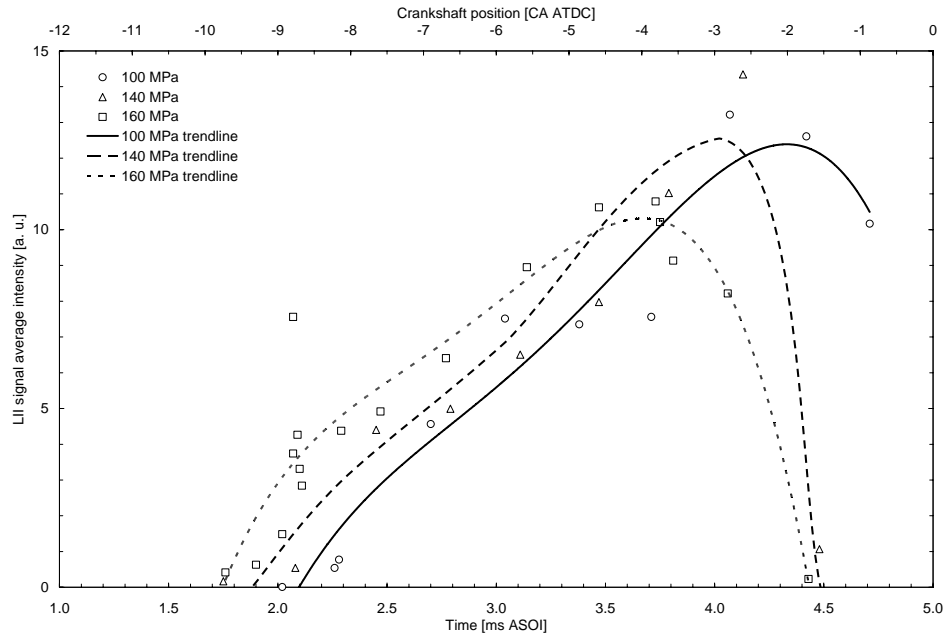


Figure 6-29. As Figure 6-27 but for an in-cylinder pressure of 8 MPa.

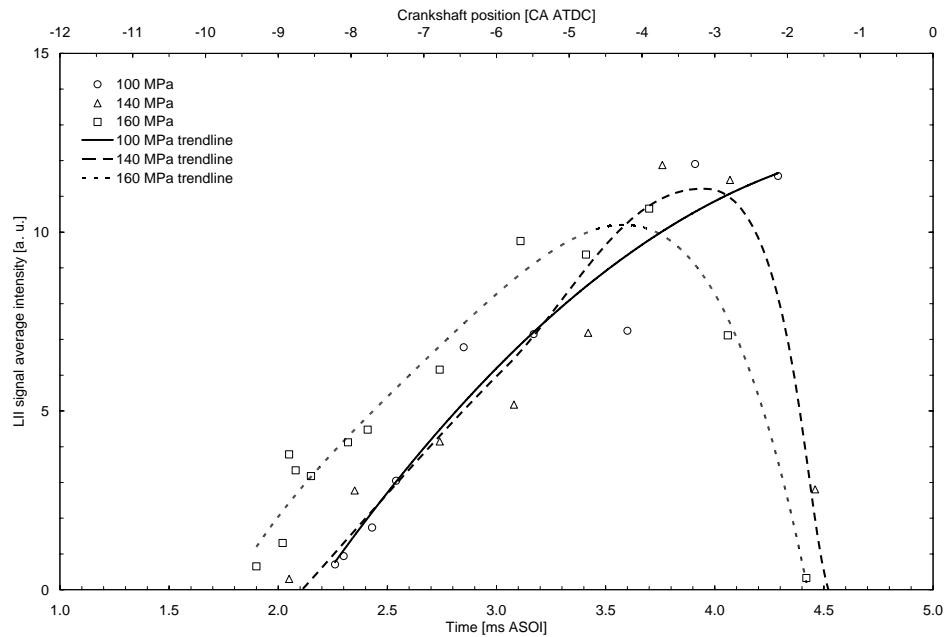


Figure 6-30. As Figure 6-27 but for an in-cylinder pressure of 9 MPa.

In all instances the first appearance of LII signal seems to occur slightly earlier for the higher injection pressure cases (140 and 160 MPa). It is interesting to consider that higher injection pressures result in increased injection rates, and therefore at any given time larger proportions of fuel will be undergoing

pyrolysis than for lower injection pressures. Consequently, it would seem reasonable to expect soot formation to initiate earlier for the higher injection pressure cases.

As discussed in Section 6.4.1, a rise in LII signal intensity was observed for the duration of the fuel injection period. It is apparent from Figures 6-27 to 6-30 that the rate at which the LII signal rises does not seem to be significantly affected by injection pressure. Since the maximum amount of soot that can be produced is directly related to the amount of injected fuel, and higher injection pressures result in higher injection rates, it is expected that an increase in injection pressure should be associated with an increased soot production rate. Although an increase in injection pressure from 100 to 160 MPa results in a 24% increase in injection rate (see Figure 6-31), it is not clear whether a corresponding increase in soot production rate would be perceptible in Figures 6-27 to 6-30.

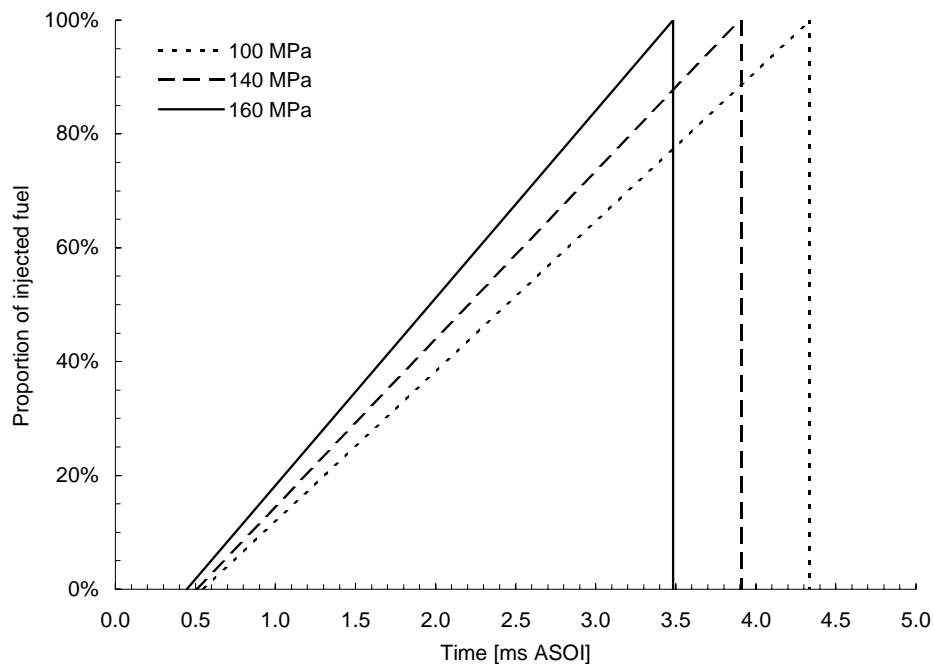


Figure 6-31. Estimated proportion of injected fuel with time for a 30 mm^3 injection at three injection pressures (100, 140 and 160 MPa), assuming full needle lift (this takes place for at least 85% of the injection duration).

Following the rise in LII intensity observed in Figures 6-27 to 6-30, maximums are reached at the end of injections (see discussion in Section 6.4.1), with values that are dependent on fuel pressure. At the highest injection pressure the lowest peaks in LII signal intensity for all in-cylinder pressures were observed.

Figure 6-32 shows the LII signal intensity profiles and flame luminosity durations for an in-cylinder pressure of 6 MPa. As follows from this figure, higher injection pressures produced smaller quantities of soot. This can be explained by the fact that higher injection pressures are generally believed to promote the production of smaller fuel droplets (Di Giorgio *et al.*, 1995) which should, in turn, result in the formation of smaller soot particles that should be more rapidly oxidised. Higher injection pressures also result in longer spray penetration lengths and higher liquid core propagation velocities. Consequently, the transfer of momentum from the liquid spray to the gas phase should be enhanced, improving the mixing of the two phases. Since a better mixing quality corresponds to an increase in the local oxygen content, it is expected that oxidation of soot should be improved. The effects of momentum transfer are expected to be particularly important in the present study due to the quiescent nature of the in-cylinder charge prior to injection (i.e. non-swirl flow).

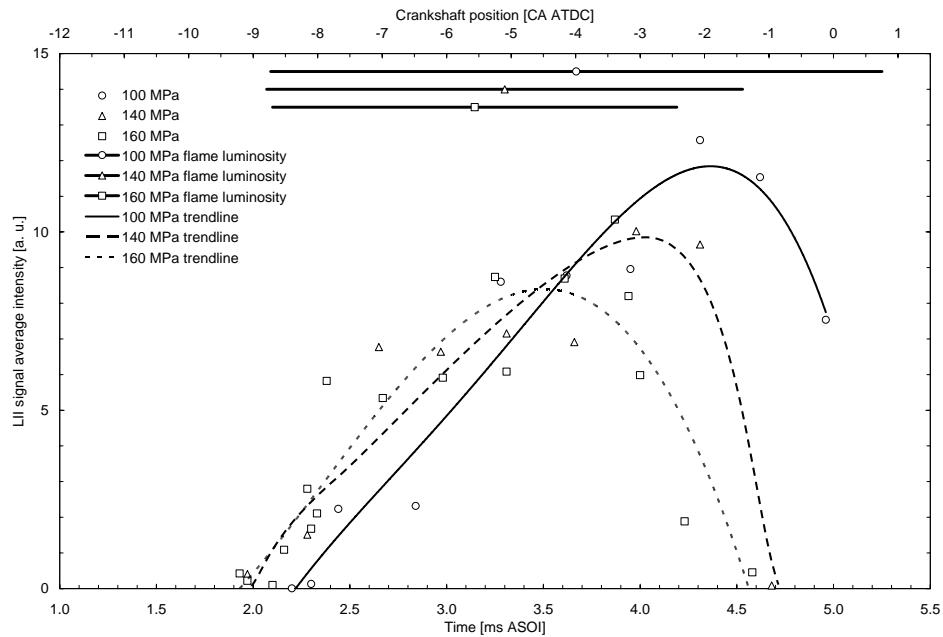


Figure 6-32. As in Figure 6-27 but with the addition of the durations of the flame luminosity (obtained by still ICCD camera, with $1 \mu\text{s}$ exposure).

It can also be seen from Figure 6-32 that flames lasted longer for lower injection pressures. This allowed more time for oxidation at the flame sheath. Since lower fuel pressures are known to result in higher particulate emissions (Bruneaux *et al.*, 1999), it can be concluded that the extended flame duration is not sufficient to oxidise the excess soot production.

An example of ensemble averaged images showing the influence of injection pressure on early soot formation is presented in Figure 6-33, for an in-cylinder pressure of 7 MPa. Although injection pressure has an apparent effect on liquid spray penetration length, the location of the first soot particles detected downstream of the tip of the spray remains almost constant. In Figure 6-33 the distance from the nozzle to the first soot particles is about 40 mm, and an increase in fuel pressure from 100 MPa to 160 MPa induces a shift of less than 3 mm.

Figures similar to Figure 6-33 are shown in Appendix C for a number of other in-cylinder pressures.

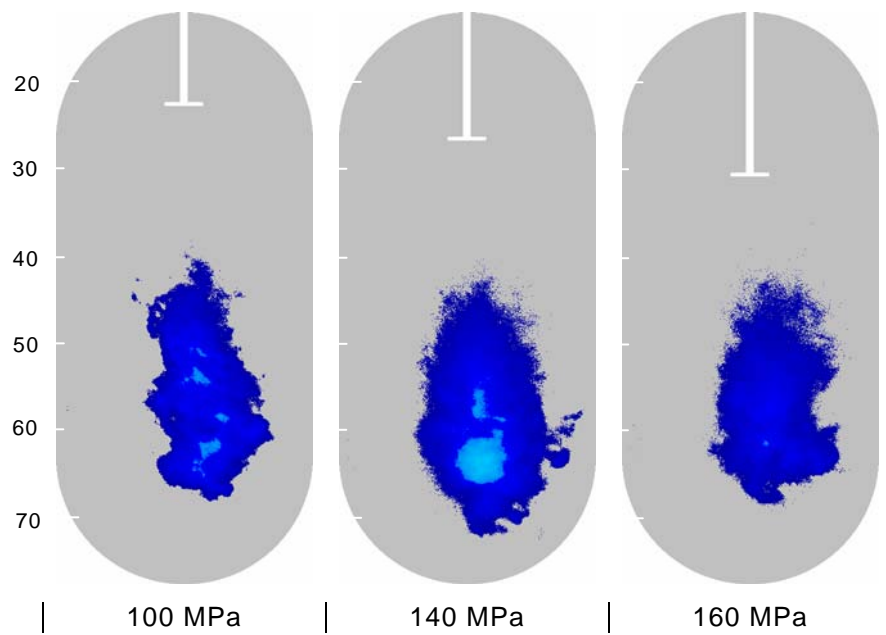


Figure 6-33. Ensemble averaged images showing the effect of injection pressure on initial soot formation sites. Images were recorded between 2.1 and 2.3 ms ASOI, for an ICP of 7.0 MPa at non-fired TDC. Contrast was enhanced for clarity, white lines show liquid fuel penetration measured by simultaneous LIS, scales indicate distances from the nozzle in millimetres.

Figure 6-34 illustrates the effect of fuel pressure on late soot concentration. While the lowest injection pressures appear to result in similar soot regions being formed, the LII image is noticeably different for an injection pressure of 160 MPa. The most striking difference is in the location of the soot region being approximately 10 mm closer to the nozzle orifice. This could be explained by the enhanced vaporisation observed for higher injection pressures (Bruneaux *et al.*, 1999), resulting in faster pyrolysis of the fuel. It is speculated that the formation of soot closer to the nozzle should be beneficial since interactions with the cylinder wall would be reduced.

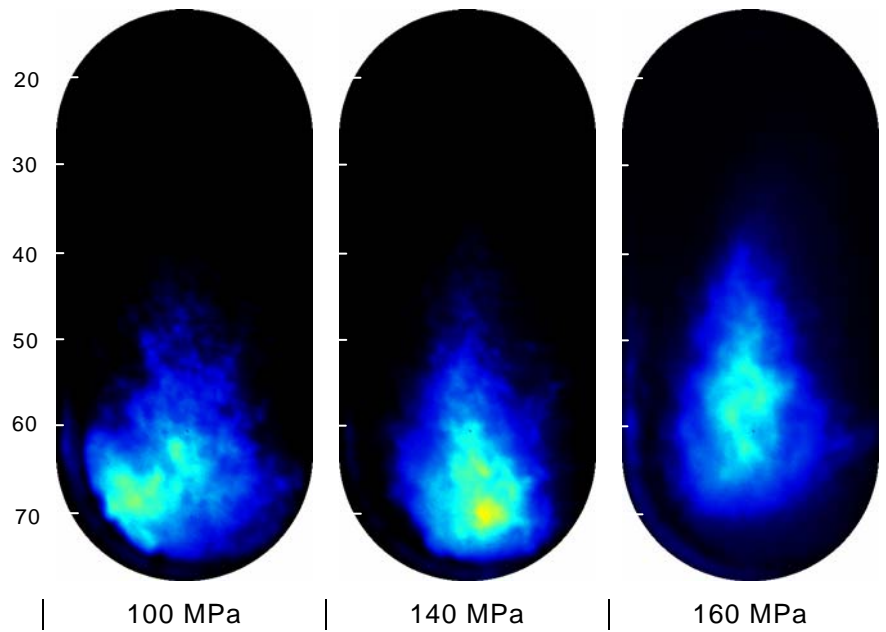


Figure 6-34. Ensemble averaged images showing the influence of injection pressure on late soot concentration zones. Images were recorded between 3.5 and 3.6 ms ASOI, for an ICP of 7.0 MPa at non-fired TDC. Scales indicate distances from the nozzle in millimetres.

It is also apparent from Figure 6-34 that the LII signal has a more homogeneous and less intense appearance for the highest injection pressure, suggesting that the soot mass is more uniformly spread within the flame.

Figures showing similar trends to Figure 6-34 are presented in Appendix C for a number of other in-cylinder pressures.

6.4.3. Detailed LII sequence

For the LII sequences presented thus far, the average time interval between two consecutive data sets was 0.33 ms (1 CA). It was observed that the original appearance of soot is a rapid process and therefore some details may not be apparent at such resolution. In order to obtain a finer series of LII images, the laser system software was automated to record a complete sequence with a data set interval of 50 μ s (0.15 CA). The resulting sequence comprises 55 images, each image being itself the ensemble average of a 30-image data set. The

engine was kept at stable in-cylinder conditions for the whole duration of the recording. These conditions are detailed in Table 6-2.

Fuel	99.96% Esso AF1313 + 0.04% Hitec 4103
Injected fuel quantity	30 mm ³
ICP at non-firing TDC	6 ± 0.2 MPa
Injection angle	-15 CA
Injection pressure	160 MPa
Intake temperature	373 ± 6 K
Nozzle type	VCO 1x0.2 mm hole

Table 6-2. Engine conditions for detailed LII sequence.

The sequence is shown in Figure 6-35 and the exact conditions for each image can be found in Appendix C. It can be seen that soot formation initiates a short distance below the liquid spray tip, approximately 2 ms after the start of injection pulse (1.7 ms after start of needle lift).

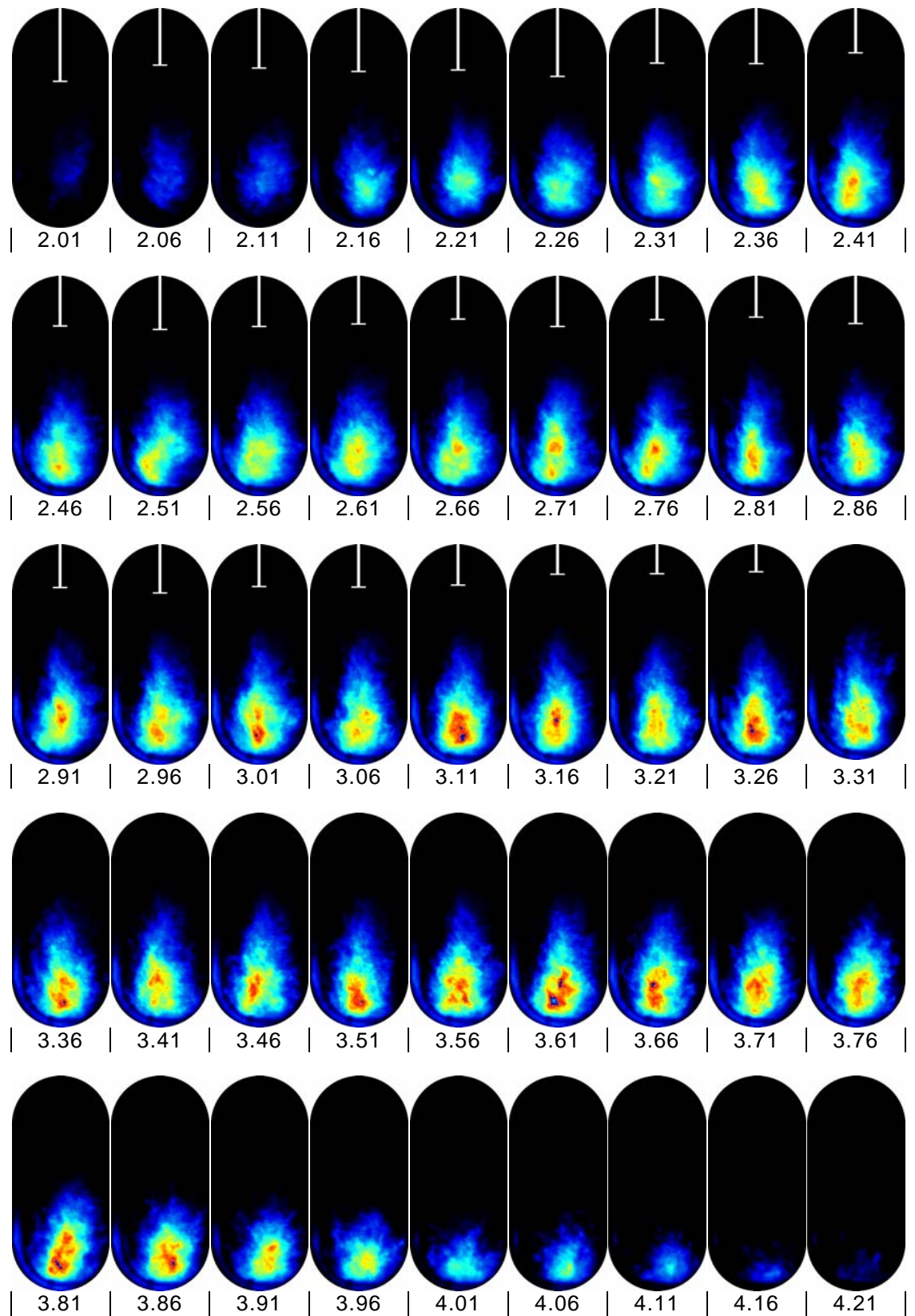


Figure 6-35. Detailed LII sequence for a 0.2 mm VCO nozzle with a 160 MPa injection pressure, 6.0 MPa ICP, and 720 K calculated temperature at TDC. Times are in milliseconds ASOI. White lines indicate liquid fuel penetration measured by simultaneous LIS.

This sequence is also presented in graphical form in Figure 6-36, where each data point is the mean intensity of its corresponding image from Figure 6-35.

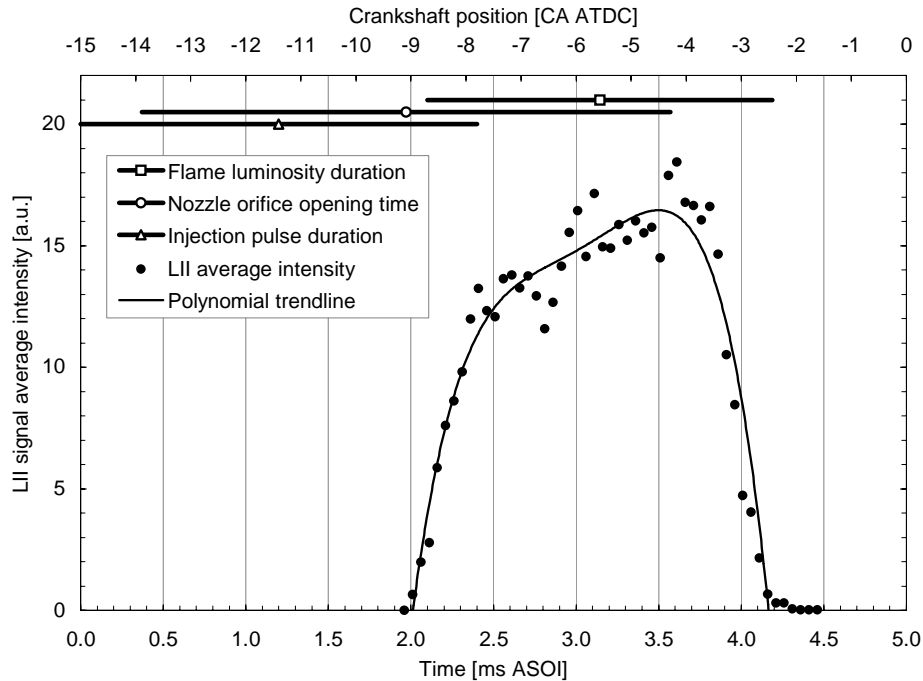


Figure 6-36. Signal intensity profile for the LII sequence presented in Figure 6-35. Durations for injection pulse, nozzle opening and flame luminosity are indicated.

Comparing Figure 6-36 with the previous LII profiles (Figures 6-16 to 6-18), one can see that a finer temporal resolution produced a clearer representation of the phases of soot production. The LII signal intensity profile presented in Figure 6-36 shows that three stages of soot production took place. The first stage is a rapid rise in LII signal that lasted for approximately 0.4 ms, corresponding to elevated soot production rates and low oxidation. An increase in flame luminosity was detected shortly after the first appearance of the LII signal. The diffusion flame, however, was established between 0.2 to 0.3 ms after the autoignition time as can be observed from the autoignition high-speed video shown in Section 5.4.1. This leads to establishment of the diffusion flame at a time between 2.3 and 2.4 ms in Figure 6-36. Then the second stage in soot formation can be distinguished. At this stage higher soot oxidation rates and significantly more fluctuations in soot production are found. This slower soot

production phase can be explained by the formation of soot from the ongoing injection, and the concurrent oxidation at the diffusion flame sheath. A typical example of a data set recorded during this stage is shown in Appendix C, and processed in Section 6.3.4. The third and final phase of soot formation is linked with the end of injection. It is recognised as a sudden decline in soot mass concentrations. While little soot is formed, the oxidation rates at the flame sheath are still high, resulting in a rapid fall in soot concentration.

A combined view of the data obtained by in-cylinder pressure measurements, high-speed video of liquid and vapour fuel spray, and LII is shown in Figure 6-37, for a 160 MPa injection pressure injection and 6 MPa gas pressure.

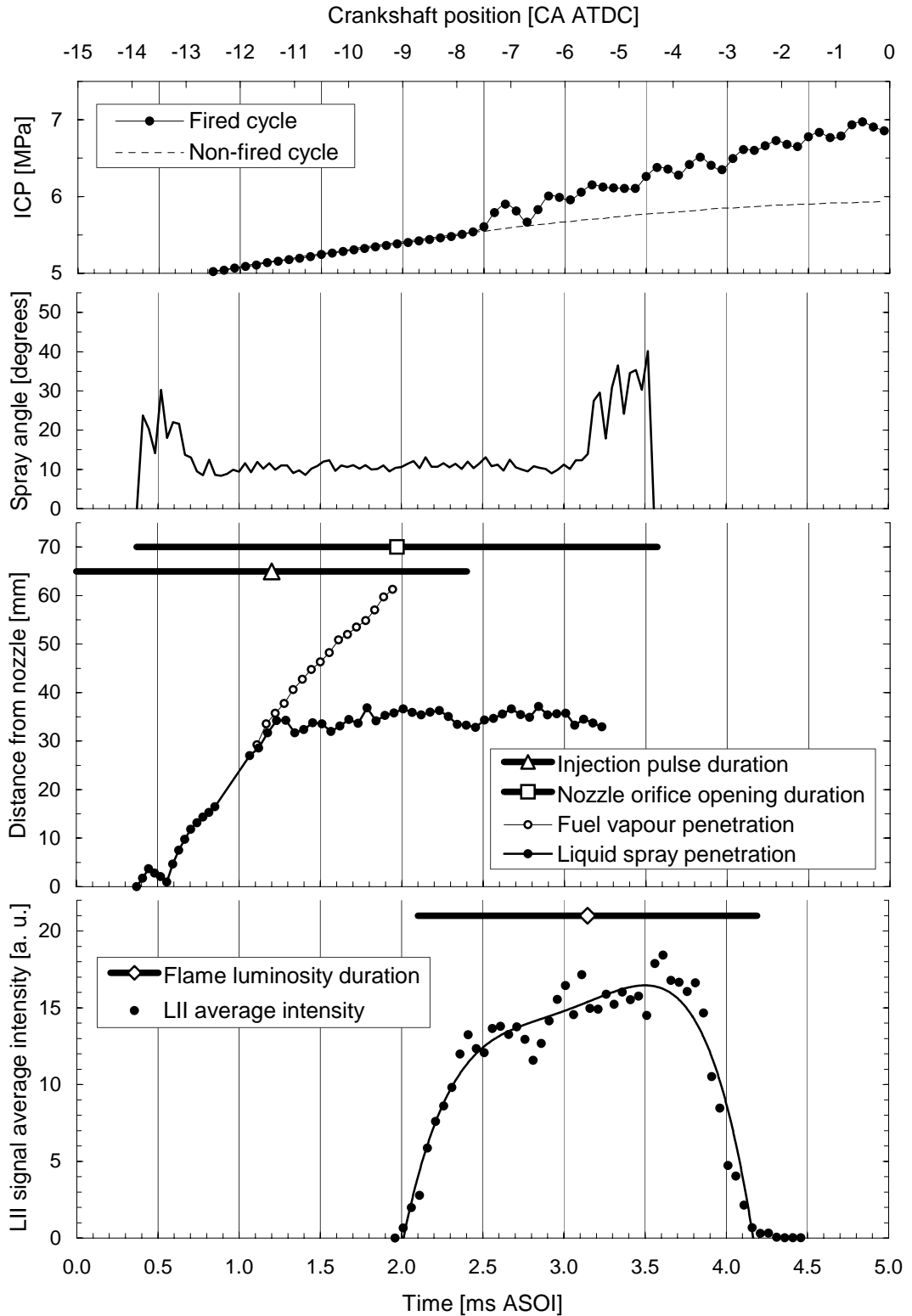


Figure 6-37. From top to bottom: in-cylinder pressure traces, spray dispersion full cone angle, fuel liquid and vapour penetrations and injection pulse width, LII of soot signal with flame luminosity duration. 160 MPa injection pressure, 6 MPa ICP, 0.2 mm VCO nozzle. Times are relative to start of injection pulse.

6.5. Conclusions of Chapter 6

By acquiring data sets of LII images throughout the soot formation periods for a range of elevated injection and fuel pressures, net soot mass production profiles were obtained for an extensive range of conditions. The conclusions drawn from the analysis of the simultaneous LII/LIS data are summarised below:

- Although high cycle-to-cycle variations in soot production were observed, the LII signal intensities were found to converge to a constant value when averaging of sufficient cycles was performed.
- The suggestion made by Flynn *et al.* (1999) that the end of production of soot precursors coincides with the end of injection was corroborated by the results presented in this chapter.
- From the analysis of the LII intensity profiles it appeared that the amount of soot produced during combustion was not noticeably affected by a change in in-cylinder pressure.
- Clustered distributions of soot were observed, similar to previously reported images although conflicting with the common approximation that soot is found evenly across the flame. It has been suggested that slugs of fuel detaching from the bulk of the liquid spray favoured soot agglomeration and inhibited soot oxidation due to the associated local depletion of oxygen. The formation of the slugs of fuel was linked to oscillations of the injector needle in the vertical direction. It is therefore suggested that a better control of the needle lift could result in a more continuous mixing between the liquid fuel and the ambient gas, ultimately leading to lower soot production.
- The combination of high-speed video recordings of flame and LII images of soot revealed a strong reduction in soot concentration across the diffusion flame sheath, confirming that oxidation rates at the flame sheath are high.
- At the highest injection pressure used in this work (160 MPa) lower soot production and more homogeneous soot mass distribution within the flames was observed, for all in-cylinder pressures cases. These effects have been related to smaller fuel droplets and better mixing quality, leading to smaller soot particles and improved oxidation, respectively.

- Although the diffusion flames produced with lower injection pressure lasted longer, it appeared that the extended oxidation time was not sufficient to oxidise the excess production of soot.
- Soot particles were detected closer to the liquid spray tip at higher injection pressures. This has been related to enhanced vaporisation of the liquid fuel. It is speculated that the formation of soot closer to the nozzle should be beneficial since interactions with the cylinder wall would be reduced.
- The recording of a LII sequence at high temporal resolution has shown that three distinct phases in soot formation could be observed. High soot production rates were observed from the ignition time until the establishment of diffusion flame. Moderate soot formation rates were observed from the start of diffusion flame until the end of injection. High soot oxidation rates were seen from the end of injection.

7. CONCLUSIONS

A high pressure diesel test facility was built at the University of Brighton in collaboration with Ricardo Consulting Engineers. The facility consisted of a rapid compression machine and was able to simulate both current and anticipated in-cylinder conditions of automotive diesel engines, while at the same time allowing good optical access to the diesel spray. The spray cone angle and penetration with time data were obtained from photographic and high-speed video recordings. The effects of droplet evaporation, breakup and air entrainment at the initial stage of spray penetration were studied theoretically. Spray autoignition was investigated using video, in-cylinder pressure, and schlieren recordings. Pseudo three-dimensional visualisation of the autoignition was achieved by simultaneous use of two high-speed video cameras at right angles to each other. The influence of in-cylinder and injection pressures on soot formation sites and relative soot concentration were studied using laser-induced incandescence.

7.1. Diesel spray characterisation

High-speed video recordings of the liquid fuel spray showed that a deflection of the injector needle resulted in a different early stage injection behaviour for the single-hole VCO nozzle when compared to a multi-hole nozzle. This resulted in the addition of a predictable delay at the beginning of the liquid penetration process. Since the subsequent liquid penetration rate was unaffected, it is valid to use a single-hole VCO nozzle and derive effects for the multi-hole if this initial delay is taken into account. The effects of fuel pressure and gas temperature on liquid spray penetration and dispersion were reported for a range of injection and in-cylinder conditions. Oscillations of the injector needle in the vertical direction were observed and are believed to have resulted in oscillations of the liquid fuel spray at 6800 Hz, and ultimately lead to slugs of fuel detaching from the spray.

The vapour penetration profiles were shown to depend on both injection pressure and in-cylinder density. It was suggested that the mechanism for the vapour transport is the gas motion induced by the liquid phase exchanging momentum from the droplets to the gas phase. Increased penetration of the vapour was observed at higher injection pressures and lower gas densities, i.e. when the liquid phase had a higher momentum.

The effects of droplet evaporation, breakup and air entrainment on spray penetration were studied theoretically for Stokes, Allen and Newton flows. The agreement between experimental measurements and the predictions of the model that included bag breakup and air entrainment processes was reasonably good. All models are expected to be valid during up to 0.1 - 0.2 ms after start of injection.

7.2. Autoignition of diesel sprays

The effects of elevated in-cylinder and injection pressures on the autoignition of diesel sprays were studied by combining pseudo three-dimensional video of the flame propagation with previous high-speed video observations of the liquid core and vapour phase. It was observed that the difference in pressure between the fuel and the ambient gas, rather than the in-cylinder pressure alone, affected the mixing quality. Autoignition was found to occur simultaneously at multiple sites within the vapour phase, downstream of the liquid core. For all the conditions tested, the ignition sites were observed to merge rapidly and propagate strictly downstream for the duration of the injection. Only after the injection had stopped, were flames observed to propagate towards the nozzle.

A reversal in the reported autoignition delay trends was observed for all injection pressures tested. Enhanced droplet breakup resulted in decreased autoignition delay times for in-cylinder pressures lower than 7 MPa. The increase of the autoignition delay with ambient pressures higher than 7 MPa is not consistent with current correlations. It was postulated that this was caused by a decrease in spray penetration, decrease of diffusion coefficient and increase in chemical delay.

7.3. Soot formation study

Simultaneous acquisition of LII of soot and LIS of liquid fuel was successfully performed for an extensive range of injection and in-cylinder pressures. The suggestion made by Flynn *et al.* (1999) that the end of production of soot precursors coincides with the end of injection was corroborated by the results presented in this thesis. From the analysis of the LII intensity profiles it appeared that the amount of soot produced during combustion was not noticeably affected by a change in in-cylinder pressure.

Clustered distributions of soot were observed, similar to previously reported images although conflicting with the common assumption that soot is found evenly across the flame. It has been suggested that slugs of fuel detaching from the bulk of the liquid spray favoured soot agglomeration and inhibited soot oxidation due to the associated local depletion of oxygen. The formation of the slugs of fuel was linked to oscillations of the injector needle in the vertical direction. It is therefore suggested that a better control of the needle lift could result in a more continuous mixing between the liquid fuel and the ambient gas, ultimately leading to lower soot production.

The highest injection pressure tested (160 MPa) exhibited lower soot production and more homogeneous soot mass distribution within the flames, for all in-cylinder pressures cases. These effects were related to smaller fuel droplets and better mixing quality, leading to smaller soot particles and improved oxidation, respectively. Soot particles were detected closer to the liquid spray tip at higher injection pressures. This has been related to enhanced vaporisation of the liquid fuel. It is speculated that formation of soot closer to the nozzle should be beneficial since interactions with the cylinder wall would be reduced. Although the diffusion flames produced with lower injection pressure lasted longer, it appeared that the extended oxidation time was not sufficient to oxidise the excess production of soot.

The recording of a LII sequence at high temporal resolution showed that three distinct phases in soot formation could be observed. High soot production rates

were observed from the ignition time until the establishment of diffusion flame. Moderate soot formation rates were observed from the start of diffusion flame until the end of injection. High soot oxidation rates were seen from the end of injection.

7.4. Recommendations for further work

The Proteus test facility was not initially designed to operate with exhaust gas recirculation, therefore the influence of EGR has not been explored. Since the intake air to the Proteus is boosted to up to 8 MPa the EGR would need to be pressurised too, precluding the recirculation of burnt gas from the tailpipe. It is suggested that reducing the skipfiring ratio and altering exhaust back pressure would lead to a lower scavenging efficiency, resulting in a proportion of burnt gases being still present in the cylinder during a subsequent injection. Since the amount of burnt gases cannot be controlled easily, the exact proportion of residual gases would need to be quantified for a range of conditions. This is currently being investigated and if successful it would be possible to repeat the experiments described in this thesis in order to quantify the effects of EGR.

It has been suggested that multiple injections during a single cycle could lead to reduced soot productions. In order to investigate the formation of soot for such injection strategies, a fast piezo injector would be required.

The laser system commissioned for the LII study is also capable of performing LIF of NO molecules. Since the productions of soot and NO_x are closely related, a study of NO-LIF similar to the LII investigation presented here would be useful.

The effects of the observed reversal in autoignition delay trends on emissions and mixing quality are still uncertain. Further work in this direction would be most beneficial. CFD simulation of the autoignition reversal could also help improve the current understanding of the fundamentals of diesel combustion.

It was suggested that a better control of the injector needle oscillations could help reduce the production of soot. More work would be required to assess the exact influence of these oscillations on fuel mixing, soot and NO_x formation.

References

- AGGARWAL, S.K., 1998. A review of spray ignition phenomena: Present status and future research. *Progress in Energy and Combustion Science*, **24**, 565-600.
- AKAGAWA, H., MIYAMOTO, T., HARADA, A., SASAKI, S., SHIMAZAKI, N., HASHIZUME, T., TSUJIMURA, K., 1999. Approaches to solve problems of the premixed lean diesel combustion. *SAE SP-1444*, 19-32, SAE paper no. 1999-01-0183.
- ALIGROT, C., CHAMPOUSSIN, J.-C., GUERASSI, N., CLAUS, G., 1997. A correlative model to predict autoignition delay of diesel fuels. SAE paper no. 970638.
- ANDRESEN, P., BATH, A., GRÖGER, W., LÜLF, H.W., MEIJER, G., TER MEULEN, J.J., 1998. Laser-induced fluorescence with tunable excimer lasers as a possible method for instantaneous temperature field measurements at high pressures. *Applied Optics*, **27**(2), 365-378.
- ARCOUMANIS, C., WHITELAW, J., 2000. Is cavitation important in diesel engine injectors? *Thiesel 2000*, Valencia, Spain, 13-15 September 2000.
- ARIAS-ZUGASTI, M., GARCIA-YBARRA, P.L., CASTILLO, J.L., 1999. Droplet vaporization at critical conditions. Long-time convective-diffusive profiles along the critical isobar. *Physical Review E*, **60**(3), 2930-2941.
- ASTARITA, M., CORCIONE, F.E., VAGLIECO, B.M., VALENTINO, G., 1999. Fuel composition effects on air-fuel mixing and self-ignition in a divided chamber diesel system by optical diagnostics. SAE paper no. 1999-01-0510.
- BADOCK, C., WIRTH, R., FATH, A., LEIPERTZ A., 1999. Investigation of cavitation in real size diesel injection nozzles. *International Journal of Heat and Fluid Flow*, **20**, 534-544.
- BAE, C.H., KANG, J., 2000. Diesel spray characteristics of common-rail VCO nozzle injector. *Thiesel 2000*, Valencia, Spain, 13-15 September 2000.
- BARITAUD, T.A., HEINZE, T.A., LE COZ, J.F., 1994. Spray and self-ignition visualization in a DI diesel engine. SAE paper no. 940681, *SAE International Congress and Exposition*, Detroit, USA, 28 February – 3 March 1994.
- BECKMAN, M.S., FARRELL, P.V., 2001. Simultaneous liquid and vapour diesel fuel spray images from a HEUI injector. *ILASS Americas, 14th Annual Conference on Liquid Atomization and Spray Systems*, Dearborn, USA, 20-23 May 2001.
- BELLAN, J., 1984. Reducing soot in diesel exhaust. *NASA Tech Brief*, **8**(1), item 102, JPL Invention Report no. 5178/NPO-15715.
- BENGTSSON, P.-E., 1996. Simultaneous two-dimensional visualization of soot and OH in flames using laser-induced fluorescence. *Applied Spectroscopy*, **50**(9), 1182-1186.
- BERGSTRAND, P., DENBRATT, I., 2001. Diesel combustion with reduced nozzle diameter. SAE paper no. 2001-01-2010.

References

- BIRD, R.B., STEWART, W.E., LIGHTFOOT, E.N., 2002. Transport Phenomena. 2nd Edition. John Wiley & Sons.
- BLACK, J.D., 1999. Laser induced incandescence measurements of particles in aero-engine exhausts. *Proceedings of SPIE - The International Society for Optical Engineering*, **3821**, 209-215.
- BO, T., CLERIDES, D., GOSMAN, A.D., THEODOSSOPOULOS, P., 1997. Prediction of the flow and spray processes in an automobile DI diesel engine. SAE paper no. 970882.
- BORMAN, G.L., RAGLAND, K.W., 1998. Combustion Engineering. McGraw-Hill.
- BRAUN-UNKHOFF, M., CHRYSOSTOMOU, A., FRANK, P., GUTHEIL, E., LÜCKERATH, R., STRICKER, W., 1998. Experimental and numerical study on soot formation in laminar high-pressure flames. *27th International Symposium on Combustion, The Combustion Institute, Boulder, USA, 2-7 August 1998*.
- BRADY, R.N., 1996. Modern diesel technology. Prentice Hall.
- BRÄUMER, A., SICK, V., WOLFRUM, J., DREWES, V., ZAHN, M., MALY, R., 1995. Quantitative two-dimensional measurements of nitric oxide and temperature distributions in a transparent square piston si engine. SAE paper no. 952462.
- BRAUN, R.D., 1987. Introduction to instrumental analysis. Chemistry Series, McGraw-Hill International Editions.
- BRUNEAUX, G., VERHOEVEN, D., BARITAUD, T., 1999. High pressure diesel spray and combustion visualization in a transparent model diesel engine. SAE paper no.1999-01-3648.
- CAMPANELLA, R. LAFORGIA, D., FICARELL, A., DAMIANI, V., 1994. Spray characteristics of five-hole V.C.O. nozzles of a diesel electro-injector. SAE paper no. 940192.
- CHIGIER, N., REITZ, R.D., 1998. Regimes of jet breakup and breakup mechanisms (physical aspects). In: Recent advances in spray combustion: Spray atomization and drop burning phenomena. Edited by Kenneth K Kuo; Published by American Institute of Aeronautics and Astronautics, Inc, 109-135.
- CHOI, D., ENAMI, M., SENDA, J., FUJIMOTO, H., KURATA, K., ASAI, G., 1999. Soot formation and oxidation process in a DI diesel engine by use of LII/LIS technique. *Proceedings of the 15th Internal Combustion Engine Symposium*.
- CHRISTENSEN, M., JOHANSON, B., 1999. Homogeneous charge compression ignition with water injection. *SAE SP-1444*, 11-19, SAE paper no. 1999-01-0182.
- CIGNOLI, F., BENECCHI, S., ZIZAK, G., 1994. Time-delayed detection of laser-induced incandescence for the two-dimensional visualization of soot in flames. *Applied Optics*, **33**(24), 5778-5782.

References

- DAILY, J.W., 1997. Laser induced fluorescence spectroscopy in flames. *Progress in Energy Combustion Science*, **23**, 133-199.
- DEC, J.E., 1991. Soot distribution in a D.I. diesel engine using 2-D laser-induced incandescence imaging. SAE paper no. 910224.
- DEC, J.E., 1997. A conceptual model of DI diesel combustion based on laser-sheet imaging. *SAE Special Publications*, **1244**, 223-252, SAE paper no. 970873.
- DEC, J.E., CANAAN, R.E., 1998. PLIF imaging of NO formation in a DI diesel engine. *SAE Transactions*, **1348**, 79-105, SAE paper no. 980147.
- DEC, J.E., ESPEY, C., 1995. Ignition and early soot formation in a D.I. diesel engine using multiple 2-D imaging diagnostics. *SAE Transactions*, **104**(3), 853-875, SAE paper no. 950456.
- DEC, J.E., ESPEY, C., 1998. Chemiluminescence imaging of autoignition in a DI diesel engine. SAE paper no. 982685.
- DEC, J.E., ESPEY, C., ZUR LOYE, A.O., SIEBERS, D.L., 1992. Soot and fuel distribution imaging in a diesel engine. *Symposium on Mechanisms and Chemistry of Pollutant Formation and Control from Internal Combustion Engines*, Washington, USA, 23-28 August 1992.
- DEC, J.E., KELLER, J.O., 1986. High speed thermometry using two-line atomic fluorescence. *Twenty-first International Symposium on Combustion*, The Combustion Institute, 1737-1745.
- DEMIRTZI, D., 2001. Spray penetration taking into account the influence of droplet evaporation. Final year project report. The University of Brighton.
- DEMTRÖDER, W., 1996. Laser spectroscopy, basic concepts and instrumentation. 2nd edition, Springer.
- DENT, J.C., 1971. A basic comparisons of various experimental methods for studying spray penetration. SAE paper no. 710571.
- DESANTES, J.M., PASTOR, J.V., MOLINA, S.A., 1999. Analysis of the combustion process in a heavy duty D.I. diesel engine through in-cylinder visualisation. *ICE*, **32**(2), 105-113.
- DI GIORGIO, F., LAFORGIA, D., DAMIANI, V., 1995. Investigation of drop size distribution in the spray of a five-hole, V.C.O. nozzle at high feeding pressure. *SAE International Congress and Exposition*, Detroit, USA, 27 February – 2 March, 1995. SAE paper no. 950087.
- DOUGLAS, J.F., GASIOREK, J.M., SWAFFIELD, J.A., 1995. Fluid mechanics. Longman.
- DRAIN, L.E., 1980. The laser Doppler technique. Wiley-Interscience Publication, John Wiley & Sons.
- ECKBRETH, A.C., 1977. Effects of laser-modulated particulate incandescence on Raman scattering diagnostics. *Journal of Applied Optics*, **48**(11), 4473-4479.
- ECKBRETH, A.C., 1996. Laser diagnostics for combustion temperature and species. 2nd edition, Gordon and Breach Publishers, 1996.

References

- EDWARDS, C.F., SIEBERS, D.L., HOSKIN, D.H., 1992. A study of the autoignition process of a diesel spray via high speed visualization. SAE paper 920108.
- ENVIRONMENT CANADA, 1998. The Green Lane Home Page. Available from: <http://www.ec.gc.ca> [Accessed 12 Jun 2000].
- ESPEY, C., DEC, J.E., 1993. Diesel engine combustion studies in a newly designed optical-access engine using high-speed visualization and 2-D laser imaging. SAE paper no. 930971.
- ESPEY, C., DEC, J.E., LITZINGER, T.A., SANTAVICCA, D.A., 1997. Planar laser Rayleigh scattering for quantitative vapor-fuel imaging in a diesel jet. *Combustion and Flame*, **109**, 65-86.
- FAETH, G.M., HSIANG, L.-P., WU, P.-K., 1995. Structure and breakup properties of sprays. *International Journal for Multiphase Flow*, **21**, Suppl, 99-127.
- FAURE, M.-A., 1997. Particle image velocimetry measurement of in-cylinder flows. Thesis (PhD), University of Brighton, United Kingdom.
- FAURE, M.-A., SADLER, M., OVERSBY, K.K., STOKES, J., BEGG, S.M., POMMIER, L.S., HEIKAL, M.R., 1998. Application of LDA and PIV techniques to the validation of a CFD model of a direct injection gasoline engine. SAE paper no. 982705.
- FAVENNEC, A.-G., LEBRUN, M., 1999. Models for injector nozzles. *The Sixth Scandinavian International Conference on Fluid Power*, Tampere, Finland, 26-28 May 1999.
- FENG, G., 2001. Spray dynamics and air motion in the cylinder of G-DI engines. Thesis (PhD), University of Brighton, United Kingdom.
- FENG, Z-G, MICHAELIDES, E.E., 2001. Heat and mass transfer coefficients of viscous spheres. *International Journal of Heat and Mass Transfer*. **44**, 4445-4454.
- FLYNN, P.F., DURETT, R.P., HUNTER, G.L., ZUR LOYE, A.O., AKINYEMI, O.C., DEC, J.E., WESTBROOK, C.K., 1999. Diesel combustion: An integrated view combining laser diagnostics. *Chemical Kinetics and Empirical Validation*, SAE SP-1444, 117-132, SAE paper no. 1999-01-0509.
- FORKEY, J.N., FINKELSTEIN, N.D., LEMPert, W.R., MILES, R.B., 1996a. Demonstration and characterization of filtered Rayleigh scattering for planar velocity measurements. *AIAA Journal*, **34**(3), 442-448.
- FORKEY, J.N., LEMPert, W.R., MILES, R.B., 1996b. Demonstration and analysis of filtered Rayleigh scattering flow field diagnostic system. *Proceedings of the 1995 Rayleigh Scattering Diagnostics Workshop*, NASA Conference Publication, n. 10186, 123-140.
- FRENKLACH, M., WANG, H., 1994. Detailed mechanism and modeling of soot particle formation. *Springer Series in Chemical Physics*, **59**, 165-192.
- GARDINER, W.C. JR., HIDAKA, Y., TANZAWA, T., 1981. Refractivity of combustion gases. *Combustion and Flame*, **40**, 213-219.

References

- GEITLINGER, H., STREIBEL, T.H., SUNTZ, R., BOCKHORN, H., 1998. Two-dimensional imaging of soot volume fractions, particle number densities, and particle radii in laminar and turbulent diffusion flames. *Twenty-Seventh Symposium (International) on Combustion*, The Combustion Institute, 1613-1621.
- GEITLINGER, H., STREIBEL, T.H., SUNTZ, R., BOCKHORN, H., 1999. Statistical Analysis of soot volume fractions, particle number densities and particle radii in a turbulent diffusion flame. *Combustion Science and Technology*, **149**, 115-134.
- GHOSH, S., HUNT, J.C.R., 1994. Induced air velocity within droplet driven sprays. *Proceedings Royal Society London*, **A444**, 105-127.
- GOSS, L.P., 1993. CARS Instrumentation for combustion applications. In: *Instrumentation for Flows with Combustion*, A.M.K.P. Taylor (ed), Academic Press, 251-322.
- GREEN, R.M., WITZE, P.O., 2002. Laser-induced incandescence and elastic-scattering measurements of particulate-matter volume fraction changes during passage through a dilution tunnel. *The 11th International Symposium on Applications of Laser Techniques to Fluid Mechanics*, Lisbon, Portugal, 8-11 July 2002.
- GREIS, A.E., GRÜNEFELD, G., BECKER, M., PISCHINGER, S., 2002. Quantitative measurements of the soot distribution in a realistic common rail D.I. diesel engine. *The 11th International Symposium on Applications of Laser Techniques to Fluid Mechanics*, Lisbon, Portugal, 8-11 July 2002.
- HABCHI, C., VERHOEVEN, D., HUYNH HUU, C., LAMBERT, L., VANHEMELRYCK, J.L., BARITAUD, T., 1997. Modeling atomization and break up in high-pressure diesel sprays. SAE paper no. 970881.
- HALSTEAD, M.P., KIRSH, L.J., QUINN, C.P., 1977. The autoignition of hydrocarbon fuels at high temperature and pressures – fitting model. *Combustion and Flame*, **30**, 45-60.
- HAY, N., JONES, J.L., 1972. Comparison of the various correlations for spray penetrations. SAE paper no. 720226.
- HENTSCHEL, W., 2000. Optical diagnostics for combustion process development of direct-injection gasoline engines. *Proceedings of the Combustion Institute*, **28**, 1119-1135.
- HENTSCHEL, W., SCHINDLER, K.-P., 1996. Flow, spray and combustion analysis by laser techniques in the combustion chamber of a direct-injection diesel engine. *Optics and Lasers in Engineering*, **25**, 401-413.
- HERZOG, P.L., 1999. Fuel injection – The key to effective low-emission diesel engines. I.Mech.E. publication S492/K1/99.
- HIGGINS, B., SIEBERS, D., 2001. Measurement of the flame lift-off location on DI diesel sprays using OH chemiluminescence. SAE paper 2001-01-0918.
- HIGGINS, B., SIEBERS, D., ARADI, A., 2000. Diesel-spray ignition and premixed-burn behavior. SAE paper 2000-01-0940.

References

- HILTON, M., BLACK, J.D., 1998. Detection of soot particles in gas turbine engine combustion gases using non intrusive FTIR spectroscopy. *Proceedings of SPIE*, The International Society for Optical Engineering, **3493**, 20-31.
- HIROYASU, H., ARAI, M., 1990. Structure of fuel sprays in diesel engines. *Transactions of the SAE*, **99**(3), 1050-1061.
- HOU, Z.X., ABRAHAM, J., SIEBERS, D.L., 1995. Modeling of diesel sprays in a very high pressure chamber, part II: Effects of combustion. *SAE Special Publications*, **1092**, 1-13, SAE paper no. 950603.
- HUH, K.Y., LEE, E., KOO, J.-Y., 1998. Diesel spray atomization model considering nozzle exit turbulence conditions. *Atomization and Sprays*, **8**, 453-469.
- HULT, J., AXELSSON, B., OMRANE, A., COLLIN, R., NYGREN, J., BENGTTSSON, P.-E., ALDÉN, M., KAMINSKI, C.F., 2002. Quantitative three-dimensional imaging of soot volume fraction in turbulent non-premixed flames. *Experiments in Fluids*, **33**, 265-269.
- INAGAKI, K., TAKASU, S., NAKAKITA, K., 1999. In-cylinder quantitative soot concentration measurement by laser-induced incandescence. *Processes of Diesel Engine Combustion*, SAE SP-1444, 105-116, SAE paper no. 1999-01-0508.
- INGLE, J.D., CROUCH, S.R., 1988. Spectrochemical analysis. Prentice-Hall International Editions.
- IYER, V.A., ABRAHAM, J., MAGI, V., 2002. Exploring injected droplet size effects on steady liquid penetration in a diesel spray with a two-fluid model. *International Journal of Heat and Mass Transfer*, **45**, 519-531.
- JACKSON, N.S., 2000. The high speed direct injection diesel engine - Future potential. *Thiesel 2000*, Valencia, Spain, 13-15 September 2000.
- JURNG, J., 1999. Experimental approaches of laser-induced incandescence technique for soot measurement. *CLEO, Pacific Rim'99*, 161-162.
- KENNAIRD, D.A., CRUA, C., HEIKAL, M., MORGAN, R., BAR, F., SAPSFORD, S., 2000. A new high pressure diesel spray research facility. *Computational and Experimental Methods in Reciprocating Engines*, I.Mech.E. Conference transactions, London, UK, 1-2 November 2000.
- KENNAIRD, D.A., CRUA, C., LACOSTE, J., HEIKAL, M.R., GOLD, M.R., JACKSON, N.S., 2002. In-cylinder penetration and break-up of diesel sprays using a common-rail injection system. *SAE 2002 Spring Fuels & Lubricants Meeting*, Reno, USA, 6-9 May 2002, SAE paper no. 2002-01-1626.
- KENNEDY, I.M., 1997. Models of soot formation and oxidation. *Progress in Energy and Combustion Science*, **23**(2), 95-132.
- KHAN, I.M., GREEVES, G., PROBERT, D.M., 1971. Prediction of soot and nitric oxide concentrations in diesel engine exhaust. *Air Pollution Control in Transport Engines*, **C142**(71), The Institution of Mechanical Engineers, 205-217.

References

- KIDO, A., KUBOTA, S., OGAWA, H., MIYAMOTO, N., 1998. Simultaneous measurements of concentration and temperature distributions in unsteady gas jets by an iodine LIF method. SAE paper no. 980146.
- KITTELSON, D.B., 1998. Engines and nanoparticles: A review. *Journal of Aerosol Science*, **29**(5/6), 575-588.
- KOBORI, S., KAMIMOTO, T., ARADI, A.A., 2000. A study of ignition delay of diesel fuel sprays. *International Journal of Engine Research*, **1**(1), 29-39.
- KOHSE-HÖINGHAUS, K., 1994. Laser techniques for the quantitative detection of reactive intermediates in combustion systems. *Progress in Energy and Combustion Science*, **20**(3), 203-279.
- KONG, S.C., SENEAL, P.K., REITZ, R.D., 1999. Developments in spray modeling in diesel and direct-injection gasoline engines. *Oil and Gas Science and Technology*, **54**(2), 197-204.
- KOSAKA, H., NISHIGAKI, T., KAMIMOTO, T., 1995. A study on soot formation and oxidation in an unsteady spray flame via laser induced incandescence and scattering techniques. SAE paper no. 952451.
- KOUREMENOS, D.A., HOUNTALAS, D.T., KOUREMENOS, A.D., 1999. Experimental investigation of the effect of fuel composition on the formation of pollutants, in direct injection diesel engines. *SAE SP-1444*, 83-90, SAE paper no. 1999-01-0189.
- KOUREMENOS, D.A., RAKOPOULOS, C.D., HOUNTALAS, D., 1990. Thermodynamic analysis of indirect injection diesel engines by two-zone modeling of combustion. *Journal of Engineering for Gas Turbines and Power*, **112**, 138-149.
- KUNIYOSHI, H., TANABE, H., SATO, G.T., FUJIMOTO, H., 1980. Investigation on the characteristics of diesel fuel spray. SAE paper no. 800968.
- KUO, K.K.-Y., 1986. Principles of Combustion. John Wiley & Sons.
- KYRIAKIDES, S.C., DENT, J.C., MEHTA, P.S., 1986. Phenomenological diesel combustion model including smoke and NO emission. SAE paper no. 860330.
- LASER COMPONENTS, 2001. Optical materials properties. Olching, Germany. Available from: <http://www.lasercomponents.de> [Accessed 4 Sep 2002].
- LEE, J.-H., IIDA, N., 2001. Combustion of diesel spray injected into reacting atmosphere of propane-air homogeneous mixture. *International Journal of Engine Research*, **2**(1), 69-80.
- LEE, M.P., PAUL, P.H., HANSON, R.K., 1987. Quantitative imaging of temperature fields in air using planar laser-induced fluorescence. *Optics Letters*, **12**, 75-77.
- LEE, K.B., THRING, M.W., BEÉR, J.M., 1962. On the rate of combustion of soot in a laminar soot flame. *Combustion and Flame*, **6**, 137-145.
- LEFEBVRE, A.H., 1989. Atomization and Sprays. Taylor & Francis.

References

- LEVICH, V.G., 1962. Physicochemical hydrodynamics. Prentice-Hall Inc.
- LIN, S.P., 1998. Regimes of jet breakup and breakup mechanisms (mathematical aspects). In: *Recent Advances in Spray Combustion: Spray Atomization and Drop Burning Phenomena*. Edited by Kenneth K. Kuo; American Institute of Aeronautics and Astronautics, Inc, 137-160.
- LOTH, E., 2000. Numerical approaches for motion of dispersed particles, droplets and bubbles. *Progress in Energy and Combustion Science*, **26**, 161-223.
- LUARD, N.G., 1994. Spray model – Notes on fuel properties. Ricardo Internal report.
- MAGNUSSEN, B.F., HJERTAGER, B.H., OLSEN, J.G., BHADURI, D., 1980. Modelling of reaction processes in turbulent flames with special emphasis on soot formation and combustion. *General Motors Symposium Particulate Carbon Formation during Combustion*, October 1980.
- MEHTA, P.S., DAS, S., 1992. A correlation for soot concentration in diesel exhaust based on fuel-air mixing parameters. *Fuel*, **71**, 689-692, June 1992.
- MELTON, L.A., 1984. Soot diagnostics based on laser heating. *Applied Optics*, **23**(13), 2201-2208, July 1984.
- MIWA, K., OHMIJA, T., NISHITANI, T., 1988. A study of the ignition delay of diesel fuel spray using a rapid compression machine. *JSME International Journal Series 2*, **31**(1), 166-173.
- MORGAN, R., WRAY, J., KENNAIRD, D.A., CRUA, C., HEIKAL, M., 2001. The influence of injector parameters on the formation and break up of a diesel spray. *2001 SAE Transactions – Journal of Engines*, **110**(3), 389-399.
- MORSI, S.A., ALEXANDER, A.J., 1972. An investigation of particle trajectories in two-phase flow systems. *Journal of Fluid Mechanics*, **55**(2), 193-208.
- MOUQUALLID, M., LISIECKI, D., LEDOUX, M., BELGHIT, A., 1998. Study of high pressure diesel sprays. 14th ILASS-Europe.
- NABER, J., SIEBERS, D.L., 1996. Effects of gas density and vaporization on penetration and dispersion of diesel sprays. SAE paper no. 960034.
- NAKAGAWA, H., ENDO, H., DEGUCHI, Y., 1998. LIF imaging of diesel spray combustion. *JSME Combustion and Modelling Symposium, COMODIA 98*, 359-364, Kyoto.
- NASA LANGLEY, 1996. Measurement Science & Technology Branch (MSTB). Available from: <http://mstb.larc.nasa.gov> [Accessed 4 Jun 2000].
- NI, T., PINSON, J.A., GUPTA, S., SANTORO, R.J., 1995. Two-dimensional imaging of soot volume fraction, by the use of laser-induced incandescence. *Applied Optics*, **34**(30), 7083-7091.
- PANTON, R.L., 1996. Incompressible flow. John Wiley & Sons.
- PARTINGTON, J.R., 1953. An advanced treatise on physical chemistry. *Physico-Chemical Optics*, **4**, Longmans.

References

- PISCHINGER, F., REUTER, U., SCHEID, E., 1988. Self-ignition of diesel sprays and its dependence on fuel properties and injection parameters. *Journal of Engineering for Gas Turbines and Power*, **110**, 399-404.
- POTZ, D., CHRIST, W., DITTUS, B., 2000. Diesel nozzle – The determining interface between injection system and combustion chamber. *Thiesel 2000*, Valencia, Spain, 13-15 September 2000.
- POZORSKI, J., SAZHIN, S., WACŁAWCZYK, M., CRUA, C., KENNAIRD, D.A., HEIKAL, M.R., 2002. Spray penetration in a turbulent flow. *Flow, Turbulence and Combustion*, **68**, 153-165.
- REITZ, D.R., 1987. Modeling atomization processes in high-pressure vaporizing sprays. *Atomization and Spray Technology*, **3**, 309-337.
- REITZ, R.D., DIWAKAR, R., 1986. Effect of drop breakup on fuel sprays. SAE paper no. 860469.
- REITZ, R.D., DIWAKAR, R., 1987. Structure of high-pressure fuel sprays. SAE paper no. 870598.
- RHIM, D., FARRELL, P.V., 2001. Effect of gas density and the number of injector holes on the air flow surrounding non-evaporating transient diesel sprays. SAE paper no. 2001-01-0532.
- RICARDO, 2002. Diesel passenger car & light commercial vehicle markets in Western Europe. Shoreham-by-Sea, UK. Available from: <http://www.ricardo.com> [Accessed 9 Sep 2002].
- ROLLER, A., ARNOLD, A., DECKER, M., SICK, V., WOLFRUM, J., HENTSCHEL, W., SCHINDLER, K.-P., 1995. Non-intrusive temperature measurements during the compression phase of a DI diesel engine. SAE paper no. 952461.
- SAVIC, S., 2000. Liquid fuel spray characteristics. Thesis (PhD), University of Brighton, United Kingdom.
- SAZHIN, S.S., FENG, G., HEIKAL, M.R., 2001a. A model for fuel spray penetration. *Fuel*, **80**(15), 2171-2180.
- SAZHIN, S.S., FENG, G., HEIKAL, M.R., GOLDFARB, I., GOLDSHTEIN, V., KUZMENKO, G., 2001b. Thermal ignition analysis of a monodisperse spray with radiation. *Combustion and Flame*, **124**(4), 684-701.
- SAZHIN, S.S., SAZHINA, E.M., HEIKAL, M.R., MAROONEY, C., MIKHALOVSKY, S.V., 1999. The Shell autoignition model: A new mathematical formulation. *Combustion and Flame*, **117**(3), 529-540.
- SAZHINA, E.M., SAZHIN, S.S., HEIKAL, M.R., BABUSHOK, V.I., JOHNS, R., 2000. A detailed modelling of the spray ignition process in diesel engines. *Combustion Science and Technology*, **160**, 317-344.
- SAZHINA, E.M., SAZHIN, S.S., HEIKAL, M.R., MAROONEY, C., 1999. The Shell autoignition model: Application to gasoline and diesel fuels. *Fuel*, **78**(4), 389-401.

References

- SCHRAML, S., HEIMGÄRTNER, C., FETTES, C., LEIPERTZ, A., 2000. Investigation of in-cylinder soot formation and oxidation by means of two-dimensional laser-induced incandescence (LII). *The 10th International Symposium on Applications of Laser Techniques to Fluid Mechanics*, Lisbon, Portugal, 10-13 July 2000.
- SCHRAML, S., WILL, S., LEIPERTZ, A., 1999. Simultaneous soot mass concentration and primary particle size measurements in the exhaust gas of diesel engines based on laser-induced incandescence (LII). *32nd International Symposium on Automotive Technology and Automation (ISATA)*, Vienna, Austria, 14-18 June 1999, Paper no. 99CPE022.
- SEITZMAN, J.M., HANSON, R.K., 1993. Planar fluorescence imaging in gases, *In: Instrumentation for Flows with Combustion*, A.M.K.P. Taylor (ed), Academic Press, 405-466.
- SEITZMAN, J.M., KYCHAKOFF, G., HANSON, R.K., 1985. Instantaneous temperature field measurements using planar laser-induced fluorescence. *Optics Letters*, **10**, 439-441.
- SEVIK, M., PARK, S.H., 1973. The splitting of drops by turbulent fluid flow. *ASME Journal of Fluid Engineering*. **95**, 53-60.
- SHIMAZAKI, N., AKAGAWA, H., TSUJIMURA, K., 1999. An experimental study of premixed lean diesel combustion. *SAE SP-1444*, 1-10, SAE paper no. 1999-01-0181.
- SHRAIBER, A.A., PODVYSOTSKY, A.M., DUBROVSKY, V.V., 1996. Deformation and breakup of drops by aerodynamic forces. *Atomization and Sprays*, **6**, 667-692.
- SIRIGNANO, W.A., 2000, Fluid dynamics and transport of droplets and spray. Cambridge University Press.
- SNELLING, D.R., SMALLWOOD, G.J., GÜLDER, Ö.L., BACHALO, W.D., SANKAR, S., 2000. Soot volume fraction characterization using the laser-induced incandescence detection method. *The 10th International Symposium on Applications of Laser Techniques to Fluid Mechanics*, Lisbon, Portugal, 10-13 July 2000.
- SOTERIOU, C., ANDREWS, R., SMITH, M., 1995. Direct injection diesel sprays and the effect of cavitation and hydraulic flip on atomization. SAE paper no. 950080.
- SOTERIOU, C.C.E., SMITH, M., ANDREWS, R.J., 1993. Cavitation hydraulic flip and the atomization in direct injection diesel sprays. I.Mech.E. paper no C465/051/93.
- TAIT, N.P., GREENHALGH, D.A., 1993. PLIF imaging of fuel fraction in practical devices and LII imaging of soot. *Berichte der Bunsengesellschaft fuer Physikalische Chemie*, **97**(12), 1619-1625.
- TESNER, P.A., SNEGIRIOVA, T.D., KNORRE, V.G., 1971. Kinetics of dispersed carbon formation. *Combustion and Flame*, **17**(2), 253-60.
- TSUJISHITA, M., HIRANO, K., YOKOO, M., SAKURAYA, T., TAKESHITA, Y., 1999. Accurate thermometry using NO and OH laser-induced fluorescence in an atmospheric pressure flame. *JSME International Journal*, series B, **42**(1), 119-126, 1999.

References

- VANDER WAL, R.L., JENSEN, K.A., CHOI, M.Y., 1997. Simultaneous laser-induced emission of soot and polycyclic aromatic hydrocarbons within a gas-jet diffusion flame. *Combustion and Flame*, **109**, 399-414.
- VANDER WAL, R.L., 1998. Soot precursor carbonization: Visualization using LIF and LII and comparison using bright and dark field TEM. *Combustion and Flame*, **112**, 607-616.
- VANDER WAL, R.L., TICICH, T.M., STEPHENS, A.B., 1998. Optical and microscopy investigations of soot structure alterations by laser-induced incandescence. *Applied Physics B – Laser and Optics*, **67**, 115-123.
- WAINNER, R.T., 1999. An analytical and quantitative analysis of the laser-induced incandescence of soot. Thesis (PhD), Georgia Institute of Technology, USA.
- WAINNER, R.T., SEITZMAN, J.M., 1999. Soot measurements in a simulated engine exhaust using laser-induced incandescence. *American Institute of Aeronautics and Astronautics (AIAA) Journal*, **37**(6), 738-743.
- WALLIS, G.B., 1969. One-dimensional two-phase flows. McGraw-Hill.
- WATRASIEWICZ, B.M., RUDD, M.J., 1976. Laser Doppler measurements. Butterworths & Co Ltd.
- WOLFRUM, J., 1998. Lasers in combustion: From basic theory to practical devices, *Twenty-Seventh Symposium on Combustion*, The Combustion Institute, 1-41.
- YANENKO, N.N., SOLOUKHIN, R.I., PAPYRIN, A.N., FOMIN, V.M., 1980. Supersonic two-phase flows with non-equilibrium particle velocities. Nauka Publishing House, Novosibirsk (in Russian).
- YOSHIHARA, Y., NISHIWAKI, K., MATSUKAWA, E., 1995. Modeling of NO formation and emission through turbulent mixing and chemical processes in diesel combustion. *IPC 8 conference*, JSAE, Yokohama, 145-150.
- YULE, A.J., SALTERS, D.G., 1995. On the distance required to atomize diesel sprays injected from orifice-type nozzles. *Proceedings of the Institution of Mechanical Engineers, Part D: Journal of Automobile Engineering*, **209**(3), 217-226.
- ZHAO, H., LADOMMATOS, N., 1998. Optical diagnostics for soot and temperature measurement in diesel engines. *Progress of Energy and Combustion Science*, **24**, 221-255.

Papers published by the author

Journals

- CRUA, C., KENNAIRD, D.A., HEIKAL, M.R., 2002. Laser-induced incandescence study of diesel soot formation at elevated in-cylinder and injection pressures. Submitted to *Combustion and Flame*.
- CRUA, C., KENNAIRD, D.A., SAZHIN, S.S., HEIKAL, M.R., 2002. Diesel autoignition at elevated in-cylinder pressures. Submitted to the *International Journal of Engine Research*.
- MORGAN, R., WRAY, J., KENNAIRD, D.A., CRUA, C., HEIKAL, M., 2001. The influence of injector parameters on the formation and break up of a diesel spray. *2001 SAE Transactions – Journal of Engines*, **110**(3), 389-399.
- POZORSKI, J., SAZHIN, S., WACŁAWCZYK, M., CRUA, C., KENNAIRD, D.A., HEIKAL, M.R., 2002. Spray penetration in a turbulent flow. *Flow, Turbulence and Combustion*, **68**, 153-165.
- SAZHIN, S.S., CRUA, C., KENNAIRD, D.A., HEIKAL, M.R., 2002. The initial stage of fuel spray penetration. *Fuel* (in press).

Conferences

- CRUA, C., 2002. Investigation of diesel pollutants formation through optical diagnostic techniques. *Engineering Research in Action*, Internal Conference, University of Brighton, Brighton, 29 January 2002.
- KENNAIRD, D.A., CRUA, C., HEIKAL, M., MORGAN, R., BAR, F., SAPSFORD, S., 2000. A new high pressure diesel spray research facility. *Computational and Experimental Methods in Reciprocating Engines*, I.Mech.E. Conference transactions, London, UK, 1-2 November 2000.
- KENNAIRD, D.A., CRUA, C., LACOSTE, J., HEIKAL, M.R., GOLD, M.R., JACKSON, N.S., 2002. In-cylinder penetration and break-up of diesel sprays using a common-rail injection system. *SAE 2002 Spring Fuels & Lubricants Meeting*, Reno, USA, 6-9 May 2002, SAE paper no. 2002-01-1626.
- LAGUITTON, O., GOLD, M., KENNAIRD, D., CRUA, C., LACOSTE, J., HEIKAL, M., 2002. Spray development and combustion characteristics for common rail diesel injection systems. *Fuel Injection Systems*, I.Mech.E. conference transactions, London, UK, 26-27 November 2002.
- MORGAN, R., WRAY, J., KENNAIRD, D.A., CRUA, C., HEIKAL, M., 2001. The influence of injector parameters on the formation and break up of a diesel spray. *SAE 2001 World Congress*, Detroit, USA, 5-8 March 2001, SAE paper no. 2001-01-0529.

Appendices

APPENDIX A : DIESEL SPRAY CHARACTERISATION	A-1
Source code for high-speed video post-processing	A-1
Experimental conditions for high-speed video of spray	A-5
Experimental conditions for liquid spray photography	A-7
Experimental conditions for vapour fuel visualisation	A-11
Standard dimensionless numbers	A-14
Effect of fuel pressure on liquid spray for low-temperature charge....	A-15
Effect of fuel pressure on liquid spray for high-temperature charge ..	A-18
Effect of gas density on liquid spray for low-temperature charge	A-21
Effect of gas density on liquid spray for high-temperature charge	A-23
Effect of gas density on vapour for high-temperature charge	A-25
APPENDIX B : AUTOIGNITION OF DIESEL SPRAYS	B-1
Experimental conditions for high-speed video of spray autoignition....	B-1
APPENDIX C : LASER-INDUCED INCANDESCENCE	C-1
Characteristics of image intensifier relay optics	C-1
Example of LII data set	C-4
Experimental conditions for LII data sets.....	C-6
Experimental conditions for LII sequence	C-10
Influence of fuel pressure on soot formation.....	C-12

Appendix A: Diesel spray characterisation

Source code for high-speed video post-processing

The listing below includes the Matlab source code for the post-processing of high-speed videos of spray. The software performs a thresholding and calculates the spray penetration for each video frame.

```

                                batchrun.m
% Post-processing software for high-speed video images.
% Created on 08/08/00 by J. B. Wray
% Last modified on 19/07/01 by C. Crua
%
% Software is sensitive to camera and nozzle position and will
% require modification for a new nozzle or camera location relative to the image.
%
% Images must be horizontal, with the injection occurring from right to left.
%
% This program executes sub programs to threshold and calculate spray penetration
% from a list of images.
%
% The output is in a data form exportable to a spreadsheet software (e.g. Excel).
% Both files are stored in the images location directory

%*****
% The following parameters should be adjusted for each set of images
%*****
ImageScale = 2.8;                % 1 mm = 2.8 pixels
InjectorX = 128+5+round(19.5*ImageScale); % For info: Injector is 19.5mm from top of windows
                                        % 128+5 is distance from left window edge to end of image
InjectorY = 32;                  % Should be the same as the centre of the windows
%*****

% Code for user to input directory for analysis
clear imaged
promptstr={'Enter directory path for the images to be processed :'};
instr=(cd);
nlines=1;
titlestr='Batch Analysis';

result=inputdlg(promptstr,titlestr,nlines,instr);

if ~isempty(result)
    directory=result{1};
else
    break;
end

% Option of displaying analysis graphically
graphics=questdlg('Show graphical results during processing?','Display Options:','Yes','No','No');

if strcmp(graphics,'No')
    graphics=0;
else
    graphics=1;
end

% Threshold setting
t=input('Input Threshold (0-255):');

% Code to load batch of images and analyse image data.
files=dir(directory);

```

Appendix A: Diesel spray characterisation

```

nbfiles=size(files,1);
ref=0;
dataq=zeros(1,1);
for i=1:nbfiles
    if files(i).isdir==0
        lengthname=size(files(i).name,2);
        image.file=files(i).name(1:lengthname);
        ref=ref+1;
        % Process image
            threshold;
            maxpen;
        imaged(ref,:)=image.file(1:lengthname);
        dataq(ref,1)=meani;
        dataq(ref,2)=maxi;
    end
end
header=['Mean' 'Max'];
disp(header);
disp(dataq);

% Create results text file
cd (base);
dlmwrite('data',dataq,'\t')

```

threshold.m

```

% Thresholding routine for multiple images.
% Run by batchrun.m
% Created on 8/08/00 by J. B. Wray
% Last modified on 19/07/01 by C. Crua

% Load image file for thresholding
base=cd;
cd (directory);
idata=imread(image.file);

% Measure data size
m=size(idata,1);
n=size(idata,2);

ImageWidth=m;
ImageHeight=n;

% Display image if option chosen
if graphics==1
    figure('Name',image.file,'Position',[10,450,570,250])
        colormap(gray);
        imagesc(idata);
        axis equal;
        axis([0 n 0 m]);
        hold on;
end

% Thresholding loop
newdata=zeros(m,n);
for y=1:n;
    for x=1:m;
        if idata(x,y)>t
            newdata(x,y)=255;
        else
            newdata(x,y)=0;
        end
    end
end

% Plot thresholded image
figure('Position',[10,124,570,250])
colormap(gray)
imagesc(newdata)
axis equal;
axis( [0 n 0 m]);

cd (base);

```

maxpen.m

Appendix A: Diesel spray characterisation

```

% Routine to detect the maximum spray penetration from the data outputted by threshold.m
% Run by batchrun.m
% Created on 8/08/00 by J. B. Wray
% Last modified on 19/07/01 by C. Crua
%
% Input data called newdata from threshold.m

% Store dimensions of input image data
[y,x]=size(newdata);

% Tags for later loop
j=x;
k=y;

% Find maximum penetration along image centre axis

mid=InjectorY;
midrow=newdata(mid,:);

while j>=1
    if midrow(j)=0    % Test for black pixel
        j=j-1;
    else
        break        % First non-black pixel found
    end
end

% Add one to estimated penetration since last black pixel is required, not first white
estpen=j+1;

% Start looking for spray tip 20 pixels before estimated penetration
j=estpen+20;
if j>ImageWidth
    j=ImageWidth;
end

% Initialise results array
result=zeros(ImageHeight-19,2);

% Initialise index for first clear element in result
i=1;

% Search rows of interest (all rows but the 10 upper and 10 lower rows where no spray is expected)
for y=10:ImageHeight-10
    % Extract row of interest from data
    data=newdata(y,:);

    % Scan across row right to left
    while j>=1
        if data(j)==0    % Test for black pixel
            if j==1    % Loop has reached the image's left edge
                result(i,1)=0;% Not a point of interest
                result(i,2)=i+9;    % i+9 since first data point is at y=10
                i=i+1;
            end
            j=j-1;
        else    % Test for white pixel
            result(i,1)=j+1;% Store data point for edge of spray
            result(i,2)=i+9;
            i=i+1;
            break
        end
    end

    j=estpen+20;    % Reset j for following row
end

% Processing of the results

% Ignore points equal to (estpen+20)
% (this means initial pixel was white so no spray tip was detected)

[a,b]=size(result);

```

Appendix A: Diesel spray characterisation

```
% Loop to check result and remove dud data
while a>=1
    if result(a,1)>=(estpen+20)
        result(a,:)=[]; % Removes dud data point
    elseif result (a,1)==0 % No edge was found
        result(a,:)=[];
    end
    a=a-1;
end

% Calculate mean penetration
[a,b]=size(result);

if a>0
    mean=(sum(result(:,1))/a);
    mini=min(result(:,1));
else
    mean=255;
    mini=255;
end

% Display penetration points
if graphics==1
    hold on;
    plot(result(:,1),result(:,2),'r-')
    plot([mean mean],[0 ImageHeight],'b-')
    plot([mini mini],[0 ImageHeight],'g-')
end

% Calculate mean and max penetration from spray tip (InjectorX,InjectorY)
meana=(InjectorX-mean);
maxa=(InjectorX-mini);

% Scale from pixel to mm
meani=meana/ImageScale;
maxi=maxa/ImageScale;
```

Experimental conditions for high-speed video of spray

Tables A-1 and A-2 list the conditions at which high-speed video recordings of liquid fuel spray were performed. Table A-1 lists the far-field videos (first 20 mm of the spray not visible), whereas Table A-2 details the conditions for close-up recordings (first 20 mm of the spray). Temperatures were calculated for a compression ratio of 9 and a polytropic coefficient of 1.3.

Test name	Injection pressure [MPa]	ICP at injection [MPa]	Temperature at injection [K]	Gas density [kg m ⁻³]
1d3	60	2.1	571	13
6d3	60	2.7	732	13
2d3	60	4.0	571	25
7d3	60	5.3	732	26
3d3	60	5.2	571	32
8d3	60	6.7	726	32
4d3	60	6.3	571	39
9d3	60	7.4	724	36
5d3	60	7.3	571	45
1d2	100	2.1	571	13
6d2	100	2.7	722	13
2d2	100	4.0	571	25
7d2	100	5.3	726	26
3d2	100	5.2	571	32
8d2	100	6.7	724	33
4d2	100	6.3	573	39
9d2	100	7.8	741	37
5d2	100	7.3	573	45
1d	160	2.1	585	13
6d	160	2.7	722	13
2d	160	4.0	583	25
7d	160	5.3	722	26
3d	160	5.2	583	32
8d	160	6.7	722	33
4d	160	6.3	594	37
9d	160	7.4	703	37
5d	160	7.3	571	45

Table A-1. Conditions for high-speed video of liquid fuel spray for a 0.2 mm VCO nozzle. Injections started at TDC, fuelling was 30 mm³.

Appendix A: Diesel spray characterisation

Test name	Injection pressure [MPa]	ICP at injection [MPa]	Temperature at injection [K]	Gas density [kg m ⁻³]
1d3Side	60	2.1	563	14
6d3Side	60	2.7	703	14
7d3Side	60	5.3	780	24
2d3Side	60	4.2	563	27
8d3Side	60	6.7	780	30
3d3Side	60	5.2	563	33
9d3Side	60	8.0	780	36
4d3Side	60	6.3	563	40
5d3Side	60	7.3	563	46
1d2Side	100	2.1	565	14
6d2Side	100	2.7	710	14
2d2Side	100	4.2	565	26
7d2Side	100	5.3	722	26
3d2Side	100	5.2	565	33
8d2Side	100	6.7	722	33
4d2Side	100	6.3	565	39
9d2Side	100	8.0	722	39
5d2Side	100	7.3	565	46
1dSide	160	2.1	569	13
6dSide	160	2.7	716	14
2dSide	160	4.2	567	26
7dSide	160	5.3	734	26
3dSide	160	5.2	567	33
8dSide	160	6.7	751	32
4dSide	160	6.3	567	39
9dSide	160	8.0	747	38
5dSide	160	7.3	567	45

Table A-2. Conditions for high-speed video close-up of liquid fuel spray for a 0.2 mm VCO nozzle. Injections started at TDC, fuelling was 30 mm³.

Experimental conditions for liquid spray photography

For each test listed in Tables A-3 to A-6, a backlit photograph of a non-combusting spray was taken using a fully manual still camera with a telephoto lens (125 mm) and two extension tubes (1+3 cm). The diffused backlighting was obtained with a high-speed argon flash lamp synchronised with the engine and delayed relative to TDC. The duration of the flash was less than 5 μ s. Kodak 400 ISO films were used and the camera aperture was set to f/8.

Test name	ICP at injection [MPa]	Temperature at injection [K]	Gas density [kg m ⁻³]	Injection pulse [ms]	Recording time [ms ASOI]
F3-5	3.0	567	19	0.90	1.03
F3-7	3.0	567	19	1.65	1.10
F3-8	3.0	567	19	1.65	1.65
F3-10	3.0	567	19	3.41	1.10
F3-11	3.0	567	19	3.41	1.65
F3-16	4.0	567	25	1.65	1.10
F3-17	4.0	567	25	1.65	1.65
F3-19	4.0	567	25	3.41	1.10
F3-20	4.0	567	25	3.41	1.65
F3-25	5.0	567	31	1.65	1.10
F3-26	5.0	567	31	1.65	1.65
F3-28	5.0	567	31	3.41	1.10
F3-29	5.0	567	31	3.41	1.65
F3-34	6.0	567	37	1.65	1.10
F3-35	6.0	567	37	1.65	1.65
F8-1A	6.0	567	37	3.41	1.10
F8-1A	6.0	567	37	3.41	1.65
F9-9A	7.0	567	44	1.65	1.10
F9-10A	7.0	567	44	1.65	1.65
F9-11A	7.0	567	44	3.41	1.10
F9-13A	7.0	567	44	3.41	1.65
F9-3A	8.0	567	50	1.65	1.10
F9-4A	8.0	567	50	1.65	1.65
F9-5A	8.0	567	50	3.41	1.10
F9-6A	8.0	567	50	3.41	1.65

Table A-3. Conditions for photographic imaging of liquid spray for a 0.2 mm VCO nozzle and an injection pressure of 60 MPa. Injections started at TDC.

Appendix A: Diesel spray characterisation

Test name	ICP at injection [MPa]	Temperature at injection [K]	Gas density [kg m ⁻³]	Injection pulse [ms]	Recording time [ms ASOI]
F4-3	3.0	567	19	0.90	1.03
F4-5	3.0	567	19	1.65	1.10
F4-6	3.0	567	19	1.65	1.65
F4-8	3.0	567	19	3.41	1.10
F4-12	3.0	567	19	3.41	1.65
F4-18	4.0	567	25	0.90	1.03
F4-20	4.0	567	25	1.65	1.10
F4-21	4.0	567	25	1.65	1.65
F4-23	4.0	567	25	3.41	1.10
F4-24	4.0	567	25	3.41	1.65
F4-27	5.0	567	31	0.90	1.03
F4-29	5.0	567	31	1.65	1.10
F4-30	5.0	567	31	1.65	1.65
F4-32	5.0	567	31	3.41	1.10
F4-33	5.0	567	31	3.41	1.65
F5-8	6.0	567	37	0.90	1.03
F5-10	6.0	567	37	1.65	1.10
F5-12	6.0	567	37	3.41	1.10
F5-13	6.0	567	37	3.41	1.65
F8-29A	7.0	567	44	0.90	1.03
F8-30A	7.0	567	44	1.65	1.10
F8-31A	7.0	567	44	1.65	1.65
F8-32A	7.0	567	44	3.41	1.10
F8-33A	7.0	567	44	3.41	1.65
F8-23A	8.0	567	50	0.90	1.03
F8-24A	8.0	567	50	1.65	1.10
F8-25A	8.0	567	50	1.65	1.65
F8-26A	8.0	567	50	3.41	1.10
F8-27A	8.0	567	50	3.41	1.65

Table A-4. Conditions for photographic imaging of liquid spray for a 0.2 mm VCO nozzle and an injection pressure of 100 MPa. Injections started at TDC.

Appendix A: Diesel spray characterisation

Test name	ICP at injection [MPa]	Temperature at injection [K]	Gas density [kg m ⁻³]	Injection pulse [ms]	Recording time [ms ASOI]
F5-16	3.0	567	19	0.90	1.03
F5-18	3.0	567	19	1.65	1.10
F5-19	3.0	567	19	1.65	1.65
F5-21	3.0	567	19	3.41	1.10
F5-22	3.0	567	19	3.41	1.65
F5-25	4.0	567	25	0.90	1.03
F5-27	4.0	567	25	1.65	1.10
F5-28	4.0	567	25	1.65	1.65
F5-30	4.0	567	25	3.41	1.10
F5-31	4.0	567	25	3.41	1.65
F6-3A	5.0	567	31	0.90	1.03
F6-5A	5.0	567	31	1.65	1.10
F6-6A	5.0	567	31	1.65	1.65
F6-8A	5.0	567	31	3.41	1.10
F6-9A	5.0	567	31	3.41	1.65
F6-12A	6.0	567	37	0.90	1.03
F6-14A	6.0	567	37	1.65	1.10
F6-15A	6.0	567	37	1.65	1.65
F6-17A	6.0	567	37	3.41	1.10
F6-18A	6.0	567	37	3.41	1.65
F8-17A	7.0	567	44	0.90	1.03
F8-18A	7.0	567	44	1.65	1.10
F8-19A	7.0	567	44	1.65	1.65
F8-20A	7.0	567	44	3.41	1.10
F8-21A	7.0	567	44	3.41	1.65
F8-11A	8.0	567	50	0.90	1.03
F8-12A	8.0	567	50	1.65	1.10
F8-13A	8.0	567	50	1.65	1.65
F8-14A	8.0	567	50	3.41	1.10
F8-15A	8.0	567	50	3.41	1.65

Table A-5. Conditions for photographic imaging of liquid spray for a 0.2 mm VCO nozzle and an injection pressure of 140 MPa. Injections started at TDC.

Appendix A: Diesel spray characterisation

Test name	ICP at injection [MPa]	Temperature at injection [K]	Gas density [kg m ⁻³]	Injection pulse [ms]	Recording time [ms ASOI]
F6-21A	3.0	567	19	0.90	1.03
F6-23A	3.0	567	19	1.65	1.10
F6-24A	3.0	567	19	1.65	1.65
F6-26A	3.0	567	19	3.41	1.10
F6-27A	3.0	567	19	3.41	1.65
F7-3A	4.0	567	25	0.90	1.03
F7-5A	4.0	567	25	1.65	1.10
F7-6A	4.0	567	25	1.65	1.65
F7-8A	4.0	567	25	3.41	1.10
F7-9A	4.0	567	25	3.41	1.65
F7-12A	5.0	567	31	0.90	1.03
F7-14A	5.0	567	31	1.65	1.10
F7-15A	5.0	567	31	1.65	1.65
F7-17A	5.0	567	31	3.41	1.10
F7-18A	5.0	567	31	3.41	1.65
F7-21A	6.0	567	37	0.90	1.03
F7-23A	6.0	567	37	1.65	1.10
F7-24A	6.0	567	37	1.65	1.65
F7-26A	6.0	567	37	3.41	1.10
F7-27A	6.0	567	37	3.41	1.65
F7-29A	7.0	567	44	0.90	1.03
F7-30A	7.0	567	44	1.65	1.10
F7-31A	7.0	567	44	1.65	1.65
F7-32A	7.0	567	44	3.41	1.10
F7-33A	7.0	567	44	3.41	1.65
F8-4A	8.0	567	50	0.90	1.03
F8-5A	8.0	567	50	1.65	1.10
F8-6A	8.0	567	50	1.65	1.65
F8-7A	8.0	567	50	3.41	1.10
F8-8A	8.0	567	50	3.41	1.65

Table A-6. Conditions for photographic imaging of liquid spray for a 0.2 mm VCO nozzle and an injection pressure of 160 MPa. Injections started at TDC.

Experimental conditions for vapour fuel visualisation

Test name	Injection pressure [MPa]	ICP at injection [MPa]	Temperature at injection [K]	Gas density [kg m ⁻³]
schv12	100	3.0	703	15
schv11	100	4.8	697	25
schv10	100	5.7	730	28
schv9	100	7.4	780	33
schv23	140	3.9	730	19
schv8	140	3.0	714	15
schv21	140	4.2	722	21
schv22	140	4.2	739	20
schv24	140	4.2	718	21
schv25	140	4.2	703	21
schv7	140	5.3	716	26
schv6	140	5.8	708	29
schv5	140	7.4	718	36
schv4	160	2.7	741	13
schv3	160	5.3	683	28
schv1	160	6.9	741	33
schv1a	160	6.9	745	33
schv2	160	7.1	728	34
schv2a	160	7.1	761	33

Table A-7. Conditions for high-speed schlieren video of vapour fuel for a 0.2 mm VCO nozzle. Injections started at TDC, fuelling was 30 mm³.

Appendix A: Diesel spray characterisation

Test name	Injection pressure [MPa]	ICP at injection [MPa]	Temperature at injection [K]	Gas density [kg m ⁻³]	Recording time [ms ASOI]
sc10a	100	2.6	712	13	1.3
sc10b	100	2.6	712	13	1.3
sc10c	100	2.6	712	13	1.3
sc11a	100	2.7	712	13	2.0
sc11b	100	2.7	712	13	2.0
sc11c	100	2.7	712	13	2.0
sc12a	100	2.7	712	13	2.7
sc12b	100	2.7	712	13	2.7
sc13a	100	6.8	722	33	1.3
sc13b	100	6.8	722	33	1.3
sc14a	100	6.9	722	34	2.0
sc14b	100	6.9	722	34	2.0
sc15a	100	6.5	722	32	2.7
sc16a	140	2.9	664	16	1.3
sc16b	140	2.9	664	16	1.3
sc16c	140	2.9	664	16	1.3
sc17a	140	2.7	728	13	2.0
sc17b	140	2.7	728	13	2.0
sc17c	140	2.7	728	13	2.0
sc18a	140	2.7	724	13	2.7
sc18b	140	2.7	724	13	2.7
sc18c	140	2.7	724	13	2.7
sc19a	140	7.6	712	37	1.3
sc19b	140	7.6	712	37	1.3
sc20a	140	7.4	720	36	2.0
sc20b	140	7.4	720	36	2.0
sc21a	140	7.4	722	36	2.7
sc21b	140	7.4	722	36	2.7
sc21c	140	7.4	722	36	2.7
sc21d	140	7.4	722	36	2.7
sc22a	140	7.4	724	36	2.3
sc22b	140	7.4	724	36	2.3
sc22c	140	7.4	724	36	2.3
sc23a	140	7.4	718	36	2.7
sc23b	140	7.4	718	36	2.7
sc23c	140	7.4	718	36	2.7
sc24a	140	7.4	722	36	2.3
sc24b	140	7.4	722	36	2.3
sc24c	140	7.4	722	36	2.3
sc24d	140	7.4	722	36	2.3

Table A-8. Conditions for schlieren imaging of vapour fuel for a 0.2 mm VCO nozzle. Injections started at TDC, fuelling was 30 mm³.

Appendix A: Diesel spray characterisation

Test name	Injection pressure [MPa]	ICP at injection [MPa]	Temperature at injection [K]	Gas density [kg m ⁻³]	Recording time [ms ASOI]
sc2a	160	2.7	726	13	1.3
sc2b	160	2.7	726	13	1.3
sc2c	160	2.7	726	13	1.3
sc3a	160	2.7	714	13	2.0
sc3b	160	2.7	714	13	2.0
sc4a	160	2.7	722	13	2.7
sc4b	160	2.7	722	13	2.7
sc4c	160	2.7	722	13	2.7
sc6a	160	6.6	722	32	1.3
sc6b	160	6.6	722	32	1.3
sc7a	160	7.4	722	36	2.0
sc8a	160	6.8	722	33	2.7
sc8b	160	6.8	722	33	2.7

Table A-8. Conditions for schlieren imaging of vapour fuel for a 0.2 mm VCO nozzle (continued).

Standard dimensionless numbers

Name	Symbol	Force ratio	Equation	Form
Mach	Ma	$\frac{\text{Inertia}}{\text{Elastic}}$	$\frac{\rho L^2 V^2}{EL^2}$	$\frac{V}{\sqrt{E/\rho}}$
Nusselt	Nu	$\frac{\text{Convective heat transfer}}{\text{Conductive heat transfer}}$	$\frac{hS\Delta T}{kL\Delta T}$	$\frac{hL}{k}$
Ohnesorge	Oh	$\frac{\text{Viscous}}{\sqrt{\text{Inertia} \times \text{Surface tension}}}$	$\frac{\mu LV}{\sqrt{\rho L^2 V^2 \times \sigma}}$	$\frac{\mu}{\sqrt{\rho L \sigma}} = \frac{\sqrt{We}}{Re}$
Reynolds	Re	$\frac{\text{Inertia}}{\text{Viscous}}$	$\frac{\rho L^2 V^2}{\mu LV}$	$\frac{\rho LV}{\mu}$
Weber	We	$\frac{\text{Inertia}}{\text{Surface tension}}$	$\frac{\rho L^2 V^2}{\sigma L}$	$\frac{\rho LV^2}{\sigma}$

Table A-9. Table of dimensionless numbers used in fluid dynamics and spray vaporisation. ρ is a density, L a length, V a velocity, h a heat transfer coefficient, S a surface, ΔT a temperature difference, k a thermal conductivity, E a modulus of elasticity, μ a dynamic viscosity, and σ a surface tension.

Effect of fuel pressure on liquid spray for low-temperature charge

All profiles show the spray liquid core penetration length for a 0.2 mm single-guided single-hole VCO nozzle, obtained by high-speed video recording.

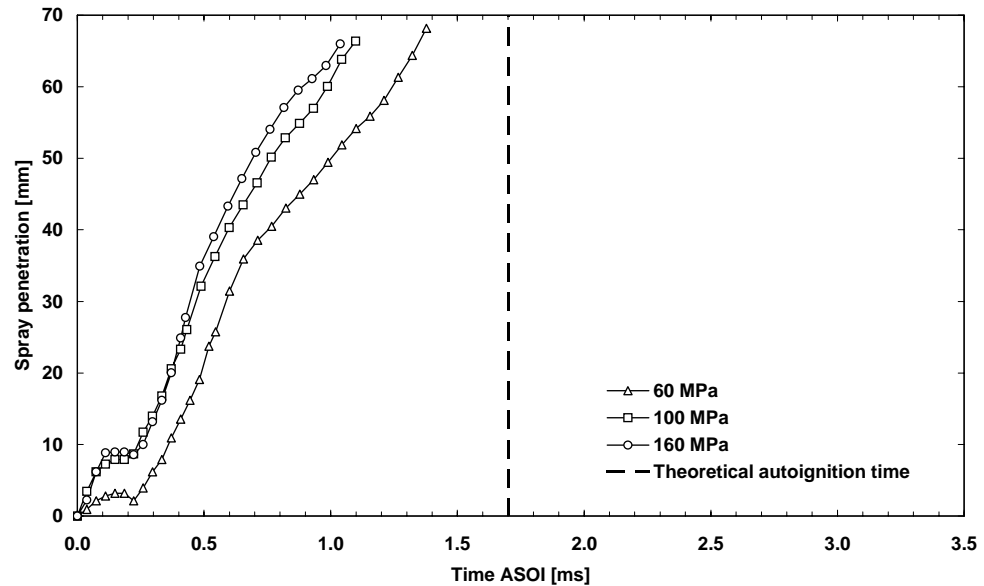


Figure A-1. Influence of injection pressure on liquid penetration for low-temperature charge. 14 kg m^{-3} in-cylinder density; 0.2 mm VCO nozzle. Broken line shows time at which ignition is highly probable.

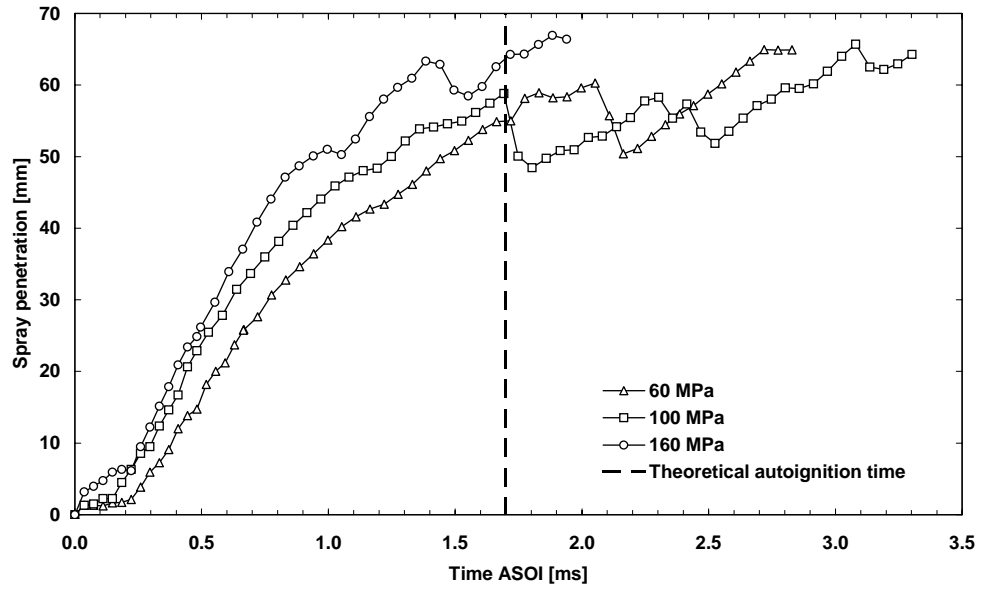


Figure A-2. Influence of injection pressure on liquid penetration for low-temperature charge. 28 kg m^{-3} in-cylinder density; 0.2 mm VCO nozzle. Broken line shows time at which ignition is highly probable.

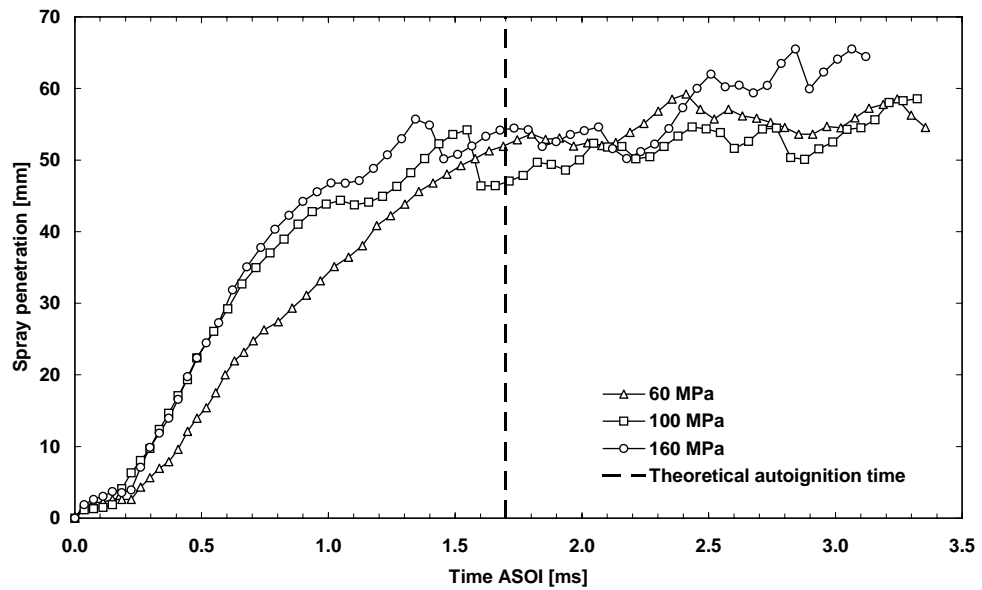


Figure A-3. Influence of injection pressure on liquid penetration for low-temperature charge. 34 kg m^{-3} in-cylinder density; 0.2 mm VCO nozzle. Broken line shows time at which ignition is highly probable.

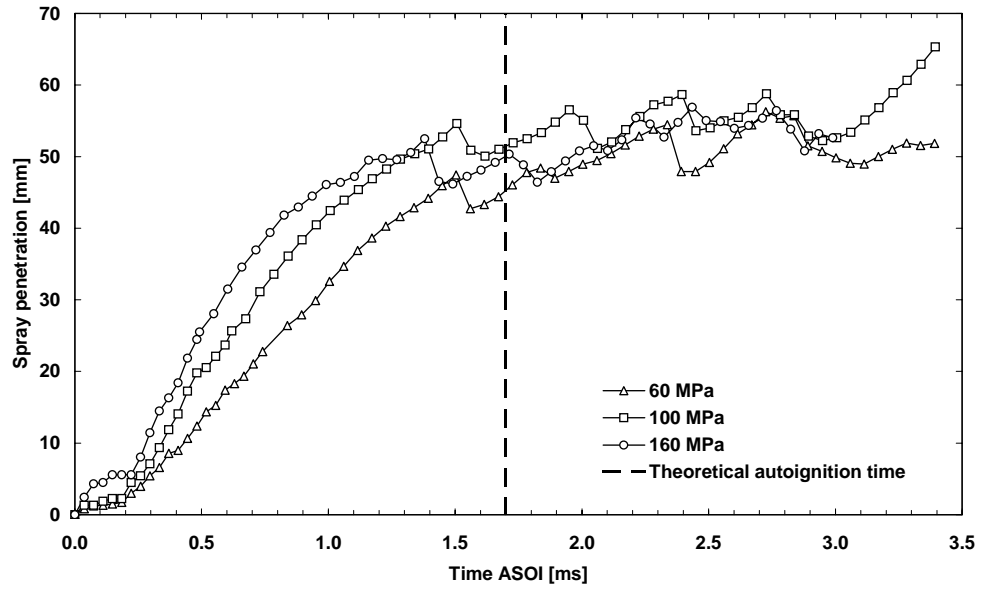


Figure A-4. Influence of injection pressure on liquid penetration for low-temperature charge. 42 kg m^{-3} in-cylinder density; 0.2 mm VCO nozzle. Broken line shows time at which ignition is highly probable.

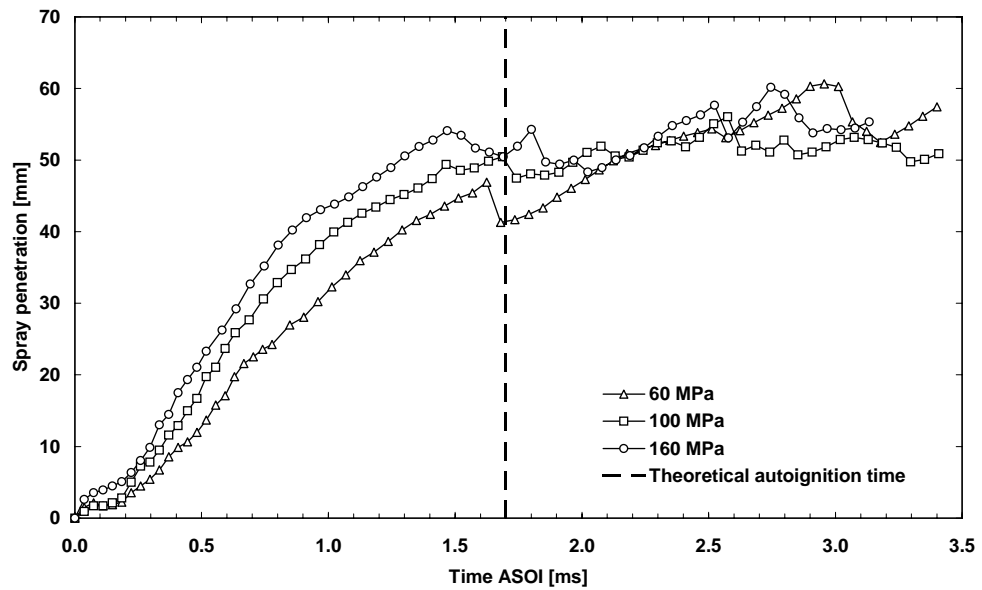


Figure A-5. Influence of injection pressure on liquid penetration for low-temperature charge. 49 kg m^{-3} in-cylinder density; 0.2 mm VCO nozzle. Broken line shows time at which ignition is highly probable.

Effect of fuel pressure on liquid spray for high-temperature charge

All profiles show the spray liquid core penetration length for a 0.2 mm single-guided single-hole VCO nozzle, obtained by high-speed video recording.

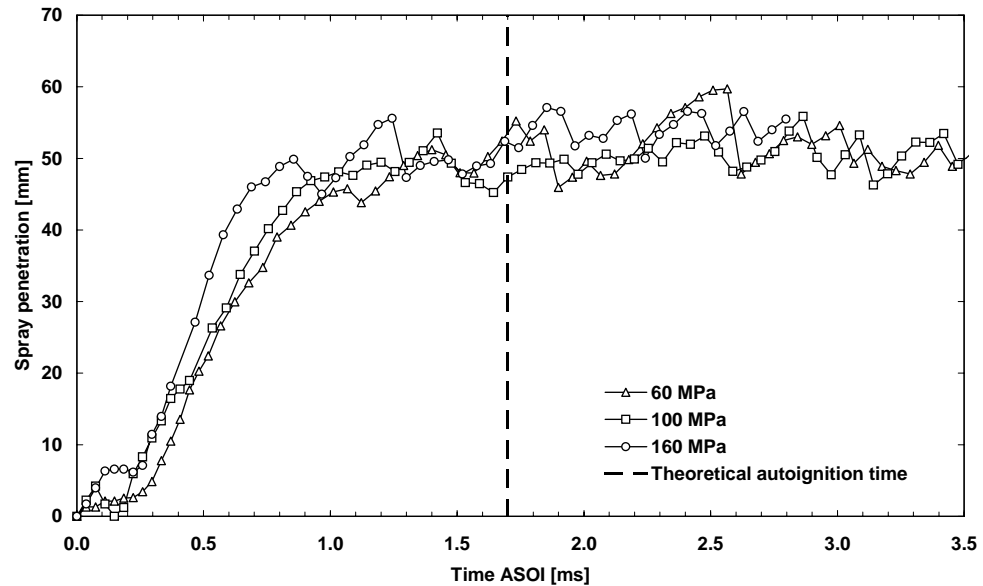


Figure A-6. Influence of injection pressure on liquid penetration for high-temperature charge. 14 kg m^{-3} in-cylinder density; 0.2 mm VCO nozzle. Broken line shows time at which ignition is highly probable.

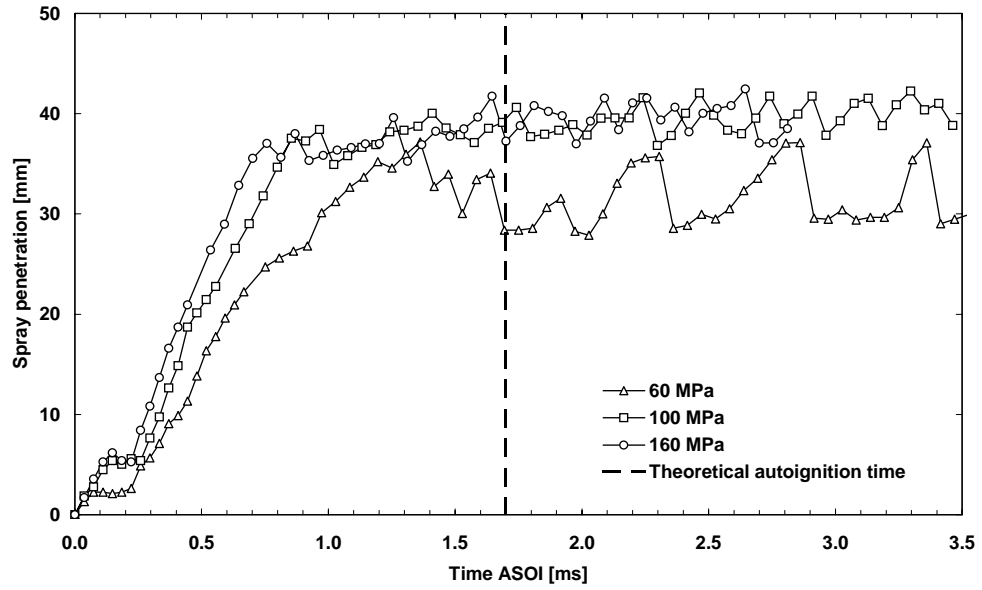


Figure A-7. Influence of injection pressure on liquid penetration for high-temperature charge. 28 kg m^{-3} in-cylinder density; 0.2 mm VCO nozzle. Broken line shows time at which ignition is highly probable.

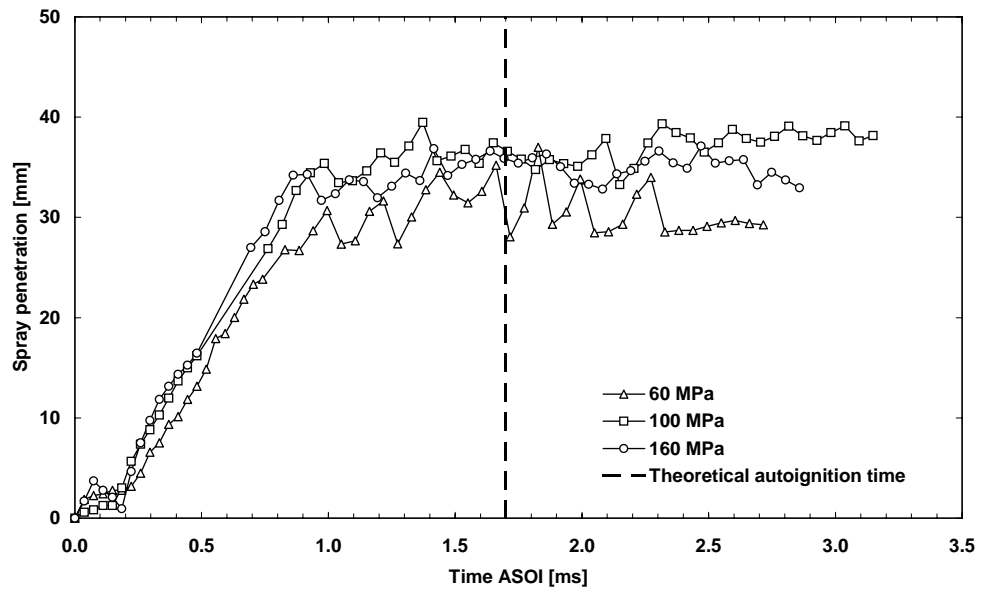


Figure A-8. Influence of injection pressure on liquid penetration for high-temperature charge. 35 kg m^{-3} in-cylinder density; 0.2 mm VCO nozzle. Broken line shows time at which ignition is highly probable.

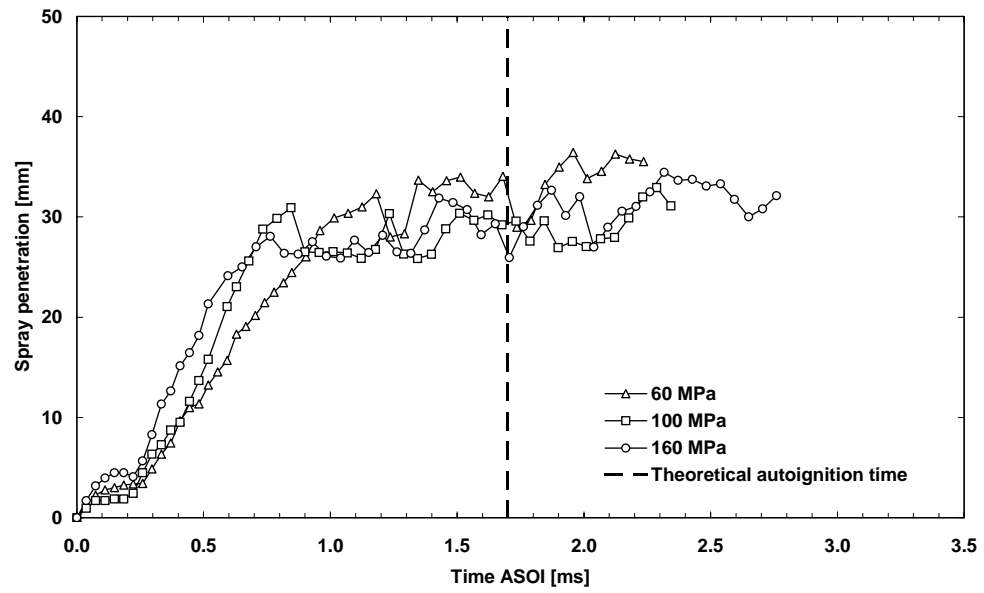


Figure A-9. Influence of injection pressure on liquid penetration for high-temperature charge. 40 kg m^{-3} in-cylinder density; 0.2 mm VCO nozzle. Broken line shows time at which ignition is highly probable.

Effect of gas density on liquid spray for low-temperature charge

All penetration profiles show the spray liquid core length for a 0.2 mm single-guided single-hole VCO nozzle, obtained by high-speed video recording.

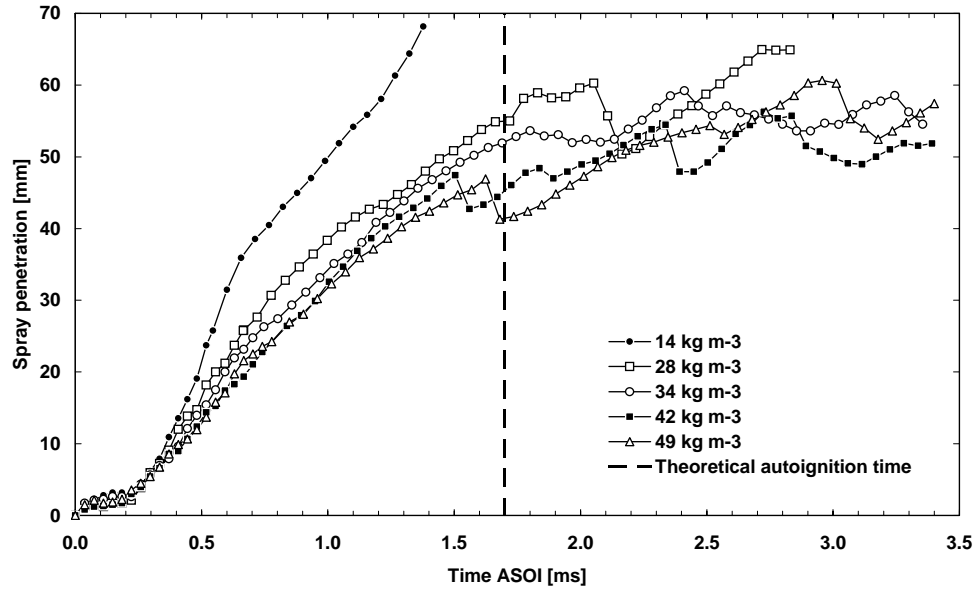


Figure A-10. Influence of ambient gas density on liquid penetration for low-temperature charge. 60 MPa injection pressure; 0.2 mm VCO nozzle. Broken line shows time at which ignition is highly probable.

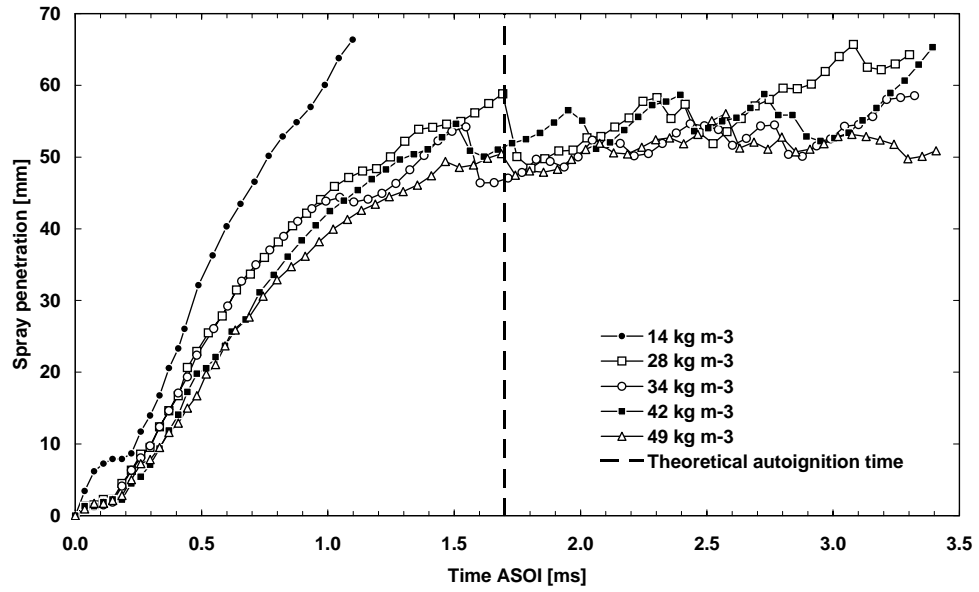


Figure A-11. Influence of ambient gas density on liquid penetration for low-temperature charge. 100 MPa injection pressure; 0.2 mm VCO nozzle. Broken line shows time at which ignition is highly probable.

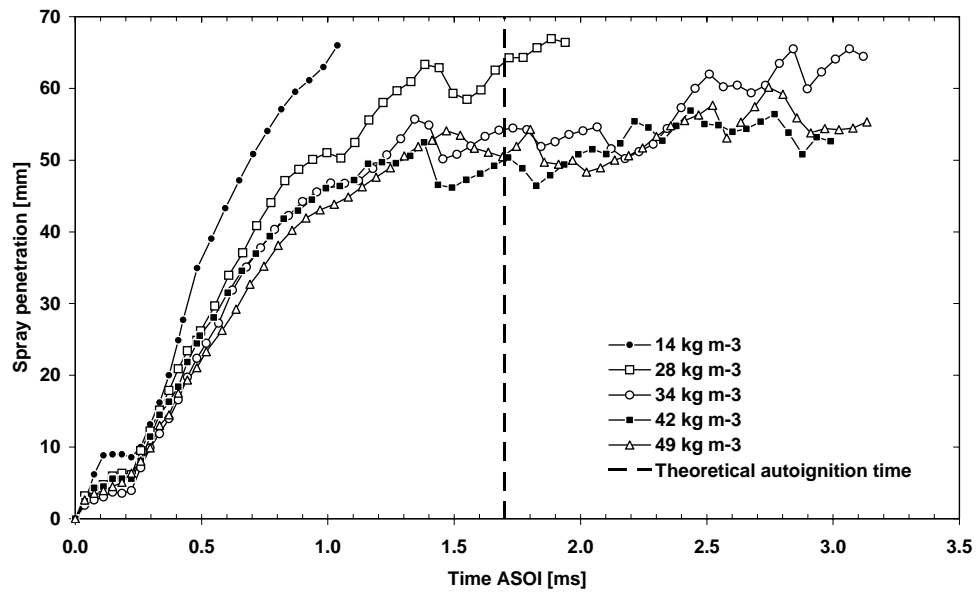


Figure A-12. Influence of ambient gas density on liquid penetration for low-temperature charge. 160 MPa injection pressure; 0.2 mm VCO nozzle. Broken line shows time at which ignition is highly probable.

Effect of gas density on liquid spray for high-temperature charge

All penetration profiles show the spray liquid core length for a 0.2 mm single-guided single-hole VCO nozzle, obtained by high-speed video recording.

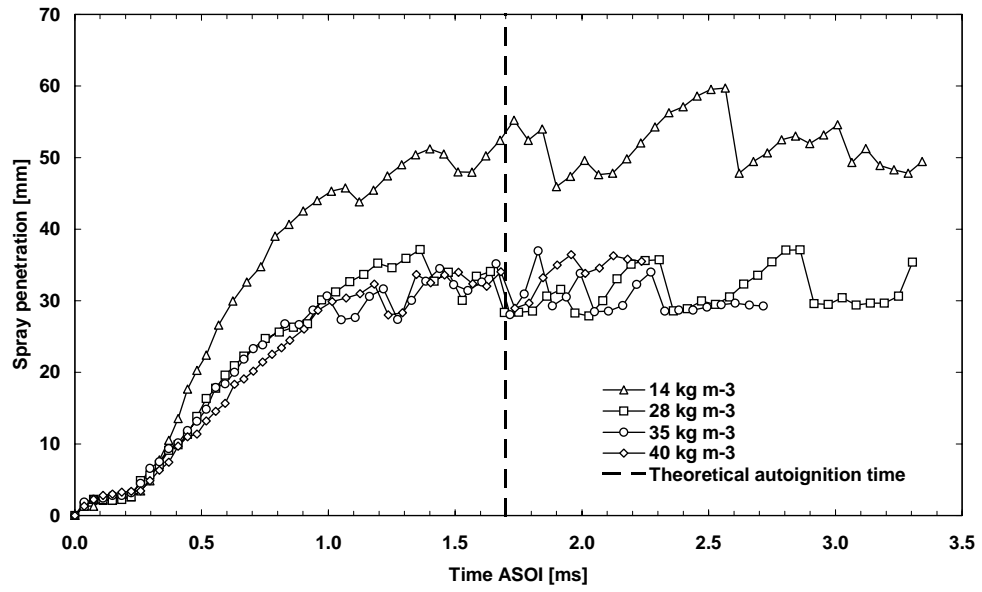


Figure A-13. Influence of ambient gas density on liquid penetration for high-temperature charge. 60 MPa injection pressure; 0.2 mm VCO nozzle. Broken line shows time at which ignition is highly probable.

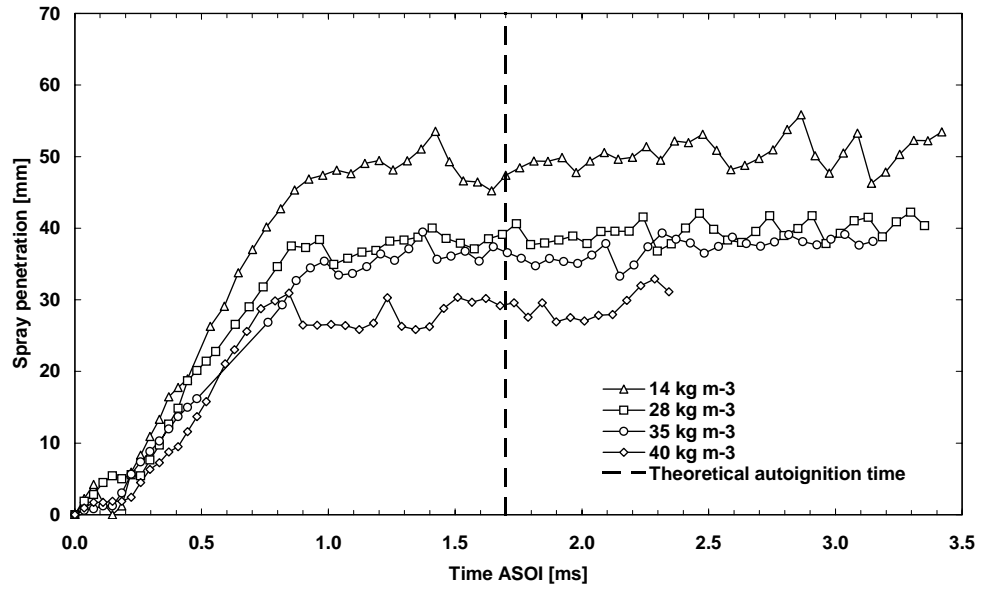


Figure A-14. Influence of ambient gas density on liquid penetration for high-temperature charge. 100 MPa injection pressure; 0.2 mm VCO nozzle. Broken line shows time at which ignition is highly probable.

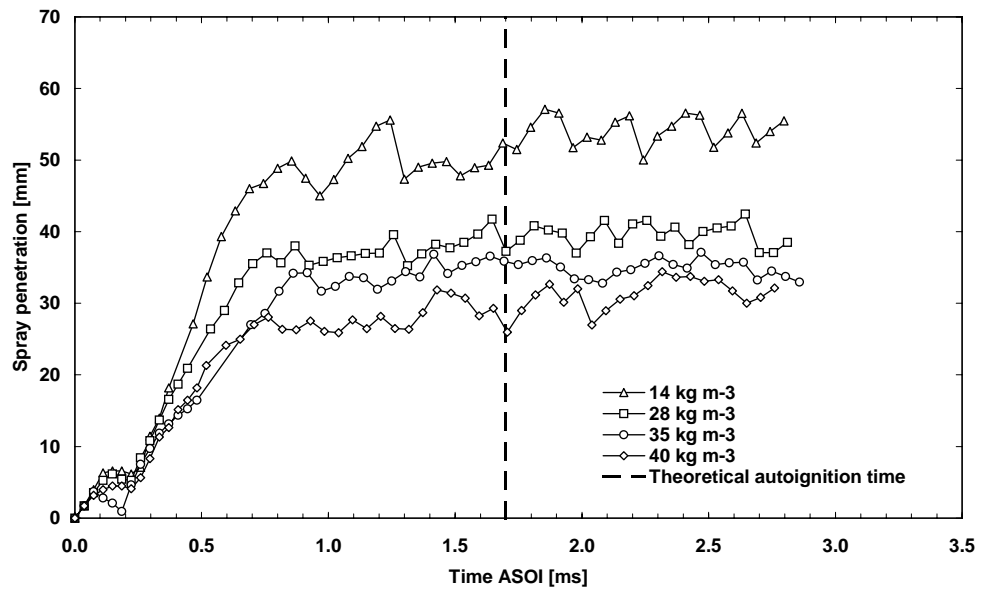


Figure A-15. Influence of ambient gas density on liquid penetration for high-temperature charge. 160 MPa injection pressure; 0.2 mm VCO nozzle. Broken line shows time at which ignition is highly probable.

Effect of gas density on vapour for high-temperature charge

All profiles show the spray vapour penetration length for a 0.2 mm single-guided single-hole VCO nozzle, obtained by schlieren high-speed video recording.

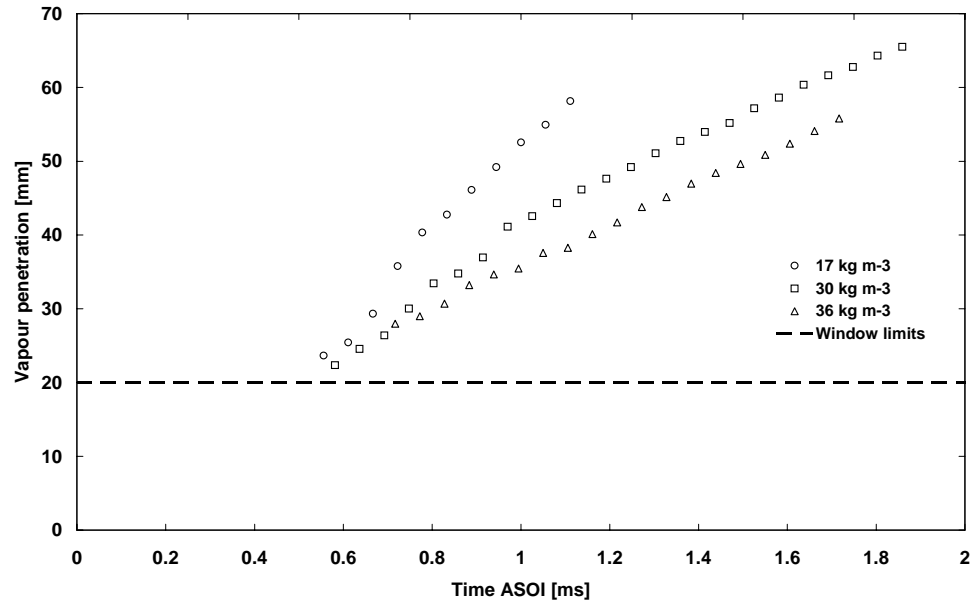


Figure A-16. Influence of ambient gas density on vapour penetration for high-temperature charge. 100 MPa injection pressure; 0.2 mm VCO nozzle. Broken line shows the limit of the window.

Appendix A: Diesel spray characterisation

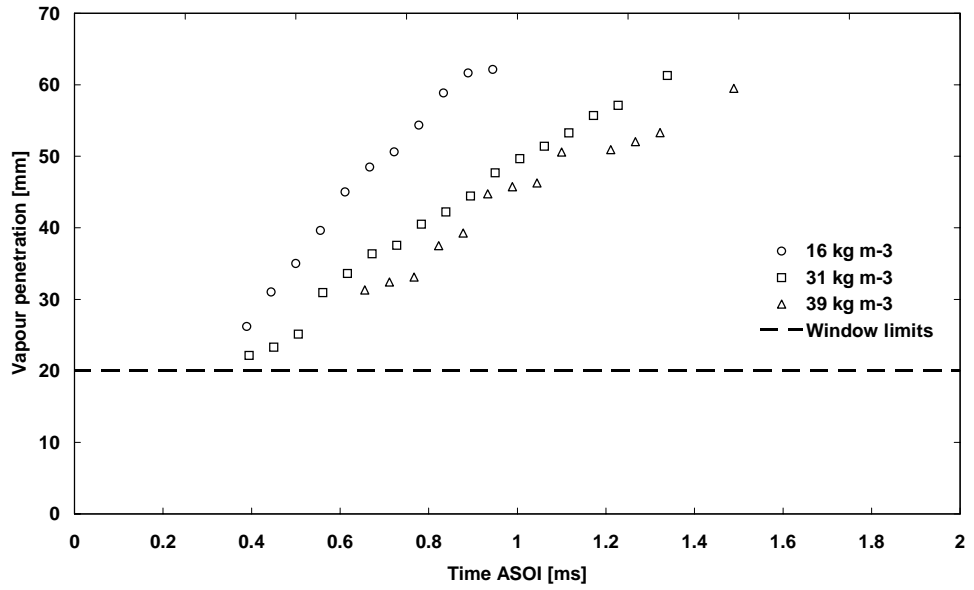


Figure A-17. Influence of ambient gas density on vapour penetration for high-temperature charge. 140 MPa injection pressure; 0.2 mm VCO nozzle. Broken line shows the limit of the window.

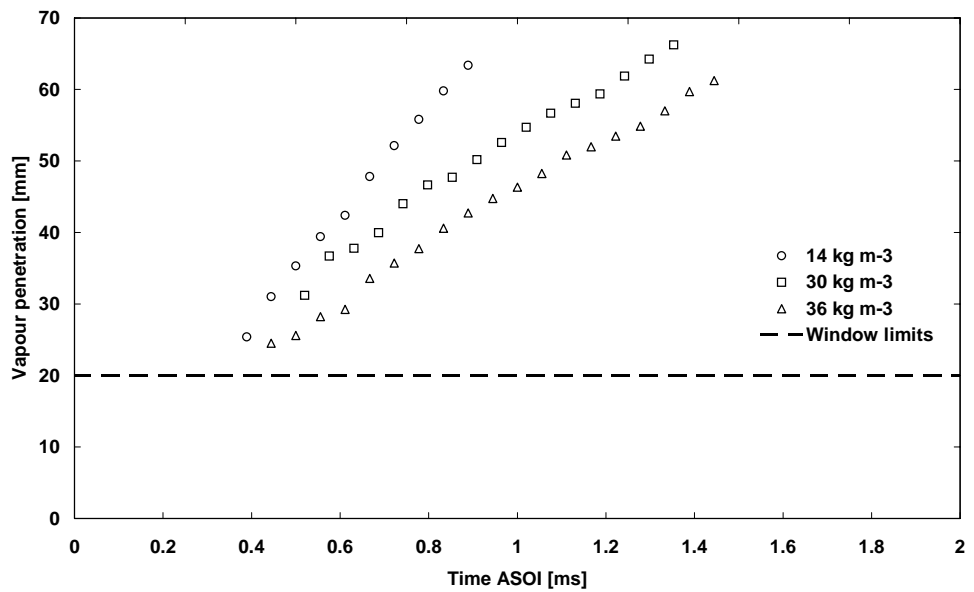


Figure A-18. Influence of ambient gas density on vapour penetration for high-temperature charge. 160 MPa injection pressure; 0.2 mm VCO nozzle. Broken line shows the limit of the window.

Appendix B: Autoignition of diesel sprays

Experimental conditions for high-speed video of spray autoignition

Temperatures were calculated for a compression ratio of 9 and a polytropic coefficient of 1.3.

Test name	Injection pressure [MPa]	ICP at non-fired TDC [MPa]	Temperature at non-fired TDC [K]	Gas density at non-fired TDC [kg m ⁻³]
50Ald	100	5.0	717	25
28Al	100	6.0	722	29
28Alrr	100	6.0	713	30
70Ald	100	7.0	720	34
31Al	100	7.5	738	36
31Alr	100	8.0	730	39
31Alrr	100	8.0	740	38
34Alrr	100	8.6	722	42
34Al	100	9.0	726	44
50Ale	140	5.0	705	25
29Al	140	6.0	720	30
29Alr	140	6.0	718	30
29Alrr	140	6.0	720	30
70Ale	140	7.0	738	34
32Al	140	8.0	726	39
32Alr	140	8.0	734	38
32Alrr	140	8.0	751	38
35Alrr	140	8.9	722	43
35Al	140	9.0	726	44
50Alf	160	5.0	715	25
30Al	160	6.0	726	29
30Alrr	160	6.0	744	29
70Alf	160	7.5	777	34
33Al	160	8.0	728	39
33Alrr	160	8.0	761	37
36Alrr2	160	8.0	722	39
36Al	160	8.5	722	41
36Alrr	160	9.0	693	46

Table B-1. Conditions for pseudo three-dimensional high-speed video of spray autoignition for a 0.2 mm VCO nozzle.

Appendix C: Laser-induced incandescence

Characteristics of image intensifier relay optics

The main characteristics of the image intensifier and CCD camera are listed in Table C-1. Figures C-1, C-2 and C-3 show the image intensifier's sensitivity, response and gain charts, respectively.

Intensifier sensitivity	
Camera sensitivity (max)	160 counts / photoelectron
Reference gain	63 (corresponds to 1 count / photoelectron)
Intensifier gate (min)	5 ns
Gating repetition rate (max)	2 kHz
CCD characteristics	
CCD resolution	1280x1024 pixels
Effective pixel size	14.5 μm
Dark image intensity	55 counts
RMS	1.8 counts
A/D conversion factor	5 electrons / count
Readout frequency	12.5 MHz
Readout time / frame	120 ms

Table C-1. Image intensifier and CCD camera characteristics.

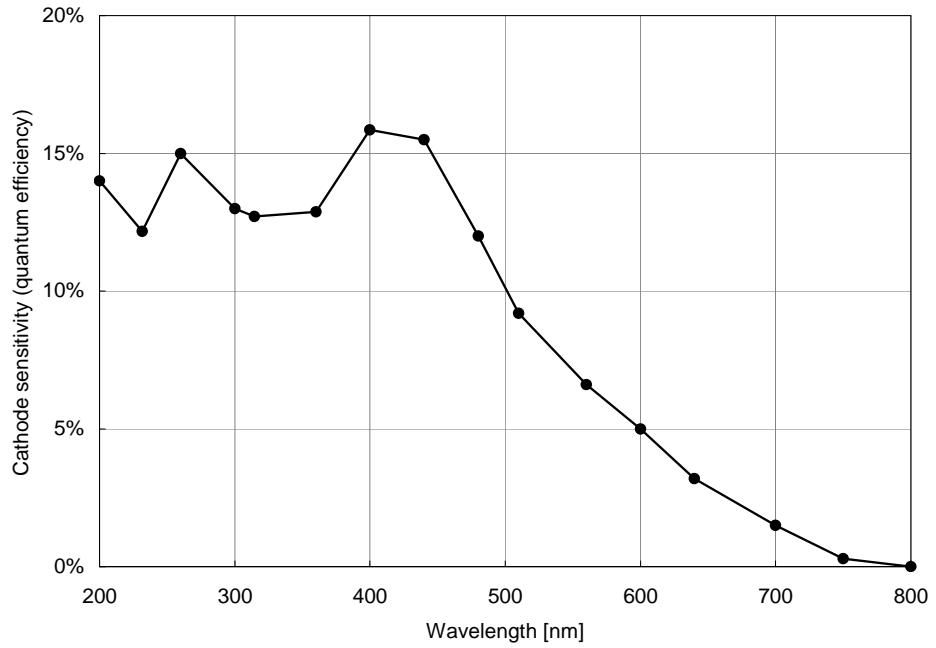


Figure C-1. Image intensifier's cathode sensitivity to signal wavelength.

It can be seen from Figure C-1 that the image intensifier's sensitivity to wavelength is nearly constant in the region of the selected LII collection wavelength (416 ± 32 nm).

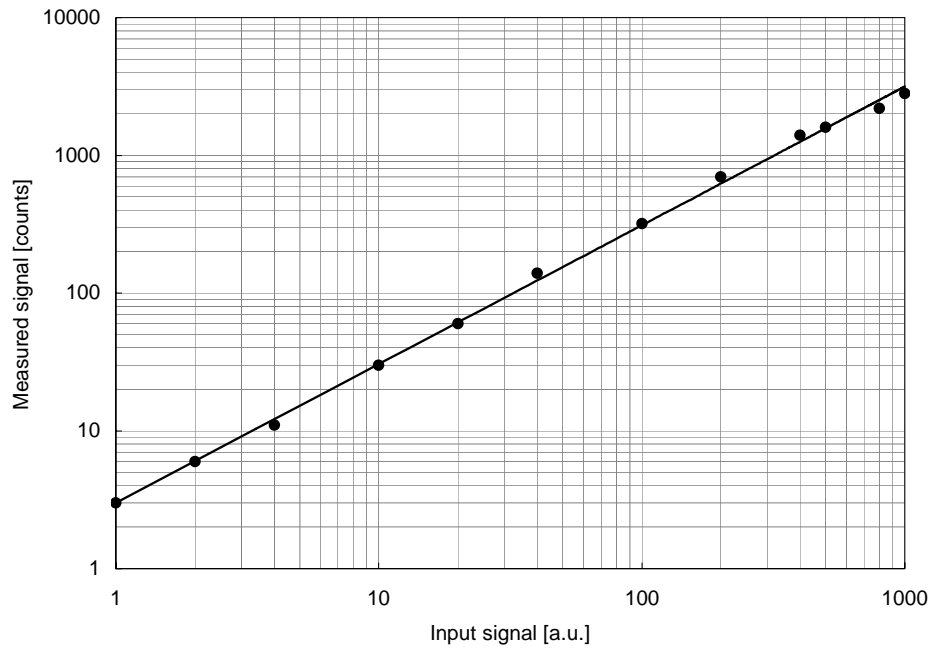


Figure C-2. CCD camera response to signal intensity.

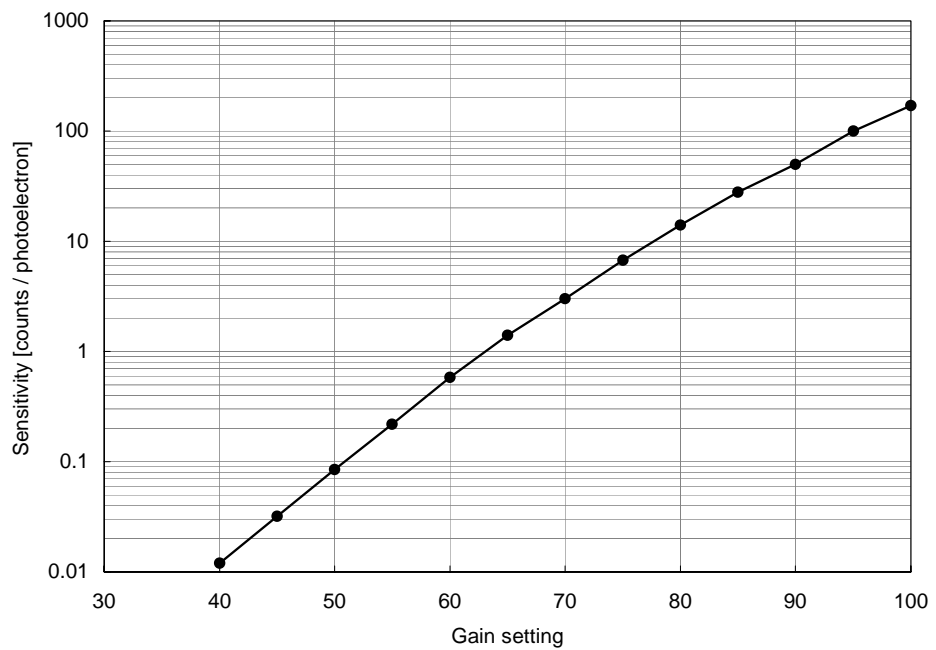


Figure C-3. Image intensifier's gain calibration. The gain used for gathering the LII data presented in Chapter 6 was 70.

Example of LII data set

A complete LII data set is presented in Figures C-4 and C-5, for an injection pressure of 140 MPa, an in-cylinder pressure of 8 MPa. All images were recorded 3.8 ms after start of injection pulse. The ensemble averaged and standard deviation images for this data set are shown in Section 6.3.4.

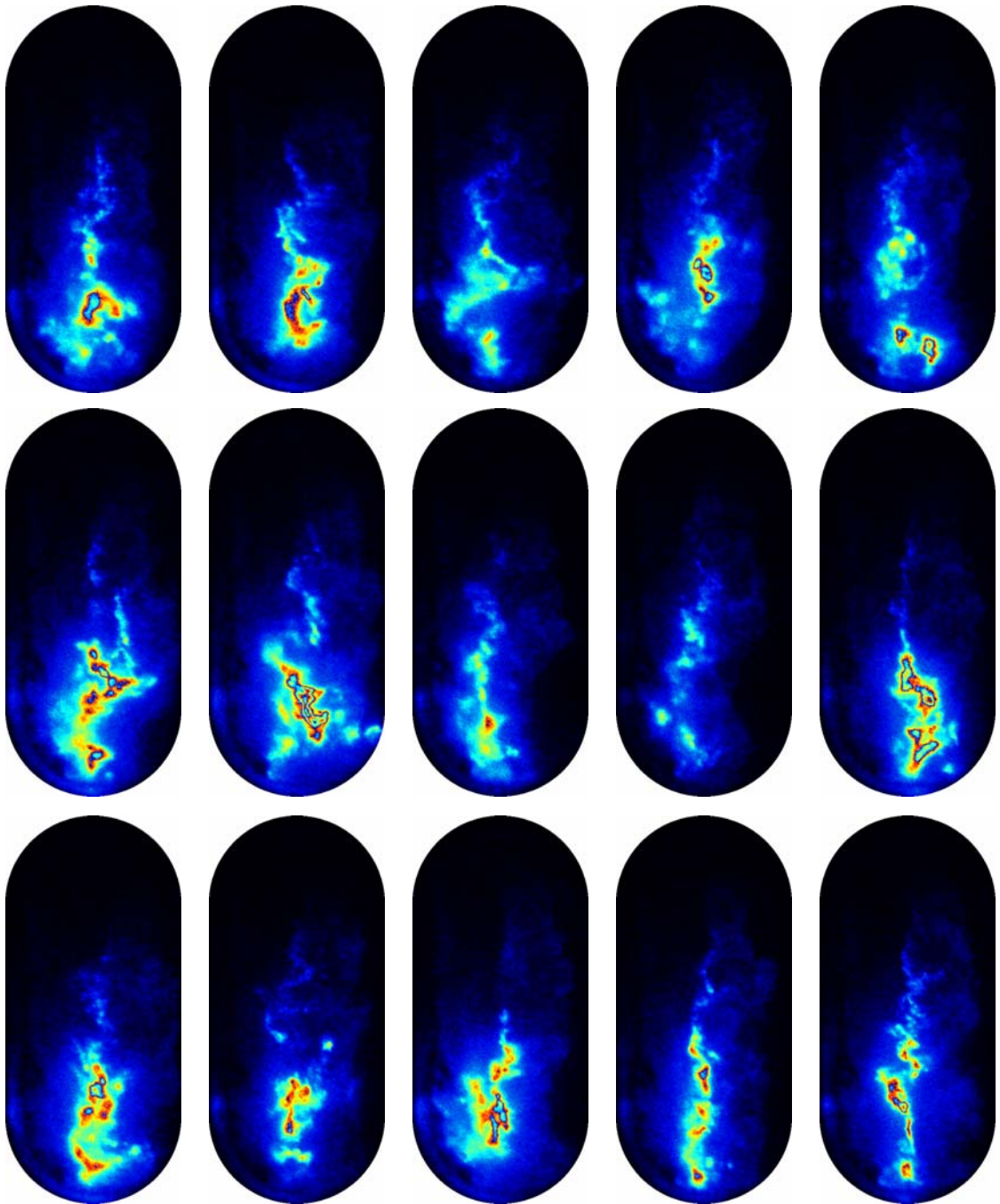


Figure C-4. LII images 1 to 15 of data set 'LII 122'.

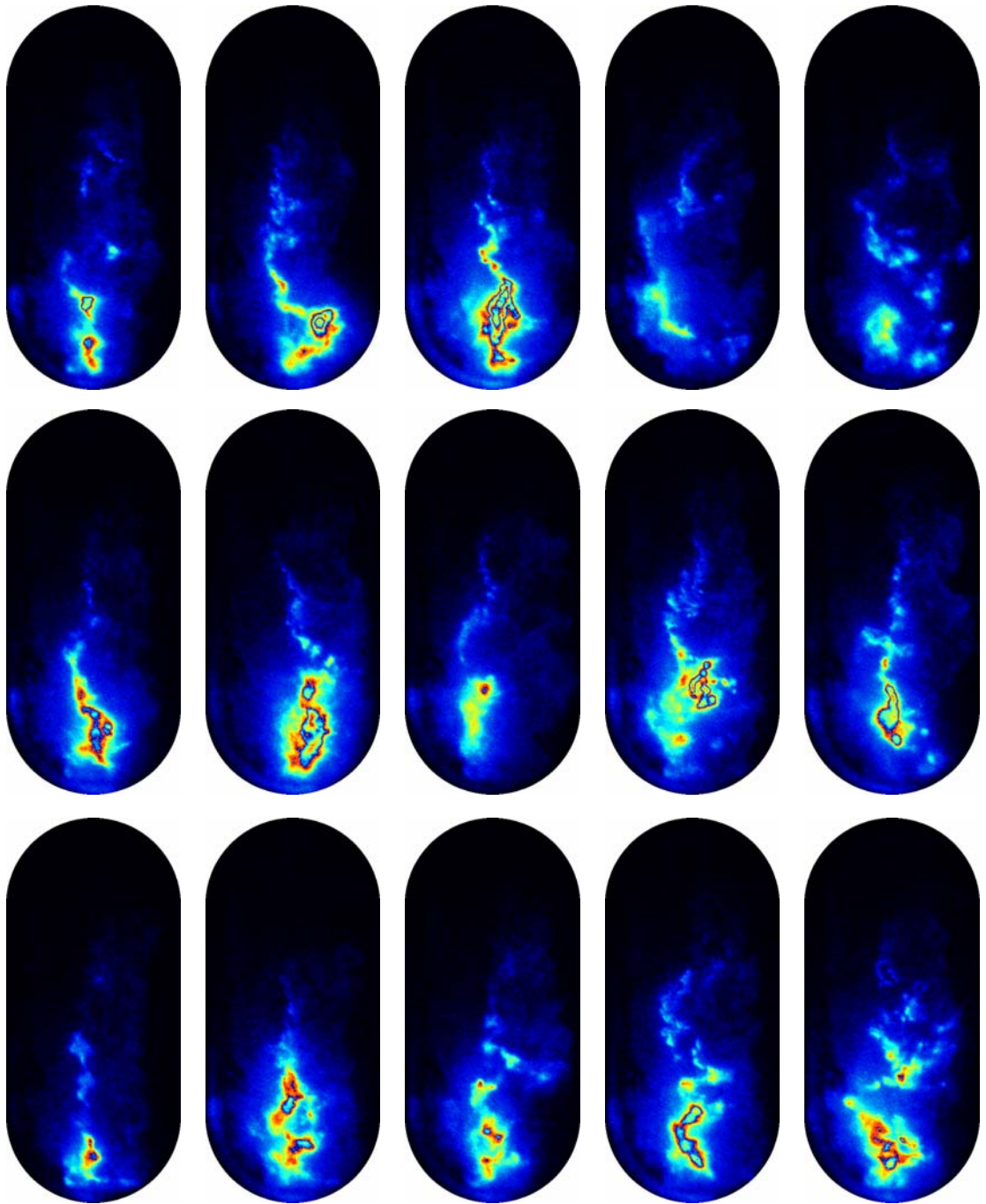


Figure C-5. LII images 16 to 30 of data set 'LII 122'.

All LII images correspond to field of views approximately 30 mm in width and 65 mm in height. The top of each image is 12 mm further down of the injector nozzle.

Experimental conditions for LII data sets

Test name	ICP at non-fired TDC [MPa]	Temperature at TDC [K]	Gas density [kg m ⁻³]	Recording time [ms ASOI]	Average intensity [a.u.]
LII136	6.0	722	29	2.2	0.01
LII140	6.0	720	30	2.3	0.13
LII144	6.0	724	29	2.4	2.23
LII148	6.0	728	29	2.8	2.32
LII153	6.0	726	29	3.3	8.60
LII157	6.0	724	29	3.6	8.78
LII161	6.0	726	29	4.0	8.96
LII165	6.0	724	29	4.3	12.57
LII169	6.0	726	29	4.6	11.54
LII173	6.0	726	29	5.0	7.54
LII137	7.0	720	34	2.1	0.01
LII141	7.0	718	34	2.3	0.91
LII145	7.0	718	34	2.4	1.16
LII149	7.0	720	34	2.7	4.54
LII154	7.0	720	34	3.2	8.89
LII158	7.0	718	34	3.5	7.44
LII162	7.0	718	34	3.9	6.81
LII166	7.0	720	34	4.2	13.65
LII170	7.0	718	34	4.5	9.94
LII174	7.0	722	34	4.9	8.71
LII138	8.0	718	39	2.0	0.01
LII142	8.0	716	39	2.3	0.77
LII146	8.0	716	39	2.3	0.54
LII150	8.0	722	39	2.7	4.57
LII155	8.0	718	39	3.0	7.52
LII159	8.0	714	39	3.4	7.36
LII163	8.0	724	39	3.7	7.56
LII167	8.0	720	39	4.1	13.22
LII171	8.0	718	39	4.4	12.61
LII175	8.0	718	39	4.7	10.17
LII139	8.6	722	42	2.3	0.94
LII143	8.6	720	42	2.3	0.71
LII147	8.6	722	42	2.4	1.74
LII164	9.0	716	44	3.6	7.24
LII172	9.0	718	44	4.3	11.57
LII168	9.1	722	44	3.9	11.90
LII151	9.2	720	45	2.5	3.05
LII156	9.2	720	45	2.9	6.78
LII160	9.2	724	45	3.2	7.15

Table C-2. LII data set averages for an injection pressure of 100 MPa.

Appendix C: Laser-induced incandescence

Test name	ICP at non-fired TDC [MPa]	Temperature at TDC [K]	Gas density [kg m ⁻³]	Recording time [ms ASOI]	Average intensity [a.u.]
LII97	6.0	726	29	2.0	0.41
LII100	6.0	732	29	2.3	1.51
LII104	6.0	726	29	2.7	6.77
LII108	6.0	728	29	3.0	6.64
LII112	6.0	724	29	3.3	7.15
LII116	6.0	724	29	3.7	6.91
LII120	6.0	720	30	4.0	10.02
LII124	6.0	728	29	4.3	9.65
LII128	6.0	722	29	4.7	0.09
LII98	7.0	718	34	1.9	0.24
LII101	7.0	722	34	2.2	1.33
LII105	7.0	720	34	2.5	4.71
LII109	7.0	722	34	2.9	6.60
LII113	7.0	722	34	3.2	7.30
LII117	7.0	722	34	3.6	7.80
LII121	7.0	712	35	3.9	9.47
LII125	7.0	718	34	4.2	9.67
LII129	7.0	722	34	4.6	0.32
LII99	8.0	718	39	1.8	0.17
LII102	8.0	720	39	2.1	0.54
LII106	8.0	718	39	2.5	4.40
LII110	8.0	722	39	2.8	4.99
LII114	8.0	718	39	3.1	6.51
LII118	8.0	718	39	3.5	7.98
LII122	8.0	714	39	3.8	11.03
LII126	8.0	714	40	4.1	14.34
LII130	8.0	714	40	4.5	1.07
LII131	8.5	726	41	4.5	2.81
LII103	8.7	728	42	2.1	0.30
LII107	8.7	722	42	2.4	2.78
LII115	8.7	728	42	3.1	5.18
LII119	8.7	722	42	3.4	7.18
LII123	8.7	722	42	3.8	11.88
LII127	8.7	718	43	4.1	11.46
LII111	8.8	722	43	2.7	4.15

Table C-3. LII data set averages for an injection pressure of 140 MPa.

Test name	ICP at non-fired TDC [MPa]	Temperature at TDC [K]	Gas density [kg m ⁻³]	Recording time [ms ASOI]	Average intensity [a.u.]
LII40	6.0	720	30	2.1	0.10
LII41	6.0	724	29	2.3	2.80
LII45	6.0	726	29	2.3	1.68
LII49	6.0	720	29	2.3	2.11
LII51	6.0	726	29	2.7	5.34
LII55	6.0	720	29	3.0	5.91
LII59	6.0	724	29	3.3	6.08
LII63	6.0	724	29	3.6	8.69
LII67	6.0	722	29	4.0	5.98
LII70	6.0	724	29	3.9	10.35
LII74	6.0	726	29	4.2	1.89
LII78	6.0	726	29	4.6	0.46
LII82	6.0	728	29	1.9	0.42
LII85	6.0	728	29	2.0	0.22
LII89	6.0	726	29	2.2	1.09
LII93	6.0	728	29	2.4	5.82
LII133	6.0	718	30	3.9	8.20
LII152	6.0	724	29	3.3	8.74
LII35	6.9	722	34	2.2	2.99
LII37	7.0	728	34	2.0	0.57
LII42	7.0	722	34	2.2	3.84
LII46	7.0	718	34	2.2	2.98
LII50	7.0	718	34	2.2	2.38
LII52	7.0	718	34	2.5	5.54
LII56	7.0	720	34	2.8	6.05
LII60	7.0	718	34	3.2	9.65
LII64	7.0	722	34	3.6	8.60
LII68	7.0	718	34	3.9	8.28
LII71	7.0	720	34	3.8	10.76
LII75	7.0	718	34	4.1	4.69
LII79	7.0	720	34	4.5	0.30
LII83	7.0	722	34	1.8	0.53
LII86	7.0	716	35	2.1	0.85
LII90	7.0	718	34	2.2	3.26
LII94	7.0	716	35	2.3	5.18
LII134	7.0	724	34	3.8	9.18

Table C-4. LII data sets for an injection pressure of 160 MPa.

Appendix C: Laser-induced incandescence

Test name	ICP at non-fired TDC [MPa]	Temperature at TDC [K]	Gas density [kg m ⁻³]	Recording time [ms ASOI]	Average intensity [a.u.]
LII36	8.0	722	39	2.1	3.74
LII38	8.0	720	39	1.9	0.63
LII43	8.0	718	39	2.1	4.27
LII47	8.0	720	39	2.1	3.31
LII53	8.0	722	39	2.5	4.92
LII57	8.0	720	39	2.8	6.41
LII61	8.0	724	39	3.1	8.95
LII65	8.0	716	39	3.5	10.63
LII69	8.0	724	39	3.8	9.14
LII72	8.0	724	39	3.7	10.79
LII76	8.0	720	39	4.1	8.22
LII80	8.0	716	39	4.4	0.23
LII84	8.0	716	39	1.8	0.42
LII87	8.0	718	39	2.0	1.48
LII91	8.0	718	39	2.1	2.84
LII95	8.0	718	39	2.3	4.38
LII135	8.0	714	39	3.8	10.21
LII39	8.5	720	42	1.9	0.65
LII44	8.5	726	41	2.1	3.78
LII48	8.5	724	41	2.1	3.34
LII62	8.6	720	42	3.1	9.75
LII77	8.6	720	42	4.1	7.11
LII92	8.6	724	42	2.2	3.18
LII54	8.7	726	42	2.4	4.47
LII58	8.7	722	42	2.7	6.16
LII66	8.7	716	43	3.4	9.37
LII73	8.7	724	42	3.7	10.66
LII81	8.7	720	43	4.4	0.33
LII88	8.7	726	42	2.0	1.31
LII96	8.8	722	43	2.3	4.12

Table C-4. LII data sets for an injection pressure of 160 MPa (continued).

Experimental conditions for LII sequence

Conditions for LII sequence shown in Section 6.4.3. Injection pressure was 160 MPa, fuelling 30 mm³, injection angle 15 CA BTDC, skipfiring ratio 3:1.

Test name	ICP at non-fired TDC [MPa]	Temperature at TDC [K]	Gas density [kg m ⁻³]	Recording time [ms ASOI]	Average intensity [a.u.]
1600 60 -15 avg01	6.0	734	29	1.96	0.01
1600 60 -15 avg02	6.0	732	29	2.01	0.65
1600 60 -15 avg03	6.0	728	29	2.06	1.99
1600 60 -15 avg04	6.0	726	29	2.11	2.79
1600 60 -15 avg05	6.0	724	29	2.16	5.86
1600 60 -15 avg06	6.0	722	29	2.21	7.59
1600 60 -15 avg07	6.0	720	30	2.26	8.60
1600 60 -15 avg08	6.0	718	30	2.31	9.81
1600 60 -15 avg09	6.0	716	30	2.36	11.98
1600 60 -15 avg10	6.0	714	30	2.41	13.24
1600 60 -15 avg11	6.0	714	30	2.46	12.33
1600 60 -15 avg12	6.0	714	30	2.51	12.08
1600 60 -15 avg13	6.0	714	30	2.56	13.64
1600 60 -15 avg14	6.0	714	30	2.61	13.79
1600 60 -15 avg15	6.0	714	30	2.66	13.26
1600 60 -15 avg16	6.0	714	30	2.71	13.75
1600 60 -15 avg17	6.0	714	30	2.76	12.93
1600 60 -15 avg18	6.0	714	30	2.81	11.57
1600 60 -15 avg19	6.0	714	30	2.86	12.67
1600 60 -15 avg20	6.0	714	30	2.91	14.15
1600 60 -15 avg21	6.0	714	30	2.96	15.55
1600 60 -15 avg22	6.0	714	30	3.01	16.44
1600 60 -15 avg23	6.0	714	30	3.06	14.55
1600 60 -15 avg24	6.0	714	30	3.11	17.15
1600 60 -15 avg25	6.0	716	30	3.16	14.96
1600 60 -15 avg26	6.0	716	30	3.21	14.90
1600 60 -15 avg27	6.0	716	30	3.26	15.87
1600 60 -15 avg28	6.0	716	30	3.31	15.21
1600 60 -15 avg29	6.0	716	30	3.36	16.02
1600 60 -15 avg30	6.0	716	30	3.41	15.52
1600 60 -15 avg31	6.0	716	30	3.46	15.76
1600 60 -15 avg32	6.0	716	30	3.51	14.49
1600 60 -15 avg33	6.0	716	30	3.56	17.88
1600 60 -15 avg34	6.0	716	30	3.61	18.43
1600 60 -15 avg35	6.0	716	30	3.66	16.78
1600 60 -15 avg36	6.0	716	30	3.71	16.65
1600 60 -15 avg37	6.0	716	30	3.76	16.06
1600 60 -15 avg38	6.0	716	30	3.81	16.62

Table C-5. Conditions for LII sequence shown in Section 6.4.3.

Test name	ICP at non-fired TDC [MPa]	Temperature at TDC [K]	Gas density [kg m ⁻³]	Recording time [ms ASOI]	Average intensity [a.u.]
1600 60 -15 avg39	6.0	718	30	3.86	14.65
1600 60 -15 avg40	6.0	718	30	3.91	10.51
1600 60 -15 avg41	6.0	718	30	3.96	8.46
1600 60 -15 avg42	6.0	718	30	4.01	4.72
1600 60 -15 avg43	6.0	718	30	4.06	4.04
1600 60 -15 avg44	6.0	718	30	4.11	2.15
1600 60 -15 avg45	6.0	718	30	4.16	0.67
1600 60 -15 avg46	6.0	718	30	4.21	0.31
1600 60 -15 avg47	6.0	718	30	4.26	0.31
1600 60 -15 avg48	6.0	718	30	4.31	0.05
1600 60 -15 avg49	6.0	718	30	4.36	0.01
1600 60 -15 avg50	6.0	718	30	4.41	0.01
1600 60 -15 avg51	6.0	718	30	4.46	0.01
1600 60 -15 avg52	6.0	718	30	4.51	0.01
1600 60 -15 avg53	6.0	718	30	4.56	0.01
1600 60 -15 avg54	6.0	718	30	4.61	0.01
1600 60 -15 avg55	6.0	718	30	4.66	0.01

Table C-5. Conditions for LII sequence shown in Section 6.4.3 (continued).

Influence of fuel pressure on soot formation

Ensemble averaged images presented in Figures C-6 to C-9 show the influence of injection pressure on early soot formation, for in-cylinder pressures between 6 and 9 MPa.

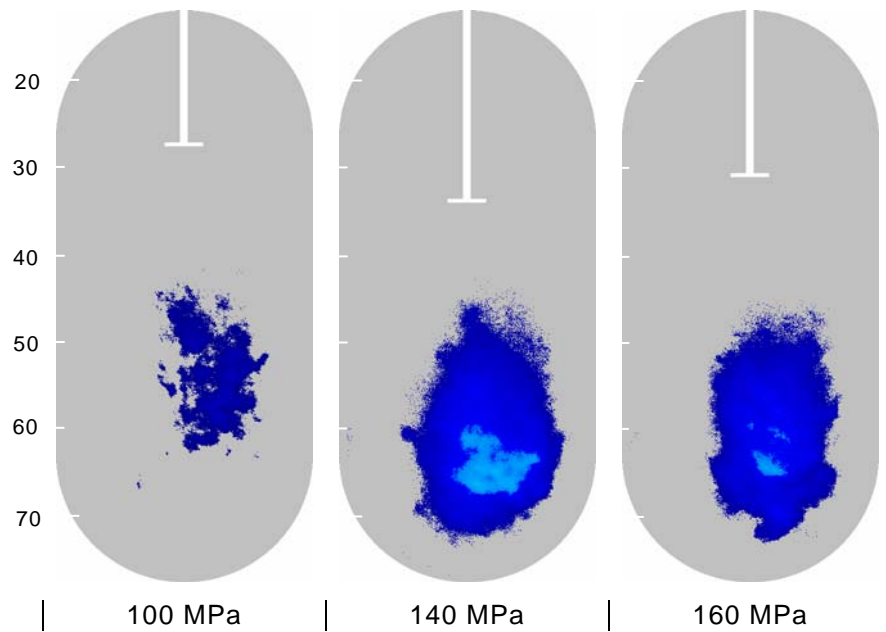


Figure C-6. Ensemble averaged images showing the effect of injection pressure on initial soot formation sites. Images were recorded between 2.2 and 2.3 ms ASOI, for an ICP of 6.0 MPa at non-fired TDC. Contrast was enhanced for clarity, white lines show ensemble averaged liquid fuel penetration measurement by simultaneous LIS, scales indicate distances from the nozzle in millimetres.

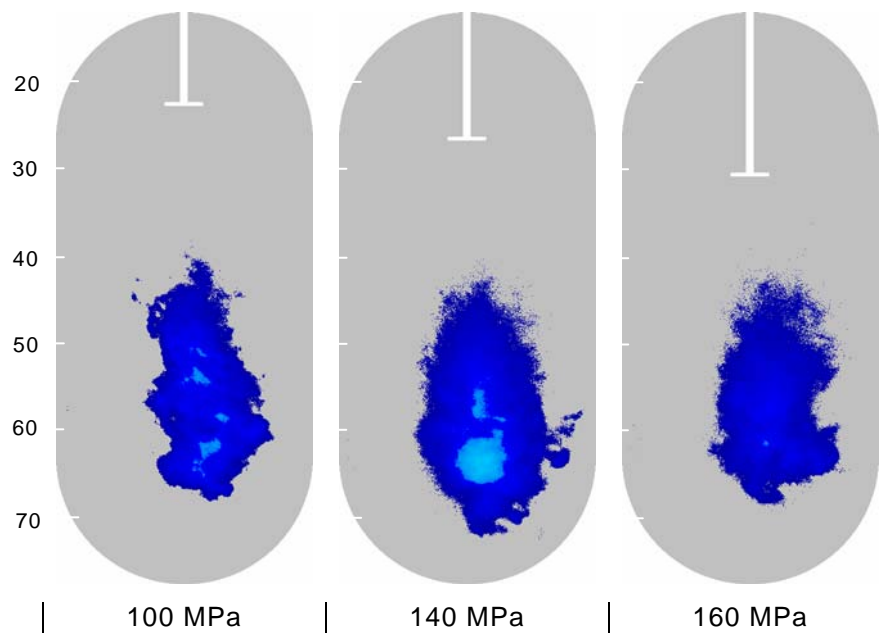


Figure C-7. As in Figure C-6 but for an ICP of 7.0 MPa at non-fired TDC. Images were recorded between 2.1 and 2.3 ms ASOI.

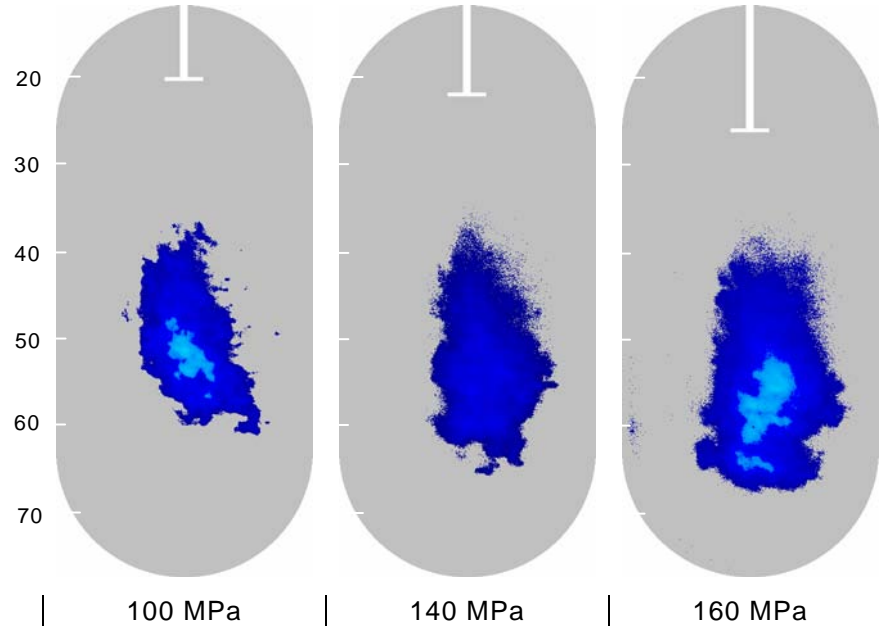


Figure C-8. As in Figure C-6 but for an ICP of 8.0 MPa at non-fired TDC. Images were recorded between 2.0 and 2.3 ms ASOI.

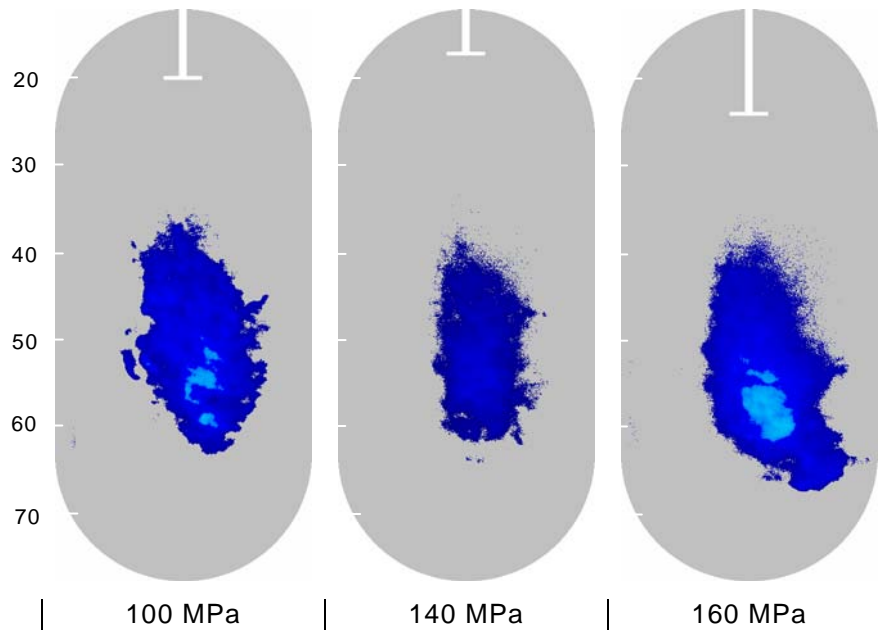


Figure C-9. As in Figure C-6 but for ICPs between 8.7 and 9.0 MPa at non-fired TDC. Images were recorded between 2.0 and 2.3 ms ASOI.

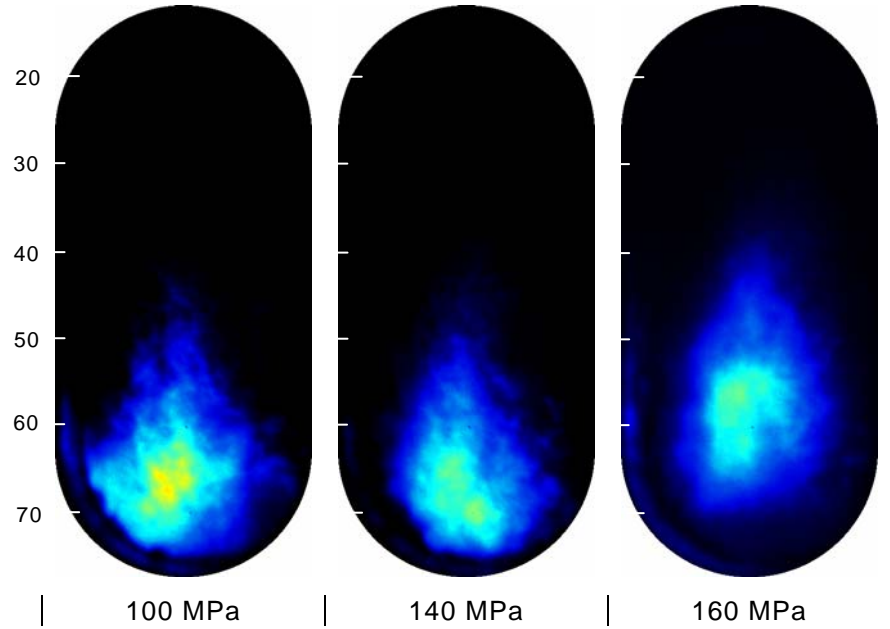


Figure C-10. Ensemble averaged images showing the influence of injection pressure on late soot concentration zones. Images were recorded between 3.6 and 3.7 ms ASOI, for an ICP of 6.0 MPa at non-fired TDC. Scales indicate distances from the nozzle in millimetres.

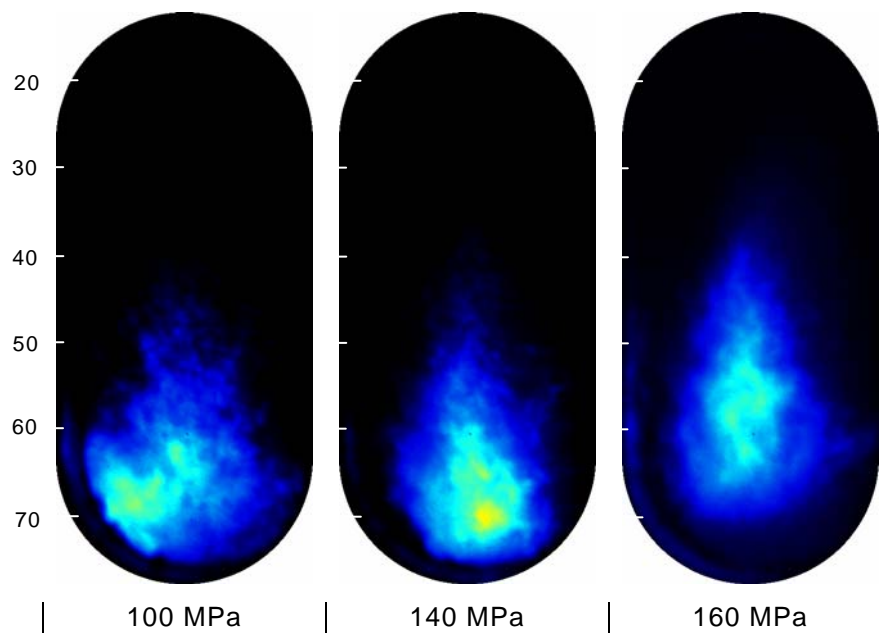


Figure C-11. As in Figure C-10 but for an ICP of 7.0 MPa at non-fired TDC. Images were recorded between 3.5 and 3.6 ms ASOI.

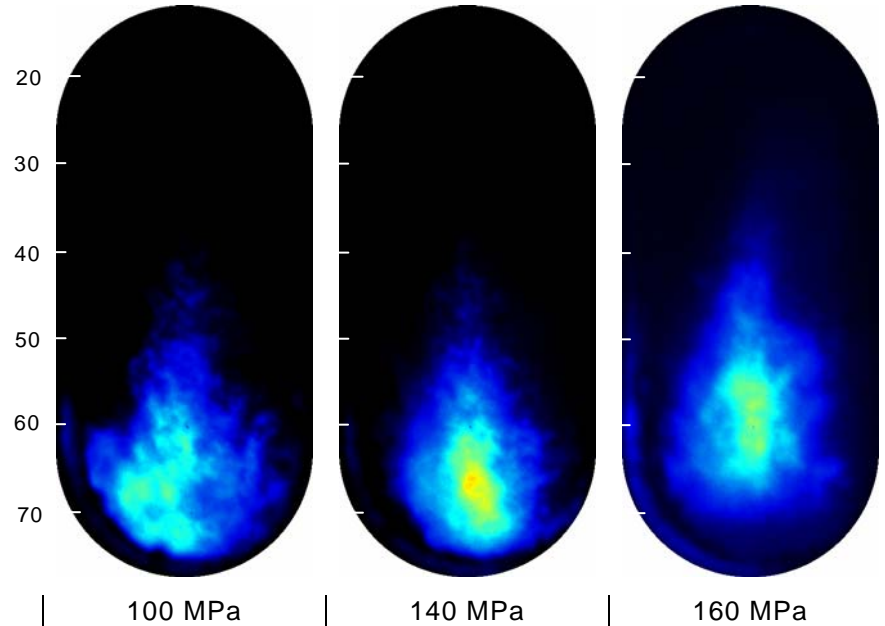


Figure C-12. As in Figure C-10 but for an ICP of 8.0 MPa at non-fired TDC. Images were recorded between 3.5 and 3.7 ms ASOI.

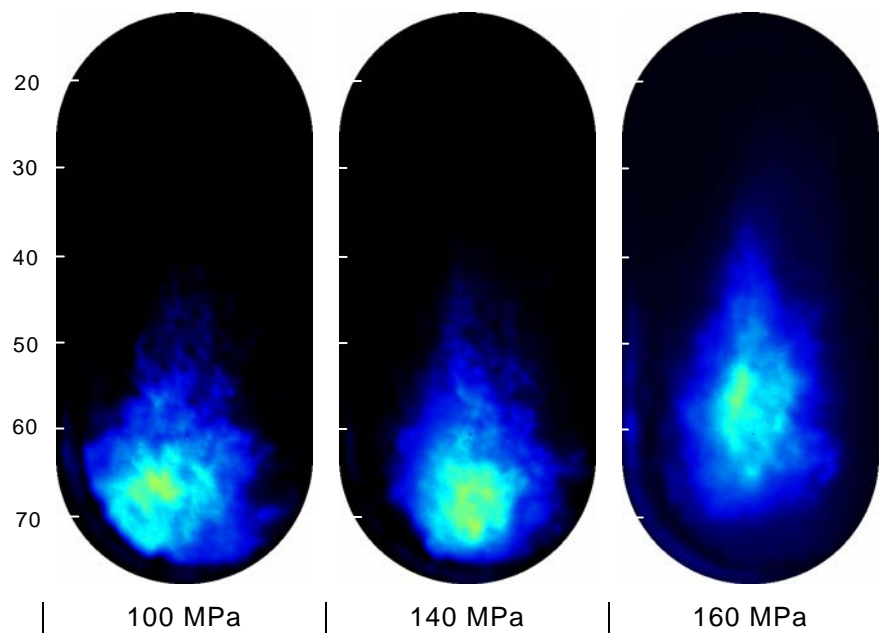


Figure C-13. As in Figure C-10 but for an ICP between 8.7 and 9.0 MPa at non-fired TDC. Images were recorded between 3.4 and 3.6 ms ASOI.